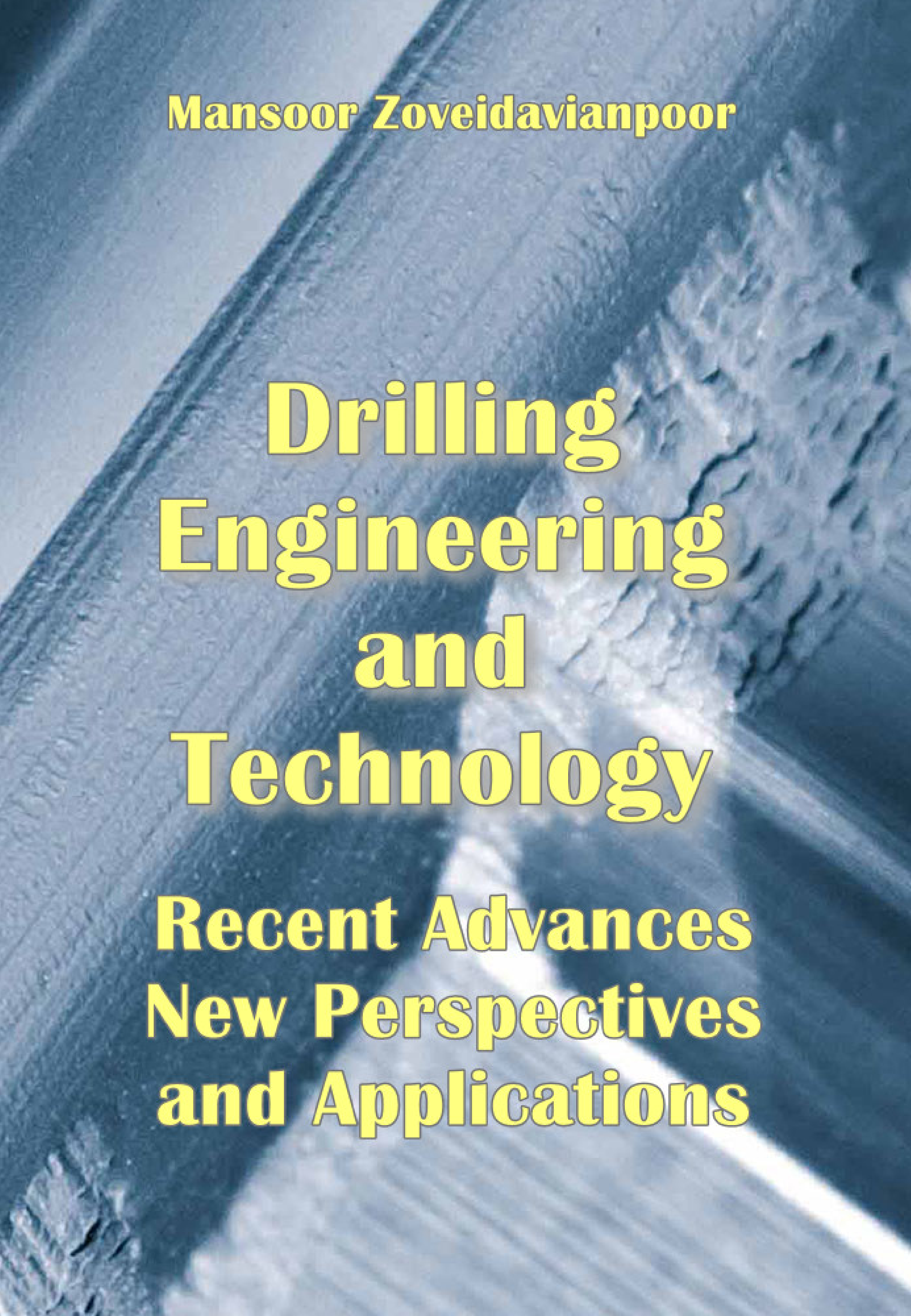

Mansoor Zoveidavianpoor

Drilling Engineering and Technology

Recent Advances New Perspectives and Applications

Chapter 1

Polymeric Nanoparticles in Drilling Fluid Technology

Nnaemeka Uwaezuoke

Abstract

New technologies are often sought to mitigate the problems associated with traditional drilling fluid formulations. Nanotechnology provides an alternative. A particle size of matter in the range of 1–100 nm in diameter (d.nm) is referred to as nanoparticle. Nanoparticles are broadly divided into various categories depending on their morphology, size and chemical properties. This size range lends their application in science and engineering. In rotary drilling operations where drilling fluid is at the center, performance and optimization issues have been observed. Use of polymer nanoparticles in mud formulations have been considered due to desirable properties such as wide specific surface area, high temperature stability and pollution resistance. Areas of application and advantages include improvement in mud rheology, fluid loss properties, improved lubricity, filter against hazard materials and cost effectiveness. Biodegradable polymeric nanoparticles possess the outlined properties and would continue to offer wider applications in drilling fluid technology now and in the nearest future due to their stable, film forming and gelatinization characteristics. To reliably estimate the quantity of polymeric nanoparticles to use, size and shape should be considered before concentration to apply to make prediction easier. Dispersion of different shapes, sizes and structures of polymeric nanoparticles might be a consideration to enhance polymer influence on fluid formulations.

Keywords: biodegradable, drilling fluid, nanoparticle, polymeric, rheology, fluid loss, thermal stability

1. Introduction

The drilling fluid is a general term for liquid-based, gas-based and combinations thereof that serves as the focus in a circulating system of a rotary drilling rig. Usually, it is designed to perform certain functions, possess the required properties to furnish the desired functions and satisfy recommended specifications when tests are conducted [1, 2]. Its design involves basic knowledge of chemistry, physics, mathematics and sound knowledge of petroleum engineering principles and oilfield practices.

2. Background

The drilling fluid provides the hydrostatic pressure necessary to balance the formation or pore pressure to control influx into the wellbore or prevent kick and blowout. This is achieved by using a densifier additive. The densifier also controls the buoyancy force for partial drillstring suspension in order to reduce the derrick load. Also, for effective wellbore cleaning and cleaning beneath the drill bit, the drilling fluid must possess viscosity as a property in addition to the required fluid hydraulics objective functions. Such objectives or combinations include hydraulic horsepower, jet velocity, Reynolds number and jet impact force. The fluid should also be able to suspend cuttings in the annulus when drilling is interrupted, and release the cuttings in the solids control equipment; the thixotropic property. Similarly, the fluid should have high heat capacity to be able to cool the drillstring and bit. It can also serve as a lubricant in the system. It is also designed to reduce or prevent formation damage and seal permeable formations by application of its fluid loss property. It must also control wellbore stability by preventing hydration of hydratable clays and retard other factors. Corrosion is also prevented by addition of agents that control the pH of the fluid. It must also be able to transmit hydraulic horsepower to the bit by maintaining its desired phase at every point. Formation evaluation must not also be interrupted. Nonetheless, in oil-based and water-based drilling fluids, it is the filtrate invasion that causes interruption of formation evaluation [3]. It is the fluid loss property that controls it. Zones of filtrate invasion and filter cake deposition are (i) the invaded zone into the formation (ii) the external cake on the wall of the wellbore and (iii) the internal cake that extends inches into the formation. An example is in the determination of petrophysical property known as resistivity. Low resistivity salty water-filled rocks are distinguishable from high resistivity hydrocarbon-filled rocks [4]. Even deep reading resistivity tools may only provide investigation data at depth not beyond the invaded zone. This leads to corrections to get the true formation resistivity that might introduce errors. This may be prevented by deposition of a suitable filter cake thickness with other qualities such as slickness, toughness and permeability. The high quality cake would prevent not only deep filtrate invasion but also formation damage.

Fluid systems have been developed to furnish and control the functions outlined. Based on the base fluid and materials deliberately added to the mud, such systems include; (i) air, gas, foam, mist (ii) calcium treated (iii) dispersed (iv) low lipids (v) non-dispersed (vi) oil/synthetic (vii) polymer (viii) saturated salt and (ix) workover fluid [5]. Cost, downhole conditions, type of well and environmental consideration are some factors that control the choice of drilling fluid type for application.

The traditional fluid systems have limitations that impede complete performance of the functions outlined. For instance, water based mud systems have the tendency to dissolve salts that might lead to density increase. Similarly, interference with oil and gas flow and clay dispersion has been potential problems. Moreso, oil based mud are not cost effective and pose environmental challenges. Gas based fluids have the tendency to cause explosion and cannot be used through water bearing formation. The stability observed under atmospheric conditions might not exist under high temperature and high pressure observed at increased depths both in marine and land environments. In deep offshore drilling, formation of hydrate also poses challenge. Though additives added to drilling fluids are expected to prevent or limit the adverse effects the conventional drilling fluids might experience, oilfield experience shows that problems still occur. New technologies are often sought to mitigate these problems. The field of nanoscience, where nanoparticles with desirable attributes are evaluated for application, provides an alternative.

3. Nanoparticles: classification and attributes in formulations

The science and technology of fine particles is known as micromeritics. Through understanding of their characteristics, thousands of nanoproducts exist, and they are mainly used in drug delivery [6, 7]. Introduction of nanoparticles in drilling fluid have been under investigation, and have been applied over a decade ago. They have the potential to create changes in size and composition that result into formulations that could be adopted for a wide range of operating conditions even in small concentrations. Nanoparticles can be organic or inorganic on the basis of molecular weight and durability. Similarly, organic nanoparticles can be natural or synthetic and involves organic or polymeric molecules. These biopolymer nanoparticles are biodegradable and highly stable in fluids and storage [8] and include cellulose nanoparticles (CNP) where cellulose nanofibers and cellulose nanocrystals are examples [9], chitosan nanoparticles, starch nanoparticles (SNP), lignin and pullulan nanoparticles, alginate and gliadin nanoparticles, polylactic acid (PLA) nanoparticles, and polycaprolactone (PCL) nanoparticles. Conventional carboxymethyl cellulose (CMC) and polyanionic cellulose (PAC) ground into smaller nanosize particles are also important substances. Cellulose is considered the most abundant biopolymer in the world.

The influence of size on the physic0-chemical properties of a substance cannot be overemphasized. Since the presentation made in 1959 by Richard P. Feynman, a Nobel laureate, on nanotechnology titled "*There's plenty of room at the bottom*", various strides in the field of nanotechnology have been recorded [10]. Nanotechnology enables evaluation of matter at nanoscale and enhances synthesis. Materials have been produced at nanoscale level. A particle size of matter in the range of 1 to 100 nanometers in diameter (d.nm) is referred to as nanoparticle, and could be 0D, 1D, 2D or 3D as reference dimension. Their surface to volume ratio is extremely high due to their submicroscopic size. It is an overlap of mesoscale, 1 to 1000 nm (polymeric nanoparticles), such as used in colloid science.

In drilling fluid formulations, with additives in the nanoparticle size range, significant improvement in drilling fluid properties have been documented [11]. Such fluids are referred to as nanofluids. This is further categorized as simple nanofluids with nanoparticles of single magnitude of particle distribution, and advanced nanofluids with diverse nanosize ranges of additives. They exhibit unique characteristics, hence, extraordinary potential for application in science and engineering [12], with particular interest in drilling fluid formulation. The base fluid could be water or oil. They have the potential to modify drilling fluid properties such as plastic viscosity, yield point, gel strength, barite sag, fluid loss volume, filter cake thickness as well as improve thermal and wellbore stability. They are also used as pollution filters for cadmium and hydrogen sulphide, for improved lubricity, heavy metal absorption [13] and reduction of torque and drag. They are applicable both in atmospheric and high-temperature high-pressure (HPHT) conditions.

They possess a variety of morphologies or shapes which help serve their objectives. **Figure 1** shows a comparison of nanoparticles with smaller and larger sized particles such as atoms and cancer cells respectively. Structures of nanoparticles contain hundreds of atoms. In other words, nanoparticles are larger in size than simple molecules and atoms by hundredfold. By size, bacteria are larger in size than nanoparticles

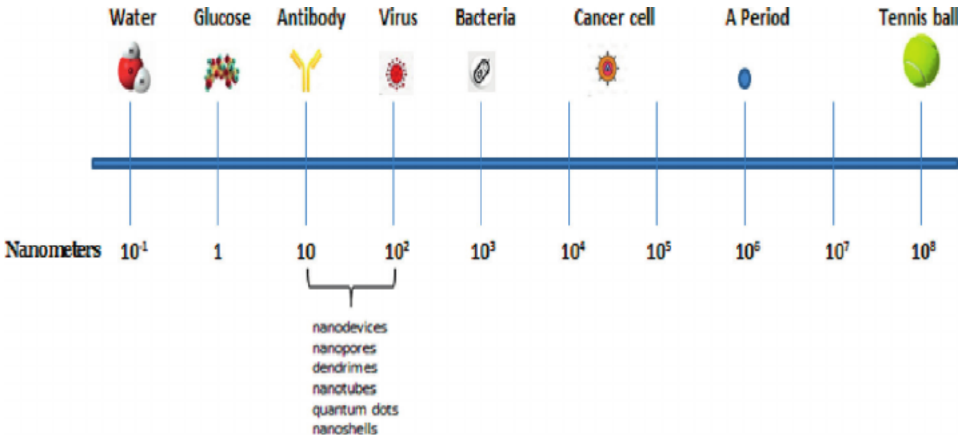

Figure 1.
Comparison of nanoparticles with other cells and atomic particles.

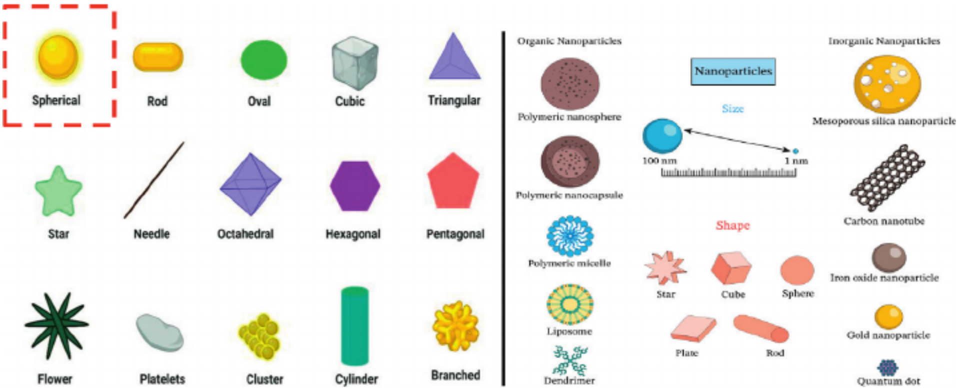

Figure 2.
Diverse shapes of nanoparticles [2, 14].

which can be used as barrier to prevent their activity. Their application in medicine has shown remarkable progress.

Nanoparticles exist in several shapes (**Figure 2**), and can further be classified based on crystallinity (amorphous and crystalline), nature of material (bimetallic, metallic chalcogenides, metallic oxides, organic, pure metals), origin and source (anthropogenic and natural), phase composition (multiphase solids, single phase solids), and shape and dimension (0D, 1D, 2D, 3D). Prism and helical shaped nanoparticles also exist.

For polymeric nanoparticles of organic origin such as cellulose and starch that are polysaccharides, the nanofluids formed exhibit unique properties and are called nanogels. They have been used both in water-based and oil-based drilling fluid formulations, where they served as viscosifier and fluid loss control additives. They are biodegradable, can act as antibacterial agents and are economically efficient since a relatively small quantity is required to create the nanogel. Generally, ceramic nanoparticles can be used for purification and pollution control activities. For instance, zinc oxide has been used to remove hydrogen sulphide in drilling muds. This is because hydrogen sulphide can dissolve in metal ions. At low concentrations, zinc oxide has been applied for antibacterial control due to high surface area to volume ratio in addition to distinctive physical and chemical characteristics. The metal nanoparticles have applications in catalysis, packaging, bio-engineering, cosmetics, water treatment, medicine and drug delivery, electronics, semiconductors, automobiles, paints, biosensors and soil pollutant removal. Carbon-based nanoparticles such as graphene can be combined with corrosion-protection chemicals to be an anti-corrosive material. In drilling fluid, it can act as a barrier to retard oxidation of hydrogen sulphide that can cause corrosion. In salty water based muds and situations where the mud becomes acidic due to intrusion of substances, graphene can serve as barrier against the chemical attack that causes corrosion. Categories of nanoparticles is shown in **Figure 3**, while their influences on drilling fluid properties and size ranges and concentrations applied are shown in **Tables 1** and **2**, respectively.

Three types of gels are recognized in drilling fluid engineering. They include (i) zero-zero gels with gel strength too low and initial or 10 s and 10 min gel strengths close to zero. It is easier for cuttings to settle or barites to sag in this system, (ii) flat gels with initial and 10 min gel strengths having similar values. Gel strength would be maintained and mud will remain pumpable after left quiescent and (iii) progressive gels where there would be appreciable difference between the initial and 10 min gel strengths, with higher 10 min gel strength value [15]. This signifies rapid gelling of drilling fluid and excessive pump pressure would be required to pump the fluid with time. Multi-walled carbon nanotubes and Yttrium oxide showed flat gels, whereas copper (II) oxide, aluminum oxide and bismuth ferrite showed progressive gels (**Table 1**). However, Silicon dioxide and Zinc oxide, both synthetic polymeric nanoparticles exhibited both flat and progressive gels. No clear trend was observed. The issue of progressive gel might be addressed by application of those materials in smaller concentration if other properties are satisfactory. Similarly, it could be

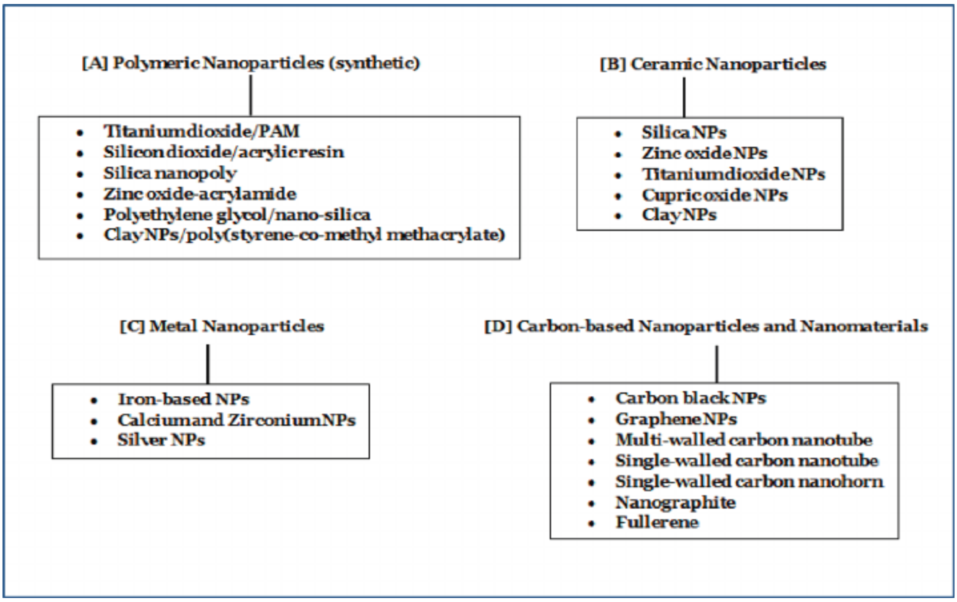

Figure 3.
Classification of nanoparticles.

Nanoparticle type	**Reported drilling fluid property value**		
	Initial gel strength [Pa]	**10 min. gel strength [Pa]**	**Fluid loss [mL]**
Silicon dioxide (SiO_2)	3.5, 13, 7	6.5, 32, 8	4.8, 7.2, 10, 5.1
Silver	—	—	2
Copper (II) oxide (CuO)	16	35	12
Multi-walled carbon nanotube (MWCNT)	4.5	7, 7	9, 5
Nanosilica	—	6	7
Sepiolite	—	—	8
Montmorillonite	—	21.5	7
Zinc oxide (ZnO)	15, 6	37, 9	14, 4.7
Graphene oxide	—	—	6.1
Aluminum oxide (Al_2O_3)	15, 11	39, 40	6
Yttrium oxide (Y_2O_3)	15	16	—
Calcium carbonate ($CaCO_3$)	—	—	5.7
Bismuth ferrite ($BiFeO_3$)	13	20	7.8

Table 1.
Nanoparticles used in drilling fluids and properties recorded [11].

observed that the carbon-based nanoparticles such as graphene, carbon and multi-walled carbon nanotubes were applied at lower concentrations (**Table 2**). Multi-walled carbon nanotube yielded a flat gel. Also, Silicon dioxide did not show any clear trend in optimal concentration when nanoparticle size was considered. In summary, carbon-based nanoparticles where the natural polymers in particular belong required addition in small concentrations to provide good gels and fluid loss properties. All the materials presented provided relatively good fluid loss properties irrespective of the types of gels observed.

4. Polymeric nanoparticles: structures, gelation and preparation

These are also known as polymer nanoparticles (PNP). Natural and synthetic (anthropologic) polymeric materials can be used to prepare nanoparticles. Whereas synthetic polymers can be derived from petroleum raw materials and are understandable due to controllable chemical composition, natural polymers are derived from animal and plant based sources [16]. Biocompatibility, biodegradability, nontoxicity at extensive scope of concentrations and economic viability are the incentives to use natural polymers. They are extracted or synthesized from different natural sources and have varying compositions as well as ubiquitous. These processes can make control difficult during application. Proteins, polysaccharides and other biodegradable polymers are examples. It is these polymeric materials that are applicable in drilling fluids for improved performance. Most natural polymers are cellulosic and gellable. As such, they can act as viscosifiers. In other applications in drilling fluid, polymer nanoparticles can be used to prevent and control corrosion [17]. Structures

Nanoparticle type	Nanoparticle size [nm]	Optimal concentration
Iron (III) oxide (Fe_2O_3)	3 and 30	0.5–2.0% wt.
Iron (III) oxide (Fe_2O_3)-clay hybrid	3 and 30	0.5% wt.
Iron (II, III) oxide (Fe_3O_4)	10–20	0.05–0.5% wt.
Silicon dioxide (SiO_2)	50	0.5% wt.
	10–20	5–10% wt.
	20	0.5% wt.
Titanium dioxide (TiO_2)	10–15	0.5–10% wt.
	20	0.1–0.3% volume fraction
Yttrium (III) oxide (Y_2O_3)	20–30	0.5–3% wt.
Copper (II) oxide (CuO) and Zinc oxide (ZnO)	50	0.1–0.5% wt.
Graphene	2.71	0.5% wt.
	<3	0.1–0.75% wt.
Multi-walled carbon nanotube (MWCNT)	30	0.001–0.1 ppb
	8–40	0.001–0.01% wt.
	100	0.1 ppb
Carbon	<200	0–1% wt.
Aluminum oxide (Al2O3)	40	0–1.5 gr.
	20	0.05% wt.
Graphite-alumina	80–400	0–0.8% wt.
Copper (II) oxide (CuO)	3	Acrylamide monomer/CuO: 10/1

Table 2.
Reported nanoparticles used in drilling fluids, size and concentration [11].

of some polymers are shown in **Figure 4**. It is seen that they contain chains of carbon held by strong covalent bonds resulting in very long molecules. However, two types of polymers (i) cross-linked and (ii) linear are common in the oil and gas industry for various purposes [18]. In linear polymers the carbon-carbon bonds form continuous chain. The outstanding valence bonds link with hydrogen. Physical attractions keep the polymeric chains together. Conversely, cross-linked polymers are formed by short covalent or ionic bonds of polymer chains linked with one another. There could be natural or synthetic types of this kind of polymers. Cross-linked polymers are stronger and more stable polymer materials. It is seen that the natural polymeric structures (**Figure 4**) could be either linear or cross-linking formed. Cellulose is a linear polymer of glucose units connected by β-1,4-glycosidic links. Starch, a mixture of amylose and amylopectin which are linear and branched chain polysaccharides is abundant. It is the chain of carbon atoms that make up organic materials that form polymers. They are categorized as organic compounds because of the presence of carbon. Another common element found is hydrogen. Whereas chitosan is a polycationic linear polymer, alginate is linear polyuronic and lignin is a 3D cross-linked irregular polyphenolic polymer. Pullulan is a linear polysaccharide formed by α-1,6-glycosidic assembly linkages. Therefore, these structures can form gels that affect the

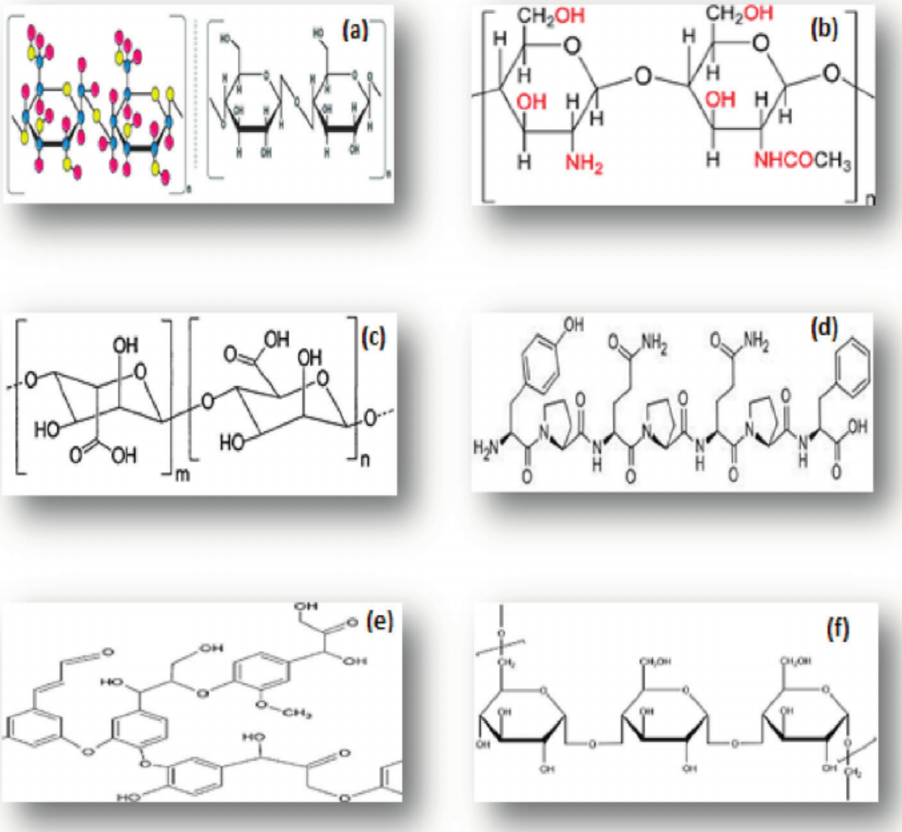

Figure 4.
Structures of (a) cellulose (b) chitosan (c) alginate (d) gliadin (e) lignin and (f) pullulan polymeric materials [16].

rheological behavior of drilling fluid formulations by influencing viscosity property. Structural units known as monomers combine to form these polymers. Moreso the long molecules from chains of carbon results in greater viscosity since the attraction due to intermolecular forces increases with longer chains. The higher intermolecular forces in the long chains give the polymers high melting point.

Moreso, based on their chemical structures, natural polymers could be proteins, polysaccharides or polyesters. Chitosan, alginates and cellulose are polysaccharides. Cellulose is more crystalline than starch, and it is the most abundant organic compound on earth. Its chemical formula is $[C_6H_{10}O_5]_n$. Chitosan derived from chitin is the second most abundant. Recently, some nano-fillers which include graphene, graphene oxide, fullerene, nanodiamond, carbon black, carbon nanotube, nanoclay and inorganic nanoparticles have been developed for application in polymeric matrices to utilize corrosion prevention characteristics. By functionality, polymers can form hydrogels and encapsulate solid particles for effective interaction and control. Ultimately, they have the capacity to influence drilling fluid properties by their (i) film forming and (ii) gelatinization characteristics, adduced to their thermal, mechanical and barrier properties.

An example of natural polymer with nanoparticles is starch. Most plants store food in the form of starch. They are polysaccharides with animal or plant origins. Studies on mechanism of starch gelatinization are not new. According to a study, the summary of its application and gelation mechanism of starch was presented [19]. The researchers concluded that their applications include oil-drilling, coating, water-holding, viscous enhancing, gelling, emulsifying, protective and encapsulating agents. Also, they hinted that starch morphology is difficult to prove. Moreso, starch macroscopic properties and internal structure (supermolecular and molecular) were recognized to have an interconnection. They highlighted temperature and time-dependence of events in the gel forming process. It was pointed that shear conditions during preparation also affect viscoelastic behavior of gelatinized starch dispersions. "It has been observed that the gelation process due to intra and inter molecular associations that result in hydrogen bonding or van der Waals attractive forces is due to hydroxyl or methyl groups and hemiacetal oxygen of sugar residues". Similarly, they projected that during the process of dissociation of amylopectin double helices coupled with increased shear; the swollen granules of a starch sample were disrupted and gave rise to amorphous gel with subsequent viscosity increase. Similarly, they highlighted the purpose of starch in food industry which was to control structure and rheology by addition of starch hydrocolloids, irrespective of whether plant, animal or microbial origin. They showed that starches swell in aqueous environments, and increase the viscosity of the system and that gels can be produced by altering the solvent's pH. Gelling (rheological) characteristics were shown to be different.

Also, a study on a starch-hydrocolloids system with leguminous *Mucuna sloanei* reported the gelatinization temperature range of 29.52–98.0°C. It was concluded that starch was converted from a semi-crystalline to an amorphous form that involved initial hydration of the amorphous regions that facilitated mobility of the molecules in the amorphous regions that was followed by reversible swelling. The reversible swelling led to dissociation of the double helices within the regions of the crystal and subsequent granule expansion as the biopolymer hydrated.

Nanoparticles generally have a core surrounded by shell as an additional layer, and surface molecules covalently linked. Whereas the core controls some properties such as the electrical and magnetic properties, the surface layers of molecules control the binding affinity. It is the right combination of the core and surface molecules that afford design flexibility and preparation. Several methods exist for production of polymeric nanoparticles. They include ball milling and polymer nanoprecipitation. Whereas ball milling involves grinding by the balls under high energy depending on the size, number of balls, slipping velocity and residence time, polymer precipitation involves dissolution in an organic solvent, and introduction into a poor solvent where the polymer chains collapse, agglomerate and precipitate out of solution. Other methods include solvent evaporation, emulsification/reverse salting-out, emulsification/solvent diffusion, sulfuric acid hydrolysis [20], ultrasound, cold plasma, thermosonication and use of enzymes.

4.1 Polymeric nanoparticles: properties, shapes

Nanoparticles exhibit a wide variety of structures as a result of the significant physical properties which include; (i) much higher surface area to volume ratio when compared with micro and macro sized materials. That provides higher surface area for contact with surrounding substances for increased reactivity. This results in the use of smaller quantity and corresponding economic advantage (ii) high degree of mobility in free-state (iii) display of quantum effects (iv) electronic (super conductivity) and optical (light adsorption and emission) activity (v) very high mechanical strength (vi) magnetic (superparamagnetism) properties (vii) thermal (fast cooling) properties (viii) chemical (catalytic) reactivity and (ix) barrier properties [10].

Particle shape plays major roles in formulation and prediction of behavior of materials. Both end properties and processes are affected by particle shape. Though most polymeric nanoparticle shapes exist as nano-spheres, challenges of creation of other shapes has been reported in nanomedicine where nanotechnology has had widespread applications [21]. Other particle shapes can be dispersed with the nanospheres to yield desirable properties as reported when chitosan was dispersed in bentonite formulation to produce improvements in thixotropy, shear thinning tendencies and better yield stress [22]. The mechanical property of a polymer has been adjusted by this approach [23]. Similarly, it has reported that particle shape has significant effects on drilling fluid properties such as fluid loss and rheological behaviors [24]. Whereas rods and plate shaped sharp-edged particles by jamming and interlocking can cause quick thickening [25] in fluids, flow would be negatively affected. Nanospherical polymeric particles would build viscosity less aggressively, in addition to enhancement of rheology (**Figure 5**).

Both organic and inorganic nanoparticles exist in diverse shapes. Whereas cellulose nanocrystals (CNC) are needle shaped, starch nanoparticles (SNP) are spherical in shape and starch granules are angular shaped for maize, pentagonal and angular shaped for rice, disk-like or lenticular for wheat; which is also roughly spherical or polygonal in shape. Similarly, chitosan has an agglomeration and nano-aggregates of particles similar to what was observed by a research [19]. The nano-aggregates of *Mucuna solannie* biodegradable polymer were presented as responsible for its utilization and influence in mud formulations. Its formulations were stable and exhibited predictable characteristics in accordance with American Petroleum Institute (API) specifications [2]. Polycaprolactone nanoparticles have spherical shape and no aggregates occur, while alginate nanoparticles can be spherical. Nanocapsules and nanospheres differ in morphology and architecture and both are nanostructures. Synthetic, biodegradable and biocompatible polymers are used to prepare polymeric nanospheres. Most polymeric nanoparticles have nanosphere structure (**Figure 6**) and a particular biopolymer was observed to have nano-aggregate structure (**Figure 7**). Whereas nanocapsule is seen as a reservoir system, the nanospheres are seen as matrix systems. Various nanoparticle shapes can be combined to influence a desired property such as barrier property. These shapes are subunits of the shapes presented in **Figure 2**.

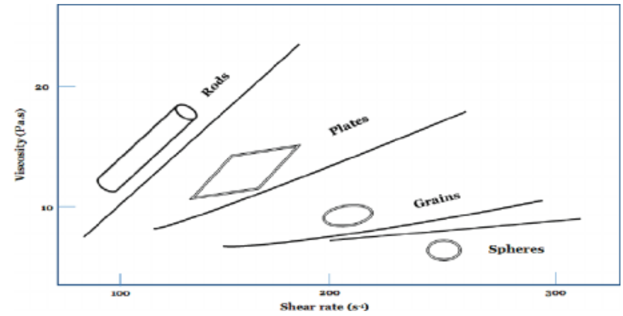

Figure 5.
Effect of particle shape on viscosity.

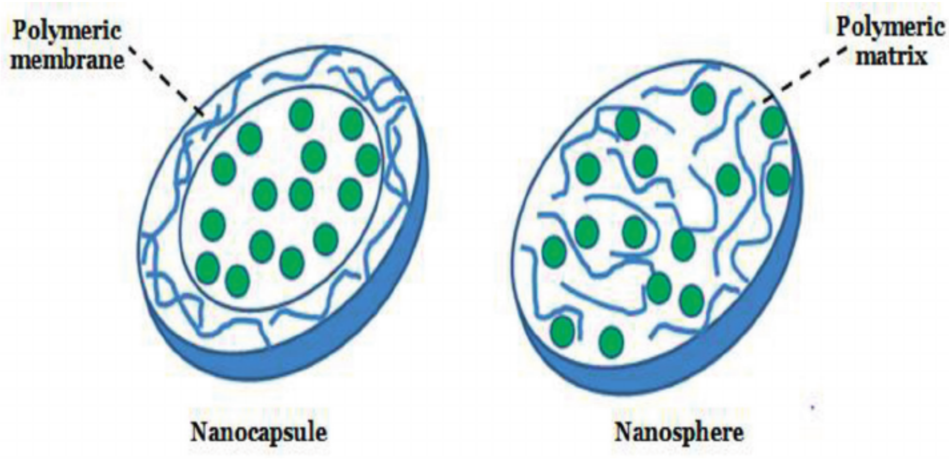

Figure 6.
Nanocapsule and nanosphere schematics.

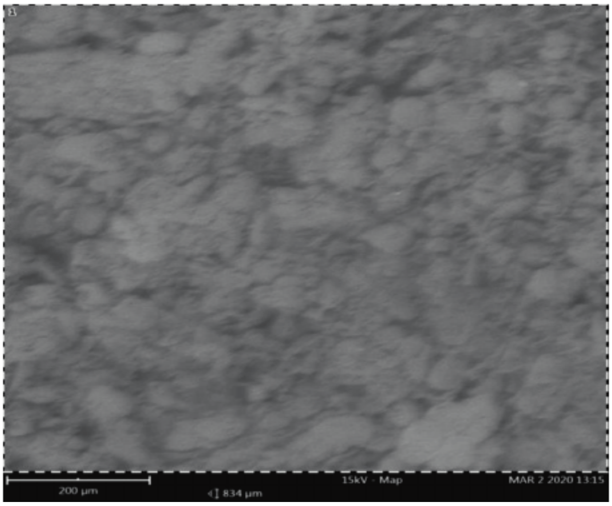

Figure 7.
Mucuna solannie scanning electron micrograph showing nano-aggregate particle shapes [19].

5. Desirable changes by addition of polymeric nanoparticles in drilling fluids

i. Nanoparticles in drilling fluids can improve filter cake quality by both plugging and bridging. Improved, thin filter cake, with non-erodible and impermeable membrane with similar attributes as conventional filter cakes can be achieved. Formation damage is reduced or prevented as a result. Also, due to the thin filter cake, contact between the wellbore and the drillstring is reduced, with resultant reduction of the tendency to experience excessive torque and drag frictional forces while rotating the drillstring and pulling or running in hole respectively. Stuck pipe incidents are reduced due to adequate clearance between the drillstring and the wellbore as a result of reduction of friction.

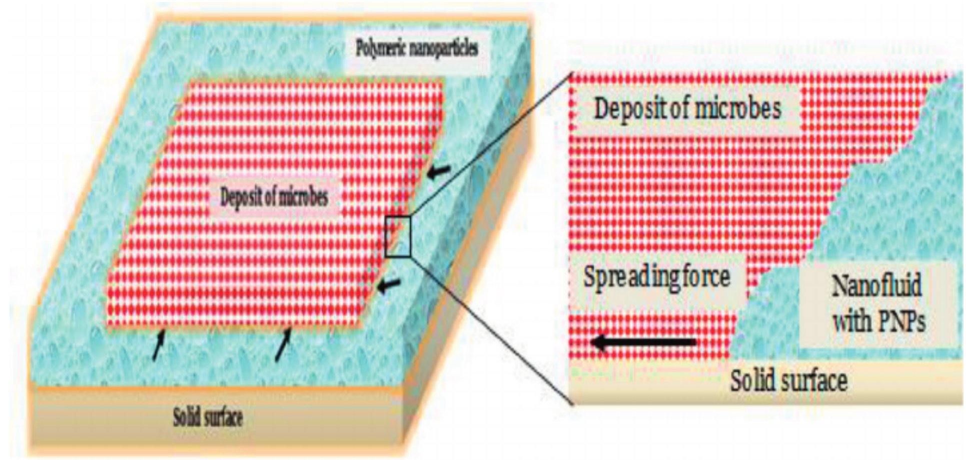

Figure 8.
Barrier creation process with nanofluid with polymeric nanoparticles.

ii. Another function of the drilling fluid is to cool the drillstring and bit. To perform this function, it must have high heat capacity. Nanoparticles such as carbon-based types have high carbon content. Carbon is highly temperature stable with long covalent bonds, which gives carbon-based nanoparticles high stability and ability to conduct heat better. The high heat conductivity property is also due to high surface area that enables heat absorption.

iii. Moreso, the concepts of spreading of simple liquids are not applicable to nanofluids. The theory of structural disjoining pressure (**Figure 8**), which explains the interaction between the particles in the nanofluid and the solid substrate is applicable [26, 27]. For lubricity, the nanoparticles, through other mechanisms, can adhere; spread and their particles ordered on the surfaces of solids such as drill pipes to lubricate. In other words, a polymeric film is deposited on the well wall and metal surfaces for lubrication. It is believed that it is the structural disjoining pressure gradient that drives the spreading of nanoparticles in nanofluids on surfaces. Nanoparticles layers with definite films spread on the solid surface with explanation of the association between the solid surface and the nanoparticles very complicated. It also yields desirable structural properties. Reduction in torque and drag are typical resultant effects.

iv. As regards wellbore instability, causes are categorized under controllable and uncontrollable factors. One of the controllable factors is physico-chemical rock-fluid interactions. Some phenomena that are responsible include swelling, osmotic pressures, hydration, strength changes and rock softening. Magnitude of near wellbore damage; quality of filter cake; formation strength, stiffness, stress history, pore water composition, mineralogy, temperature; and properties of wellbore fluid all combine to determine the significance of these phenomena. However, a filter cake made of nanoparticles with desirable properties can fix potential problems. Similarly, selection of right size range of nanoparticles in a drilling fluid, typically not greater than one-third of the pore throat enables effective bridging and plugging. Natural polymeric nanoparticles function by plugging the pore spaces. Due to their cellulosic nature, the deformable structures enable them to squeeze into the throats. Since the traditional method of switching from water based to oil based to solve shale swelling problem due to water absorption, which can cause environmental problems is prevented by addition of nanoparticles, cost efficiency is achieved.

v. In cavernous, vugular formations and fractures in rocks, drilling fluid losses may be encountered. In that case, mud level in the wellbore will drop and hydrostatic pressure would be affected leading to influx, well kick or blowout. Also, there would be severe economic impact due to loss of mud. The traditional solution had been use of micro and macro sized particles for effective size distribution in drilling fluids as loss control materials. They include mica, paper, cellophane, nutshells, cottonseed hulls and sized calcium carbonate. Addition of nanoparticles would create more effective and stable particle size distribution for lower porosity and permeability seals for loss circulation control. Polymeric nanoparticles can plug into the tiny pores to provide a robust and stable lost circulation material.

vi. Shear thinning (pseudoplastic) and non-Newtonian behavior is a desirable drilling fluid property. Flow behavior index in the range of 0.3 to 0.8 would yield drilling fluid of such attributes. The resulting velocity profile is then used to evaluate the carrying capacity. Cuttings transport at low shear rate is the best indicator of hole cleaning. Since viscosity of polymer systems is shear rate independent, inclusion of polymeric nanoparticles in drilling fluids can create improved cuttings carrying capacity at very low and adequately high flow rates.

vii. Various forms of corrosion exist such as aqueous, atmospheric, galvanic and stray-current corrosion. Others are molten salt, liquid metal, high-temperature gaseous, pitting, crevice and filiform corrosion. Aside titanium, microbial corrosion affects all types of alloys. It is caused by biofilms. It is a kind of corrosion caused by microbes such as Acidithiobacillus thiooxidans, Thiobacillus thioparus, and Thiobacillus concretivorus. Some of the bacteria associated with microbiologically influenced corrosion (MIC) are sulphate reducing bacteria, iron-reducing bacteria and acid-producing bacteria [28, 29]. Similarly, hydrogen sulphide causes hydrogen embrittlement or sulphide stress cracking in pipes. To prevent pollution and corrosion from toxic gases such as hydrogen sulphide, nanoparticles can be effective. Zinc oxide has been used for the purpose [30]; because hydrogen sulphide can react with metal ions, and insoluble metal sulphides are formed. Similarly, concentration cells caused by these bacteria can cause and enhance galvanic corrosion, which may appear as pitting corrosion in pipelines during drilling referred to as microbial corrosion. This form of corrosion can be prevented by both organic and inorganic nanoparticles that are introduced in the drilling fluid (**Figure 7**). Another form of cost efficiency is achieved since the pipelines could be reused due to extended lifespan without rapid deterioration and degradation due to corrosion and associated wears. The polymeric nanoparticles of organic origin when used in drilling fluids would have biological significance in prevention and treatment of this form of microbial corrosion by preventing formation of biofilm on the metal surface [31]. Also, polylactic acid (PLA) has potential application for this purpose. In summary, it will be like from "biofilm formation" to "biofilm protection". It is

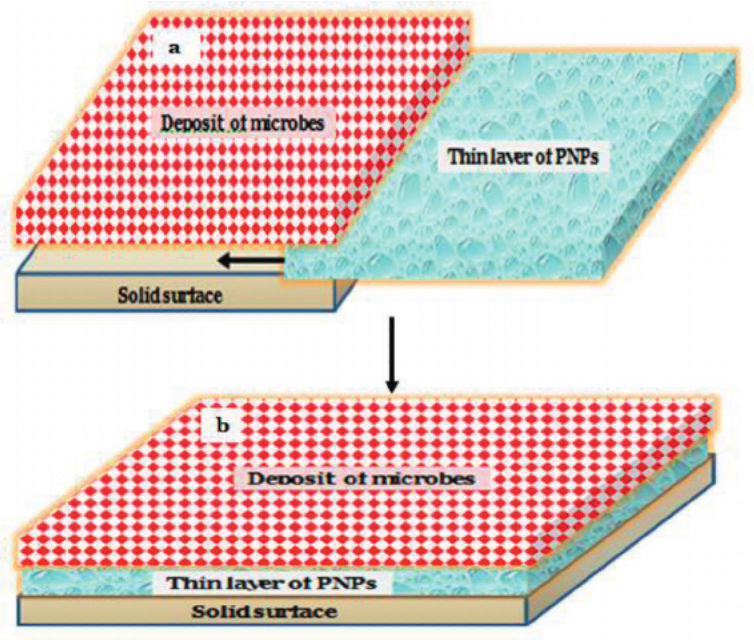

Figure 9.
(a) Film formation with structural disjoining pressure and (b) barrier between the surfaces finally created.

mainly the barrier properties of the nanoparticles, in association with other attributes that are utilized (**Figure 9**). This is a form of biological treatment.

viii. Most factors are responsible for hole cleaning and cutting carrying capacity of drilling fluids. Considering the velocity profile of fluid with cuttings in the annulus, with the annulus modeled as a pipe, profiles for laminar flow are distinguishable from turbulent flow regimes. The flow behavior index as one of the determinants of velocity profile is preferred to have a value less than unity, or preferably in the range 0.3 to 0.8 for shear thinning fluids. It is desirable for drilling fluids to have flow behavior index within this rang; the closer to the lower boundary, the better. Nanoparticles have the potential to gel the drilling fluid to fall within that range since addition of nanoparticles increases friction within the fluid layers which results in increase in viscosity causing a nanogel to be developed. Flow behavior index of unity would define Newtonian fluids which are not considered good for drilling fluid behavior. Similarly, for values above unity, the fluid would behave dilatant. Consider **Figure 10** for fluid flow dynamics.

ix. It shows the velocity profile in the annulus of a wellbore modeled as a pipe. At the center where velocity is at its maximum, friction might be zero; whereas at the pipe wall or well wall, velocity might be zero and friction at its maximum. Velocity diminishes from the center to zero towards the well or pipe wall. To extend the velocity at the center outwards such that more cutting are subjected to that velocity for more efficient hole cleaning, it is the flow behavior index that might be lowered to achieve that as shown by the chain line. Polymer nanoparticles can provide a more effective nanofluid gel to give appropriate flow behavior index value.

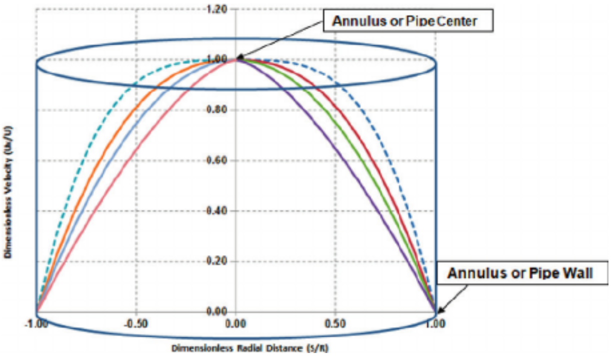

Figure 10.
Velocity profiles; with n = 0.42 (highlighted in chain-line) in comparison with other profiles with higher flow behavior index, n.

x. Moreso, during transport of cuttings in the annulus, there is continuous shearing and the nanoparticles are agitated and encapsulate the cuttings to help carry and suspend them due to encapsulation of the solids; an excellent feature exhibited by polymers. Ability of drilling fluids to release these cuttings at the surface is a basic function. This is achieved by the shale shaker that agitates the returning drilling fluid. The nanoparticles are rearranged accordingly and detach from the cuttings. This causes shear thinning of the drilling fluid that frees and releases the cuttings, and they are separated from the drilling fluid. This is known as thixotropic property.

xi. In particular, shale formations have permeability in nanodarcy scale; micro and macro sized fluid loss control additives may never be effective since formation of filter cake is hindered. These additives that are supposed to plug the pore spaces are larger and might not be able to. Mixture of particle sizes might yield a thick and ineffective filter cake. The reduced annulus size causes stuck pipe and high torque and drag. If clay hydration occurs, wellbore instability will result. Control of wellbore instability causes excess rig time and subsequent rise in investment cost. The challenge is tackled with the use of nanoparticles as fluid loss control additives. These particles can plug into or bridge the pore spaces.

xii. Also, when drilling in deep water environment, conditions favorable for hydrate formation may arise. They include low temperature and high pressure conditions which could be altered by the use of inhibitors. With thermodynamic inhibitors for inhibition, the temperature for hydrate formation will be lesser or the pressure for hydrate formation will be greater. Operation status might be altered to prevent stable hydrate formation towards the left of the hydrate formation curve. Due to the capacity of nanoparticles to absorb heat because of the high surface area; the hydrate formation temperature is suppressed to a lower level. This discourages hydrate formation since a condition would be affected. Alteration of fluid properties due to elimination of water from the fluid as a result of hydrate formation and increase in fluid density are prevented.

xiii. Bit balling which could be caused by formation type, hydraulic factors, too high hydrostatic pressure in the wellbore, poor bit design and high weight on bit can result in low rate of penetration. When polymeric nanoparticles are added to the drilling fluid, films such as nanocellulose biopolymer–based biofilms and starch nanoparticles [20, 32] deposited on the drill bit can help retard development of bit balling for improved drilling efficiency due to their barrier properties. Prevention of clay hydration for hydratable clays in the cuttings would also prevent bit balling.

6. Summary

New technologies are often sought to mitigate the problems associated with traditional drilling fluid formulations. The field of nanoscience, where nanoparticles with desirable attributes are evaluated for application, provides an alternative. Natural and synthetic (anthropologic) polymeric materials can be used to prepare nanoparticles. Two types of polymers (i) cross-linked and (ii) linear are common in the oil and gas industry for various purposes. Their shapes and sizes influence applications. They are also biodegradable, can act as antibacterial agents and are economically efficient since a relatively small quantity is required to create the nanogel. They have the potential to modify drilling fluid properties such as plastic viscosity, yield point, gel strength, barite sag, fluid loss volume, filter cake thickness as well as improve thermal and wellbore stabilities. They are also used as pollution filters, for improved lubricity, heavy metal absorption and reduction of torque and drag. They are applicable in diverse conditions both on land and marine environments.

7. Conclusion

Shortcomings of traditional drilling fluid additives can be overcome with nanoparticle additives. At deeper drilling depths with physical, chemical and thermal challenges, micro and micro sized additives might not be effective, leading to performance problems. Nanoparticles of which polymeric nanoparticles are the organic types have the potential to influence all the components in the circulating system where the drilling fluid is the main consideration. From the metals, the drilling fluid and its compositions and the surrounding wellbore, the impact of nanoparticles cannot be over emphasized. Conditions such as the pH of medium, nanoparticle concentration, particle size and shape are factors that determine performance of nanoparticles in nanofluids. Modification of rheological properties, reduction of fluid loss, deposition of thin and effective filter cake, thermal stability, friction reduction due to formation of polymeric film, improvement of wellbore stability, and hydrate inhibition are areas of application. However, addition of nanoparticles might have insignificant effect on mud weight. Due to their effectiveness and cost efficiency, more areas of influence and application will continue to emerge so long as drilling in harsh and remote environments in the frontier basins remain the option for increased production output in a world in need of petroleum and natural gas. Potential problem might be the issue of recovery of the materials and their influences on the fluid properties. Dispersion of different shapes and structures of polymeric nanoparticles might be considered to enhance their influences on fluid formulations.

References

[1] Caenn R, Darley H, Gray G. Composition and Properties of Drilling and Completion Fluids. 6th ed. Houston, TX: Gulf Professional Publishing, Elsevier Inc.; 2011. pp. 92-101

[2] API RP 13D. Recommended Practice on the Rheology and Hydraulics of Oil-Well Drilling Fluids. 17th ed, American Petroleum Institute; 1995. pp. 1-86

[3] Salazar J, Torres-Verdín C. Quantitative comparison of processes of oil-and water-based mud-filtrate invasion and corresponding effects on borehole resistivity measurements. Geophysics. 2009;**74**:E57-E73. DOI: 10.1190/1.3033214

[4] Akinsete OO, Doyinsola AA. Effects of mud filtrate invasion on well log measurements. In: Paper Presented at the SPE Nigeria Annual International Conference and Exhibition, Lagos, Nigeria. Paper Number: SPE-184308-MS. United States of America: Society of Petroleum Engineers; 2016. DOI: 10.2118/184308-MS

[5] Pal S. Drilling Fluid Engineering. Pal Skalle & Ventus Publishing ApS; 2010

[6] Hamida RS, Mohamed A, Alya R, Bin-Meferij M. Cyanobacteria—A promising platform in green nanotechnology: A review on nanoparticles fabrication and their prospective applications. International Journal of Nanomedicine. 2020;**15**:6033-6066. DOI: 10.2147/IJN.S256134

[7] Zielińska A, Carreiró F, Oliveira AM, Neves A, Pires B, Venkatesh DN, et al. Polymeric nanoparticles: Production, characterization, toxicology and ecotoxicology. Molecules. 2020;**25**:3731. DOI: 10.3390/molecules25163731

[8] Feracci H, Gutierrez BS, Hempel W, Gil IS. Chapter 8—Organic nanoparticles. In: de la Fuente JM, Grazu V, editors. Frontiers of Nanoscience. Vol. 4. Elsevier; 2012. DOI: 10.1016/B978-0-12-415769-9.00008-X

[9] Li M, Wu Q, Song K, Lee S, Qing Y, Wu Y. Cellulose nanoparticles: Structure–morphology–rheology relationships. ACS Sustainable Chemistry & Engineering. 2015;**3**(5):821-832. DOI: 10.1021/acssuschemeng.5b00144

[10] Khan I, Saeed K, Khan I. Nanoparticles: Properties, applications and toxicities. Arabian Journal of Chemistry. 2019;**12**(7):908-931. DOI: 10.1016/j.arabjc.2017.05.011

[11] Cheraghian G. Nanoparticles in drilling fluid: A review of the state-of-the-art. Journal of Materials Research and Technology. 2021;**13**. DOI: 10.1016/j.jmrt.2021.04.089

[12] Vryzas Z, Kelessidis VC. Nano-based drilling fluids: A review. Energies. 2017;**10**(4):540. DOI: 10.3390/en10040540

[13] Schneider WDH, Dillon AJP, Camassola M. Lignin nanoparticles enter the scene: A promising versatile green tool for multiple applications. Biotechnology Advances. 2021;**47**:107685. DOI: 10.1016/j.biotechadv.2020.107685

[14] Lesson Explainer: Nanoparticles. Available from: https://www.nagwa.com/en/explainers/640142370207/ [Accessed: May 05, 2022]

[15] Drilling Fluids Processing Handbook (ASME). 30 Corporate Drive, Suite 400, Burlington, MA 01803, USA Linacre House, Jordan Hill, Oxford OX2 8DP,

UK: Gulf Professional Publishing is an imprint of Elsevier; 2005

[16] Jarai BM, Kolewe EL, Stillman ZS, Raman N, Fromen CA. Chapter 18 polymeric nanoparticles. In: Nanoparticles for Biomedical Applications. Elsevier; 2020. pp. 303-324. DOI: 10.1016/B978-0-12-816662-8.00018-7. ISBN: 978-0-12-816662-8

[17] Kausar A. Corrosion prevention prospects of polymeric nanocomposites: A review. Journal of Plastic Film and Sheeting. 2019;**35**:181-202. DOI: 10.1177/87560879188060270

[18] Berdugo-Clavijo C, Scheffer G, Sen A, Gieg LM. Biodegradation of polymers used in oil and gas operations: Towards enzyme biotechnology development and field application. Polymers. 2022;**14**(9):1871. DOI: 10.3390/polym14091871

[19] Igwilo KC, Uwaezuoke N, OmoregbeeKO, HezekiahA, AmaefuleCV, Onyejekwe IM. Rheological evaluation of Mucuna solannie for non-aqueous mud additive in drilling operations. Upstream Oil and Gas Technology. 2021;**7**. DOI: 10.1016/j.upstre.2021.100054

[20] Li M, Wu Q, Song K, Qing K, Wu Y. Cellulose nanoparticles as modifiers for rheology and fluid loss in bentonite water-based fluids. ACS Applied Materials & Interfaces. 2015;**7**(8):5006-5016. DOI: 10.1021/acsami.5b00498

[21] Champion JA, Katare YK, Mitragotri S. Particle shape: A new design parameter for micro- and nanoscale drug delivery carriers. Journal of Controlled Release: Official Journal of the Controlled Release Society. 2007;**121**(1-2):3-9. DOI: 10.1016/j.jconrel.2007.03.022

[22] Abu-Jdayil B, Mamdouh G, Karam AA, Mohamed D. The effect of biopolymer chitosan on the rheology and stability of Na-Bentonite drilling mud. Polymers. 2021;**13**(19):3361. DOI: 10.3390/polym13193361

[23] Chow TS. The effect of particle shape on the mechanical properties of filled polymers. Journal of Materials Science. 1980;**15**:1873-1888. DOI: 10.1007/BF00550613

[24] Falahati N, Routh A, Chellappah K. The effect of particle properties and solids concentration on the yield stress behaviour of drilling fluid filter cakes. Chemical Engineering Science: X. 2020;**7**:1-8. DOI: 10.1016/j.cesx.2020.100062

[25] Israr HA, Yahya M, Salim Y. A review on stab and spike resistance performance of shear thickening fluids (STF) impregnated fabrics. In: 12th International Conference on Latest Trends in Engineering and Technology (ICLTET'2017) Kuala Lumpur (Malaysia). 2019. pp. 37-42. DOI: 10.15242/IIE.E0517022

[26] Wasan D, Nikolov A, Kondiparty K. The wetting and spreading of nanofluids on solids: Role of the structural disjoining pressure. Current Opinion in Colloid & Interface Science. 2011;**16**(4). DOI: 10.1016/j.cocis.2011.02.001

[27] Chengara A, Nikolov AD, Wasan DT, Trokhymchuk A, Henderson D. Spreading of nanofluids driven by the structural disjoining pressure gradient. Journal of Colloid and Interface Science. 2004;**280**(1):192-201. DOI: 10.1016/j.jcis.2004.07.005

[28] Natarajan KA. Chapter 12—Biofouling and microbially influenced corrosion. In: Biotechnology of Metals. Elsevier; 2018. pp. 355-393. DOI: 10.1016/B978-0-12-804022-5.00012-8

[29] Cramer SD, Covino BS. ASM Metals Handbook Volume 13A: Corrosion: Fundamentals, Testing, and Protection. Park, OH: ASM International Materials; 2003

[30] Sayyadnejad MA, Ghaffarian HR, Saeidi M. Removal of hydrogen sulfide by zinc oxide nanoparticles in drilling fluid. International Journal of Environmental Science and Technology. 2008;**5**:565-569. DOI: 10.1007/BF03326054

[31] Javaherdashti R, Alasvand K. Chapter 3—An introduction to microbial corrosion. In: Biological Treatment of Microbial Corrosion. Elsevier; 2019. pp. 25-70. DOI: 10.1016/B978-0-12-816108-1.00003-3

[32] Campelo PH, Anderson SS, Clerici MTPS. Starch nanoparticles: Production methods, structure, and properties for food applications. Current Opinion in Food Science. 2020;**33**:136-140. DOI: 10.1016/j.cofs.2020.04.007

Chapter 2

Utilization of Biopolymers in Water Based Drilling Muds

Imtiaz Ali, Maqsood Ahmad, Aftab Hussain Arain,
Vahid Atashbari and Asif Zamir

Abstract

With the increase in energy demand, deeper wells drilling is one of the solutions to fulfill the energy demand, which demands specialized drilling mud formulation. These muds are composed of thermally stable materials that can sustain in high-temperature conditions. Biopolymers are widely used out of various mud additives for improving the rheology and filtration characteristics of mud. Owing to the high temperature and poor thermal stability of such additives, these additives lose their primary functions, resulting in the nonproductive time and irreversible problems. The book chapter highlights the uses of water-based mud, its limitations, and the degradation of biopolymers. Various additives' significance and susceptibility in harsh borehole conditions have been discussed. The existing additives used for the rheological and filtration characteristics improvements and their shortcomings are presented. Furthermore, the field applications of native and modified polymeric-based mud formulations have been further examined and presented.

Keywords: drilling fluids, nondamaging muds, high-pressure, high temperature

1. Introduction

Oil well drilling operation is a common and important process in the petroleum industry. Drilling fluid is an essential operational fluid that plays an exceptional part in drilling engineering. In a rotary drilling operation, drilling fluids are circulated continuously in the wellbore and drilling string [1]. Drilling mud serves a variety of functions, including cleaning and transporting the borehole, maintaining the borehole integrity, reducing formation damage, and cooling and lubricating the tools. Water-based muds are popular due to their low cost and environmental protection requirements. It generally comprises water, clay, and other chemical additives for different purposes.

Various problems are encountered during drilling a wellbore, including clay swell-ing, shale instability, bit balling, drill string accretion, high torque and drag, differen-tial sticking, and fluid losses. These issues put a substantial cost on the overall drilling operation. These issues further increase with the increase in the wellbore depth. In addition, the conventional muds containing clay, weighting agents, and pH control-lers could not be applied in such conditions. This is due to the interaction of such fluids with the clay minerals resulting in the variation in the mechanical properties by clay swelling. Hence, the design and selection of appropriate mud additives are the most critical factors that need to be considered. Oil-based muds (OBMs) are conventionally preferred due to their better thermal stability and nonreactive nature but due to the environmental concerns and their higher costs make them uneconomical. Thus, high-performance water-based containing eco-friendly additives are preferred. The concept of high-performance water-based drilling mud has been suggested for decades. It is a water-based drilling mud with acceptable rheology, minimal filtrate loss, high shale inhibition, good lubricity, and plugging properties [2].

The high-performance water-based mud (HPWBM) system was developed to enhance WBM performance while also providing an eco-friendly alternative to oil-based muds (OBM) while mimicking OBM drilling features. Various laboratory and field applications confirmed the HPWBM in replacing OBM by efficaciously accomplishing the objectives. HPWBMs have been recently developed as OBM alternatives, although not all kinds of HPWBM have been able to replace OBM on more complex wells. With the ever-increasing push for greater environmental performance and greater restrictions on the disposal of OBM cuttings, the petroleum industry is trying to design a WBM that can replicate OBM's performance [3].

High-performance muds are particularly advantageous to conventional water-based systems because they provide faster penetration rates, enhanced hole cleaning, greater shale inhibition, and improved wellbore stability. The high-performance muds can deliver appropriate rheology and fluid stability under HTHP conditions, withstand high solids loading and deliver a high tolerance to brine or salt contamination, so the high-performance fluid is recommended for drilling the gypsum-salt formations and the reservoirs with natural fractures and inter-bedded shale. Such muds only tolerate operating temperatures up to 300°F because they depend on biopolymer-based viscosifiers. Deeper exploration in extreme high-temperature reservoirs (>300°F) requires new drilling fluid technologies.

2. Drilling mud properties

The success of any drilling fluid is dependent on the composition of the mud additives, which alters the mud properties. The two most common properties, including rheological and filtration, are primarily controlled while designing a drilling mud. Both properties can be improved with the utilization of mud additives. Various additives are added to the drilling to maintain the mud rheological and filtration characteristics. During drilling of the pay zone section, various polymers are added to replace bentonite to minimize the damage due to solids intrusion into the pay zone section. Such bentonite-free muds can form a thin and removable filter cake on the borehole wall and thus reduces the formation damage. Some of the most commonly used biopolymers are xanthan gum, guar gum, diutan gum, cellulose, lignins, and starches.

Generally, the viscosity is maintained lower for such muds, but more focus is paid to the filtration characteristics. It is worth mentioning that most water-based mud has shown best fitting with power-law and Herschel-Bulkley model. The laboratory experiments and field applications have observed that the flow behavior index (n) and consistency index (k) are the primary parameters controlling the cuttings transportation. The lower the flow behavior index and the higher the consistency index will perform better in cuttings transportation.

3. Mud properties modification

Two key parameters of drilling mud are generally investigated, including rheological and mud filtration. Mud rheological properties include plastic viscosity (PV), apparent viscosity (AV), gel strength (GS), yield point (YP), and yield stress (YS), while filtration properties consist of fluid loss volume, filter cake thickness, porosity, and permeability. Both the properties are dependent on the proper mud composition. The clay and polymeric materials generally enhance mud rheology, while the fluid loss additives such as starch and other nano-based materials reduce the fluid loss and cake thickness. Starch is a commonly used additive for improving both the rheological and filtration characteristics of mud.

Shale inhibition is another primary factor that requires attention during the mud design. Wellbore instability due to shale swelling and fluid loss of drilling mud is the main challenge the oil and gas industry faces. Shale is generally a water-sensitive material and causes swelling resulting in other drilling issues. Different additives, including salts and other amine-based materials, have been tested to improve shale stability. Several studies have been conducted to modify mud properties. For instance, a water-based mud was developed using an appropriate amine derivative, poly-ethoxylated alkyl diamine as a potential shale inhibitor agent instead of other conventional alternatives. The developed mud has optimally improved the performance of previously formulated HPWBMs [4].

Shale inhibition of amine derivative was examined using a new procedure, namely WSP, which showed better performance in bentonite-based mud systems. The system was found appropriate and an excellent alternative to OBM and SBM when tested in the South China Sea deepwater well. The mud displayed better performance by excellent shale stability, clay inhibition, lubricity, and high rate of penetration (ROP). The mud showed lower cost due to no issue caused during the drilling operation [5].

4. Biopolymers application in water-based muds

Water-based drilling fluids are an economical and eco-friendly alternative for successfully drilling a wellbore. Both conventional and high-performance muds generally use biopolymers to enhance rheological characteristics, provide acceptable viscosity, suspend solids, and control filtrate loss in the wellbore. A few examples are natural biomaterials derived from plants or microorganisms such as starch, guar, xanthan, and their chemically modified substitutes.

Biopolymers used for drilling fluids can be classified as plant-based or microbial-based, depending on their source. For instance, guar gum and locust bean gum are the most widely used plant-based materials. Guar gum is a nonionic linear polymer obtained from the seeds of the guar plant composed of the sugars galactose and mannose. On the other hand, locust bean gum is isolated from the fruit of the legume *Ceratonia siliqua*, and its structure is similar to guar except for the ratio of galactose to mannose, which influences its solubility in water. It has been observed that the galactose content directly relates to the water solubility. Thus the guar shows better solubility than locust bean gum.

Another kind of biopolymer that is mostly employed in water-based systems is bacterially produced polymers. Xanthan gum is a typical and mostly used additive of this type. It has a more branched structure than other gums and is very efficient, offering shear-thinning rheological behavior that is almost optimal for drilling fluid applications. Similarly, welan gum is a negatively charged (anionic) gum formed by bacteria belonging to the Alcaligenes genus fermenting sugar. It is observed that it exhibits better viscosity and salt resistance.

Various studies have highlighted the importance of biopolymers for the improvement of mud properties. For example, nitrocellulose-based muds were developed in a study, which showed enhanced rheological and filtration properties. It was used in high-performance, water-based fluids as a renewable, non-hazardous, and cost-effective alternative to synthetic polymers, with the added feature of maintaining and optimizing fluid characteristics [6]. Likewise, diutan gum was used as a drilling mud viscosifier, resulting in retaining their viscosities up to 232°C, when sodium erythorbate, potassium formate, and polyethylene glycol were added to the formulations [7].

5. Role of biopolymers in HPWBMs

Various additives are used in the mud with different dosages to enhance the viscosity of drilling mud. During drilling the pay zone section, the main concern is to reduce the invasion of filtrate and solids into the exposed formation. This invasion can cause irreversible problems that cause multiple folds decline in production. Thus, nondamaging mud containing biopolymer and other acid-soluble materials are added to the mud for drilling of such zones. Various biopolymers, including gums (xanthan, guar, and diutan), lignins, starches (both native and modified), cellulose, etc., are widely used in oil well drilling. These gums have been further modified to increase their thermal stability and salt resistance functionality. **Figure 1** shows xanthan, diutan, and guar gum structure.

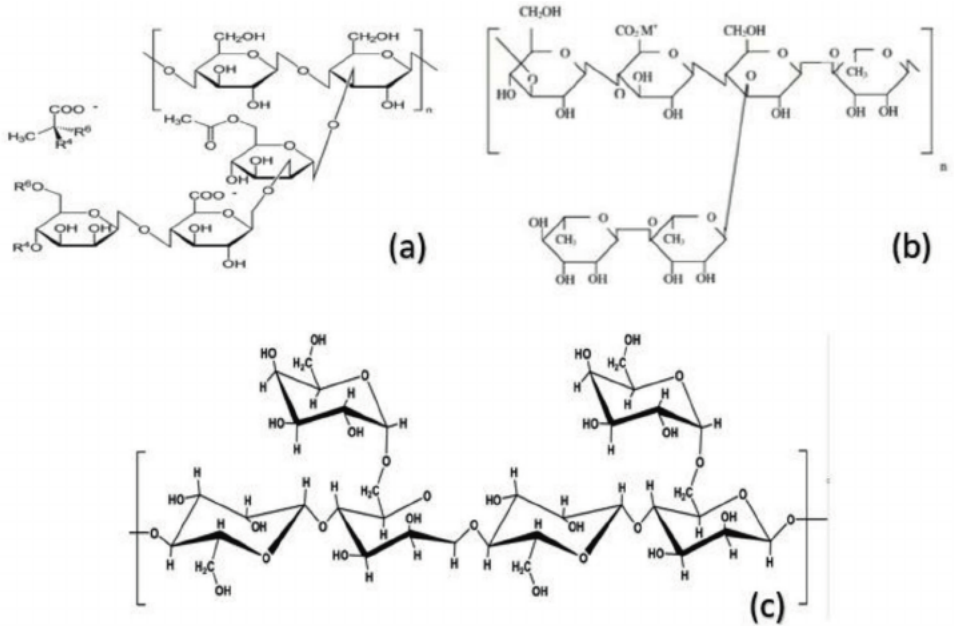

Figure 1.
Structure of (a) xanthan gum [8], (b) diutan gum [9], and (c) guar gum [10].

Due to the environmental concerns about the usage of huge quantities of chemicals and their disposal issues, the oil industry is looking for bio-based/biodegradable materials with very little or no impact on the environment. Therefore, various waste products and other biomaterials have been investigated to substitute the hazardous chemicals used in recent years. These materials include but are not limited to agarwood waste, rice husk, psyllium husk, and groundnut husk: dates, grass, wood, pistachio shell, mandarin peels, palm tree leaves, green olive pits, Cupressus cones powder, etc. The mentioned materials showed that the mud containing these agents could significantly improve the mud properties. Moreover, the overdependence on such expensive commercial materials is reduced by utilizing such additives. These materials are easily available everywhere, and their proper utilization can reduce the extra cost and ensure environmental cleanliness.

6. Role of nanomaterials in HPWBMs

Nanomaterials are synthesized substances with a size ranging from 1 to 100 nanometers (nm) and are therefore used in very small dimensions. These materials have numerous applications in various fields, including automotive, electronics, pharmaceuticals, etc. In recent years their applications were also observed in the petroleum industry in different areas. In drilling fluids, nanomaterials have been used for borehole stability, filtrate loss reduction, and enhancing the rheology of mud blends. Such materials are characterized by an extremely high surface area to volume ratio due to their nano-sized particles. Nanoparticles offer enormous characteristics to reduce frictional resistance between drilling pipes and side holes and optimize torque and drag due to their extraordinarily thin and fine structure. Furthermore, NPs have broad drilling capabilities in high pressure and high temperature (HPHT) environments due to their wider surface area [11, 12].

Numerous nanomaterials, including graphene oxide, graphene nanoplatelets, titanium oxide, aluminum oxide, cupric oxide, CNT, multi-walled carbon nanotube (MWCNT) nanosilica, clay, metals, and carbon-based NPs, have been used to enhance the performance of WBMs. It was observed that the mud containing nanoparticles possesses enhanced physical and chemical properties, which enhances its efficiency. Graphene nanoparticles were found to be an excellent binding agent because these can develop a compact, impermeable, and thinner mud cake. This allows nano-pores to be physically plugged, limiting filtrate losses. As a result, using the graphene family improves wellbore stability [13].

Additionally, nanoparticles have been introduced as lubricants to minimize friction between the wellbore and the drill string, lowering the risk of a stuck pipe. **Figure 2** shows how nanoparticles have a higher surface area than macroparticles of the same volume.

In water-based mud systems, polymers nanoparticles such as TiO_2/PAM nanocomposite depicted reduced filtrate loss volume and filter cake thickness while enhancing the formulated mud's rheology [14]. Likewise, SiO_2/acrylic nanocomposites showed improved thermal stability [15]. Numerous studies have concluded that the synthesized composites showed improvements in rheology and lubricity while a reduction was observed in the filtrate loss. Some of the common nanoparticles with potential applications in drilling fluids are summarized in **Table 1**.

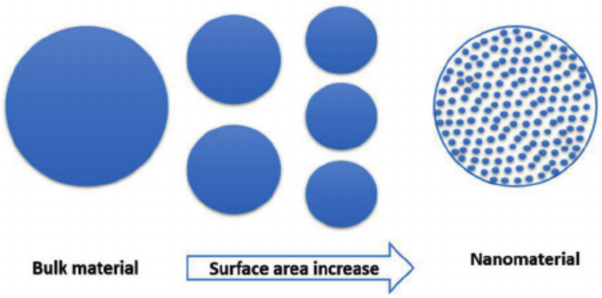

Figure 2.
Comparison of nanoparticles surface area with bulk material.

Nanoparticles	Functions	Reference
TiO_2-polyacrylamide hybrid	Reduced filtrate loss and improved mud viscosity	Sadeghalvaad and Sabbaghi [14]
CuO and ZnO	Improved viscosity at HPHT	William et al. [16]
Nanosilica	Filtrate prevention	Cai et al. [17], Fakoya and Shah [18]
Graphene oxide	Filtrate control agent in HPHT	Kosynkin et al. [19]
Nanosilica, multi-walled Carbon Nanotube	Improved rheology and filtration of mud, shale inhibition	Hoelscher et al. [20]
MWNT-polymer hybrid	Fluid loss reduction at HPHT conditions	Ito et al. [21]
Silica NPs	Filtrate reducer for drilling fluid at ultra-high temperature	Mao et al. [22]
Nano clay	Enhancing mud cake reduction	Zamir and Siddiqui [23]
Sepiolite NPs	Improving the rheological and filtration properties of mud	Al-Malki et al. [24]

Table 1.
Nanoparticle applications in drilling muds.

7. Field applications of high-performance WBMs

In response to increasing environmental restrictions and economic concerns, there has been an upsurge in demand for water-based muds (WBMs) in the last 15 years, particularly for off-shore operations. Industry operators and service providers demanded Water-based muds to substitute the stable and inhibitive invert emulsion fluids. Some of the most common problems with WBM are hole washouts, poor hole cleaning, bit balling, tight holes, inappropriate reaming and stuck pipe, shakers screens blockage, reducing total solids control equipment (SCE) performance, logging difficulties, and running casing are all associated with the appropriate mud design [25].

Numerous fields have applied HPWBMs to overcome the encountered problems, including complex formation drilling, high-temperature drilling, borehole instability, and high collapse stress formations. In China, the complex formations containing mudstone, fine sandstone, mudstone intercalated with salt rock, and pure salt rock were successfully drilled using HPWBMs. The mud exhibited better clay inhibition, rheological and filtration characteristics, and rate of penetration and was environmentally safe [26].

A well having issues during drilling including borehole instability, risk of induced losses, and tight hole owing to the presence of unstable shale was successfully drilled using HPWBM. The well was drilled to total depth without any NPT attributable to drilling fluid or hole cleaning. A gauge hole was drilled with minor washouts. The cuttings were distinct, suggesting good inhibition. In comparison to the fluid applied in former wells, the proposed HPWBM system demonstrated its superiority and efficiency [3].

Similarly, in South China's deepwater well drilling operation, a high-efficiency mud system was determined to be acceptable, and the well application revealed that the selected mud is an excellent alternative to OBM or SBM [5]. HPWBM has been successfully deployed in different fields in Dubai, which contain higher reactive clays and have reached higher degrees of inclination [25].

A new HPWBM was designed to fill the gap between conventional WBM and emulsion-based mud systems in terms of drilling performance. The mud has been tested in the field with some of the most challenging onshore, deepwater, and continental shelf wells. These wells would otherwise have been drilled with oil or synthetic-based mud [27].

Scleroglucan as a mud additive has also been used during drilling of gas field exploration in various fields. The field experiments confirmed its salt and thermal stability and found a stable additive up to 80°C.

8. Limitations of biopolymers

Generally, the biopolymers have lower thermal stability and degrade at higher temperatures. The salts, calcium, and bacterial resistance also negatively impact the performance of the mud containing biopolymers. Thus other additives such as bactericides are added to prevent the bacterial attack. Owing to the reduced thermal stability, either the native materials are modified by adding more functionalized groups into their main chain or the addition of two or more biopolymers is used. The former is economical compared to the second one. In a study, the synergic effect of xanthan and diutan gum enhanced the performance of water-based drilling fluids and showed shear-thinning behavior [28].

Different researchers have attempted to modify the biopolymers for drilling fluid applications. Starch is one of the most widely used additives, which improves both rheology and the filtration behavior of the muds. Starches have been modified using chemical, physical and enzymatic approaches. The usage of starch in the petroleum industry is in the drilling fluids, enhanced oil recovery, and completion fluids. A variety of starches are available, which are generally used for food applications. Pregelatinized starch (PGS) has been used in the oil industry due to its lower costs. Carboxymethyl starches (CMSs) are also very common, showing better thermal stability and salt resistance in WBMs. The combination of polyanionic cellulose (PAC) with the modified starch shows significant improvements in terms of mud rheology and filtration. Acetylated and grafted starches also showed promising results in WBMs.

Acknowledgements

The authors would like to thank the Ministry of Higher Education (MOHE), Malaysia, for providing financial assistance under FRGS/1/2020/TK0/UTP/02/3.

Nomenclature

HPWBMs	high-performance water-based mud
PAC	polyanionic cellulose
OBM	oil-based mud
SCE	solids control equipment
SBM	synthetic based mud
HPHT	high-pressure high temperature
NPs	nanoparticles
CNT	carbon nanotubes
PGS	pregelatinized starch
CMS	carboxymethyl starch
MWCNT	multi-walled carbon nanotube
ROP	rate of penetration

References

[1] Li X, Jiang G, Shen X, Li G. Poly-l-arginine as a high-performance and biodegradable shale inhibitor in water-based drilling fluids for stabilizing wellbore. ACS Sustainable Chemistry & Engineering. 2020;**8**(4):1899-1907

[2] Huang X-B et al. Laponite: A promising nanomaterial to formulate high-performance water-based drilling fluids. Petroleum Science. 2021;**18**(2):579-590

[3] Pino RM, Elhabrouk I, Addagalla A, Jadhav PB. Customized drilling fluids design to drill challenging sections using high-performance water-based mud. In: Presented at the SPE Kingdom of Saudi Arabia Annual Technical Symposium and Exhibition. 2018

[4] Gholizadeh-Doonechaly N, Tahmasbi K, Davani E. Development of high-performance water-based mud formulation based on amine derivatives. In: Presented at the SPE International Symposium on Oilfield Chemistry. 2009

[5] Huaike L, Tie G, Lei G, Jiansheng L. High performance water-based drilling fluids—A high efficiency muds achieving superior shale stability while drilling deepwater well with HPHT in South China Sea. Science. 2019;**7**(4):98-103

[6] Hall LJ, Deville JP, Santos CM, Rojas OJ, Araujo CS. Nanocellulose and biopolymer blends for high-performance water-based drilling fluids. In: Presented at the IADC/SPE Drilling Conference and Exhibition. 2018

[7] Akpan EU, Enyi GC, Nasr G, Yahaya AA, Ahmadu AA, Saidu B. Water-based drilling fluids for high-temperature applications and water-sensitive and dispersible shale formations. Journal of Petroleum Science and Engineering. 2019;**175**:1028-1038

[8] Petri DFS. Xanthan gum: A versatile biopolymer for biomedical and technological applications. Journal of Applied Polymer Science. 2015;**132**:23

[9] Sonebi M. Rheological properties of grouts with viscosity modifying agents as diutan gum and welan gum incorporating pulverised fly ash. Cement and Concrete Research. 2006;**36**(9):1609-1618

[10] Thombare N, Jha U, Mishra S, Siddiqui MZ. Guar gum as a promising starting material for diverse applications: A review. International Journal of Biological Macromolecules. 2016;**88**:361-372

[11] Smith SR, Rafati R, Haddad AS, Cooper A, Hamidi H. Application of aluminium oxide nanoparticles to enhance rheological and filtration properties of water based muds at HPHT conditions. Colloids and Surfaces A: Physicochemical and Engineering Aspects. 2018;**537**:361-371

[12] Bera A, Belhaj H. Application of nanotechnology by means of nanoparticles and nanodispersions in oil recovery-A comprehensive review. Journal of Natural Gas Science and Engineering. 2016;**34**:1284-1309

[13] Ikram R, Mohamed Jan B, Sidek A, Kenanakis G. Utilization of eco-friendly waste generated nanomaterials in water-based drilling fluids: State of the art review. Materials. 2021;**14**(15):4171

[14] Sadeghalvaad M, Sabbaghi S. The effect of the TiO2/polyacrylamide nanocomposite on water-based drilling

fluid properties. Powder Technology. 2015;**272**:113-119

[15] Huang X, Sun J, Lv K, Liu J, Shen H, Zhang F. Application of core-shell structural acrylic resin/nano-SiO2 composite in water based drilling fluid to plug shale pores. Journal of Natural Gas Science and Engineering. 2018;**55**:418-425

[16] William JKM, Ponmani S, Samuel R, Nagarajan R, Sangwai JS. Effect of CuO and ZnO nanofluids in xanthan gum on thermal, electrical and high pressure rheology of water-based drilling fluids. Journal of Petroleum Science and Engineering. 2014;**117**:15-27

[17] Cai J, Chenevert ME, Sharma MM, Friedheim J. Decreasing water invasion into Atoka shale using nonmodified silica nanoparticles. SPE Drilling & Completion. 2012;**27**(01):103-112

[18] Fakoya M, Shah S. Enhancement of filtration properties in surfactant-based and polymeric fluids by nanoparticles. In: SPE Eastern Regional Meeting. 2014

[19] Kosynkin DV et al. Graphene oxide as a high-performance fluid-loss-control additive in water-based drilling fluids. ACS Applied Materials & Interfaces. 2012;**4**(1):222-227

[20] Hoelscher KP, Young S, Friedheim J, De Stefano G. Nanotechnology application in drilling fluids. In: Offshore Mediterranean Conference and Exhibition. 2013

[21] Ito M et al. Nanocomposites for HPHT sealing system for harsh downhole environments. In: SPWLA 19th Formation Evaluation Symposium of Japan. 2013

[22] Mao H, Qiu Z, Shen Z, Huang W. Hydrophobic associated polymer based silica nanoparticles composite with core–shell structure as a filtrate reducer for drilling fluid at ultra-high temperature. Journal of Petroleum Science and Engineering. 2015;**129**:1-14

[23] Zamir A, Siddiqui N. Investigating and enhancing mud cake reduction using smart nano clay based WBM. Journal of Petroleum Environment. 2017;**8**(315.10):4172

[24] Al-Malki N, Pourafshary P, Al-Hadrami H, Abdo J. Controlling bentonite-based drilling mud properties using sepiolite nanoparticles. Petroleum Exploration and Development. 2016;**43**(4):717-723

[25] Nasrallah M, Nour M, Savari S. Customized high-performance water-based mud delivers superior results while driving down cost by successfully drilling through the most troublesome shale formations in the United Arab Emirates. In: Presented at the International Petroleum Technology Conference. 2022

[26] Long L et al. Application of innovative high density high-performance water-based drilling fluid technology in the efficient development and production of ultra-deep complicated formations in the Tian Mountain Front Block in China. In: Presented at the Offshore Technology Conference Asia. 2018

[27] Dye W et al. New water-based mud balances high-performance drilling and environmental compliance. SPE Drilling & Completion. 2006;**21**(04):255-267. DOI: 10.2118/92367-PA

[28] Akpan EU, Enyi GC, Nasr GG. Enhancing the performance of xanthan gum in water-based mud systems using an environmentally friendly biopolymer. Journal of Petroleum Exploration and Production Technology. 2020;**10**(5):1933-1948

Chapter 3

Advances in Well Control: Early Kick Detection and Automated Control Systems

Olugbenga Olamigoke and Isa James

Abstract

The devastating impact of the Macondo blowout incident has underscored the need for effective well barriers, early kick detection systems, and increased automation of well-control operations toward successful drilling and completion operations particularly in deep offshore environments. Early kick detection systems should be capable of detecting a gas influx both during drilling and tripping operations regardless of the drilling fluid system with minimal false-negative alarms, while automated control systems regain well-control eliminating delays or omissions due to human error. In this chapter, developments in the deployment of early kick detection and automated control systems in conventional and managed pressure drilling operations are reviewed. We discuss the use and placement of surface sensors such as the Coriolis flowmeter, smart flowback fingerprinting when the rig pumps are off, real-time gas monitoring along the marine riser and downhole measurements complimented with machine learning algorithms for early kick detection. We then focus on the application of automated well-control systems for managed pressure drilling operations for which gas kicks are circulated without stopping the pumps or shutting in the well and in conventional well operations requiring intelligent tool joint space-out prior to well shut in especially for deep offshore operations.

Keywords: early kick detection, automated well control, gas influx, well barriers, managed pressure drilling, Coriolis flowmeter

1. Introduction

Drilling into deep lying subsurface formations, both onshore and offshore, is required to produce petroleum which is critical to meeting the world's energy mix. A rightly sized drilling rig suited to the operating environment with trained crew, provided by a drilling contractor, is deployed with other service contractors providing services such as drilling fluid engineering and mud logging to drill and complete the well according to the approved well plan. A multidimensional effort termed "Well control" is employed during drilling and completion operations to ensure that formation fluids are brought safely to the surface and subsequently processed to useful forms of fuel and petrochemical feedstock.

The drilling rig is equipped with a well control system which is basically consist of the Blowout Preventer (BOP) stack, the choke manifold, accumulator unit, and a diverter assembly. The BOP stack may be a surface BOP stack as is the case on all land, jack-up and platform drilling operations or a subsea BOP stack which is used for all floating drilling rigs. The BOP is used to seal the wellbore to contain a *kick* thereby shutting-in the well. A *kick* is the unintended flow of fluids from the formation into the wellbore due to the lowering of the hydrostatic pressure provided by the drilling fluid below the formation pore pressure. A typical BOP stack consists of an annular preventer on top, followed three ram-type preventers including a full-bore drilling spool to enable connection of the kill and choke lines. A typical surface BOP stack is shown in **Figure 1(a)**. The subsea stack includes additional control valves and lines to foster remote operation of the BOP within acceptable reaction times as illustrated in **Figure 1(b)**. The hydraulic power required for operating the well control equipment (preventers, automatic valves, and chokes) is provided by the accumulator unit according to its working pressure rating. The choke manifold which generally consists of a manual choke and a remote-controlled choke is used to control the backpressure on the well while circulating out a kick. The choke manifold also provides the least restricted flow possible in case the well cannot be controlled, and the formation fluids need to be flared at a safe distance from other equipment. A diverter assembly is used to divert a gas kick encountered at shallow depth in a safe direction when only a conductor casing is installed as the surrounding formation tends to be too weak to contain a shut-in kick. Generally, an annular-type preventer is installed on top of the conductor pipe beneath which a diverter line of large enough diameter to sustain unrestricted flow is run to a pit [1, 3, 4]. The position of a diverter system is shown in **Figure 1(b)**.

Loss of well control is widely recognized as a major hazard in the oil and gas industry with far-reaching consequences including loss of drilling personnel, negative environmental impact, loss of investments and damage to the companies' reputation [4]. The loss of well control is always initiated by a kick. The failure in detecting

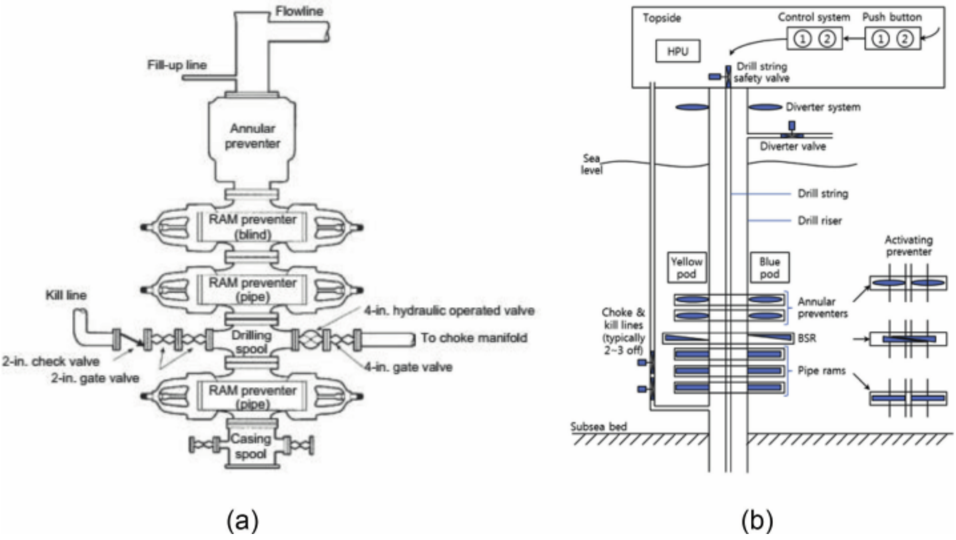

Figure 1.
Left picture (a): a typical surface BOP stack arrangement [1]. Right picture (b): a schematic subsea BOP configuration [2].

a kick or a malfunction in the well control system could result in an uncontrolled flow of formation fluids into the wellbore. This unwanted and uncontrolled flow of fluids is called a blowout [1, 4]. The Loss of well control (LOWC) is thus defined as uncontrolled flow of formation fluids such as gas, oil, water into a separate formation (underground blowout) or exposed at the surface (surface blowout). In addition to equipment failure, a blowout can also result from violation of procedures or human error. The loss of well control is not restricted to the drilling and completion phase as it can occur during work-over activities, and less frequently during production and in abandoned wells [5].

In this chapter we give an overview of essential principles pertinent to maintaining well control such as the role of well barriers and barrier activation in the event of a well control incident. We then discuss conventional kick detection methods, their limitations and early kick detection systems especially for deep offshore operations. We further discuss the adoption of early kick detection and automated well control in managed pressure drilling operations. Finally, automated well control for conventional drilling operations is presented especially the application of artificial intelligence in greatly minimizing human error and thereby increasing the safety of drilling and completion operations regardless of the working environment.

2. Well barriers for maintaining and regaining well control

A well barrier, an item that prevents the fluid flow from the well to the surrounding, is essential to maintaining well control. The two-barrier principle is widely adopted by different regulatory authorities across different petroleum provinces. These two barriers, which are required to be independent of each other, are usually categorized as *primary* and *secondary* barriers with the primary barrier being the closest to the reservoir—the potential source of formation fluids. During the drilling phase, the hydrostatic pressure exerted by drilling fluid is the primary barrier. Thus, the use of the term *primary well control* which refers to prevention of formation fluids into the wellbore by a static drilling-fluid column. The active secondary barrier while drilling is the BOP while the wellhead seals, casing, and cement serve as passive secondary barriers. One exception to the two-barrier rule applies while drilling the top-hole i.e., the first hole section drilled prior to the installation of the Surface BOP on the wellhead. If primary control is lost while drilling the top-hole, the formation fluids from the well are rerouted away from the drilling rig via a diverter [1, 5]. For completion or work-over operations, the designation of a barrier as either primary or secondary is dependent on activities executed during this phase. While the barriers are similar to the drilling barriers for certain aspects of the operation, towards the end of operations sequence, the barriers will be mechanical only, similar to the ones which exist in the production phase. For example, operations carried out through tubing with the well underbalanced with respect to reservoir pressure no longer have the wellbore fluid as a barrier. In a production or injection wells, where packers exist, they will typically become the primary barriers, as they seal off the annulus, the tubing below the surface-controlled subsurface safety valve (SCSSV), and the SCSSV. On the other hand, the secondary barrier envelope would be made up of the tubing above the SCSSV, the X-mas tree main flow side, the casing/wellhead, and the annulus side of the X-mas tree. While the loss of well control can occur anytime during drilling operations, the risk associated with loss of well control is assessed during the well planning phase which precedes well construction [5, 6].

A well control incident occurs when there is a failure either of the barrier(s) or in activating the barrier(s) resulting in an unintentional flow of formation fluid into the wellbore, another formation or to the external environment [7, 8]. The unintended flow of fluids from the formation into the wellbore (a kick) can occur due to several reasons such as insufficient drilling fluid weight (density), not properly filling the drilled hole either while tripping in or out of the well (adding pipe to the drill string to lower it further into the wellbore or removing pipe from the drill string to bring it closer to the surface), swabbing (a decrease in bottomhole pressure due pulling the drill string too quickly), cutting of the drilling fluid by the formation fluids (reduction of drilling fluid weight due to dilution with gas) and lost circulation.

When drilling conventionally, following a kick, loss of well control is prevented by activating the BOP, which in this case is secondary barrier. Failure to close the BOP timely following loss of primary well control would result in increasing influx volume and flow in the annulus of the well. The risk of inability to close the BOP grows with increase in the flow rate. Therefore, successful activation of the BOP is increased by early kick detection. Where there is a substantial kick size, there exist a high chance of subsurface leaks occurring, this can be mitigated by a fast shut-in [1, 4]. Following closure of the BOP valves, the well is circulated with a higher density drilling fluid using one of the three constant bottomhole pressure (BHP) methods namely wait-and-weight method, driller's method, and the concurrent method. If properly applied, constant pressure at the hole bottom is achieved and prevent additional influx into the well [1, 5].

3. Conventional kick detection

3.1 Kick indicators

There are certain indicators that of primary importance to kick detection. Two of these indicators provide positive signs of influx into the wellbore during drilling while third indicator is relevant to recognizing a kick during tripping operations. To recognize a kick while drilling, two major changes in the rig fluid circulating system (while the rig pumps are on) need to be detected. The first primary indicator is a flow rate increase while pumping at a constant rate as this signifies that the formation is aiding the rig pumps move fluid up the annulus via an influx into the wellbore. The second sign of primary importance while drilling is an increase in pit (mud tank) volume not attributable to surface interventions such as building addition drilling fluid volumes. Fluids entering the wellbore will displace an equal volume of drilling fluid in the flowline and cause an increase in pit level (referred to as *pit gain*). This change in pit level could take some time due to the tank surface area. Surface losses of circulated mud in the return line, shale shakers and transfer tanks supplementing the main mud tanks would have to be accounted for so that the pit gain can be reliable. While tripping the drill string, the kick indicator of primary importance is flow from the well when the rig pumps are off. One notable exception to this (returns from the well with the rig pumps off being a kick indicator) is when a slug is pumped downhole resulting in heavier mud in the drill string than in the annulus [1, 4].

In addition to these primary kick indicators there are warning signs while drilling which if promptly responded to will keep the well under control and prevent the occurrence of a well control incident. These warning signs (secondary indicators) include abrupt increase in the rate of penetration while drilling called a drilling break, increase in torque and drag, changes in mud properties, increase in the shape and size of cuttings, decrease in shale density, increase in gas readings during tripping, connection, circulation or drilling, increase in the temperature of the drilling fluids returns and decrease in the calculated d-exponent. As these secondary indicators are not consistent in all situations they need to be considered collectively. They nonetheless give indication to the potential for an underbalanced situation [1, 4].

3.2 Auxiliary drilling rig equipment for kick detection

The American Petroleum Institute (API 53) standard for auxiliary equipment complimentary to both surface and subsea BOP installations, related to monitoring primary and secondary kick indicators, stipulates that the drilling rig has a trip tank, pit volume measuring and recording devices and a flow rate sensor [9]. The flow rate sensor on conventional drilling rigs is typically the flow paddle type for which the frequency (and voltage signal) generated is proportional to the flow rate. While the flow paddle meter is a low cost, low maintenance solution, it is not suitable for solid-laden fluids and gas flow [10]. It is recommended that the flow rate sensor is mounted in the flow line for early detection of formation fluid entering the wellbore or a loss of returns. The trip tank, a low-volume calibrated tank, that can be isolated from other surface drilling fluid system equipment should be capable of accurately measuring the amount of fluid entering and returning from the well with readout of half a barrel (0.0795 m^3) volume change. The trip tank is primarily used to measure the amount of drilling fluid required to fill the wellbore while tripping in or out of hole to ascertain whether the drilling fluid volume matches pipe displacement. The trip tank can also be used to measure volumes gained or lost in the annulus. The pit volume measuring and recording devices on the rig should be capable of automatically transmitting pneumatic or electric signals from sensors mounted on the drilling fluid pits to recorders and signaling devices on the rig floor such that pit volume gain or loss can be detected [4, 6, 9]. A Pit Volume Totalizer system meets these requirements on conventional drilling rigs. It is a centralized processor into which signals from sensors are fed. Flow into the wellbore is monitored using a mechanical or proximity type mud pump stroke counter while the rate of returns from the wellbore is monitored via a paddle flow type sensor placed in an open flowline. The level in the mud pits can be monitored using a mud level probe or an ultrasonic-type level sensor which can account for solids build up at the bottom of the tank that may affect float type readings [6].

These measurements, that aid in kick detection, are frequently monitored at the driller's console and corroborated by the mud logger's monitoring system. The conventional kick detection system is designed to raise alarms based primarily on threshold readings of delta flow (the difference between inlet and outlet flow rates) and pit gain over time. Mathematically, the delta flow method is represented thus:

$$\Delta Q = Q_i - Q_o \tag{1}$$

where; $\Delta Q > 0$ indicates lost circulation; and $\Delta Q < 0$ indicates that a kick has occurred [11]. The drilling crew should be able to recognize a kick volume of 5 bbl (0.795 m^3) or less during trips while a kick volume of 10 bbl (1.590 m^3) or less should be recognized while drilling. A flow check is performed if improper hole fill up is noticed during a trip as measured by the trip tank. If the flow check is positive the well should be shut in, conversely, the drill string should be run back to the bottom and the well circulated bottoms up [4, 9].

3.3 Auxiliary drilling rig equipment for kick detection

Mud logging as a service is typically provided under Surface Logging Services which involves the use surface measurements to infer formation and wellbore properties. Real time monitoring of data obtainable through mud logging provides several parameters for kick detection which include increase in pit volume (pit gain), pump rate, return flow rate, rate of penetration (ROP), total gas, connection gas and drop in pump pressure. None of these parameters requires sophisticated downhole electronics or advanced signal processing. These parameters can be categorized into instantaneous parameters (drilling parameters) and lagged parameters. The drilling parameters are ROP, pit gain, pump pressure, pump rate and return flow rate. The lagged parameters, on the other hand, comprise gas parameters delayed by the lag time. Lag time, a definite time interval that is always required for pumping the drilled formation cuttings and drilling fluid from the hole bottom to the surface, depends on both the volume of drilling fluid in the annulus and the flow rate at which the drilling fluid is circulated. Correlating the frequency and level of the connection gas with respect to the mud weight can give an accurate indication of differential pressure and thus indicate near-balance or underbalanced drilling. With the pumps off, the equivalent circulating density decreases to the static drilling fluid weight. The connection gas, as an indicator of underbalanced situation, reflects as sharp peaks on the mud log. This is contrasted to total gas readings which increase in a smooth fashion due to drilling through a gas formation without corresponding increase in pore pressure. The lag time of the gas peak due to connection gas would be relative to when pumps are off. Hence, human interpretation (provided by the mud logging engineer or mud logger) is required to continuously monitor and analyze acquired parameters for decisive actions to prevent or mitigate a well control incident [12–14].

3.4 Limitations of conventional kick detection systems

While these traditional monitoring systems for kick detection are somewhat reliable, their response time is somewhat slow and thus potentially aggravate the initial problem of the gas influx in some scenarios. An overview of loss of well control (LOWC) events that occurred after the BOP had been landed on the wellhead in the US Gulf of Mexico (Outer Continental Shelf) between 2011 and 2015 showed that kicks were not detected before the well started flowing to the surface or surrounding formations in 50% of the recorded cases. It was inferred that the LOWC events could have been prevented if the kicks had been observed early. Case studies of the Macondo blowout and the Bardolino loss of well control event further emphasize the importance of an efficient and adaptable early kick detection system. The Macondo accident resulted in the loss of 11 lives, the release of 680,000 m^3 (4,250,000 bbls) of crude oil in 85 days to the environment, billions of dollars in economic damages and mitigations arising from the event. The Bardolino incident, on the other hand, due to early detection of kick and proper interpretation of the signs of kick, was managed without any spill or loss of life [5, 7, 8, 15].

Gas kick detection is particularly challenging in deep offshore environments for several reasons. First, as the water depth increases, the safe drilling fluid operating window between the fracture and formation pressures narrows. Secondly, relying on lagged parameters becomes increasingly unreliable with increasing depth in ultra-deep waters where bottoms-up circulation can take as much as 4 h. In event that the well kicks during this period, the kick volume increases, and the time spent waiting for the kick indicators reduces the drillers' ability to mitigate potential impact. Thirdly, the solubility of gas from the formation in non-aqueous drilling fluids under high pressure could lead to large gas volumes being dissolved in the drilling fluid until the saturation pressure is attained. Gas solubility in these drilling fluids such as oil-based systems could be as high as 100 times greater in solubility than in water-based systems. Consequently, gas remains dissolved (and largely undetected) in the drilling fluid during a kick until much lower pressures are encountered towards the surface as pit gain as compared to the bottom of the marine riser. This gas influx initially translates to undiscernible increase in pit gain until the gas is released at shallow depths which could compromise well integrity and ultimately blowout. This masking of influx gas has been found to worsen with increase in the mud flow rate. Fourthly, currents and wave motion further influence measurements on marine vessels which make early kick detection difficult. Fifthly, in subsea wells for which kicks have been detected and the well shut-in, dissolved gas could hamper subsequent circulations carried out to restore well control by blockage of choke and kill lines due to the formation of hydrates at low temperatures [16–18]. The limitations are being addressed through more sensitive early kick detection systems.

4. Developments in early kick detection for conventional drilling

The following criteria have been set for assessing the success of a kick detection system—how early kicks are detected, how the system is able to eliminate or minimize the number of false alarms, the sensitivity and accuracy of the sensor(s), and its ease of installation [19]. An early kick detection (EKD) system has been described as a system of hardware, Intelligent Control Unit (ICU) and control software with the capability to detect an influx of formation fluids into the borehole during well operations. An advanced EKD system utilizes high precision equipment with ICU/software providing advanced models and algorithms for greater automation and comparison to controlled well conditions. As with simple EKD systems, audio and visual alarms are an integral part of any EKD system to provide real-time assessment [20]. Advances in EKD systems will be considered in terms of sensor function and sensitivity, sensor location (surface versus downhole measurement), and algorithms for efficient kick detection. Each of the previously mentioned primary kick indicators (increase in flow rate while pumping at a constant rate, pit gain and flow from the well when the pumps are off) are measured with different sensors with differing physical principles.

4.1 Surface sensors for early kick detection

Ultrasonic level sensors are preferred for measuring mud pit gain because they provide for greater sensitivity and accuracy as compared to other float meters (magnetostrictive, optical and differential pressure). They require low maintenance, and some models have a response time as low as 1 s thus very suitable for real time monitoring of the mud tank level [6, 21].

As regards flow measurement, there are two approaches: volumetric flow or mass flow measurement. The former is achieved using positive displacement flow measurements (such as pump stroke counters) or by employing flowmeters which provide estimates of velocity such as electromagnetic, turbine, ultrasonic, and vortex flowmeters [6]. Electromagnetic flowmeters installed both in the pump output and return flowlines have been used in implementing the delta flow approach for kick detection especially where there is the restriction of space [11, 13]. Electromagnetic flowmeters have the advantages of simple structure with no moving parts and no obstruction of fluid flow by throttle parts or its flow path. Therefore, there is no resultant additional pressure loss, wear, blockage, or corrosion of the inner lining due to solids-laden flow [22]. However, their applicability is limited to water-based drilling fluid [23]. It has been reported that the accuracy of electromagnetic flowmeters for early kick detection can be improved by installation in a V-shaped flowline segment on the outlet flow path as challenges with transient large flow passage and solids deposition were resolved [24].

The use of ultrasound flowmeters is an alternative to electromagnetic measurement applicable in both water-based and oil-based drilling fluid. This type of flowmeters works on the principle that part of the reflected ultrasonic waves that get transmitted into the pipe wall from drilling muds gets transferred into Lamb waves and subsequent a relationship between the reflected signal frequency and the flow rate is obtained. The method is nonintrusive but suffers from great attenuation of ultrasound waves in mud. This problem is resolved by continuous detection of non-oriented reflected ultrasound Doppler frequency shift, which relates the drilling fluid flow rate to the collected repeated Lamb waves. A related flow rate algorithm is obtained through the even distribution characteristics of the reflection angles [25]. The installation of three ultrasonic sensors in an open channel with Venturi constriction provided high accuracy flow rate measurement comparable to electromagnetic flowmeter measurements which are not susceptible to cuttings settlement at low flow velocity [23].

However, the most proven meter for EKD is the Coriolis flowmeter: this is based on the mass flow measurement principle. It can provide mass flow rate, density, and temperature measurements of liquids and gases within a single meter in the presence of either water-based or oil-based drilling fluid. Coriolis flowmeters provide mass flow rate measurements independent of the physical properties of the fluid and are unaffected by changes fluid properties due to fluctuations in density, viscosity, temperature, or composition. Flow measurements can be transmitted in real time so that software models are updated and EKD is achieved. In the Coriolis flowmeter a rotation force is created as the flow loop rotates about a secondary axis in response to the circulation of drilling fluid through a circular path about a primary axis. This force is directly proportional to the angular momentum of the fluid flow around the circular path (which gives a direct indication of mass flow rate) while frequency at which flow tube vibrates provides a direct measure of the fluid density. However, the flow and density measurement accuracy of the Coriolis sensor becomes degraded by entrained gas fractions exceeding 5% [5, 26]. The pressure rating limited to about 3000 psi (207 bar) precludes it use to the standpipe and the pump suction line [6, 20]. The use of the density compensated Coriolis meter is limited in precise kick detection when the mud pumps are off with no flow as is the case when making connections or tripping. Active mud circulation through the Coriolis flow meter is required for a measurement to be taken [20]. Optimal performance of the Coriolis mass flowmeter is obtained with high profile, dual-tube sensors with low tube frequency [26]. A Coriolis meter installed on a conventional rig is shown in **Figure 2**.

4.2 Smart flowback fingerprinting

Kick detection based on surface measurements especially the delta flow approach that compares the flow rate into the well and the flow rate of the returns from the well as an indicator of either an influx or loss scenario could be complicated as issues such

Figure 2.
Coriolis installation on the bell nipple of a conventional drilling rig. N.B.: The arrows indicate the bypass and flow direction through the Coriolis from bottom to top [26].

as wellbore breathing or ballooning and changing thermal conditions could mask the occurrence of a kick. Borehole ballooning or breathing occurs when slow mud losses occur during drilling ahead and a subsequent flowing of the well when the pumps are off during a connection operation or flow check. Therefore, changes in mud pit volume during a drill pipe connection are keenly monitored. This is critical because kicks frequently occur during drill pipe connections [6, 27]. To address the masking of kicks, Smart Flowback Fingerprinting was developed, a method of kick detection using an automated process to monitor wellbore flowback. It uses statistical analysis to interpret flowback data obtained during static conditions in which the rates-of-change for multiple successive drilling fluid flowback cycles to the mud pits are compared and analyzed [28]. It is expected that under static conditions, drilling fluid flowback cycles will have a repeatable profile when measured over successive cycles. Thus, any departure from the expected flowback profile could indicate a formation fluid influx. The technology enables real time detection of flowbacks exceeding normal volumes, without human intervention, with minimal false alarms depicted clearly as threshold and alarm curves. The system can accurately identify influx of formation fluids as distinguished from wellbore breathing and flowback which occurs when the well is static [28, 29].

4.3 Downhole sensors for early kick detection

The closer the location of real-time kick indicator sensors to the formation, the earlier the kick would be detected. Real-time downhole sensing alternatives for kick detection have been developed. Measurement while drilling (MWD) combined with

Logging while drilling (LWD) provides a viable alternative to surface measurements for kick detection. MWD tools are added to the drilling bottomhole assembly (BHA) to take electro-mechanical measurements while drilling, simultaneously. They are very effective in guiding the drill bit to the target pay zone, the acquisition of wellbore deviation directional surveys and the measurement of drilling mechanics data such as downhole torque, pressure, and vibration, with real time transmission of acquired data to the surface. A major MWD application that aids in kick detection is the accurate downhole BHP measurement via the Pressure While Drilling (PWD) tool using high-accuracy quartz pressure gauges. The PWD tool enables continuous annular and wellbore downhole pressure monitoring so that BHP is kept within the safe drilling window [6, 13].

LWD tools provide petrophysical data such as porosity, resistivity, density, and gamma ray. As regards kick detection, three key measurements affected by borehole fluids are density, electrical resistivity, and acoustic velocity. Bulk density as measured by the gamma density tool will decline as the drilling fluid is diluted by a gas kick. An influx of petroleum fluids will result in a clear increase in electrical resistivity in either water-based or oil-based fluids while the compressional wave velocity in drilling fluids will increase with an influx of gas. MWD/LWD tools are in-built with electronic sensors and batteries packaged in the housing in such a way that they do not impede the high flow rates that occur during drilling. However, a major drawback with using MWD/LWD tools is the requirement of a minimum fluid flow rate for signal transmission to the surface in real time. This implies that there would be no data transmission at low flow rates (a minimum of 130 gallons/min is required for some tools), during connections and when other periods when the pumps are turned off. There are other challenges with mud pulse telemetry which include the reduction in the data transmission rate with increased depth and signal attenuation in compressible drilling fluids such as OBM. While MWD/LWD sensors can measure large amounts of formation evaluation and kick detection related data, mud pulse telemetry only allows data transmission at low rates which results in a time lag between the time the mud pulse reaches the surface and when it is generated downhole. In addition, MWD/LWD tools are limited to measuring data at the bottomhole assembly (BHA) which is placed a few meters above the drill bit. These challenges limit MWD/LWD applicability for real time data transmission in ultradeep wells [6, 13].

The limitations posed by mud pulse telemetry in transmitting downhole measurements to the surface in real-time can be resolved with the Wired Drill Pipe (WDP) system. The WDP system has an embedded high strength coaxial cable and low-loss inductive coils incorporated into each joint of drill pipe during manufacture. This wired communication channel through drill pipe transfers signals at rates of about 57,000 bits/s, this is several orders of magnitude faster than is attainable via mud pulse telemetry or electromagnetic telemetry. It transmits alternating electrical signals between the BHA and the surface systems. In addition to measuring data near the drill bit and high bandwidth, WDP allows for data measurement along the entire length of the drill pipe string [5]. The use of fiber optic sensing as real-time downhole sensing option for kick detection has been proposed. Fiber optic measurements, Distributed Temperature Sensing (DTS) and Distributed Acoustic Sensing (DAS) are already in the use for injection and production flow profiling, determination of crossflow across different zones and detection of flow behind casing in completed wells. The applicability of fiber optic sensing during drilling operations has only been tested for gas monitoring in the marine riser. The fiber optic cable is installed in a similar manner to a flexible production riser installation. Data transmission is achieved by launching an intense laser pulse into the sensing fiber which gets scattered spontaneously as it interacts with the crystalline structure in the silica-based core of a fiber optic cable which is affected by thermal and pressure variations. A fraction of the back scattered light is captured and transmitted through the fiber guided modes and propagated towards a fast photodetector. The changes in the back-scattered light can be related to the acoustic and thermal variations along the fiber with its spectrum consisting of a Rayleigh band, Brillouin band, and Raman band which are used in DTS, DAS and Distributed Strain Sensing. Once the propagation time of a pulse at a particular wavelength is known along a fiber of specific refractive index, the position of the interaction can be located and the perturbation in the measure quantity on the fiber determined [16].

4.4 The use of numerical modeling and machine learning to aid early kick detection

Flow modeling and simulation is critical for testing and validating early kick detection systems. Mathematical models which account for two-dimensional and three-dimensional transient multiphase flow with due consideration to different flow regimes within the drilling assembly and the annuli, heat transfer between the surrounding formation and the wellbore, and gas solubility are required to adequately capture wellbore dynamics during a kick scenario. Numerical techniques such as Computational Fluid Dynamics, though computationally extensive, are being employed to solve these equations due to the limitations of simplified one-dimensional models and empirical models with simplified assumptions [30]. The use of flow modeling as a kick detection method has been highlighted. Wellbore flow is simulated using a "representative" hydraulic model and then compared to the projected flow rate with actual measured flow rates. Non-linear variations in fluid properties such as density, rheology, gel strength due to multiphase flow (in some cases three phase flow—gas influx, liquid flow, and cuttings transport) are difficult to accurately model thus limiting its use in early kick detection [16]. It is worth noting that most published flow models for EKD are homogeneous-type one-dimensional two-phase drift flux models due to the simplicity of calculating phase velocity and gas fraction [30].

The machine learning approach has also been utilized for kick detection. Data employed has been obtained from different sensors on either actual drilling rigs or lab-scale experiments. Different input parameters have been tested which include majorly prior highlighted primary and secondary kick indicators. Different models have been tested such as Bayesian classifier, decision tree, k-nearest neighbor, random forest, support vector machine, different neural networks, and autoregressive models [31, 32]. Extensive gas-kick datasets were generated autonomously via 108 tests from a pilot-scale test well experimental setup equipped with a complete drilling system and a comprehensive mud logging system for surface monitoring of relevant drilling and geological parameters complimented with Doppler wave sensors just above the BOP for riser monitoring of gas migration and downhole pressure monitoring via pressure gauges. A managed pressure drilling system was coupled to the rig setup with a gas injection system. A polycrystalline diamond compact drilling bit with a bottomhole assembly was used to drill autonomously through a synthetic rock sample. The experimental setup was designed to simulate an actual gas-kick incident that occurred at approximately 4100 m (13,452 ft) during a drilling operation with a water depth of approximately 1000 m (3281 ft). Data preparation and analysis was performed which included raw-data exploration, data cleaning, signal/noise-ratio analysis, feature scaling, outlier removal, and feature selection using a random forest algorithm which resulted in reduction from the initial 24 parameters to 11 parameters considered important for kick detection. Four parameters (ROP, BHP, Doppler amplitude, and differential flow out capturing delta flow) were considered of utmost importance in early kick detection. The data was further labeled using a six-level risk likelihood criterion instead of the typical two-state alarms ("kick" or "no kick"). The splitting ratio for time-series dataset was 63%, 7%, and 30% among the training, validating, and testing sets, respectively. Of the four machine learning algorithms tested, decision tree, *k*-nearest neighbors, support vector machine, and long short-term memory (LSTM), the LSTM recurrent neural network algorithm showed the best performance, with early detect gas kicks and proper classification into the six kick alarm levels with minimal false negatives. The maximum detection time delay was 7 s only, which provides sufficient time margin to address the gas kick scenarios. The value in supplementing surface kick detection related parameters with continuous Doppler-ultrasonic-wave parameters measured at the mudline and downhole BHP was demonstrated [33].

5. Early kick detection and automatic control in managed pressure drilling

The need for early kick detection systems is further underscored in the implementation of Managed Pressure Drilling (MPD); an adaptive drilling process that enables fast and precise control of the annular pressure profile throughout the wellbore during drilling and completion operations. The accurate monitoring of flow and pressure conditions in the well is achieved due to the closed-loop circulation system (as compared to conventional drilling with an open annulus). Influx and loss situations are detected earlier in systems where MPD is employed as compared to conventional drilling. With MPD the safety of personnel onboard the rig is enhanced since a gas kick circulated with drilling fluid to the surface through the mud-gas separator without either reducing the BHP or stopping the pumps. The risk of sticking pipe is reduced as a kick can be handled without rotating the pipe [34]. Any influx into the wellbore during MPD will be safely contained to avoid continuous influx of formation fluids. Thus, the emergency well control requirements may not be required as the MPD system is set up for its occurrence. MPD has found wide applicability in projects with technical complexity and narrow pressure windows thus enabling the continuation of operations which would have been adjudged unfeasible [35]. The application this technology (MPD) has been shown to achieve automated dynamic well control as well as reduced non-productive time by allowing influx circulation at full rate. It removes human factors intrinsic in conventional well control and the need for flow check, making the need for shutting in the well and consequently the use of the BOP optional [36].

There are three fundamentally different MPD variants implemented based on the operating conditions with different objectives regarding pressure control and influx management. First, Constant Bottomhole Pressure (CBHP) method, BHP is controlled by continuous automatic adjusting of the choke to track the pre-defined pressure profile to eliminate any kick or fluid loss in a relatively unknown and narrow drilling margin. Then, the Dual Gradient Drilling method is used in offshore operations where the return mud does not travel through a large diameter drilling riser as the method reduces the number of casings required. The pressure gradient below the mudline is isolated from the drilling mud gradient above removing the impact of the water depth on the drilling operations. Third, the Pressurized Mud Cap Drilling method entails the use of a sacrificial fluid like water to manage the mud losses in the highly depleted formation. Of these three MPD variants, the CBHP is the most common variant adopted for drilling in deep offshore environments [14]. The implementation of MPD systems can be considered based on the control parameter such as surface backpressure (SBP), fluid density, fluid rheology, annular fluid level, circulating friction and hole geometry of which SBP is the most used control parameter [34].

MPD-CBHP is typically achieved through a rotating control device (RCD) installed on the surface or subsea BOP to seal the annulus from the atmosphere and closing around the drill pipe. The returns from the well are diverted from the rig floor through a choke manifold while allowing for both pipe rotation and reciprocation. Thus, tripping and drilling operations can be performed while the returns are diverted through the choke manifold. The SBP which is propagated throughout the annulus is used to control the BHP to a desired setpoint by manipulation of the choke openings [34, 35, 37]. The MPD choke manifold is installed separately in parallel with the rigs main flow line and the conventional rig choke manifold. This set-up makes allowance for circulations through the MPD manifold and circulations by conventional methods [35]. The RCD is not considered as a well barrier as regards well control operations [38]. In floating drilling rigs, the RCD is installed below the slip joint with flow diverted through flexible lines to the return system. With this setup, the effect of the rig heave on the circulating volume in the riser is canceled, thus, this remains [5]. The automated choke manifold is run on control systems with a programmable logic controller which could be set to control the valve percentage opening and closing. In addition, the automated choke manifold is connected to auxiliary mud or nitrogen pump to provide the surface back pressure (SBP), as well as monitor flow rates in and out of the wellbore [38]. MPD systems also includes a backpressure pump, flowmeter, and software algorithm. The equipment layout depends on whether the system is manual requiring an operator to control annular pressure via opening and closing of the choke valve, semi-automatic for which the choke is automatically adjusted to obtain the predetermined surface pressure using hydraulics software and automatic requiring a PLC which is programmed with hydraulics software connected to the choke and the backpressure pump that controls the desired annular pressure automatically [5]. A MPD system is illustrated in **Figure 3**.

This dynamic well control method (MPD) is only applicable for influxes up to a certain volume as the kick tolerance (the maximum influx volume that can be handled and safely circulated out of the well) could be as low as 10 bbl (1.590 m^3) in some deep offshore wells. This necessitates early kick detection via flow measurements. In general, MPD systems provide EKD by using comparison of flow out (return flow) to flow in as a primary kick indicator i.e., delta flow. Coriolis flowmeters are applied for precise monitoring of both flow into the wellbore and flow out with high accuracy. Early gas detection can be achieved by monitoring the annular pressure along the wellbore with pressure sensors mounted at different depths and transmitted via WDP. Replicator stations are used for boosting the pressure signals transmitted along the WDP [5, 35]. A Venturi channel is typically used after the choke controller before the return flow line for flow out measurements towards EKD [39].

Although the level of automation in the different MPD systems varies, an automated response can be initiated to a kick scenario with a fully automated choke that includes a kick detection algorithm. When the MPD system automatically detects an influx, it can respond by increasing the backpressure which actively increases the BHP, accelerating the end of the influx cessation over a passive shut-in response.

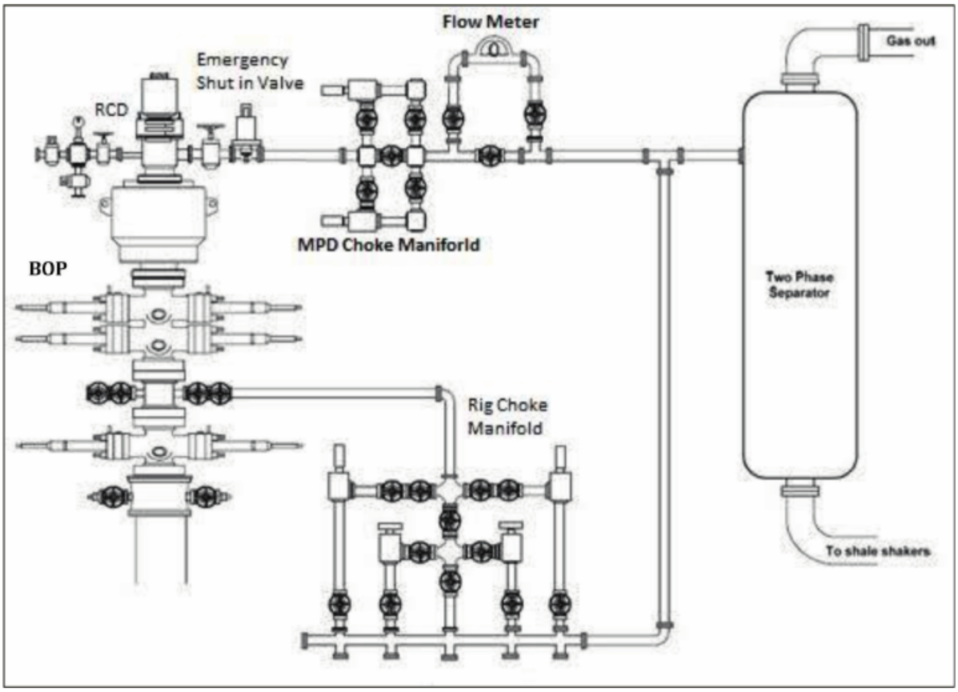

Figure 3.
A schematic of a MPD system [27].

In this way, an automated MPD system can reduce kick severity by increasing kick detection resolution thereby reducing inflow time and consequently volume, continual circulation during initial response, maintaining annular friction and preventing a decline in BHP thereby minimizing influx flow rate and volume, and increasing the BHP through active choke manipulation thereby reducing the time to end of influx and overall kick volume. This system provides real time comparison to modeled controlled conditions and automated well control response and signals the driller for necessary actions when specified thresholds are exceeded [6].

The design of pressure control systems for MPD drilling operations requires accurate modeling of the system hydraulics. However, accurate modeling of drilling systems implies to use of highly complex models involving parameterized, nonlinear, nonconservative hyperbolic Partial Differential Equations (PDEs) completed by nonlinear and implicit boundary conditions. These model features render its numerical simulation computationally expensive and make the controller design cumbersome. Model order reduction techniques have been proposed for the construction of models that combine reduced complexity with high predictive capacity. A reduced bias method capable of handling localized nonlinearities has been applied for the modeling of well dynamics under MPD [40]. An alternate approach, the use of real-time high fidelity flow modeling approximates the results of offline complex PDEs but relaxes the model accuracy during the transient phases by assuming a fixed temperature profile and the linear Bingham Plastic model [41]. These hydraulic models are implemented in the controller. Model-predictive control (MPC) techniques which utilize knowledge about the wellbore dynamics and monitored parameters on the rig to compensate for measured changes are adjudged the most appropriate for

MPD operations. MPC techniques have been found superior to simple Proportional-Integral-Derivative controllers [34]. Proper tuning of the automated MPD control systems is necessary to minimize challenge of instability of a non-robust control system of which oscillating choke position is a sign [6]. The difficulty in handling flow-in changes with high precision is also addressed by a robust MPC system [34]. Automated control during MPD is achieved by implementing reduced order high fidelity flow models within an optimal MPC framework.

6. Automated well control for conventional drilling operations

Traditionally, well control is a manual safety critical process with reliance on the driller to shut-in the well once an influx is detected. It requires high cognitive workload from the driller who is also saddled with repetitive well construction tasks for extended periods. The driller is the member of the drilling rig crew responsible for operating drilling rig equipment on the rig floor. While the capacity and preparedness of the driller is enhanced by regular training and drills, unforeseen events can unsettle him; thus, making him vulnerable to error. The driller could also be distracted by extraneous factors which could adversely impact on his performance. The role of human errors in the occurrence of LOWC events has been considered crucial as 42% of published incidents between 2014 and 2021 were attributed to human factors [42]. This encompasses the skill of the drilling personnel in recognizing a well control situation and restoring well control. It has been noted that undue reliance on human intervention in well control situations could be dangerous. Thus, organizational, and human failures could be eliminated by increasing the level of automation in well control. Automating processes allows well operations to be more reliable and consistent, effectively improving the performance of drillers. Consequently, the implementation of automation within the well control envelope is expected to contribute significantly to enhance safety and efficiency. Even though full automation of the well control process is yet to be adopted within the industry, there are technological developments towards bridging this gap [5, 6, 42].

A system, known as Automated Well Control (AWC), which fully automates kick detection and shut-in sequences during drilling operations has been developed by Safe Influx. This system enables continuous real-time monitoring of the well and manages influx flow automatically by ensuring fast identification of the influx of formation fluids into the wellbore and rapid response via immediate decision-making; thus, ensuring the influx size is minimized and the risk to people and the environment mitigated [42]. This system is classified to be on level 2 according to the automotive automation classification [42, 43]. The topology of the AWC system is shown in **Figure 4**. The well control process is automated such that once a kick is detected, the AWC system will actively control the drilling rig by performing a series of commands. Firstly, the drill string is spaced out such that an incompatible pipe connection across the BOP valve to be actuated is moved to facilitate safely shutting in the BOP. Secondly, the top drive is stopped, and the rig pumps shut down. Thirdly, the BOP is shut-in [44]. The system footprint of the automated control system on the drilling rig is a Programmable Logic Controller (PLC) and a Human Machine Interface (HMI) screen. The HMI screen can be incorporated into the rig's existing HMI screen for ease of operation by the driller. The PLC uses control algorithms to accurately monitor the parameters from the existing sensor package and control the existing rig equipment [45].

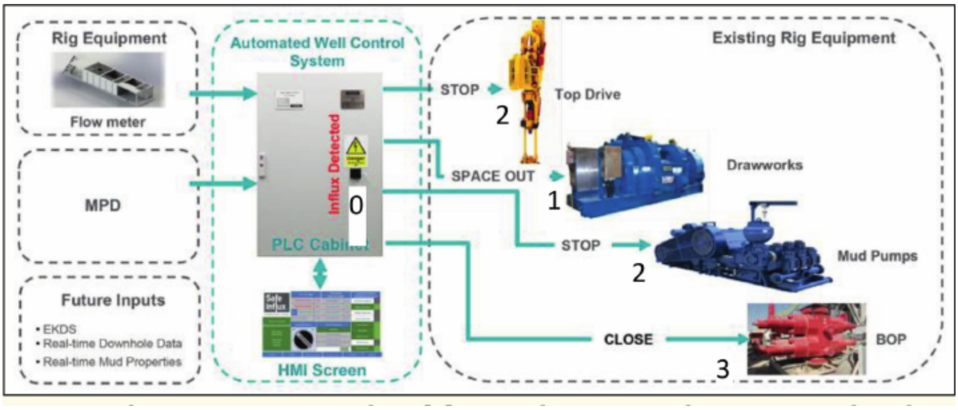

Figure 4.
The AWC system topology [45]. N.B.: The automated steps are numbered.

The space out of the drill string following kick detection is not trivial. A Well Control Space Out technology for this purpose has been developed. The technology comprises of an internet-of-things environment that links cameras and an edge server which implements deep-learning models for the real-time processing of video images recording the drill string above the drill floor. Automatic object detection is used to keep track of tool joints relative to known BOP dimensions; while video analysis of the recording is displayed on a dashboard detailing the state and steps to be followed in a well control incident without the need for any time-consuming, manual calculations. A regional convolutional neural network is used for image classification. This technology, which ensures that the BOP valve is not closed across a tool joint, is a key component towards the implementation of an automated closed-loop control system [3]. The technology is represented with a schematic in **Figure 5**.

Once the AWC system has been installed and tested, the driller is required to configure certain parameters prior to commencement of drilling operations. This includes the setup of space out parameters and the selection of the equipment whose control will be ceded to AWC system such as the top drive, mud pumps, drawworks, and BOP. This ensures that the Operator or Drilling Contractor policy can be implemented, so that the Operator and Drilling Contractor can be assured that for the duration of the well a robust assurance process is in place for well control [44]. In the case of an influx of formation fluids, the driller is alerted both visually and audibly at the HMI by the system, indicating that the AWC sequence has commenced. The system then takes control of the prior specified equipment that the human operator would have operated to regain well control [42].

The AWC system has been extensively tested on drilling simulators to verify how the system functioned in a wide range of scenarios. The system was also put to test at a well control training event involving a large group of drillers. Each driller performed a manual shut in on a particular well programmed into a well control simulator. Even though each driller had prior knowledge of an impending kick, the smallest influx volume shut-in by the drillers ranged from 1.27 m^3 (7.99 bbl) to 5.08 m^3 (31.96 bbl), with the typical volume being about 3 m^3 (18.87 bbl). When the Automated Well Control system was activated to automatically shut-in the same influx volume, the shut-in volume was under 0.32 m^3 (2.02 bbl), an order of magnitude less than any human driller achieved [42].

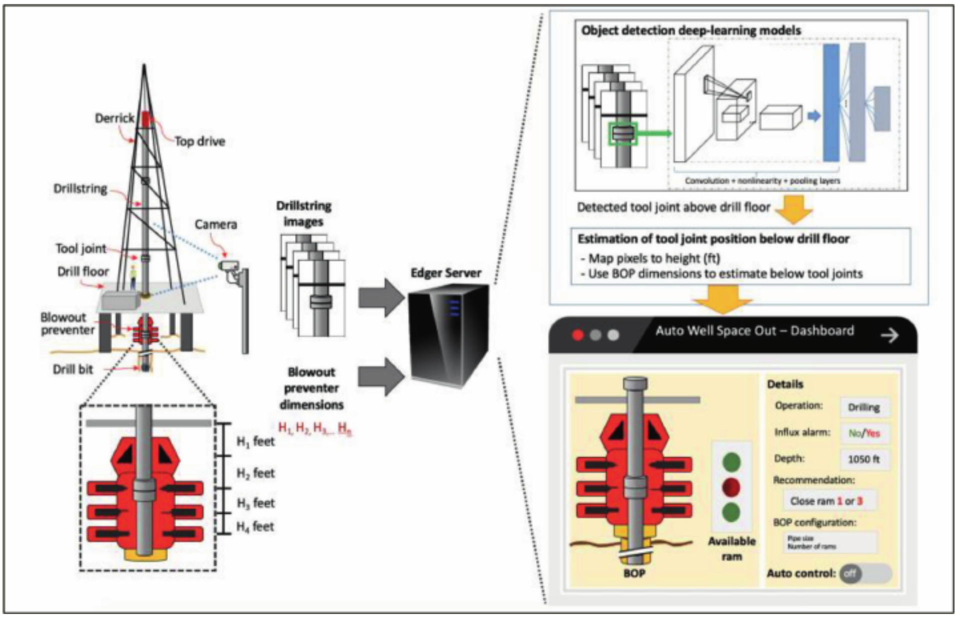

Figure 5.
The well control space out technology illustrated [3].

A full field trial of the was successfully conducted in Aberdeen, UK, where the minimum viable product of the AWC system was interfaced with a conventional land rig for the purpose of demonstrating automated well control. A series of 20 different tests were performed to test full functionality during normal drilling ahead operations and the effects of incorrect set up. The AWC system proved its functionality of the standard system under the different scenarios and operational requirements tested. Furthermore, the AWC system has been interfaced successfully with a MPD system. This integration of both systems provides automated primary and secondary well control, which allow wells to be drilled and constructed with a very high level of efficiency and integrity [46]. The AWC system is currently designed for the drilling phase with certification to operate on either a cyber-rig or a traditional rig [42].

7. Conclusion

The deployment of EKD systems has become imperative for executing drilling and completion operations in deep offshore environments which are prone to LOWC incidents to prevent the dire consequences of past accidents. The Coriolis mass flowmeter is integral to EKD systems for accurate differential flow measurements. Other meters such as electromagnetic flowmeters and Venturi channels with ultrasonic sensors are used when operational constraints limit the use of Coriolis mass flowmeters. Downhole monitoring, along the marine riser down to the mudline via ultrasonic Doppler sensors transmitted via optical fiber and near the drill bit through pressure while drilling, has proven valuable in complementing surface measurements in achieving EKD. Smart fingerprinting using machine learning algorithms help in minimizing false alarms which could arise due to well breathing and ballooning when the pumps are off. Automation in well control can be achieved for conventional overbalance drilling operations by coupling an AWC system to the drilling rig for fast well shut-in or through automated CBHP-MPD for a closed annulus. For future well projects with high LOWC risks, EKD with AWC whether for an open or closed annulus should be incorporated into the well program prior to well construction to ensure safe project delivery.

Acknowledgements

The support of the management of the University of Lagos and the Department of Chemical and Petroleum Engineering is acknowledged.

Conflict of interest

The authors declare no conflict of interest.

Nomenclature

AWC	Automated Well Control
BHA	Bottomhole Assembly
BHP	Bottomhole Pressure
BOP	Blowout Preventer
CBHP	Constant Bottomhole Pressure
DAS	Distributed Acoustic Sensing
DTS	Distributed Temperature Sensing
EKD	Early Kick Detection
HMI	Human Machine Interface
ICU	Intelligent Control Unit
LOWC	Loss of Well Control
LSTM	Long Short-Term Memory
LWD	Logging while Drilling
MPC	Model-Predictive Control
MPD	Managed Pressure Drilling
MWD	Measurement while Drilling
PDE	Partial Differential Equation
PLC	Programmable Logic Controller
PWD	Pressure while Drilling
RCD	Rotating Control Device
ROP	Rate of Penetration
SBP	Surface Backpressure
SCSSV	Surface-Controlled Subsurface Safety Valve
WDP	Wired Drill Pipe

References

[1] Mitchell RF, Miska S, editors. Fundamentals of Drilling Engineering. 1st ed. Texas: Society of Petroleum Engineers; 2011. p. 696

[2] Chung S, Kim S, Yang Y. Use of hazardous event frequency to evaluate safety integrity level of subsea blowout preventer. International Journal of Naval Architecture and Ocean Engineering. 2016;**8**(3):262-276. DOI: 10.1016/j.ijnaoe.2016.03.005

[3] Magana-Mora A, Affleck M, Ibrahim M, Makowski G, Kapoor H, et al. Well control space out: A deep-learning approach for the optimization of drilling safety operations. IEEE Access. 2021;**9**:76479-76492. DOI: 10.1109/ACCESS.2021.3082661

[4] Aberdeen Drilling Schools. Well Control for the Rig-Site Drilling Team. 4th rev ed. Aberdeen: Aberdeen Drilling School Ltd.; 2002

[5] Holand P. Loss of Well Control Occurrence and Size Estimators, Phase I and II. Final Report for BSEE. Vol. No. ES201471/2. Trondheim, Norway: ExproSoft; 2017

[6] Wood Group Kenny. Evaluation of Automated Well Safety and Early Kick Detection Technologies. Report No. 100107.01-DR-REP-0004. Washington, DC: Bureau of Safety and Environment Enforcement (BSEE); 2015

[7] Norwegian Oil and Gas Association. Recommended Guidelines for Classification and Categorization of Well Control Incidents and Well Integrity Incidents. Report No. 135. Stavanger, Norway: Norsk olje&gass; 2021

[8] Fraser D, Lindley R, Moore D, Vander SM. Early kick detection methods and technologies. In: Proceedings of the SPE Annual Technical Conference and Exhibition; October 27-29, 2014. Amsterdam: SPE; 2014. DOI: 10.2118/170756-MS

[9] American Petroleum Institute. Recommended Practices for Blowout Prevention Equipment Systems for Drilling Wells. API Recommend Practice 53. 3rd ed. Washington: API Publishing Services; 1997

[10] InstrumentationTools. Working Principle of Paddle Wheel Flow Meters. [Internet]. 2022. Available from: https://www.instrumentationtools.com/working-principle-of-paddle-wheel-flow-meters [Accessed: May 16, 2022]

[11] Speers JM, Gehrig GF. Delta flow: An accurate, reliable system for detecting kicks and loss of circulation during drilling. SPE Drilling Engineering. 1987;**2**:359-363. DOI: 10.2118/13496-PA

[12] Ahmed MA, Hegab OA, Sabry A. Early detection enhancement of the kick and near-balance drilling using mud logging warning sign. Egyptian Journal of Basic and Applied Sciences. 2016;**3**(1):85-93. DOI: 10.1016/j.ejbas.2015.09.006

[13] Tost B, Rose K, Aminzadeh F, Ante MA, Kick HN. Detection at the Bit: Early Detection Via Low Cost Monitoring; NETL-TRS-2-2016; EPAct Technical Report Series. Albany: U.S. Department of Energy; 2016. p. 48

[14] Huque MM, Imtiaz S, Rahman A, Hossain M. Kick detection and remedial action in managed pressure drilling: A review. SN Applied Sciences. 2020;**2**:1178. DOI: 10.1007/s42452-020-2962-2

[15] St. John MF. Macondo and Bardolino: Two case studies of the human factors

of kick detection prior to a blowout. In: Proceedings of the Offshore Technology Conference; 2-5 May 2016. Texas: SPE; 2016. DOI: 10.4043/26906-MS

[16] Feo G, Sharma J, Kortukov D, Williams W, Ogunsanwo T. Distributed fiber optic sensing for real-time monitoring of gas in Riser during offshore drilling. Sensors. 2020;**20**:267. DOI: 10.3390/s20010267

[17] Ma Z, Vajargah AK, Chen D, van Oort E. Gas kicks in non-aqueous drilling fluids: A well control challenge. In: Proceedings of the SPE/IADC Drilling Conference and Exhibition; 6-8 March 2018; Texas: SPE; 2018. DOI: 10.2118/189606-MS

[18] Teodoriu CB. An experimental investigation of kicks when gases are in solution: The dormant kick story. In: Proceedings of the AADE Fluids Technical Conference and Exhibition; 14-15 April 2020; Texas; SPE; 2020. AADE-20-FTCE-041

[19] Hargreaves D, Jardine S, Jeffryes B. Early kick detection for deepwater drilling: New probabilistic methods applied in the field. In: Proceedings of the SPE Annual Technical Conference and Exhibition; 30 September 2001; New Orleans; SPE; 2001. DOI: 10.2118/71369-MS

[20] Office of Offshore Regulatory Programs. Early Kick Detection BAST, Step 1.2 of the BAST Determination Process. Report No. 2, Washington, DC; Bureau of Safety and Environmental Enforcement; 2017

[21] Drexelbrook. Measuring Drilling Fluid Level in Mud Tanks. AMETEK Inc. [Internet]; 2015. Available from: https://www.drexelbrook.com/learningzone/application-notes/oil-production/measuring-drilling-fluid-level-in-mudtanks [Accessed: May 16, 2022]

[22] Ge L, Li H, Wang Q, Wei G, Hu Z, Liao J, et al. Design and optimization of annular flow electromagnetic measurement system for drilling engineering. Journal of Sensors. 2018;**4645878**:1-12. DOI: 10.1155/2018/4645878

[23] Chhantyal K, Viumdal H, Mylvaganam S. Soft sensing of non-Newtonian fluid flow in open Venturi Channel using an array of ultrasonic level sensors—AI models and their validations. Sensors. 2017;**17**:2458. DOI: 10.3390/s17112458

[24] Sun H, Lao L, Li D, Tao Q, Ma H, Li H, et al. Optimization of suitable measurement position through fluid dynamics in early kick detection. In: Proceedings of the International Petroleum Technology Conference; 26-28 March 2019; Bejing; SPE; 2019. DOI: 10.2523/IPTC-19528-MS

[25] Zhou Q, Zhao H, Yufa H, Li S, Jiang S, Zhang H. Research on mud flow rate measurement method based on continuous doppler ultrasonic wave. International Journal of Optics. 2017;**4750290**:1-12. DOI: 10.1155/2017/4750290

[26] Smart D, Russell C, Simons M. Understanding and Selecting Coriolis Technology for Drilling Fluid Monitoring. Micro Motion Inc. [Internet]; 2013. Available from: https://www.emerson.com/documents/automation/white-paper-understanding-and-selecting-coriolis-technology-for-drilling-fluid-monitoring-micro-motion-en-64258.pdf [Accessed: May 16, 2022]

[27] Nas S. Kick detection and well control in a close wellbore. In: Proceedings of the IADC/SPE Managed Pressure Drilling and Underbalance Operations Conference and Exhibition; 5-6 April 2011; Denver; SPE; 2011. DOI: 10.2118/143099-MS

[28] Ali TH, Haberer SM, Says IP, Ubaru CC, Laing ML, Helgesen O, et al. Automated alarms for smart flowback fingerprinting and early kick detection. In: Proceedings of the SPE/IADC Drilling Conference and Exhibition; 5-7 March 2013; Amsterdam; SPE; 2013. DOI: 10.2118/163474-MS

[29] Hughes B. Smart Flowback Fingerprinting Service. Baker Hughes: Houston, TX; 2014

[30] Sleiti AK, Takalkar G, El-Naas MH, Hasan AR, Rahman MA. Early gas kick detection in vertical wells via transient multiphase flow modelling: A review. Journal of Natural Gas Science and Engineering. 2020;**80**:103391. DOI: 10.1016/j.jngse.2020.103391

[31] Osarogiagbon A, Muojeke S, Venkatesan R, Khan F, Gillard P. A new methodology for kick detection during petroleum drilling using long short-term memory recurrent neural network. Process Safety and Environmental Protection. 2020;**142**:126-137. DOI: 10.1016/j.psep.2020.05.046

[32] Yin H, Si M, Li Q, Zhang J, Dai L. Kick risk forecasting and evaluating during drilling based on autoregressive integrated moving average model. Energies. 2019;**12**:3540. DOI: 10.3390/en12183540

[33] Yin Q, Yang J, Tyagi M, Zhou X, Hou X, Wang H, et al. Machine learning for deepwater drilling: Gas-kick-alarm classification using pilot-scale rig data with combined surface-riser-downhole monitoring. SPE Journal. 2021;**26**(4):1773-1799. DOI: 10.2118/205365-PA

[34] Stakvik JA, Berg C, Kaasa G, Graham R. Model-based control in managed pressure drilling. In: Proceedings of the SPE/IADC Drilling Conference and Exhibition; 14-16 March 2017; The Hague SPE; 2017. DOI: 10.2118/184649-MS

[35] Vajargah AK, Hoxha BB, van Oort E. Automated well control decision-making during managed pressure drilling operations. In: Proceedings of the SPE Deepwater Drilling and Completions Conference; 10-11 September 2014; Texas; SPE; 2014. DOI: 10.2118/170324-MS

[36] Kinik Z, Gumus F, Osayande N. Automated dynamic well control with managed-pressure drilling: A case study and simulation analysis. SPE Drilling & Completion. 2015;**30**:110-118. DOI: 10.2118/168948-PA

[37] Sehsah O, Iturrios C, Mahmood A, Abdallah K. Historical performance analysis and upcoming development of rotating control devices in the Kingdom of Saudi Arabia. In: Proceedings of the International Petroleum Technology Conference; 13-15 January 2020; Dhahran; SPE; 2020. DOI: 10.2523/IPTC-20238-MS

[38] Darmawan GR, Prasetyo A. Drilling the undrillable: A review of Indonesia onshore managed pressure drilling (MPD) operation experiences. PETRO. 2022;**10**(4):211-217. DOI: 10.25105/petro.v10i4.12482

[39] Jinasena A, Holta H, Jondahl MH, Welahettige P, Aamo OM, Sharma R, et al. Model based early kick/loss detection and attenuation with topside sensing in managed pressure drilling. In: Proceedings of SIMS; 22-24 September 2020; Finland; SPE; 2020. DOI: 10.3384/ecp20176236

[40] Abbasi MH, Iapichino L, Naderi Lordejani S, Schilders W, van de Wouw N. Reduced basis method for managed pressure drilling based on a model with local nonlinearities. International Journal for Numerical

Methods in Engineering. 2020;**121**: 5178-5199. DOI: 10.1002/nme.6362

[41] Abbasi MH, Iapichino L, Naderi Lordejani S, Schilders W, van de Wouw N. Model predictive control and estimation of managed pressure drilling using a real-time high Fidelity flow mode. ISA Transactions. 2020;**105**:256-268. DOI: 10.1016/j.isatra.2020.05.035

[42] Atchison B. Automated well control: A step change in safety. Digital Chemical Engineering. 2022;**3**:100022. DOI: 10.1016/j.dche.2022.100022

[43] United States Department of Transportation. Automated Vehicles for Safety. [Internet]. 2021. Available from: https://www.nhtsa.gov/technology-innovation/automated-vehicles-safety. [Accessed: May 30, 2022]

[44] Atchison BW. Automated well control: from automated detection to automated shut-in. In: Proceedings of the IADC/SPE Middle East Drilling Technology; 25-27 May 2021; Abu Dhabi; SPE; 2021. DOI: 10.2118/202091-MS

[45] Atchison BW, Sarpangal V. Automated well control versus traditional well control—A human error comparison process. In: Proceedings of the IADC/SPE International Drilling Conference and Exhibition; 8-10 March 2022; Texas; SPE; 2022. DOI: 10.2118/208786-MS

[46] Atchison BW, Wuest C. The integration of managed pressure drilling (MPD) and automated well control technology. In: Proceedings of the IADC/SPE Managed Pressure & Underbalanced Operations Conference & Exhibition; 14-16 September 2021; Virtual; SPE; 2021. DOI: 10.2118/206385-MS

Chapter 4

Advanced Technology of Drilling and Hydraulic Loosening in Coal Bed Methane Using a Cavitation Hydrovibrator – Experience and Prospects

Yuriy Zhulay and Olexiy Nikolayev

Abstract

Modern progressive technologies use static fluid injection into seams for safe and cost-effective operation of coal seams. However, the deterioration of mining and geological conditions leads to a significant decrease in the efficiency of the process of methane sequestration from coal seams in case of increase in the depth of development of gas-bearing coal seams. This deterioration is due to a change in the stress-strain state of deep rock massifs, their low permeability, strong anisotropy of soft coal, leading to an increase in dynamic manifestations of rock pressure in the form of sudden outbursts of coal and gas, and rock destructions with catastrophic consequences. An advanced technology for hydraulic loosening and recovery of methane from gas-bearing coal seams, based on the creation of hydrodynamic impulses in a well surface and their transformation into mechanical vibration loading to coal seam, was developed. Such impact to the coal mass leads to the development of a system of cracks. As a result, the efficiency of coalbed hydraulic loosening increases, the zones of moistening and unloading of the formation increase, the gas emission of methane is intensified, the level of dust formation and the resistance of coal to cutting during its destruction are reduced.

Keywords: coalbed gas drainage technology, gas explosion, coalbed methane, coalbed wells, cavitation hydrovibrator

1. Introduction

The main problem of safe coal mining from gas-bearing coal seams is methane contained in the sorbed (bound) state in the system of natural coal cracks. The gas content of methane in dangerous concentrations in coal seams leads to sudden releases of methane, as well as to its explosions and coal dust, leading to catastrophic consequences and numerous deaths. In the main coal-producing countries of the world

(China, United States, Russia, Australia, Ukraine, etc.), the development of highly gas-bearing coal seams is carried out using surface and underground drilling methods as well methods for extracting methane.

However, as the world experience in solving the problems of mine safety shows, the existing technological solutions for the extraction of methane in the development of gas-bearing coal seams are not always effective.

Thus, in [1], a quantitative analysis of the death of personnel in the mines of China for the period from 2006 to 2010 was carried out. Gas accidents account for a significant portion of the death toll in Chinese coal mining has been claimed. The causes of these accidents and the influence of mine ownership on death frequency are considered.

The state of methane safety of coal mines in Russia is constantly considered at the international symposia "Miner's Week." In particular, in [2], the conceptual approaches to the problem of coal mine methane in Russia are considered. It is shown that out of the 105 operating mines, 78% of the mines are dangerous in terms of the maximum methane content, and 45% of the mines are especially dangerous. Kuzbass (Russia) is the main region of the country, where problematic methane-unsafe coal mines are concentrated.

In 2006 and 2007, 256 miners died from coal methane problems due to the lack of reliable degassing systems in Russian mines. At the same time, degassing systems are widely and effectively used in such developed coal-producing countries, as the United States, Australia, etc. In these countries, coal mining with a methane content of more than 9 m^3/ton is legally prohibited.

Ukraine is one of the countries with the highest (in the world) number of miner's deaths per 1 million ton coal. So, in 2007, in the Donets Basin, at the "Zasiadko" mine, as a result of a gas (methane) explosion, 106 miners and rescuers died. In 2015, methane exploded at the same mine at a depth of 1230 m. Since 1991, 107 people have died in one of the most dangerous in the Donbas mine (the "Sukhodolskaya-Vostochnaya" mine) due to sudden outbursts of methane gas.

According to the authors of this study, the main reason for the mass death of miners is the reluctance of the coal enterprises owners to invest in a direct solution to the problem of methane safety, including the development of new technologies for extracting and capturing methane with its isolated removal to the surface or into mine workings, with dilution to its safe concentrations.

1.1 Analysis of recent research and publications on drilling wells for degassing gas-bearing coal seams

Currently, ensuring the methane safety of coal mining is carried out by two ways.

The first way is the land-based method of extracting methane. It provides early degassing of mine fields through wells drilled from the surface and increases the efficiency of methane extraction due to cavern formation or hydraulic fracturing. In Russia, such work was initiated by Academician A.A. Skochinsky about 60 years ago in the Karaganda basin. More than 50 million tons of coal reserves were processed on 10 mine fields through 140 wells. To date, more than 30 million tons of coal have been mined in the early degassing zones.

Degassing of mine fields through wells drilled from the surface was also used in a number of mines in Ukraine. Such work was also carried out at the "Zasyadko" and "Sukhodolskaya-Vostochnaya" mines.

However, this method of degassing does not provide the necessary efficiency from the standpoint of ensuring outburst hazard. This is due to the fact that, for economic reasons, wells are drilled at a distance of 200 or 300 m from each other and between them there are non-degassed sections of mine fields.

Note that the ground-based method of extracting methane continues to improve. Thus, in China, new technologies are being developed for degassing deep-seated coal seams [3] and multilateral radial borehole hydraulic fracturing "initiating the development of a fracture, increasing the permeability of coal and increasing the volume of gas drainage in the opening zone" (i.e. the technology increases fractures, enhancing coal permeability and raising gas drainage volume in the uncovering area.) [4].

The second way is the degassing of a coal seam from underground workings by static injection of liquid into it was an effective addition to the first method of extracting methane and reduced the problem of outburst hazard.

An analysis of the methods and means of combating gas and dust factors in countries with the most developed coal industry shows that to date, injection of liquid into coal seams is the fundamental method. Due to the preliminary moistening of the coal mass, dust formation and the intensity of gas emission during the destruction of coal are reduced.

In the world practice of conducting mining operations in these areas, a large amount of scientific and technical research has been carried out, on the basis of which regulatory documents have been developed that regulate the conduct of work, their control and evaluation of efficiency. At the same time, an increase in the depth of field development, changes in mining and geological conditions and properties of the coal rock massif have led to a significant decrease in the effectiveness of preventive measures. Analysis of studies shows that under conditions of great depths, the possibilities of fluid injection in a static mode have been exhausted. The widely used methods of hydraulic loosening and hydraulic pressing of the marginal part of outburst-prone formations become insufficiently effective. When fluid is injected, there are cases of spontaneous water breakthrough into the mined-out space and premature hydraulic pressing of the edge part of the formation with the threat of provoking a gas-dynamic phenomenon.

Considering that the equipment and technology for the use of hydraulic loosening and hydraulic pressing are almost the same (they differ only in the parameters of holes or wells and the effect achieved), their main disadvantage can be considered an uncontrolled process of fracturing, which reduces the efficiency of fluid filtration throughout the thickness of the layers and interlayers that make up the coal seam. In addition, the increase in the efficiency of measures related to the injection of liquid into the coal rock mass is constrained by the mining and geological factor—the presence of rocks prone to soaking, collapse, and heaving, and the mining factor—the formation of unloading zones and increased rock pressure in front of the working face. The fluid permeability coefficient k in these zones has directly opposite values, from the free flow of fluid flow through fractures, to the virtual absence of fluid filtration at all (see **Figure 1**).

There is a clear inverse relationship between the water permeability of coal seams and the value of rock pressure P. In case of increase in rock pressure, it decreases and, conversely, as the rock pressure decreases, the water permeability of the formation increases. In the marginal, unloaded zone of the formation, the permeability of coal has a maximum value. As the distance from the bottom of the working to the depth of the array, it increases and in the zone of maximum stresses it is practically equal to zero. Further, as the rock pressure decreases, the filtration properties of the formation

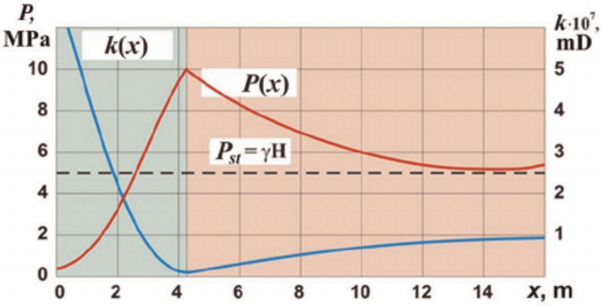

Figure 1.
Water permeability of coal k *and the rock pressure* P *from the distance* X *of the working face.*

increase and approach a constant natural value. As practice has shown, when the filtration chamber is located in the unloaded zone, the injected fluid is filtered through cracks into the mined-out space, and when the chamber is located in the zone with increased rock pressure, due to the low water permeability of coal, an uncontrolled process of hydraulic pressing occurs. In this case, the provoking of explosion of methane and coal dust is possible.

The solution to this problem became possible after a number of experimental studies of pulsed fluid injection. In recent years, significant results in this direction have been obtained at the Institute of Geotechnical Mechanics of the National Academy of Sciences of Ukraine (IGTM NASU) in the development of methods and hydropulse action means. The solution to this problem is based on the use of the phenomenon of a periodically stalled cavitation flow of the injected fluid passes through a cavitation hydraulic vibrator.

The cavitation hydraulic vibrator, as an integral part of the drilling tool, was developed by the Institute of Technical Mechanics of the National Academy of Sciences of Ukraine (ITM NASU). This was a new direction in the development of well drilling technologies with submersible impact machines that create dynamic loads on the rock cutting tool using the effects of hydrodynamic cavitation [5]. The drilling tool with a cavitation hydraulic vibrator (for dynamic loads creation in the range of sound frequencies close to the natural frequency of the rock being destroyed) has undergone a full range of experimental studies on hydraulic and drilling stands [6]. An adequate mathematical model of the hydraulic vibrator dynamics has been developed. The model describes complex dynamic processes in the flow channel of the hydraulic vibrator and the vibrator interaction with the drill string structure [7]. The main results of the new technology with the use of the hydrovibrator are presented in [8].

The above studies allowed IGTM NASU in a short time to develop a new method and technology for hydropulse loosening of coal seams [9], as well as a device [10], which implements this method. A significant amount of laboratory research was carried out to substantiate the geometric and operating parameters of the hydrovibrator. At the enterprise of the “Krasnodonugol” PJSC, the hydropulse device was tested under industrial conditions. The new technological schemes and criteria for evaluating the effectiveness of fluid pulsed injection into outburst-hazardous coal seams were developed.

Below are the main results of research into the new technology effectiveness for drilling and loosening outburst hazardous coal seams in a special stand and in industrial coal mining.

2. Bench test for hydropulse coal seam loosening technology using a cavitation generator of fluid pressure oscillations

The main results on the experimental study of the physical processes occurring in the hydrovibrator flow channel and their characteristic features are presented in [8]. It is shown that the most developed fluid oscillations are observed for a hydraulic system with the Venturi tube diffuser angle β, greater than 16°.

The object of this study is the dynamic characteristics of the hydraulic vibrator and their correspondence to the optimal modes of impulse action during the loosening of outburst-prone gas-rich coal seams with methane extraction from them. The layout of such hydraulic vibrator is shown in **Figure 2**.

The cavitation generator 1 with a post-diffuser hydraulic tube 5 was called a hydraulic vibrator. The presence of such a hydraulic tube is especially important to eliminate the loss of pulsed energy for case of the generator operates in a flooded liquid jet. The geometric parameters of the cavitation hydraulic vibrator were determined taking into account the implementation of the level of hydraulic pulsating loads for effective loosening coal seams. At the same time, the coal physical and mechanical properties and the characteristics of serial pumping units used in mines were taken into account [10].

The geometric parameters of the cavitation hydraulic vibrator designed for loosening outburst hazardous gas-rich coal seams are given in **Table 1**.

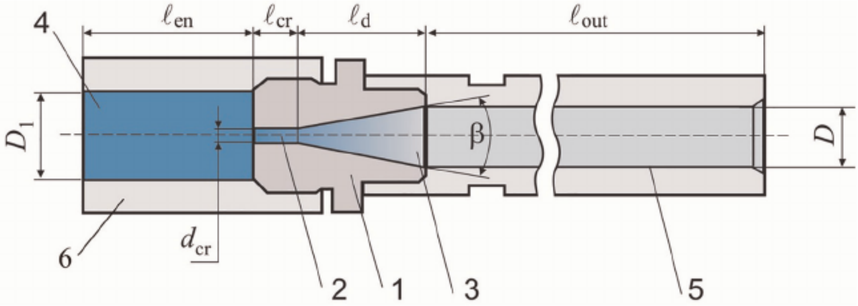

Figure 2.
Simplified schematic of the hydraulic vibrator structure. 1 is Venturi tube; 2 is critical section; 3 is diffuser with β *= 20°; 4 is input tube; 5 is post-diffuser hydraulic tube, 6 is feed pipeline.*

Geometrical parameter	Size
The diameter d_{cr} of the generator critical (throat) section, mm	2.5
The length ℓ_{cr} of the generator critical section, mm	3.0
The diameter D of the generator diffuser at the output section, mm	10
The length ℓ_d of the generator diffuser, mm	21.3
The opening angle of the generator diffuser – β, °	20
The diameter D of the hydraulic vibrator tube, mm	10
The length ℓ_{out} of the hydraulic vibrator tube, mm	100
The diameter D_1 of the inlet feed pipeline, mm	12
The length ℓ_{en} of the inlet feed pipeline, mm	120

Table 1.
The main geometrical parameters of the tested hydraulic vibrator.

The hydraulic vibrator with a set geometry is characterized by the regime parameters—the total inlet pressure P_1, and the head pressure P_2 and fluid flow rate Q through hydraulic vibrator and the main dynamic parameters—the fluid pressure self-oscillations range ΔP (peak to peak values) and the frequency f of fluid self-oscillations in the hydraulic tube of the hydraulic vibrator.

The study of the parameters of high-pressure fluid injection through boreholes or wells into coal seams during preventive measures to prevent gas-dynamic phenomena in the faces of development workings is a complex experimental task. The injection parameters are determined by the pressure drop and the volume of the fluid injected into the reservoir, while the stress state and the mass discharge zone are determined by the parameters of the seismoacoustic signal and the well sealing depth.

A stand for modeling the operating conditions of the cavitation hydraulic vibrator in a well should ensure the reliability of instrumental measurements of its characteristics, taking into account the mining and geological conditions of occurrence of outburst hazardous coal seams and their properties. When developing such stand, the possibilities of using the technical means and serial equipment available at the mines should be taken into account.

For physical modeling of the cavitation hydrovibrator operation in a well, the Institute of Geotechnical Mechanics of National Academy of Sciences of Ukraine (IGTM NASU) developed the special stand installation [11]. The parameters of commercially available mining equipment and the physical and mechanical properties of coal in its place of occurrence are the initial data for the development of the stand and testing of the hydraulic vibrator. In view of the foregoing, the stand should provide the fluid pressure at the inlet to the hydraulic vibrator P_p from 5 to 32 MPa at the volumetric flow rate Q from 20 to 120 l/min (according to the parameters of pumping units), according to the properties of the coal seam (foremost, gas pressure in the seam), the water pump pressure head must be from 1.0 to 20.0 MPa.

A schematic diagram of the developed stand design for hydraulic testing and determining the efficiency of the cavitation hydrovibrator in the well is shown in **Figure 3**.

A system of pressure sensors and visual equipment is connected to the developed bench installation. The system registers the operating parameters (the bench fluid flow rates and pressures) with the supply of signals through an amplifier to a personal computer. Along the pumps there is an inlet manifold 4, which has a nipple connection with the inlet pipe of each pump. The outlet pump nozzles are connected in parallel to the high pressure pipeline 8, which goes to the site of the test object. The tank is connected via valve 10 through filter 11 to the inlet of the make-up pump with fluid flow rate of Q = 160 l/min and discharge pressure P_{bp} = 7 MPa, which ensures uninterrupted operation of high-pressure pumps 5, 6, and 7. The system is powered from switchboard 15. For ensuring the required water flow through the test object, the pump control panel allows researchers to turn on from one to three pumping units at the same time.

The stand systems are able to maintain pressure at the inlet to the hydrovibrator P_p up to 32 MPa for fluid flow rates from 20 to 120 l/min and smoothly adjust the head pressure P_b in the range from 0.05 to 0.9 of the fluid feed pressure.

The technological capabilities of the hydraulic test bench and operation simulation of the cavitation hydrovibrator make it possible to carry out autonomous tests of the hydrovibrator (**Figure 4a**) to determine the parameters of the oscillatory process in the hydraulic channel of the hydrovibrator ΔP_1 and f) and by immersing it directly into the simulator pipeline (**Figure 4b**). At the same time, the various options of the

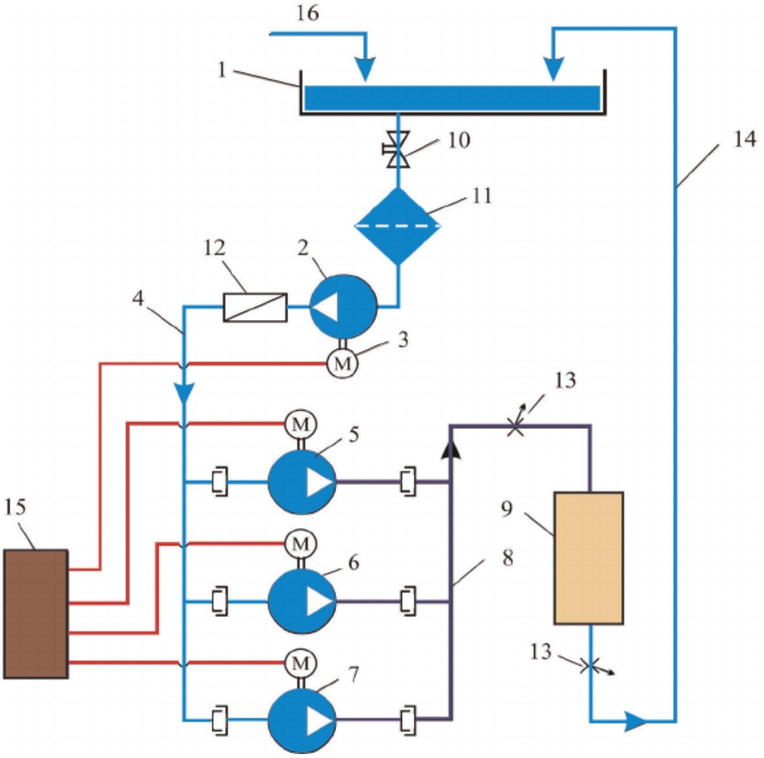

Figure 3.
Schematic diagram of the stand for hydraulic testing and operation simulation of the cavitation hydrovibrator in a well condition. 1 is the tank with the 8 m^3 volume; 2 is make-up auxiliary pump; 4 is the pump inlet pipeline; 5–7 are the three high pressure pumps; 9 is the cavitation hydrovibrator; 10 is an intake valve; 11 is a filter; 12 is a fluid flow meter; 13 is the adjustable throttles for setting pressures at the inlet and outlet of the tested hydrovibrator; 14 is drain pipeline; 15 is electrical panel; 16 is water pipeline.

hydrovibrator location in the well model [11] were tested. As a result of testing and comparing their results in terms of efficiency, the final version was chosen (**Figure 4b**).

The well model (well simulator) includes an inlet hydraulic channel 1, connected by means of a nipple to a flexible high-pressure stand hose, the cavitation hydraulic vibrator 2 with an outlet hydraulic tube 3, a well simulator pipeline 4 (with a diameter of 42 mm), at the outlet of which the booster throttle 5 is installed. The booster throttle is connected to the drain pipeline of stand 6.

The values of fluid pressure at the inlet to the hydrovibrator and the average volumetric fluid flow rate through hydrovibrator, as well as the ranges of the fluid pressure pulses in the well simulator pipeline ΔP_2, ΔP_3, ΔP_4, and ΔP_5 at different distances from the inlet section to the well simulator (**Figure 4**) and oscillation frequency f, are the main physical quantities that characterize the hydropulse effect on the coal seam.

All measured parameters are distributed over the dynamic principle into two categories: the static parameters, which change with time at frequencies less, than 4 Hz, and dynamic parameters, which change with time at frequencies above 4 Hz. The dynamic parameters are the values of fluid pressure pulsations at the cavitation hydrovibrator outlet and in the pipeline simulator of the well and the fluid oscillation frequency.

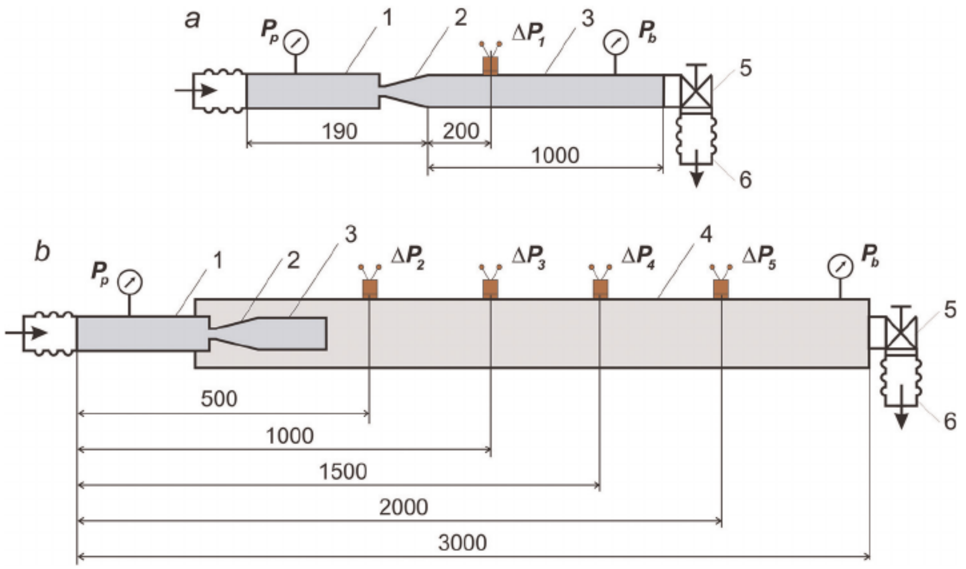

Figure 4.
Schematic diagram for the cavitation hydrovibrator autonomous tests in the well model. 1 is inlet hydraulic pipeline; 2 is cavitation hydraulic vibrator; 3 is adapter; 4 is well simulator pipeline; 5 is retaining throttle; 6 is stand drain pipeline.

To measure static pressure parameters, technical pressure gauges with a reduced error of 0.6% are used, which makes it possible to determine the average pressure value at the pressure gauges' location. The flow rates of bulk fluid through the device were determined by a turbine fluid flow rate sensor with a reduced error of 1%. It is installed directly in the measured pipeline in front of the inlet pumps manifold.

The measurement of fluid dynamic pressure is based on the direct registration of the full pressure values using appropriate pressure sensors by converting a physical quantity into an electrical signal.

The block diagram of the system for measuring the dynamic parameters of the cavitation generator during bench tests is shown in **Figure 5**.

As primary transducers, inductive total pressure sensors of the DDI-20 type are used, which measure the pressure value up to $P_{\max}$ = 60 MPa per pulse. The sensor has a sensitive membrane, at a given distance from which an inductive coil is installed. The principle of operation of the sensor is based on the change in the inductance of the coil depending on the deflection of the membrane under the influence of static-dynamic pressure. The natural frequency of the membrane is not less than 20,000 Hz, the hysteresis is not more than 2%, the nonlinearity of the calibration characteristic in the pressure range from 0 to $P_{\max}$ is not more than 5%.

The sensor is included in one arm of the high-frequency inductive bridge, which is located in the IVP-2 converter. The inductive high-frequency two-channel transducer IVP-2 is a secondary transducer in the system for measuring rapidly changing pressures and is designed to convert the complex resistance of the sensor into electrical voltage. The change in the inductance of the sensor, due to the pressure acting on the membrane, turns into a deviation of the initial voltage of the IVP-2.

The brief description of IVP-2 converter is as follows:

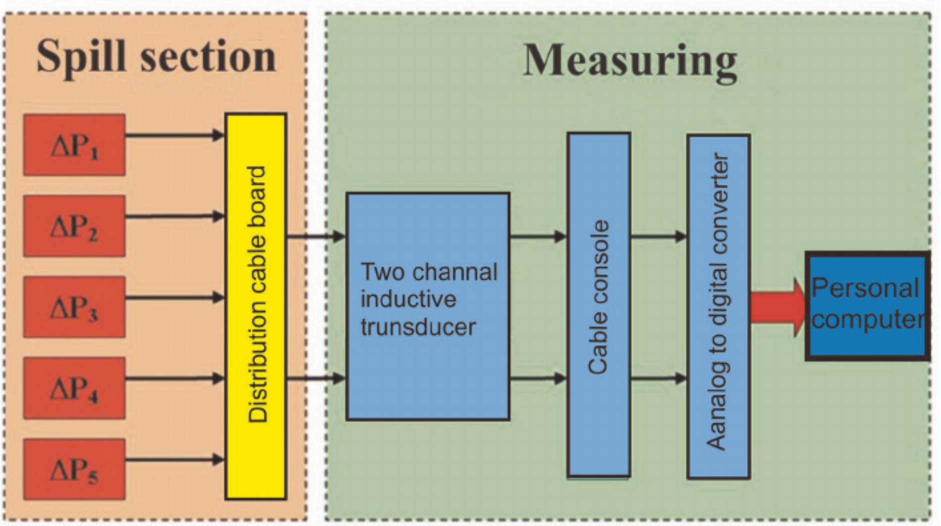

Figure 5.
Schematic diagram of the stand measuring system of dynamic parameters of hydraulic test.

- carrier frequency is 40,000 Hz;
- measurement of pressure pulsations in the frequency range from 0 to 10,000 Hz;
- the unevenness of the amplitude-frequency characteristic in the frequency range up to 8000 Hz is no more than 10%, and at the frequency range from 8000 to 10,000 Hz is no more than 20%.

The signal from the DDI-20 sensor through the IVP-2 converter enters the multichannel analog information input board, converted into a digital form by the analog-to-digital converter, and fed to a PC. The total reduced error of pressure measurements by the DDI-20 sensor with the IVP-2 transducer is 5.19% [11].

Processing of test results is also divided into two types. Static parameters are calculated according to the developed template in the Excel package. For dynamic parameters, the primary records from the analog-to-digital converter are recalculated into physical values and presented in the form of a graph in the time domain for further analysis using Excel.

During studying the characteristics of the experimental sample of the hydrovibrator, the input throttle (see **Figure 3**) set the pressure at the inlet to the hydrovibrator P_p = 5; 10; 20; 30 MPa. At each steady-state pressure at the inlet P_p, the outlet throttle changed discretely the outlet pressure P_b. At steady-state values of pressure at the inlet and outlet, by the "Measurement" command, control and measurements of dynamic parameters are carried out with a registration time of at least 10 s at each frequency.

As an example of evaluating the application of the measurement technique and processing the research results, **Figure 6** shows the oscillogram recording the pressure value p_1 in time in the hydraulic channel of the hydrovibrator with d_{cr} = 2.5 mm at inlet pressures P_p = 10 MPa and pressure head P_b = 1.6 MPa.

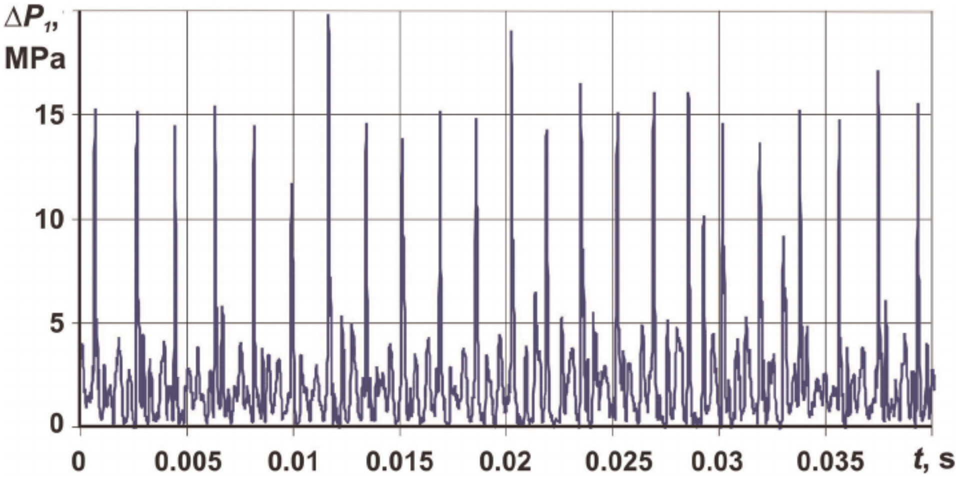

Figure 6.
A fragment of the time recording the pressure p_1 *at the outlet of the cavitation hydrovibrator with* d_{cr} *= 2.5 mm at* P_p *= 10 MPa and* P_b *= 1.6 MPa.*

It can be seen from **Figure 6** that periodic pressure oscillations p_1, are observed at the outlet of the hydrovibrator, have a shock character with a steep front of pressure rise and fall. This type of oscillation in hydrodynamics is called pressure pulsation and is characterized by the frequency and range of pressure self-oscillations.

The frequency of pulsations of pressure self-oscillations at the outlet of the hydrovibrator is due to the occurrence of the periodic-stall cavitation mode and is determined from the oscillogram by the formula $f = n/t$. Here n is the number of pulsation periods; t is the duration of n periods of pulsations in seconds.

The range of pressure self-oscillations ΔP_1 at the experimental hydrovibrator outlet is the difference between the maximum $p_{1\max}$ and minimum $p_{1\min}$ pressure values in the pulse $\Delta P_1 = p_{1\max} - p_{1\min}$. By a similar way, the magnitudes of pulsations ΔP_2, ΔP_3, ΔP_4, ΔP_5 in the pipeline simulator of the well are determined.

The results of autonomous tests of the hydraulic vibrator are presented as dependences of the range of pressure self-oscillations ΔP_1 and pulse frequency f on the water pressure head P_b. In this case, the values of pressure at the inlet to the hydrovibrator and the volumetric flow rate of liquid through it were P_p = 5; 10; 20 and 30 MPa and Q = 0.45, 0.64, 0.91, and 1.11 l/s, respectively.

Note that the dependences of the range of pressure oscillations ΔP_1 on the water pressure head P_p at various discharge pressures P_b are in satisfactory agreement with similar theoretical dependences obtained by calculations using the refined linear model [12]. This is clearly seen from **Figure 7a**, which shows these dependencies. The relative error does not exceed 20%.

For case of the hydraulic vibrator operates in the studied range of water pressure head changes, the regime of periodically stalled cavitation is realized in its flow part and fluid pressure P_1 oscillations occur, which are caused by the collapse of cavitation cavities in the hydraulic channel. At a fixed value of the water pressure head P_b, an increase in pressure P_p at the inlet to the experimental sample of the hydrovibrator leads to an increase in the oscillatory value of pressure ΔP_1. For case of the pressure P_b = 4 MPa with the increase in discharge pressure P_p from 10 to 30 MPa, the pressure pulse value ΔP_1 increases from about 10 to 38 MPa.

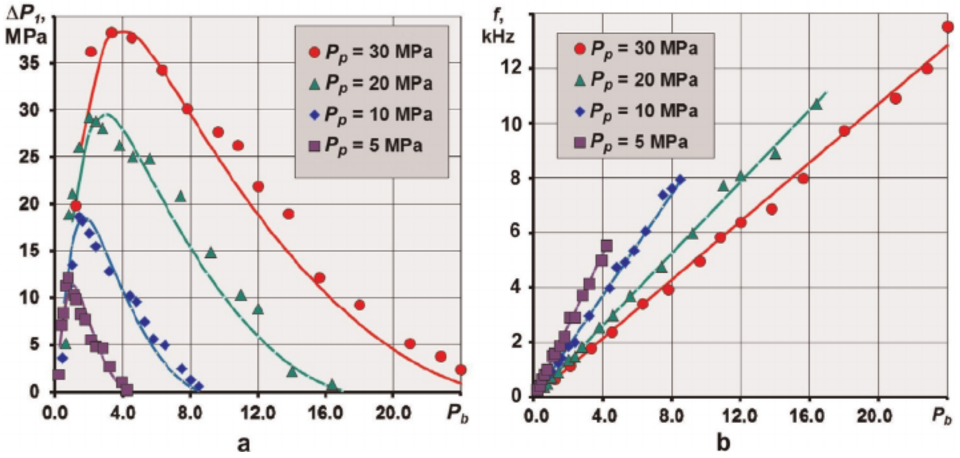

Figure 7.
Experimental and calculated dependences of the pressure oscillations range of ΔP_1 *and the pulse frequency* f *on the outlet pressure* P_b.

Dependences $\Delta P_1(P_b)$ for different values of pressure P_p have a maximum in the range of pressure head P_b from 0.14 and up to 4 MPa. As the discharge pressure P_p increases, the maximum pressure range value of ΔP_1 shifts toward higher P_b values. The maximum value of the pressure range ΔP_1 is approximately in from 1.3 to 2.5 times higher than the static pressure P_p at the hydrovibrator inlet. At the same time, as the discharge pressure P_p increases, the ratio $\Delta P_1/P_p$ decreases.

The location of the experimental points (see **Figure** 7) relative to the theoretical dependences of the frequency f of the fluid pressure cavitation self-oscillations in the hydrovibrator on the water pressure head P_b [13] indicates their satisfactory convergence. The relative error does not exceed 10%. At a fixed value of the back pressure P_b, an increase in the pressure P_p at the inlet to the hydraulic vibrator leads to a decrease in the frequency f. Thus, at the value of the water pressure head P_b = 4 MPa with an increase in the discharge pressure P_p from 5 to 30 MPa, the frequency of cavitation self-oscillations decreases from 5000 to 2100 Hz.

It should be noted that an increase in inlet pressure P_p of the hydraulic vibrator expands its operating range in terms of pressure head and is located in the operating range from 0.05 to 0.8 P_p.

Experimental modeling of hydraulic loosening of a coal seam by the cavitation hydraulic vibrator was performed on a well simulator in accordance with the schematic shown in **Figure 3**. The study of the hydrovibrator performance was carried out in modes in accordance with the mining and geological conditions of occurrence of outburst-hazardous seams of the "Sukhodolskaya-Vostochnaya" and "Molodogvardeiskaya" mines of the "Krasnodonugol" Association (Ukraine).

As an example, **Figure 8** shows an oscillogram of fluid pressure oscillations behind a hydraulic vibrator in various sections of a well simulator. The injection pressure in this case was P_p = 21 MPa at the fluid volume flow rate of Q = 55 l/min, which corresponds to the mining and geological conditions of the formation at a depth of 1300 m ("Sukhodolskaya-Vostochnaya" mine).

It can be seen from **Figure 8** that the water pressure head of P_b changes from 1 to 14 MPa, in all sections along the well simulator length, the periodic pressure of the ΔP_2, ΔP_3, ΔP_4, ΔP_5 oscillations are observed with a steep front of pressure rise and fall. The pressure ranges ΔP are symmetrical with respect to the average pressure value P_b.

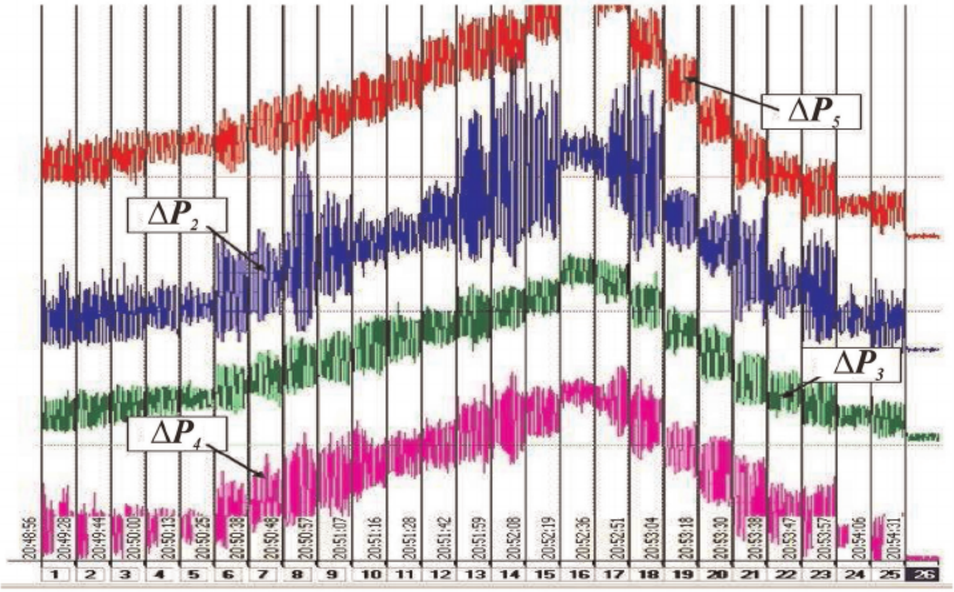

Figure 8.
The time recording of fluid pressure (ΔP_2, ΔP_3, ΔP_4, ΔP_5) oscillations at different sections of the well simulator length.

Processing of time oscillograms with recording of fluid pressure fluctuations along the length of the well simulator of the ΔP_2, ΔP_3, ΔP_4, ΔP_5 (averaged over eight measurements of their values) was performed by the standard "Oscilloscope" program and is shown in **Table 2**. It corresponds to the regimes of hydraulic loosening of the coal seam in mines.

The results of testing the device in the well simulator in the form of dependences of the values of pulsation ranges of ΔP in various sections of the pipeline along its length (see **Figure 3**) on the water pressure head of P_b are shown in **Figure 8** at P_p = 21 MPa, Q = 55 l/min and **Figure 9** at P_p = 11 MPa, Q = 40 l/min.

An analysis of these experimental data shows that fluid pressure oscillations exist in the entire range of the P_b the water pressure head change (from 1 to 12 MPa) studied. The change in the range of pressure pulsations of the ΔP_2, ΔP_3, ΔP_4, ΔP_5 from the pressure head P_b (see **Figure 9**) is nonlinear. There are two pronounced maxima. The first one is at pressure head of P_b from 4.1 to 5.1 MPa and frequency f from 2200 to 2700 Hz. For these values of P_b and f pressure fluctuations are realized in different sections of the well simulator: ΔP_2 = 13.8 MPa, ΔP_3 = 10.2 MPa, ΔP_4 = 8.97 MPa, ΔP_5 = 8.58 MPa. The second one is at $P_b \approx 11.1$ MPa and $f \approx 6500$ Hz, at which the pressure rages are ΔP_2 = 15.6 MPa, ΔP_3 = 8.8 MPa, ΔP_4 = 7.6 MPa, and ΔP_5 = 6.4 MPa.

The results of testing the hydraulic vibrator in the well simulator at P_p = 11 MPa, Q = 40 l/min (**Figure 10**) show that fluid pressure pulsations exist in the entire studied range of water pressure P_b from 1 to 8 MPa.

The change in the values pressure oscillations of ΔP_2, ΔP_3, ΔP_4, ΔP_5 on the water pressure head P_b is nonlinear with a pronounced maximum P_b (about 3.1 MPa) at the oscillations frequency f equal to 2260 Hz.

For the indicated values of P_b и f in different sections of the well simulator, the pressure pulsations ΔP_2 = 11.97 MPa, ΔP_3 = 10.89 MPa, ΔP_4 = 10.31 MPa и

Test data at P_p is 21 MPa and Q is 55 l/min “Sukhodolskaya-Vostochnaya”						**Test data at P_p is 11 MPa and Q is 40 l/min “Molodogvardeyskaya”**					
P_b, MPa	**f, Hz**	**ΔP_2, MPa**	**ΔP_3, MPa**	**ΔP_4, MPa**	**ΔP_5, MPa**	**P_b, MPa**	**f, Hz**	**ΔP_2, MPa**	**ΔP_3, MPa**	**ΔP_4, MPa**	**ΔP_5, MPa**
1.1	1140	6.28	5.87	5.25	4.82	1.1	801	5.56	4.98	4.25	3.92
1.6	1216	6.83	5.99	5.41	4.98	1.6	1165	7.03	6.81	5.48	4.83
2.1	1426	7.19	6.29	5.79	5.08	2.1	1529	8.53	7.85	6.86	6.08
3.1	1619	8.17	6.79	5.98	5.30	2.6	1893	9.45	8.79	8.36	7.86
4.1	2224	11.0	9.79	8.92	8.58	3.1	2257	11.97	10.89	10.31	9.59
5.1	2695	13.8	10.3	8.97	7.81	3.6	2621	10.54	10.12	9.52	8.93
6.1	3055	8.99	7.74	6.91	7.08	4.1	2985	9.32	9.09	8.65	8.08
7.1	4102	7.11	6.86	6.01	5.18	4.6	3349	8.718	8.63	7.507	7.28
8.1	4585	5.99	4.97	4.76	4.46	5.1	3713	7.24	7.25	6.92	5.81
9.1	5280	5.58	4.81	4.10	4.19	5.6	4077	6.71	6.32	5.92	5.43
10.1	6187	12.2	7.99	6.89	5.51	6.1	4441	5.32	4.94	4.41	4.48
11.1	6506	15.6	8.84	7.59	6.35	6.6	4805	4.99	4.77	4.38	4.31
12.1	7226	10.2	6.94	4.87	3.67	7.1	5169	4.81	4.62	4.01	4.35
					4.82	7.8	5678	4.58	4.41	3.79	4.16

Table 2.
The results of processing the test data of the hydraulic vibrator in the well simulator at P_p *is 21 MPa, Q = 55 l/min and at* P_p *= 11 MPa, Q = 40 l/min.*

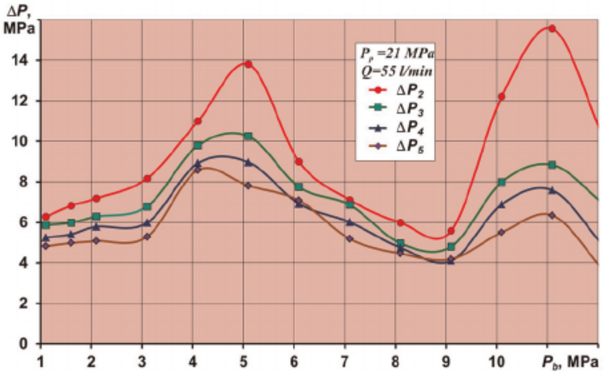

Figure 9.
Dependences of pressure oscillations ΔP ranges at various sections of the well simulator on the outlet pressure P_b *at* P_p *= 21 MPa and Q = 55 l/min.*

ΔP_5 = 9.59 MPa are realized. That is, the dynamic pressure range ΔP along the length of the well simulator slightly decreases, the attenuation process occurs.

The theoretical substantiation of the hydrodynamic parameters of the impulse action was carried out using the data of P. M. Mokhnachev and V. V. Pristash [14], where the rate of coal deformation is expressed in the following form

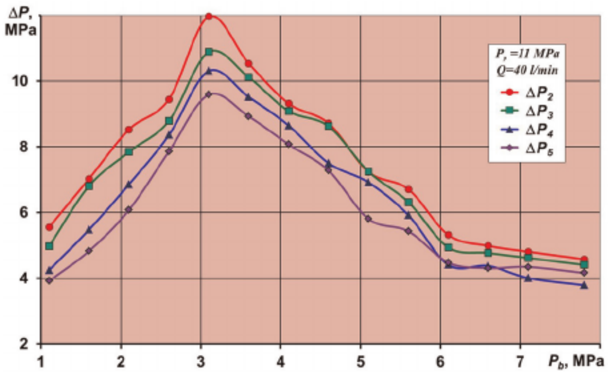

Figure 10.
Dependences of pressure oscillations ΔP *ranges at various sections of the well simulator on the outlet pressure* P_b *at* P_p = *11 MPa and* Q = *40 l/min.*

$$\dot{\varepsilon} = \frac{d\varepsilon}{dt} = \frac{\Delta P \cdot f}{E}, \tag{1}$$

where ε is linear deformation of coal; ΔP is impulse pressure; f is pulse frequency; E is modulus of elasticity of coal.

Due to the urgency of the problems of rock bumps and sudden outbursts, VNIMI [15] investigated the properties of outburst coals. Here, at the first time, the drop in the coal strength was discovered. In this case, a particularly sharp decrease in strength is observed in the range of strain rates from 1 to 10 c^{-1}.

Taking into account the above, the expression (1), for the ultimate case of the coal deformation rate equal to 10 c^{-1}, is transformed as follows:

$$\Delta P = \frac{10E}{f}. \tag{2}$$

Figures 11 and **12** show the theoretical dependences of the optimal values of pressure fluctuations on the frequency of their repetition, calculated by expression (2)

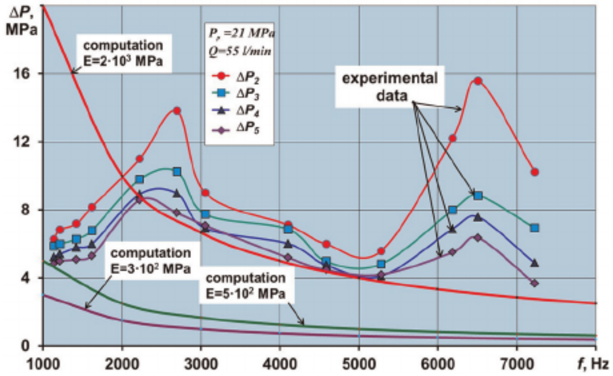

Figure 11.
Theoretical dependences of the optimal values of pressure pulsations ΔP *on their repetition rate f and experimental data of the fluid pulsed action implemented by the hydraulic vibrator in the well simulator at* P_p = *21 MPa and* Q = *55 l/min.*

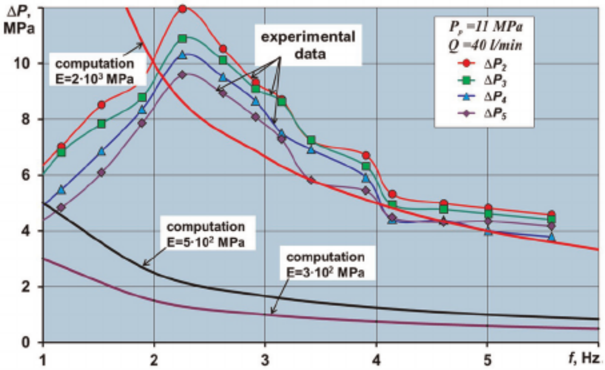

Figure 12.
Theoretical dependences of the optimal values of pressure pulsations ΔP *on repetition rate f and experimental data of the fluid pulsed action implemented by the hydraulic vibrator in the well simulator at* P_p = *11 MPa and* Q = *40 l/min.*

(for the values of the modulus of elasticity of coal along the bedding $E = 3{\cdot}10^2$; $5{\cdot}10^2$ MPa; and in the vertical direction to the seam $2{\cdot}10^3$ MPa).

It also presents experimental data on the pulsed action of the fluid implemented in the well simulator with a change in backwater pressure in the range from 2 to 12 MPa and an injection pressure of 21 MPa (**Figure 11**). This corresponds to the conditions of loosening outburst hazardous coal seams at the coal occurrence depth from 1100 to 1300 m ("Sukhodolskaya – Vostochnaya" mine, Ukraine). Experimental data were obtained by measuring pressure oscillations at section distances of 0.5, 1.0, 1.5, and 2.0 m from the hydrovibrator outlet (see **Figure 3**).

The given dependencies allowed to substantiate the optimal values of the parameters of hydrodynamic loosening of outburst-hazardous coal seams of the "Sukhodolskaya-Vostochnaya" mine. The optimal values of the hydraulic vibrator parameters must meet the following requirements:

1. The values of pressure pulses generated by the hydraulic vibrator should reach from 6 to 16 MPa.

2. The fluid pressure pulse frequency must be in the oscillations range from 1500 to 7000 Hz.

For the "Molodogvardeyskaya" mine (Ukraine), testing of the hydraulic vibrator in the well simulator was carried out at P_p = 11 MPa with the fluid flow rate of Q = 40 l/min. This corresponds to coal seam occurrence depths from 700 to 800 m. The coal seam hydraulic resistance does not exceed 6 MPa.

An analysis of the given dependencies made it possible to substantiate the optimal dynamic parameters of loosening of outburst-hazardous coal seams of the "Molodogvardeiskaya" mine (Ukraine). The optimal dynamic parameters must meet the following requirements:

1. The values of fluid pressure pulses generated by the hydraulic vibrator should reach from 4 to 10 MPa;

2. The fluid pressure pulse frequency must be in the range from 1500 to 6000 Hz.

As can be seen from the presented data, the parameters of dynamic loading of the coal seam during pulse loosening with a hydraulic vibrator satisfy the conditions of theoretical dependences of the optimal values of pressure pulsations on their frequency. The operating points of the hydraulic vibrator in both cases (see **Figures 11** and **12**), as a rule, are higher than the corresponding theoretical dependencies. It should be noted that the indicated range was chosen for the values of the coal modulus E from $3{\cdot}10^2$ to $5{\cdot}10^2$ MPa during compression along the bedding, since it is in this direction that the dynamic action sets in motion cracks inclined toward the bedding, i.e., in the direction of low permeability of the coal seam in the natural state.

Considering the physical process of hydropulse loosening of the coal seam, it should be noted that at the beginning of the operation of the hydraulic vibrator in the range of low water pressure head in the seam, when the level of pulse values and their repetition rate are below the optimal values of the hydropulse action parameters, cracks in the coal seam will not develop. The water pressure head, due to pumping fluid into the coal seam, will increase. Upon reaching the value of $P_b \geq 2$ MPa, the generator dynamic parameters will automatically move into the range of values of ΔP and f, equal to or exceeding the optimal values of coal seam hydropulse loosening. That is, the hydraulic vibrator, as it were, switches to the self-regulation mode. This will allow effective loosening of the coal seam in the directions of compression along the bedding and along the normal to the seam.

The results of the presented bench tests and the conclusions obtained from them made it possible to proceed to work to evaluate the effectiveness of the hydraulic pulse loosening device in industrial (mines) conditions and compare the results obtained with the data of static fluid injection into the reservoir according to the standard procedure [16].

3. Efficiency of hydraulic vibrator operating modes during pilot works on impulse loosening of outburst hazardous coal seams

For pilot testing the effectiveness of the hydraulic vibrator in loosening outburst hazardous coal seams by the manner prescribed by the rules [16], mining experimental sites were selected. The regulatory and technical documentation necessary for the work was developed, agreed, and approved. Mining and experimental studies of the hydraulic vibrator were carried out in difficult mining and geological conditions of the "Sukhodolskaya-Vostochnaya" and the "Molodogvardeiskaya" mines of "Krasnodonugol" Open Joint Stock Company. The schematic diagram of the hydraulic vibrator and its placement in the well is shown in **Figure 13**.

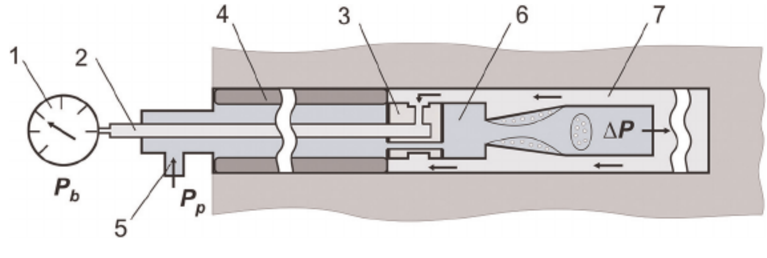

Figure 13.
Schematic diagram of the hydraulic vibrator for hydropulse loosening of coal seams. 1 is manometer; 2 is channel for measuring back pressure; 3 is fluid flow separator; 4 is sealer (l_s is hydrovibrator sealing length); 5 is tee; 6 is hydraulic vibrator; 8 is filtration part of the well.

The hydraulic vibrator for hydropulse loosening of coal seams works as follows. The high-pressure water flow through the fluid flow distributor 3 and the tee 5 enters the inlet of the hydraulic vibrator 6. It converts the stationary fluid flow into a pulsating flow, which propagates into the well filtration part 8 and is transferred to the coal mass. The pulse repetition rate lies in the range from 1 to 7 kHz. Impact fluid pressure self-oscillations, reducing the internal and contact coal friction, initiate the development of shear deformation and cracking in differently inclined planes.

The equipment for hydroimpulse loosening of coal seams consists of: the pumping unit 4, the pulse loosening device, including the hydraulic vibrator 10, the Taurus-type sealer 9, the high-pressure hoses 7, and control equipment (the fluid flow meter, pressure gauges 7 and 8). The equipment was installed according to the scheme in **Figure 14**.

Mining and experimental work were carried out in two stages. At the first stage, the hydraulic loosening work was carried out by standard (static injection) [16]. The second stage of the hydraulic loosening work was made by the hydraulic impulse method. According to the results of the studies, the parameters of the two methods were compared and the effectiveness of hydroloosening was evaluated. The results of control and efficiency evaluation were documented in the protocol of mining and experimental work.

The formation hydraulic loosening according to the standard procedure was stopped after the pressure drop in the well was not less than 30% of the maximum pressure. The hydropulse action and evaluation of its effectiveness were carried out under the control of the system of sound catching equipment (ZUA - 98). The hydraulic loosening also stopped when the generator switched to “idle mode.” The scope of studies to evaluate hydroimpulse loosening compared to static loosening and to establish the rational working hydrodynamic parameters of pulse loosening of outburst-hazardous coal seams in “Krasnodonugol” mines of amounted to 34 hydroloosening cycles according to the standard mining methodology and 20 hydroloosening cycles in the operation mode of pulsed fluid injection.

As an example, **Figure 15** shows the processes of change in time of the inlet average pressure of the hydraulic vibrator and the pressure in the well during loosening of the outburst-prone formation at a depth of 1300 m of the “Sukhodolskaya-Vostochnaya” mine (a). Fluid injection was carried out through the well with the diameter of 42 mm and the length of 7 m with sealing for the length of l_s = 5 m (see **Figure 13**).

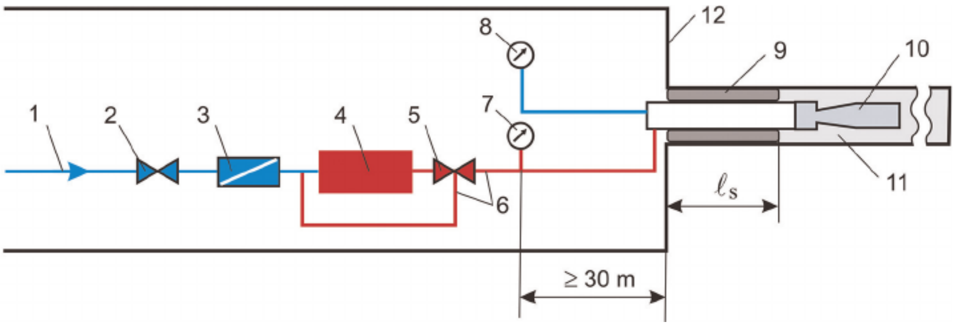

Figure 14.
Schematic diagram of equipment installation in the face preparatory development during hydraulic loosening of coal seams. 1 is water supply; 2 is valve; 3 is flow meter; 4 is pumping unit; 5 is control valve; 6, 8 are pressure gauges for measuring fluid pressure; 7 is high-pressure sleeve; 9 is sealer; 10 is hydraulic vibrator; 11 is well filtration part; 12 is mining face.

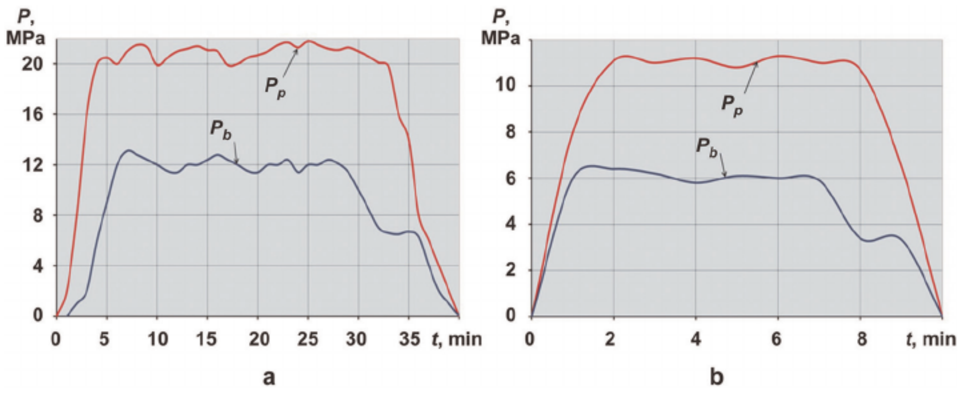

Figure 15.
The time dependence of the inlet hydrovibrator average pressure P_p *and pressure head at the filtration part of the well* P_b *at a depth of 1300 m (a) and of 617 m (b).*

A similar loosening process is also presented here for outburst-prone layer at a depth of 617 m of the "Molodogvardeiskaya" mine (b). Fluid injection was carried out through a well with the diameter of 42 mm and the length of 6 m with sealing for the length of l_s = 4 m (see **Figure 14**).

Based on instrumental measurements of injection and water pressure head in the "Sukhodolskaya-Vostochnaya" mine, the following operation modes of hydropulse loosening of the coal seam were established:

- initial operation mode, complete filling of the well with water, and increase of injection pressure and water head in it (from 0 to 5 min);
- active operation mode of hydropulse loosening (see **Figure 16**) at a steady fluid pressure head in the well (from 5 to 30 min);

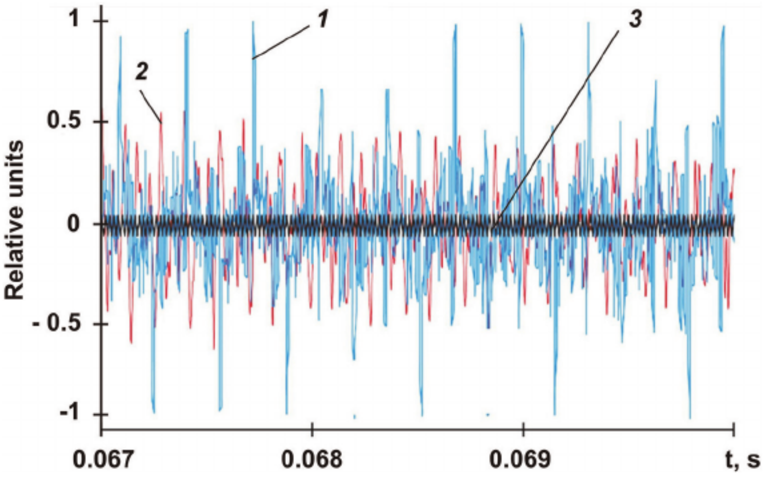

Figure 16.
The seismogram at the active operation mode of coal seam hydropulse loosening. 1 is the coal seam crack development signal; 2 is the acoustic signal of the operation range of hydraulic impulse loosening: 3 is the acoustic signal of the pumping unit.

18

- the mode of the completion of the active operation process, with a drop in the pressure of the fluid pressure head in the filtration part of the well with from about 30% or 50% of nominal pressure head level (from 32 to 36 min).

After the completion of the active operation process of cracking, hydropulse loosening becomes ineffective.

The seismogram at the active operation mode of hydropulse loosening of the reservoir by the ZUA-98 equipment is shown in **Figure 16**.

The nature of the time dependence of the acoustic signal of the pressure head oscillations in the well (see the curve 2 in **Figure 16**) during pulse loosening indicates operation of the hydrovibrator in the mode of periodically stalled cavitation. As a result, a system of cracks develops in the coal seam (see the curve 1 in **Figure 16**), which sharply reduces its hydraulic resistance upon completion of the active stage of hydropulse loosening.

The results of pulse loosening of the outburst-prone coal seam of the "Molodogvardeiskaya" mine are shown in **Figure 15b**. As in the previous case, there are three modes of loosening the coal seam:

- the mode of filling the well with water with an increase in injection pressure and backwater in it (from 0 to 1 min);
- active stage, at a steady backwater pressure in the filtration part of the well (from 1 to 7 min);
- completion of the active stage, with a drop in the pressure of the liquid back-up in the filtration part at the level from 30–50% (i.e., from 8 to 36 min).

The results of monitoring the loosening regimes (initial, active, and final stages) of this coal seam are detailed in [17].

A pilot test of the effectiveness of a hydraulic vibrator when loosening outburst-hazardous coal seams showed that the pressure of fluid back-up in a well is a fundamental criterion for controlling the completion of the hydroloosening process. The unloading zone of the coal seam at the same time increased from 4 to 8 m. The transformation of the static fluid injection mode into a hydropulse effect on the formation made it possible to achieve:

- absence of formation leaks along layering cracks, at which static injection was completed;
- the appearance at the bottom of the working of a lot of seeps and abundant dripping, relatively evenly distributed over the area of the bottom around the well;
- the two-time increase in specific gas release through adjacent wells per meter of exposed coal surface [18] compared with static injection.

An analysis of the results of the study of the hydraulic loosening parameters under static and pulsed fluid injection modes at the "Sukhodolskaya-Vostochnaya" and "Molodogvardeiskaya" mines has made a comparative assessment of their effectiveness (see **Table 3**). In the static mode (without cavitation self-oscillations), the fluid

Fluid injection mode	Time injection, min	Pressure head P_p, MPa		Fluid volume, Q, m^3
		max	min	
“Sukhodolskaya-Vostochnaya” mine				
Static	92	27	20	1.72
Impulse	40	21	16	0.75
Decrease in time injection on:	56%			56%
“Molodogvardeiskaya” mine				
Static*	15	16	10	1.28 (0.83*)
Impulse	10	11	10	0.50
Decrease in time injection on:	33%			61%

Table 3.
Comparative assessment of the efficiency of static and pulse modes of fluid injection (is case of fluid broke through the working face along the coal seam).*

injection pressure P_p was determined within ranges from 0.75 to 1.0γH, where γ and H are the average overlying rocks specific gravity and the formation depth. The required volume of injected fluid was determined by calculation in accordance with the instruction [U]. Under hydropulse action, the pressure P_p range is less than $(0.75)\gamma H$, and the injected fluid volume was measured by the flow meter upon completion of the hydraulic loosening process.

Visual observations showed that for case of *(see **Table 3**.) during static injection of fluid at the “Molodogvardeiskaya” mine, after 15 min of hydraulic action, fluid broke through the working face along the coal seam. This did not allow to pump the standard fluid volume of 1.28 m^3. For operation in hydrovibrator mode with pulsed fluid injection, no fluid released into the working face from the coal seam.

An analysis of the data given in the table shows that, in accordance with the accepted conditions of hydraulic loosening and evaluation of its effectiveness, the use of hydropulse action allowed, on average, to reduce the time of fluid injection into the reservoir and the volume of fluid injected into the reservoir by more than two times.

4. Conclusions

The advanced technology of drilling and coal seam hydraulic loosening by pulsed fluid injection using a cavitation hydrovibrator has a number of advantages compared with the technology of static fluid injection. The technology achievements consist in the possibility of discrete-pulse impact on the coal seam and lead to a significant increase in the permeability of coal, a decrease in its hydraulic resistance, and an increase in injectivity. This allows researchers to increase the rate of injection of fluid supplied to the coal mass while reducing time costs. As a result, the efficiency of hydraulic loosening increases, the zones of moistening and unloading of the formation increase, the gas emission of methane is intensified, the level of dust formation and the resistance of coal to cutting during its destruction are reduced.

The hydraulic vibrator has a number of advantages over other well-known impulse hydraulic means, such as:

- ease of manufacture, lack of moving parts, long service life, exclusion of the transmission of fluid vibrations to the pump, which increases its service life;

- the design of the generator is organically suited to the technology of hydraulic loosening of the coal massif, does not require modification of the equipment, and allows intensifying the processes of gas release at lower specific energy costs compared with traditional technologies.

References

[1] Lei W, Yuan-Ping C, Hong-Yong L. An analysis of fatal gas accidents in Chinese coal mines. Safety Science. 2014; **62**:107-113. DOI: 10.1016/j.ssci.2013.08.010

[2] Puchkov L, Slastunov S, et al. Conceptual approaches to ensuring the methane safety of coal mines in Russia and the CIS for 2007-2010. Mining Information and Analytical Bulletin, Moscow, MSGU. 2007;**13**:9-36 (in Russian)

[3] Wang L, Liu S, Cheng Y, Yin G, Zhang D, Guo P. Reservoir reconstruction technologies for coalbed methane recovery in deep and multiple seams. International Journal of Mining Science and Technology. 2017;**27**(2):277-284. DOI: 10.1016/j.ijmst.2017.01.026

[4] Li H, Liu Y, Wang W, Liu M, Liu J, Ma J, et al. A method of quick and safe coal uncovering by hydraulic fracturing in a multibranch radial hole with a coalbed methane well. American Chemical Society Omega. 2020; **11**(5(37)):23672-23686. DOI: 10.1021/acsomega.0c02383

[5] Pilipenko V. Cavitation Self-Oscillations. Kyiv: Naukova Dumka Publishing Company; 1989. p. 316 (in Russian)

[6] Zhulay Yu, Nikolayev O. Results of tests and modelling of the system 'drilling rig with hydraulic vibrator – rock'. Naukovyi Visnyk Natsionalnoho Hirnychoho Universytetu. 2020;**1**:11-17. DOI: 10.33271/nvngu.2020-1/011

[7] Nikolayev O, Zhulay Yu. Kvasha Yu, Dzoz N. Evaluation of the vibration accelerations of drill bit for the well rotative-vibration drilling using the cavitation hydrovibrator. International Journal of Mining and Mineral Enginee ring. 2020;**11**(2):102-120. DOI: 10.1504/IJMME.2020.108643 p

[8] Zhulay Yu, Nikolayev O. Mining technology. In: Hammond A, Donnelly B, Ashwath N, editors. Sonic Drilling with Use of a Cavitation Hydraulic Vibrator. London: Intechopen; 2021. DOI: 10.5772/ITexLi.100336

[9] Patent 73023 Ukraine, IPC E21B 43/26 (2007.01). Method of hydropulse loosening of coal seams. Zberovsky V, Zhulay Yu, Vasiliev D, Nikiforov A, Kolchin G, Angelovsky O, et al. Applicant and patent owner of IGTM NAS of Ukraine. No. in 2012 01719; Application 16.02.12; publ. 10.09.12, Bull. No. 17. p. 8 (in Ukrainian)

[10] Vasiliev L, Zhulai Yu, Zberovsky V, Moiseenko P, Trokhimets N. Patent 87038 Ukraine, IPC E21F 5/02. (2007.01). In: Device for hydropulse impact on the coal seam Applicant and patent owner of IGTM NAS of Ukraine. No. a 2007 10209; stated 13.09.07; publ. 10.06.09, Bull. № 11. 4 p. (in Ukrainian)

[11] Zberovsky V, Zhulay Yu, Angelovsky A, Chugunkov I. Bench installation for modeling the operation of the cavitation generator in a well. Geotechnical mechanics: Collection scientific papers, IGTM NAS of Ukraine. Dnepr. 2009;**82**:190-198 (in Russian)

[12] Zhulay Y, Nikolayev O, Kvasha Y. Comparative analysis of methods for calculating the amplitudes of pressure oscillations generated by a cavitation generator. Aviation and Space Technology and Technology. 2018;**3/147**: 58-68 (in Russian). DOI: 10.32620/aktt.2018.3.08

[13] Zhulay Yu, Voroshilov A, Komarov S. Development of a calculation and experimental method for determining the frequencies of cavitation oscillations. Collection scientific papers NSU of Ukraine. Dnipro. 2015;**48**:140-146 (in Russian)

[14] Mokhnachev M, Pristash V. Dynamic strength of rocks. Moscow: Nauka; 1982. p. 142 (in Russian)

[15] Lodus E, Romanovsky S. Influence of strain rate on strength and brittleness of shock coals and rock salt Rock pressure and rock bumps. Leningrad: All-Russian Research Institute of Mining Geomechanics and Mine Surveying; 1976;**9**:151-154 (in Russian)

[16] Standard of the Ministry of Coal Industry of Ukraine. SOU 10.1.001740088-2005. Rules for Conducting Mining Operations in Seams Prone to Gas-Dynamic Phenomena: Approved. Kyiv Ministry of Coal Industry of Ukraine: Ministry of Coal Industry of Ukraine; 2005. p. 225 (in Russian)

[17] Zberovsky V. Evaluation of the effectiveness of hydropulse impact on a coal seam by acoustic monitoring methods. Geotechnical mechanics: Collection scientific papers, IGTM NAS of Ukraine. Dnepr. 2017;**132**:74-84 (in Russian)

[18] Zhulay Yu, Vasiliev L, Trohiets N, Zberovsky V, Moiseenko P. Intensification of gas release from coal mass by injection of fluid into it using the cavitation generator. In: Mining Information and Analytical Bulletin. Moscow: Moscow State University for the Humanities. 2007;**13**:251-259 (in Russian)

Chapter 5

Asymptotic Solutions for Multi-Hole Problems: Plane Strain versus Plane Stress Boundary Conditions in Borehole Applications

Manal Alotaibi and Ruud Weijermars

Abstract

The elastic response of circular cylindrical holes in elastic plates is analyzed using the linear superposition method (LSM) to assess the impact of plate thickness on the stress state for the thin- and thick-plate solutions. Analytical solutions for stress accumulations near holes in elastic plates are relevant for a wide range of practical applications. For example, detailed analyses of the stress concentrations near boreholes piercing rock formations are needed during drilling operations to avoid premature fracturing due to tensile and shear failure. Stress concentrations near tiny holes in very thick plates approach the solution of a plane strain boundary condition; for large holes in very thin plates, the solution of a plane stress boundary condition will apply. For most practical cases, the response will be intermediate between the plane stress and plane strain end members, depending on the relative dimensions of the thickness of the elastic volume penetrated and the hole diameter. A nondimensional scaling parameter is introduced to quantify for which hole radius to plate thickness ratio occurs the transition between the two types of solutions (plane strain versus plane stress). Moreover, in this study, we consider the case of the presence of the internal pressure load in the analysis of the stress concentrations near boreholes. This consideration is important to carefully assess the magnitude of the elastic stress concentrations and their orientation near the hole in the rock formation when the pressure load of the mud is added to the borehole during drilling operations. For holes subjected to an internal pressure only, there is no difference between the plane stress (thin-plate solution) and plane strain solutions (thick-plate solutions). For cases with far-field stress, the plane strain solution is more sensitive to the Poisson's ratio than the plane stress solution. Multi-hole problems are also evaluated with LSM and the results are benchmarked against known solutions of different methods.

Keywords: displacement fields, linear superposition method (LSM), multi-hole solutions, plane strain, plane stress

1. Introduction

This study seeks to clarify the accuracy and possible limitations of the classical analytical solutions of Kirsch [1]—for the stress tensor field in linear-elastic plates pierced by one or more circular holes under certain far-field stress and internal pressure loads—when used in practical applications. These solutions are widely applied in wellbore-stability models and tunneling applications, and regularly involve the superposition of elastic displacements due to various boundary forces (far-field and internal pressure-loading) acting on the holes. Such situations have been systemically evaluated for linear-elastic isotropic and anisotropic rocks under a plane stress assumption [2–4].

However, recurrent concerns prevail related to the accuracy of results when using the solutions of [1] without modifications in wellbore-stability models. For example, the density of drilling mud pumped into the space between the wellbore and the drill string during drilling operations needs to be selected such that fracturing due to tensile and shear failure will not occur [5–7]. Obviously, the magnitude of the elastic stress concentrations and their orientation near the hole in the rock formation will rapidly vary when the pressure load of the mud is added to the borehole. When there is no internal pressure on the wellbore, the stress concentration factor for uni-axial far-field stress is always 3 (and for a biaxial compression reaches 4 [8]). However, when a net pressure is exerted on the wellbore's interior, the induced elastic deformation of the host rock increases or decreases the stress concentrations induced by the far-field stress, and therefore both contributions must be carefully evaluated, preferably in real-time, during drilling operations [9]. The need for real-time analysis is also the reason why superposed analytical solutions are still in vogue and cannot easily be replaced by solution methods that require gridding and have consequent longer computation times.

An additional concern is whether the standard plane stress solution of Kirsch [1] is accurate enough, whether a plane strain approach should be used, or any other approach. The plane stress solution is an end member solution for so-called thin plates; the other end member would be a thick-plate approach (plane strain assumption); each is often portrayed as 2D solution but in fact considers the state of 3D strain and stress, respectively, at all times. Although prior studies have evaluated the difference between plane strain and plane stress solutions, typically only the maximum stress concentrations are compared without analyzing the stress states further away from the boreholes. Also, the effect of the internal pressure loading superposed in the far-field stress anisotropy is normally only evaluated for arbitrarily chosen cases, which is why additional systematic evaluations in our study are merited.

Other concerns arise when multiple wells are drilled in close proximity from the same surface location and the stress interference due to the mutual interaction between the wells needs to be accounted for in the wellbore stability models. Our analysis considers both single-hole solutions and solutions for the superposition of multi-holes, all with or without individually varying pressure loads in addition to the far-field stress loading. The method of solution used is the linear superposition method (LSM) first named in ref. [3], which adds the elastic displacement vectors due to various contributions (usually boundary forces) to the elastic distortion and then solves the stress tensor field using an appropriate constitutive equation for linear elasticity.

The present analysis revisits the basic solutions for plane stress and plane strain, points out some earlier errors in displacement equations appearing in standard textbooks, and then proceeds to compute and compare the two end-member solutions (plane stress and plane strain). We also quantify the delta between thin and thick-plate solutions for multi-hole problems using the LSM method (analytical superposition of displacements) for which plane stress solutions were first given in ref. [3]. Plane strain solutions are developed in the present study to quantify the delta between the solutions due to the assumed boundary condition. Additionally, the LSM multi-hole results are validated against—(1) photo-elastic contour patterns for a 5-hole problem of Koslowska [10], and (2) a numerical example of Yi et al. [11]. The present study is limited to hole analysis based on a linear elasticity assumption for isotropic elastic plates; borehole analysis of anisotropic media was given in prior work [4, 9], applying equations developed for plane stress cases in [12].

2. Prior work

The petroleum, mining, and geotechnical tunneling industry have embraced the Kirsch equations for stability analysis of cylindrical boreholes in isotropic media. The governing equations for the Kirsch solution are based on Airy's stress function. A fact easily overlooked and little emphasized is that the equations introduced by Kirsch [1] assume a boundary condition of plane deviatoric stress, which would strictly limit the use of the Kirsch equations to cases that comply with the original boundary condition of plane stress. In spite of this limitation, the Kirsch equations are routinely applied in wellbore stability computations that may potentially yield inaccurate results if initially assumed boundary conditions in the analytical solutions are not met in the field application. For example, one may suggest that it may be more appropriate for deep boreholes in thick formations to use a thick-plate analysis (plane strain boundary condition), rather than the thin-plate analysis that fully justifies the use of the original Kirsch equations.

In nature and in real manufactured materials, the plane stress solution would only be valid for very large holes in very thin plates, such as for rivets in thin airfoils used in aircraft. However, for very thick elastic media perforated by tiny holes, such as in the case of boreholes penetrating rock formations of several kilometers thickness, the plane strain boundary condition seems more appropriate. We, therefore, evaluated what may be the actual inaccuracy creeping into the analysis of the stress concentration magnitude due to variations in the boundary conditions. Unwarranted wellbore stability problems may occur if the stress state in the well appears to deviate from plane stress proxy solutions. The delta between the stress solutions for the thin and thick-plate approaches is fully quantified in the present study for a variety of cases.

2.1 Evaluation by Clark

The notion that considerable differences may arise between stress magnitudes in elastic plates due to different transverse boundary conditions (such as plane stress versus plane strain) if subjected to otherwise the same far-field stress has been long recognized. That the stress differential may become significant was quantified in a study by Clark [13] for a uniform plate of finite, uniform thickness (and no holes) loaded with time-dependent far-field sinusoidal stresses at a lateral edge of the plate. Three cases were highlighted in ref. [13], scaling the problem with a typical wavelength, l, of the sinusoidal load and the plate thickness, $2h$. For $\frac{2h}{l} \to 0$, we have plane stress (when the wavelength of stress applied is very large as compared to thickness). For $\frac{2h}{l} \to \infty$, we have plane strain (when the wavelength of stress applied is very small as compared to thickness). When the wavelength is comparable to the thickness $\frac{2h}{l} = 1$, the maximum stress at the edges of the plate may be up to 20% larger than for "elementary plane stress" (also termed "generalized plane stress" or "very thin plate theory"), which occurs when $(\frac{2h}{l} \to 0)$. The stress concentration values obtained for $\frac{2h}{l} = 1$ exceed the plane strain solution $(\frac{2h}{l} \to \infty)$ by 31%. Clark [13] also emphasized that the generalized 2D plane stress solution for isotropic elastic plates is independent of the Poisson's ratio and neglects totally the transverse and normal stresses. Given the results of Clark [13], it is by no means obvious whether we may neglect the variations in both the stress concentrations and the stress transverse to an elastic plate with finite thickness and a boundary condition that is somewhere close to halfway between plane strain and plane stress. Below we discuss this quandary of the impact of boundary conditions on stress concentrations and transverse stresses for isotropic elastic plates with circular holes. Although the stress magnitude differentials according to ref. [13] may not be applicable to static loading cases (see later), borehole stability may be adversely impacted by seismic events, given the considerable differences in stress magnitude solutions when sinusoidal stress loads of different wavelengths are applied.

2.2 Evaluation by Green

Green [14] considered a linear elastic plate scaled by thickness $2h$ perforated by a hole of typical radius a. He introduced a practical dimensionless scaling parameter $\frac{a}{h}$ with hole radius in the nominator and plate half-thickness in the denominator. For a thick plate $\left(\frac{a}{h} \to 0\right)$, a plane strain boundary condition can be assumed (in this case the strain in the z-direction $\varepsilon_{zz} = 0$). For a thin-plate solution $\left(\frac{a}{h} \to \infty\right)$, a plane stress boundary condition can be assumed (in this case the stress in the z-direction $\sigma_{zz} = 0$). The impact of boundary conditions—on the stress concentrations and transverse stresses in elastic plates with circular holes—that are midway between those leading to either perfect plane stress or perfect plane strain cases were reviewed by Green [14]. He posited that the case $\frac{a}{h} = 1$ would lie midway between the two extremes of plane strain $\left(\frac{a}{h} \to 0\right)$ and plane stress $\left(\frac{a}{h} \to \infty\right)$ boundary conditions. Based on 3D calculations for the case $\frac{a}{h} = 1$ ("midway" boundary condition), the stress concentration halfway the total depth of the plate at $z = 0$ in the rim of a single hole in a location transverse to the applied far-field stress, $\sigma_{xx-\infty}$, increased to 3.10 $\sigma_{xx-\infty}$. If $\sigma_{xx-\infty} > 0$, we have a tension under the engineering sign convention, and hence 3.10 $\sigma_{xx-\infty}$ is an increased tension. At the plate's surface $z = h$ (for the case $\frac{a}{h} = 1$), the maximum stress concentration was less: 2.81 $\sigma_{xx-\infty}$.

For both plane strain and generalized plane stress, the maximum stress concentration averaged over the thickness of the plate should be equal to $3\sigma_{xx-\infty}$ [14]. This solution is exact for plane strain (thick plates) where—from a theoretical point of view—there may exist no variation in the maximum stress concentration near the hole for any depth z. However, for the finite-thickness plate (case with $\frac{a}{h} = 1$), only the averaged value will be $3\sigma_{xx-\infty}$, as is evident from [14] treatise. Again, at $z = 0$ at the rim of a single hole, we have 3.10 $\sigma_{xx-\infty}$ (+3% different from $3\sigma_{xx-\infty}$), while at the surface of the plate at $z = h$, the maximum stress concentration was lowered to $2.81\sigma_{xx-\infty}$ (-6% different from 3 $\sigma_{xx-\infty}$). The stress attenuation at the hole rim in the longitudinal direction parallel to $\sigma_{xx-\infty}$ appeared to vary from $-1.10\ \sigma_{xx-\infty}$ at $z = 0$ (a compression +10% above $-\sigma_{xx-\infty}$), while at the surface of the plate at $z = h$ the stress concentration was $-0.81\ \sigma_{xx-\infty}$ (19% below $-\sigma_{xx-\infty}$). Likewise, in ref. [15], Yang et al. found stress concentrations between two interacting holes in a finite-thickness elastic plate are maximum only at $z = 0$, but decrease toward the surface of the plate $(z \to h)$. Also, as the plates thicken, the maximum stress concentration shifts gradually to the surface of the plates.

According to [16] "generalized plane stress"-theorem, variations in stress concentration values throughout the thickness of a plate coinciding with the (x, y)-plane can be neglected and only the average values of the remaining stress are estimated. However, as Green [14] showed for solutions at the rim of a circular hole, there will be variations in stress concentrations over depth $0 \leq z \leq h$ when the plate has a finite thickness, characterized by $\frac{a}{h}$. However, for $\frac{a}{h} = 1$, the average maximum stress concentration would only deviate about 3% from the average values. Green [14] concluded that the generalized plane stress theory gives "fairly good" estimations for the average values of stress concentrations at the hole in a stressed plate with boundary conditions "midway" between plane stress and plane strain (adopting $\frac{a}{h} = 1$ for this case).

2.3 Other evaluations

In our opinion, there can be little doubt that plane strain is the obvious boundary condition when boreholes are drilled in thick formations. So, the question is, what (if any) corrections are necessary when applying the Kirsch equations for plane stress to compute the stress concentrations near real-world boreholes. This question is addressed below considering two cases (A and B), as previously evaluated in ref. [4].

The plane stress boundary condition $\left(\sigma_{zz} = \sigma_{xz} = \sigma_{yz} = 0\right)$ assumed in the Kirsch solution in ref. [1] implies that the mean stress $\overline{\sigma}$ in the thin elastic plate $\left(\frac{a}{h} \to \infty\right)$ is everywhere given by: $\overline{\sigma} = \frac{\sigma_{xx}+\sigma_{yy}}{3}$ (Case A). For plane strain, the mean stress $\overline{\sigma}^*$ within the thick plate's $(x, y)-$plane of the thick plate $\left(\frac{a}{h} \to 0\right)$ is given by $\overline{\sigma}^* = \frac{(1+\nu)\left(\sigma^*_{xx}+\sigma^*_{yy}\right)}{3}$ (Case B), introducing the Poisson's ratio ν. The longitudinal stress is given by $\sigma^*_{zz} = \nu\left(\sigma^*_{xx} + \sigma^*_{yy}\right)$; the longitudinal strain along the borehole is absent $\varepsilon^*_{zz} = 0$. For the special case of $\nu = 0$, the longitudinal stress will vanish, but rocks have Poisson's ratio closer to 0.25.

We may assume that the mean stresses for adjacent plane strain and plane stress sections of a borehole will be nearly identical stress concentration requirements such that we may equate the mean stress expressions for Case A and for Case B, from which it follows that $\frac{\sigma_{xx}+\sigma_{yy}}{\sigma^*_{xx}+\sigma^*_{yy}} = 1 + \nu$. This relationship says that the magnitude of the principal stresses $\sigma_{xx} + \sigma_{yy}$ acting in a plane stress section of the borehole will be larger than the plane strain case $\sigma^*_{xx} + \sigma^*_{yy}$ by a factor $1 + \nu$ (about 125% in practice, using $\nu = 0.25$). For plane stress, the longitudinal strain component is given by $\varepsilon_{zz} = -\frac{\nu}{E}\left(\sigma_{xx} + \sigma_{yy}\right)$, where E is Young's modulus of the material, which for practical situations with thin-bedded rock strata are negligibly small strains that can be easily accommodated by the discontinuities in strain occurring due to variations in the elastic constants when the drill bit moves from one rock layer into the next.

3. Methodology

The series of analytical expressions used to produce the solutions in Section 4 are outlined in Section 3. We start out with the generic elastic displacement equations for a single hole in an infinite plate subjected to far-field stress (Section 3.1), which can be solved for plane strain (Section 3.2) or plane stress (Section 3.3) boundary conditions. Although these expressions are basic, some confusing errors occur in both primary (journal papers) and secondary (textbooks) literature, which need to be pointed out (see respective sections below). What is new in our approach is that we do not solely focus on the stress concentrations at the hole but solve the stress magnitudes and principal stress orientations throughout the plates for a finite domain near the hole (Section 4) based on the equations given in Section 3.

The difference or delta between the stress magnitudes due to a plane strain or plane stress assumption is quantified in an explicit expression (Section 3.4). Because boreholes are commonly pressured from the inside by a net mud pressure, we also evaluate the displacements due to the internal pressure on the wellbore (Section 3.5). The equations of Sections 3.1–3.5 are all given in polar coordinates, but the far-field stresses in nature are typically uniform in Cartesian directions, which is why we switch to Cartesian coordinates in Sections 3.6. The use of Cartesian coordinates is essential for our analysis of both single-hole problems (Section 4.1) and multi-hole solutions (Section 4.2). Ultimately, when all the vector displacements have been computed and converted to strains, constitutive equations are needed (Section 3.7) to convert certain strain tensor fields, for any given set of elastic moduli to the corresponding stress field. The systematic series of equations in Sections 3.1 to 3.7 was used to produce the results in Section 4.

3.1 Hole displacement equations

In the theory of linear elasticity, stress quantities are linear functions of the displacement gradients expressed as strain quantities. Let us analyze the elastic displacements around a circular cylindrical hole of radius a, in an infinite plate subjected to far-field stress, $\sigma_{xx-\infty}$, acting along the x-axis. Analytical solutions for the displacement equations in polar coordinates (r, θ) are (see ref. [17]):

$$u_r = \frac{\sigma_{xx-\infty}}{8\,G} a \left\{ \frac{r}{a} (\kappa - 1 + 2\cos 2\theta) + \frac{2a}{r} \left[1 + \left(\kappa + 1 - \frac{a^2}{r^2} \right) \cos 2\theta \right] \right\} \tag{1}$$

$$u_\theta = \frac{\sigma_{xx-\infty}}{8\,G} a \left[-\frac{2r}{a} + \frac{2a}{r} \left(1 - \kappa - \frac{a^2}{r^2} \right) \right] \sin 2\theta \tag{2}$$

Above expressions capture the displacements for either plane strain or plane stress, depending upon the value inserted for κ, to be readily able to convert solutions for plane stress to plane strain, and vice-versa. In the above example, the solution for plane strain is given by substituting $\kappa = 3 - 4\,\nu$; for plane stress, one should use $\kappa = (3 - \nu)/(1 + v)$. Physically, the plane stress boundary condition applies to thin plates, while the plane strain condition applies to thick plates. The delta between the displacements and associated stress concentrations outcomes of the two approaches has not been made explicit, either for single or multiple holes, in any prior study.

3.2 Plane strain solution for the hole with uniaxial far-field stress

Using Eqs. (1) and (2) and substituting $\kappa = 3 - 4\,\nu$ for plane strain, the displacement solutions are:

$$u_r = \frac{\sigma_{xx-\infty}}{4\,Gr}\left\{r^2(1 - 2\,\nu + \cos 2\theta) + a^2\left[1 + \left(4(1-\nu) - \frac{a^2}{r^2}\right)\cos 2\theta\right]\right\} \tag{3}$$

$$u_\theta = -\frac{\sigma_{xx-\infty}}{4\,Gr}\left[r^2 + a^2\left(2(1 - 2\,\nu) + \frac{a^2}{r^2}\right)\right]\sin 2\theta \tag{4}$$

The above expressions for plane strain may be formulated using Young's modulus, E, instead of the shear modulus, G, substituting $G = E/2(1+\nu)$ into Eqs. (3) and (4):

$$u_r = \sigma_{xx-\infty}\left(\frac{1+v}{2Er}\right)\left\{r^2(1 - 2v + \cos 2\theta) + a^2\left[1 + \left(4(1-v) - \frac{a^2}{r^2}\right)\cos 2\theta\right]\right\} \tag{5}$$

$$u_\theta = -\sigma_{xx-\infty}\left(\frac{1+v}{2Er}\right)\left[r^2 + a^2\left(2(1-2v) + \frac{a^2}{r^2}\right)\right]\sin 2\theta \tag{6}$$

It is worth noting that a textbook by Goodman [18] has wrongly truncated terms in his Eq. (7.2a) and a sign error occurs in his Eq. (7.2b). Moreover, Kirsch's Equations [1] are quoted in his Eq. (7.1a–c) with a wrong statement that these would be valid for plane strain; the quoted equations are for plane stress boundary conditions. Several other sources [19–20] have promulgated the use of wrong equations similar to Goodman's (without mentioning the source). The original Kirsch equations are widely used, but also widely misused or marred by misprinted equations in the literature. For example, Eq. (3.15) in [21] has a typo, and dropped a plus sign between two terms, for the radial stress around a single borehole.

3.3 Plane stress solution for the hole with uniaxial far-field stress

With the expressions of Sections 2.1 and 2.3 in place, we now solve Eqs. (1) and (2) for plane stress by substituting $\kappa = (3-\nu)/(1+v)$; the corresponding displacement solutions are:

$$u_r = \frac{\sigma_{xx-\infty}}{4\,Gr}\left\{\frac{1-v}{1+v}r^2 + a^2 + \left(\frac{4a^2}{1+v} + r^2 - \frac{a^4}{r^2}\right)\cos 2\theta\right\} \tag{7}$$

$$u_\theta = -\frac{\sigma_{xx-\infty}}{4\,Gr}\left[\frac{1-v}{1+v}\,2a^2 + r^2 + \frac{a^4}{r^2}\right]\sin 2\theta \tag{8}$$

The above expressions for plane stress may be formulated using Young's modulus, E, instead of the shear modulus, G, substituting $G = E/2(1+\nu)$ into Eqs. (7) and (8):

$$u_r = \sigma_{xx-\infty}\left(\frac{1+v}{2Er}\right)\left\{\frac{1-v}{1+v}r^2 + a^2 + \left(\frac{4a^2}{1+v} + r^2 - \frac{a^4}{r^2}\right)\cos 2\theta\right\} \tag{9}$$

$$u_\theta = -\sigma_{xx-\infty}\left(\frac{1+v}{2Er}\right)\left[\frac{1-v}{1+v}\,2a^2 + r^2 + \frac{a^4}{r^2}\right]\sin 2\theta \tag{10}$$

Eqs. (9) and (10) are identical to those given in [22] (p. 740–742) and were used in a prior study focused on multi-hole problems under plane stress [3].

Separately, we checked for the computational integrity of the plane strain displacement solutions of Section 3.2 by applying a standard conversion substitution, as explained in Appendix A.

3.4 Delta between plane strain and plane stress solutions with uniaxial far-field stress

The residual displacements when subtracting Eqs. (9) from (5), and (10) from (6), respectively, are:

$$u_r = \sigma_{xx-\infty}\left(\frac{1+v}{2Er}\right)\left\{\left[r^2(1-2v+\cos 2\theta)+a^2\left[1+\left(4(1-v)-\frac{a^2}{r^2}\right)\cos 2\theta\right]\right]\right.$$

$$\left.-\left[\frac{1-v}{1+v}r^2+a^2+\left(\frac{4a^2}{1+v}+r^2-\frac{a^4}{r^2}\right)\cos 2\theta\right]\right\},$$

$$= -\sigma_{xx-\infty}\left(\frac{v^2}{Er}\right)\left\{r^2+2a^2\cos 2\theta\right\}. \tag{11}$$

$$u_\theta = -\sigma_{xx-\infty}\left(\frac{1+v}{2Er}\right)\left\{\left[r^2+a^2\left(2(1-2v)+\frac{a^2}{r^2}\right)\right]\sin 2\theta-\left(\frac{1-v}{1+v}2a^2+r^2+\frac{a^4}{r^2}\right)\sin 2\theta\right\}$$

$$= \sigma_{xx-\infty}\left(\frac{v^2}{Er}\right)\left(2a^2\sin 2\theta\right). \tag{12}$$

3.5 Plane strain and plane stress solutions for the hole with internal pressure

From [23] general solution for a hollow cylinder (with infinite axial length) pressured inside and outside with different pressures, can be obtained a simple displacement solution for a hole in an infinite plate by letting the outer radius of the cylinder go to infinity such that only the term remains for the radial displacement due to the pressure inside the cylinder:

$$u_r = -P\frac{a^2}{r}\frac{1+v}{E} = -P\frac{a^2}{r}\frac{1}{G} \tag{13}$$

$$u_\theta = 0 \tag{14}$$

Above displacement field is due to a hole internally pressurized under plane strain boundary conditions and assumes *P* is given as a negative value when causing compression (as in mechanical engineering sign conventions); if we prefer to use *P* as a positive input, the minus sign in Eq. (13) must be dropped. Following ref. [3], we will consider positive *P* inputs (so minus sign will be dropped from Eq. (13) in the rest of this paper).

Plane strain solutions formulated with *G* can be converted to plane stress solutions by replacing ν with $\frac{\nu}{1+\nu}$ (e.g., [17], page 115). Eq. (13) when formulated with

G is identical to the plane strain solution, as applied in ref. [3], which means the plane stress solution is independent of ν. Therefore, the delta or residual displacement, in this case, will be zero. The displacement solution for an internally pressured hole in an infinite plate appears insensitive to the thickness of the plate, which can be understood via physical reasoning as follows. Adopting the definitions in [14] treatise on 3D stress systems in isotropic plates, for $\frac{a}{h} \to \infty$ we have a thin-plate problem (plane stress) and for $\frac{a}{h} \to 0$ we have a thick-plate problem (plane strain). In all 3D solutions for plane stress and plane strain cases, the solutions are identical in planes midway the plates at $h = 0$. However, when the plates possess a finite thickness, differences in solutions for plates with holes subjected to a far-field stress under plane strain and plane stress arise when studying solutions, where $h \to 0$. The internally pressured hole solution is insensitive to plate thickness, because for both plane strain and plane stress cases, the pressure on the hole is assumed uniform along h, so essentially does not allow stresses to occur normal to the plate by strictly maintaining the pressure equal to P even at the rim of the hole near the surface (see Section 4).

3.6 Conversion to Cartesian coordinates

The conversion of the displacement solutions from polar to Cartesian coordinates is practical for single-hole and multi-hole analysis (which requires superposition) of practical borehole problems because the far-field (tectonic) stresses are assumed more or less constant in the three individual Cartesian directions. It is emphasized here that the solutions in Cartesian and polar coordinates only differ in coordinate transformation to facilitate the visualization of either polar or Cartesian vector displacements, each with their corresponding solutions for the stress and strain tensor components. However, the principal stresses remain invariant to the coordinate system used. The conversion from polar to Cartesian coordinates follows the same steps as in Eqs. (12–17) of ref. [3].

3.6.1 Cartesian coordinates of plane strain solutions (uniaxial far-field stress)

The displacement Eqs. (5) and (6) in polar vector coordinates (u_r, u_θ) are converted to Cartesian displacements vector coordinates (u_x, u_y) using the appropriate coordinate transformation equations (see Appendix B for details):

$$u_x = u_r \cos\theta - u_\theta \sin\theta, \quad u_y = u_r \sin\theta + u_\theta \cos\theta$$

We get:

$$u_x = \sigma_{xx-\infty}\left(\frac{1+v}{2E}\right)\left\{\left[(x^2+y^2)(1-2v)+x^2-y^2+a^2+4a^2(1-v)\left(\frac{x^2-y^2}{x^2+y^2}\right) - a^4\left(\frac{x^2-y^2}{(x^2+y^2)^2}\right)\right]\left(\frac{x}{x^2+y^2}\right) + \left[2xy+(1-2v)\left(\frac{4a^2xy}{x^2+y^2}\right)+\frac{2a^4xy}{(x^2+y^2)^2}\right]\left(\frac{y}{x^2+y^2}\right)\right\} \tag{15}$$

$$u_y = \sigma_{xx-\infty}\left(\frac{1+v}{2E}\right)\left\{\left[\left(x^2+y^2\right)(1-2v)+x^2-y^2+a^2+4a^2(1-v)\left(\frac{x^2-y^2}{x^2+y^2}\right)\right.\right.$$

$$\left.\left.-a^4\left(\frac{x^2-y^2}{\left(x^2+y^2\right)^2}\right)\right]\left(\frac{y}{x^2+y^2}\right)-\left[2xy+(1-2v)\left(\frac{4a^2xy}{x^2+y^2}\right)+\frac{2a^4xy}{\left(x^2+y^2\right)^2}\right]\left(\frac{x}{x^2+y^2}\right)\right\} \tag{16}$$

3.6.2 Cartesian coordinates of plane stress solutions (uniaxial far-field stress)

The displacement Eqs. (9) and (10) were converted to Cartesian coordinate in ref. [3] as:

$$u_x = \sigma_{xx-\infty}\left(\frac{1+v}{2E}\right)\left\{\left[\frac{1-v}{1+v}\left(x^2+y^2\right)+a^2+\left(\frac{4a^2}{1+v}+x^2+y^2-\frac{a^4}{x^2+y^2}\right)\left(\frac{x^2-y^2}{x^2+y^2}\right)\right]\right.$$

$$\left.\times\left(\frac{x}{x^2+y^2}\right)+\left[\left(\frac{1-v}{1+v}2a^2+x^2+y^2+\frac{a^4}{x^2+y^2}\right)\left(\frac{2xy}{x^2+y^2}\right)\right]\left(\frac{y}{x^2+y^2}\right)\right\} \tag{17}$$

$$u_y = \sigma_{xx-\infty}\left(\frac{1+v}{2E}\right)\left\{\left[\frac{1-v}{1+v}\left(x^2+y^2\right)+a^2+\left(\frac{4a^2}{1+v}+x^2+y^2-\frac{a^4}{x^2+y^2}\right)\left(\frac{x^2-y^2}{x^2+y^2}\right)\right]\right.$$

$$\left.\times\left(\frac{y}{x^2+y^2}\right)-\left[\left(\frac{1-v}{1+v}2a^2+x^2+y^2+\frac{a^4}{x^2+y^2}\right)\left(\frac{2xy}{x^2+y^2}\right)\right]\left(\frac{x}{x^2+y^2}\right)\right\} \tag{18}$$

Eqs. (15)–(18) are valid for a borehole centered at the origin. For holes with their centers shifted to an arbitrary location (x_s, y_s), we replace x by $(x - x_s)$ and y by $(y - y_s)$. For multiple wellbore problems, as in ref. [3], we add the following terms to Eqs. (15) and (16) for the plane strain case:

$$u_x = \frac{-(n-1)}{n}\,\frac{\sigma_{xx-\infty}\left(1-v^2\right)}{E}x \tag{19}$$

$$u_y = \frac{(n-1)}{n}\,\frac{\sigma_{xx-\infty}v\left(1-v^2\right)}{E(1-v)}y \tag{20}$$

and the following terms to Eqs. (17) and (18) for the plane stress case:

$$u_x = \frac{-(n-1)}{n}\,\frac{\sigma_{xx-\infty}}{E}x \tag{21}$$

$$u_y = \frac{(n-1)}{n}\,\frac{\sigma_{xx-\infty}v}{E}y \tag{22}$$

where n denotes the number of boreholes. The total displacement vectors ($u_{x,\mathrm{total}}$ and $u_{y,\mathrm{total}}$) due to all holes combined can be computed by the following summations:

$$u_{x,\mathrm{total}} = \sum_{i=1}^{n} u_{x,i} \tag{23}$$

$$u_{y,\mathrm{total}} = \sum_{i=1}^{n} u_{y,i} \tag{24}$$

3.6.3 Cartesian coordinates of delta between plane strain and plane stress solutions (uniaxial far-field stress)

Using the same transformation as in Section 3.6.1, Eqs. (11) and (12) are converted to Cartesian coordinate (see Appendix B for details):

$$u_x = -\sigma_{xx-\infty}\left(\frac{v^2}{E(x^2+y^2)}\right)\left[\left(x^2+y^2+2a^2\frac{x^2-y^2}{x^2+y^2}\right)x+\left(4a^2\frac{xy}{x^2+y^2}\right)y\right] \tag{25}$$

$$u_y = -\sigma_{xx-\infty}\left(\frac{v^2}{E(x^2+y^2)}\right)\left[\left(x^2+y^2+2a^2\frac{x^2-y^2}{x^2+y^2}\right)y-\left(4a^2\frac{xy}{x^2+y^2}\right)x\right] \tag{26}$$

One can also obtain Eqs. (25) and (26) by subtracting Eqs. (17) and (18) from Eqs. (15) and (16) (see Appendix B).

3.6.4 Cartesian coordinates of plane stress/plane strain solutions for a single hole with internal pressure

The polar coordinate solutions of Section 3.5 have been transformed to Cartesian coordinates, using the appropriate coordinate transition equations of Section 3.6.1:

$$u_x = P\left(\frac{a^2}{x^2+y^2}\right)\left(\frac{1+v}{E}\right)x \tag{27}$$

$$u_y = P\left(\frac{a^2}{x^2+y^2}\right)\left(\frac{1+v}{E}\right)y \tag{28}$$

3.7 Constitutive equations

From the displacement field equations, once converted to Cartesian coordinates, one may compute the displacement gradients to obtain the strain tensor components in every location of the elastic medium:

$$\varepsilon_{xx} = \frac{\partial u_x}{\partial x} \tag{29}$$

$$\varepsilon_{yy} = \frac{\partial u_y}{\partial y} \tag{30}$$

$$\varepsilon_{xy} = \frac{1}{2}\left[\frac{\partial u_x}{\partial y}+\frac{\partial u_y}{\partial x}\right] \tag{31}$$

In the present study, we follow the mechanical engineering convention where extension and tension are positive. Once the strain components have been identified for our specific problem, the stresses in each point of the elastic medium can be resolved using the constitutive equations. The following equations are valid for either plane strain or plane stress, depending on the value assigned to κ with a linear elasticity assumption [17]:

$$\varepsilon_{xx} = \frac{1}{8G}\left[(\kappa+1)\sigma_{xx} + (\kappa-3)\sigma_{yy}\right] \tag{32}$$

$$\varepsilon_{yy} = \frac{1}{8G}\left[(\kappa-3)\sigma_{xx} + (\kappa+1)\sigma_{yy}\right] \tag{33}$$

$$\varepsilon_{xy} = \frac{\sigma_{xy}}{2G} \tag{34}$$

The constitutive equation for plane strain is given by substituting $\kappa = 3 - 4\,\nu$; for plane stress, one should use $\kappa = (3-\nu)/(1+v)$. Separately, when G is used in the equations, the solutions for plane stress may be converted to plane strain by replacing ν with $\nu/(1-\nu)$, which means replacing $(3-\nu)/(1+\nu)$ by $(3-4\nu)$. Likewise, solutions for plane strain may be converted to plane stress by replacing ν with $\nu/(1+\nu)$, which means replacing $(3-4\nu)$ by $(3-\nu)/(1+\nu)$. The strain in the z-direction, ε_{zz}, vanishes for plane strain but does not necessarily vanish for plane stress ($\sigma_{zz} = \sigma_{xz} = \sigma_{yz} = 0$) where it is given by:

$$\varepsilon_{zz} = -\frac{v}{E}\left(\sigma_{xx} + \sigma_{yy}\right) = -\frac{v}{1-v}\left(\varepsilon_{xx} + \varepsilon_{yy}\right) \tag{35}$$

The principal strain magnitude can now be obtained as follows:

$$\varepsilon_1, \varepsilon_2 = \frac{\varepsilon_{xx} + \varepsilon_{yy}}{2} \pm \sqrt{\left(\frac{\varepsilon_{xx} - \varepsilon_{yy}}{2}\right)^2 + \varepsilon_{xy}{}^2} \tag{36}$$

4. Results

A MATLAB code was written to evaluate—for specific hole arrangements—the delta between the plane strain and the plane stress solutions based on the algorithms developed in Section 3. We consider holes of equal and different radii, with and without far-field stress, with and without internal pressures, and the pressure of individual holes may be varied. All solutions given are for static conditions, in the sense that time-dependent changes are not considered in the present study. Two types of borehole problems are addressed: single hole (Section 4.1) and multi-hole (Section 4.2).

4.1 Single-hole problems

The principal stress distributions σ_1 and σ_2 are computed using

$$\sigma_1 = \frac{1}{2}\ \sigma_{xx} + \sigma_{yy}\ + \left[\sigma_{xy}^2 + \frac{1}{4}\ \sigma_{xx} - \sigma_{yy}\ ^2\right]^{\frac{1}{2}} \tag{37}$$

$$\sigma_2 = \frac{1}{2}\left(\sigma_{xx} + \sigma_{yy}\right) - \ \sigma_{xy}^2 + \frac{1}{4}\left(\sigma_{xx} - \sigma_{yy}\right)^2\ ^{\frac{1}{2}} \tag{38}$$

$$(\qquad)\ \left[\qquad(\qquad)\right]$$

Inputs	
Hole positions (x, y)	**(0,0)**
Hole radii, a[m]	0.2
Poisson's ratio, $\nu[-]$	0.3
Far-field stress, σ [MPa]	10
Internal pressure, P[MPa]	10
Number of boreholes, n	1
Young's modulus, E [GPa]	50

Table 1.
Model inputs used for the single-hole problem.

The first case considers a single hole subject to either.
Case 1–1: a far-field stress only,
Case 1–2: an internal pressure only,
Case 1–3: the superposed Cases 1–1 and 1–2.

Model inputs are given in **Table 1**. A comprehensive comparison of the vector displacement fields, strain tensor components, principal strains, stress tensor components, and principal stresses for all the above cases is given in Appendix C.

4.1.1 Case 1–1: single hole subject to a far-field stress

Figure 1 quantifies the delta of the principal stress distributions σ_1 and σ_2 for the plane strain and plane stress boundary conditions in the case of applying far-field

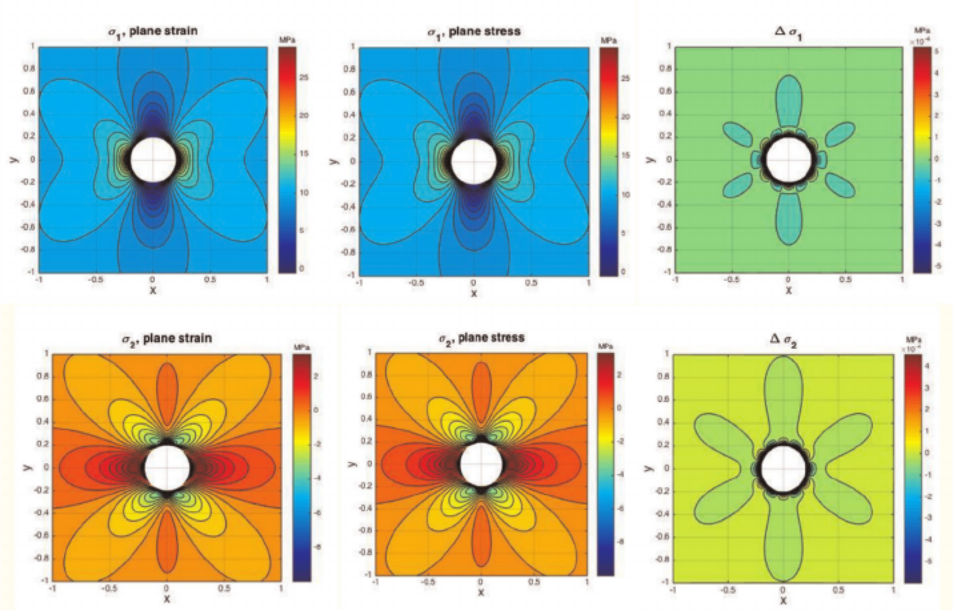

Figure 1.
Principle stress distributions σ_1 (top row) and σ_2 (bottom row) for single hole subject to far-field stress. The first column is for plane strain boundary conditions, the second column is for plane stress boundary conditions, and the third column quantifies the difference (delta) between the first and second cases.

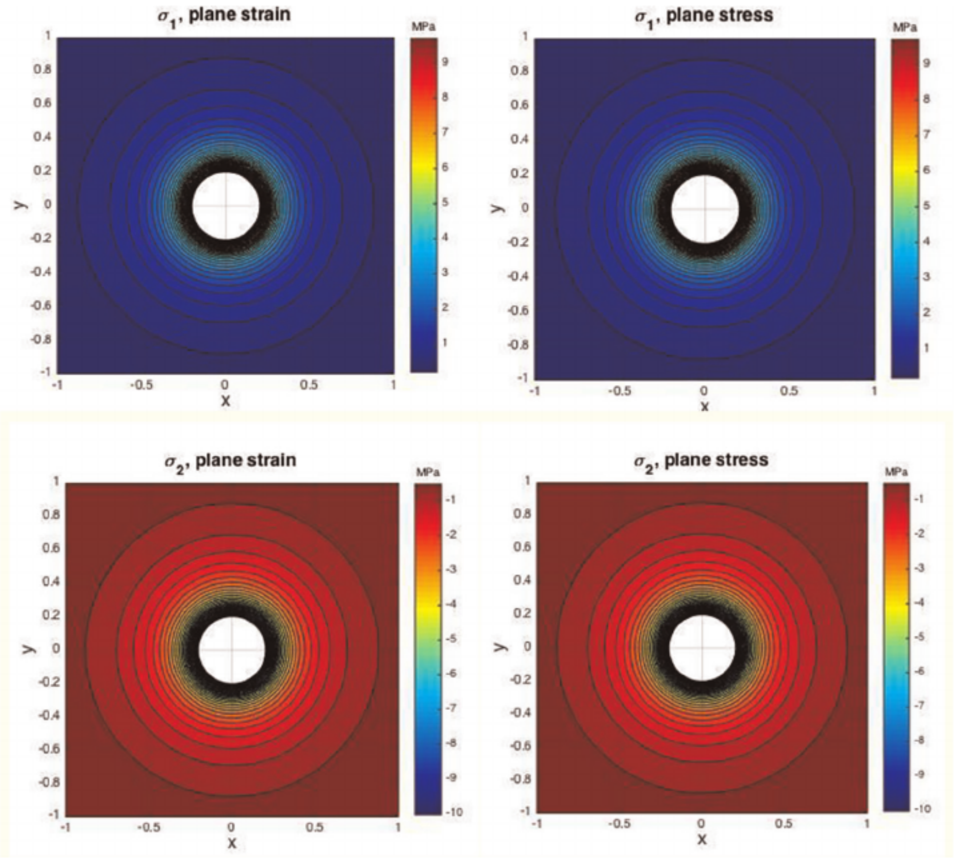

Figure 2.
Principle stress distributions σ_1 *(top row) and* σ_2 *(bottom row) for single hole subject to internal pressure. The first column is for the plane strain boundary condition; the second column is for the plane stress boundary condition.*

stress only. The first column in **Figure 1** is for plane strain boundary conditions, the second column is for plane stress boundary conditions, and the third column represents the residual of the principal stress magnitude.

4.1.2 Case 1-2: single hole subject to internal pressure

For the hole using only internal pressure, the principal stress solutions for plane strain and plane stress are identical (**Figure 2**) due to the same displacement fields (see the reasoning in Section 3.5).

4.1.3 Case 1-3: superposed cases 1-1 and 1-2

The superposed Cases 1–1 and 1–2 seem trivial, but the deltas in **Figure 3** differ from those in **Figure 1**. The explanation is that the displacements due to the internal pressure on the hole add lateral uniform volumetric displacements that shift the locations where the deltas occur. When the internal pressure on the hole increases, the overall delta remains limited.

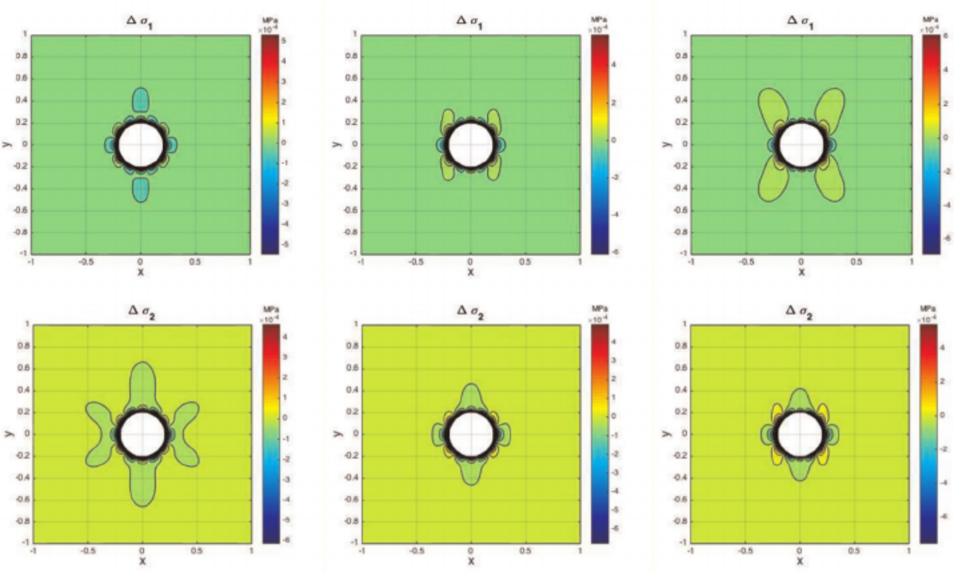

Figure 3.
The residual of the principle stress distributions σ_1 *(top row) and* σ_2 *(bottom row) for a single hole subject to far-field stress (10 MPa) and different internal pressure loads (first column:* P = 1 *MPa, second column:* P = 5 *MPa, and third column:* P = 10 *MPa).*

4.2 Multi-hole problems

For multi-hole modeling, the elastic displacements due to the individual contributions are superposed, then converted to the overall stress state via the constitutive equations. The procedure has been previously applied and was coined the Linear Superposition Method (LSM) in prior work. For perfect analytical accuracy of LSM multi-hole solutions, the superposition patterns would require perfect symmetry patterns for hole arrangements and endless repetitions as in the method of images. This symmetrical superposition principle also lies at the heart of earlier analytical multi-hole stress interference solutions [24–27].

A previous multi-hole solution departing from symmetric superposition by instead using randomly placed holes was assumed a valid approach [28]. The 11-hole problem in ref. [28], solved by them with a system of linear algebraic equations using a complex boundary integral method based on truncated Fourier series, was closely matched with an LSM solution [29]. We are well aware that LSM solutions for arbitrarily placed holes would be only asymptotically correct, due to hole patterns lacking symmetry. However, based on close matches of LSM-based solutions with photo-elastic patterns in our prior studies [4], as well as a comparison against Abaqus solutions in [30] our conclusion was that LSM gives very reliable results even for randomly placed hole arrangements.

To further support the practical reliability of LSM solutions for randomly placed holes, several new comparisons of stress field solutions with LSM for multi-hole problems with those obtained with other methods are given below. These comparisons are for a photo-elastic prototype strain and stress visualization (Case 2–1) and a prototype solution based on a finite element solution method (Case 2–2).

4.2.1 Case 2–1: photo-elastic prototype

For multi-hole analysis, we first consider a traditional example of photo-elastic visualization of displacement and strain components. The 5-hole photo-elastic prototype (**Figure 4**) has a total thickness of 5 mm (3 mm aluminum and 2 mm photo-elastic coating). The aluminum strips are 100 mm wide and 450 mm long. The long dimension may be assumed well suited for an infinite plate solution. However, the lateral width of 100 mm leaves only 30 mm between the boundaries of the outer holes (all have radii of 10 mm) and the left and right boundaries of the elastic plate.

A point that has been little elaborated is whether photo-elastic experiments typically represent thin- or thick-plate solutions, that is, represent plane stress or plane strain solutions. Theoretically, solutions for a plane stress boundary condition would apply to holes in very thin strips (for which σ_{zz} will be negligibly small). However, when a plate is "thicker" instead of $\sigma_{zz} \rightarrow 0$, we will have the $\epsilon_{zz} \rightarrow 0$, and the boundary condition approaches a plane strain case. For exactly what "finite thickness" of an elastic strip with holes, the plane stress solutions would need to be replaced by a plane strain solution has never been made explicit.

The accurate LSM solutions for either an infinite plate [with thin plate $\left(\frac{a}{h} \rightarrow \infty\right)$ or a thick plate $\left(\frac{a}{h} \rightarrow 0\right)$ solutions] will not be able to perfectly match the photo-elastic prototype with finite width, finite length, and for $0 < \frac{a}{h} < \infty$. Nonetheless, we can still use LSM to investigate which solution (plane strain or plane stress) gives the best approximation for a particular case. We tested for both, following [14] reasoning (summarized in Section 2.2 of the present study), for $\frac{a}{h} \rightarrow \infty$ we have a thin-plate problem (plane stress); for $\frac{a}{h} \rightarrow 0$ we have a thick-plate problem (plane strain).

4.2.2 Case 2–1: results

Model inputs are given in **Table 2**. Match attempts of **Figure 4 b-d** contour patterns with plane strain and plane stress LSM codes are given in **Figures 5**–**7**,

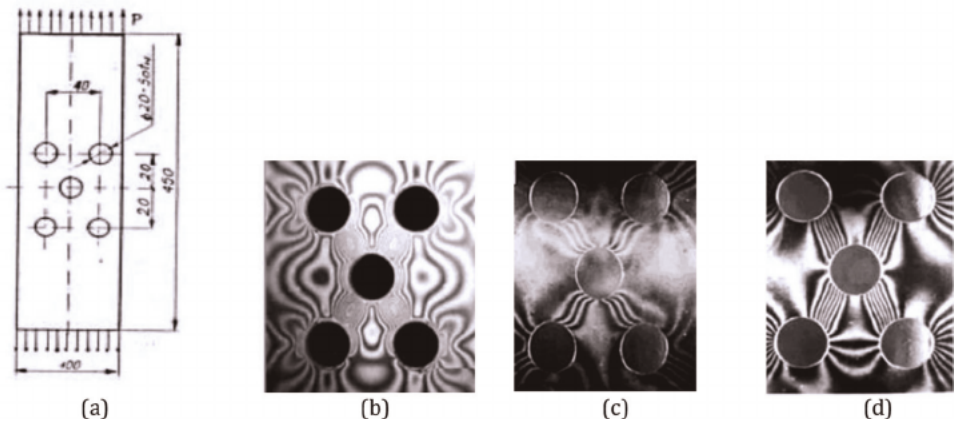

(a) (b) (c) (d)

Figure 4.
The 5-hole photo-elastic prototype. (a) Plate dimensions, (b) isochromatic pattern for strain state, (c) $u(x,y)$ displacement magnitude contours, (d) $v(x,y)$ displacement magnitude contours (after [10]).

Inputs		
hole positions (x, y)	Center hole	(0,0)
	Top right	(0.3,0.2)
	Top left	(−0.3,0.2)
	Bottom left	(−0.3,-0.2)
	Bottom right	(0.3,-0.2)
Hole radii, a[m]		0.1
Poisson's ratio, $\nu[-]$		0.4
Far-field stress, σ [MPa]		10
Number of boreholes, n		5
Young's modulus, E [GPa]		50

Table 2.
Model inputs used for 5-hole problem.

respectively. Any mismatches near the right and left margins of the sample may be due to differences in lateral boundary conditions: the photo-elastic strip has a finite width, while our solutions are for an infinite plate. The lateral boundary may be simulated by a mirror-image approach, but was not pursued in the present study. Separately, comprehensive comparisons of the vector displacement fields, strain tensor components, principal strains, stress tensor components, and principal stresses are given in Appendix D.

For the elastic prototype of **Figure 4**, the model scaling used was $\frac{a}{h} = 2$, which means the elastic displacement field (**Figures 6** and 7) and resulting strain state (**Figure 5**) in the plane of view represent the plane stress solution. The LSM method is used in this example for both plane stress and plane strain solution to validate this theoretical result. Clearly, the LSM plane stress solutions (**Figures 5c**–**7c**) are closer (but not "exactly") to the contour patterns in **Figures 5a**-**7a**, respectively, than the LSM plane strain solutions (**Figures 5b**–**7b**).

4.2.3 Case 2-2: Numerical benchmark; solution paths

The accuracy of the LSM-based solutions was benchmarked in prior studies [3, 29], against results from independent solution methods (e.g., [28]), with excellent matches. Here we benchmark LSM in a multi-hole solution against the independent numerical solution for the tangential stress concentrations in the rim of a 5-hole problem by Yi et al. [11]. The 5-hole configuration studied is part of an infinite plate subject to a uniaxial far-field compression, with dimensions as shown in **Figure 8**. The numerical solution method (based on the finite element method) was validated by Yi et al. [11] against a prior analytical-numerical solution (based on a Laurent series method [31]).

The 5-hole problem of **Figure 8** has its holes positioned slightly different than those in **Figure 4**. We used the exact same 5-hole setup as in **Figure 8** to solve the tangential stresses with our LSM code. To quantify the radial and tangential stresses in a particular polar coordinate system (r, θ), one may follow two different computational paths.

Path 1: Use $x = r\cos\theta$ and $y = r\sin\theta$ as inputs for the Cartesian displacement equations. For specific locations (r, θ), such as at the rim of the central hole in

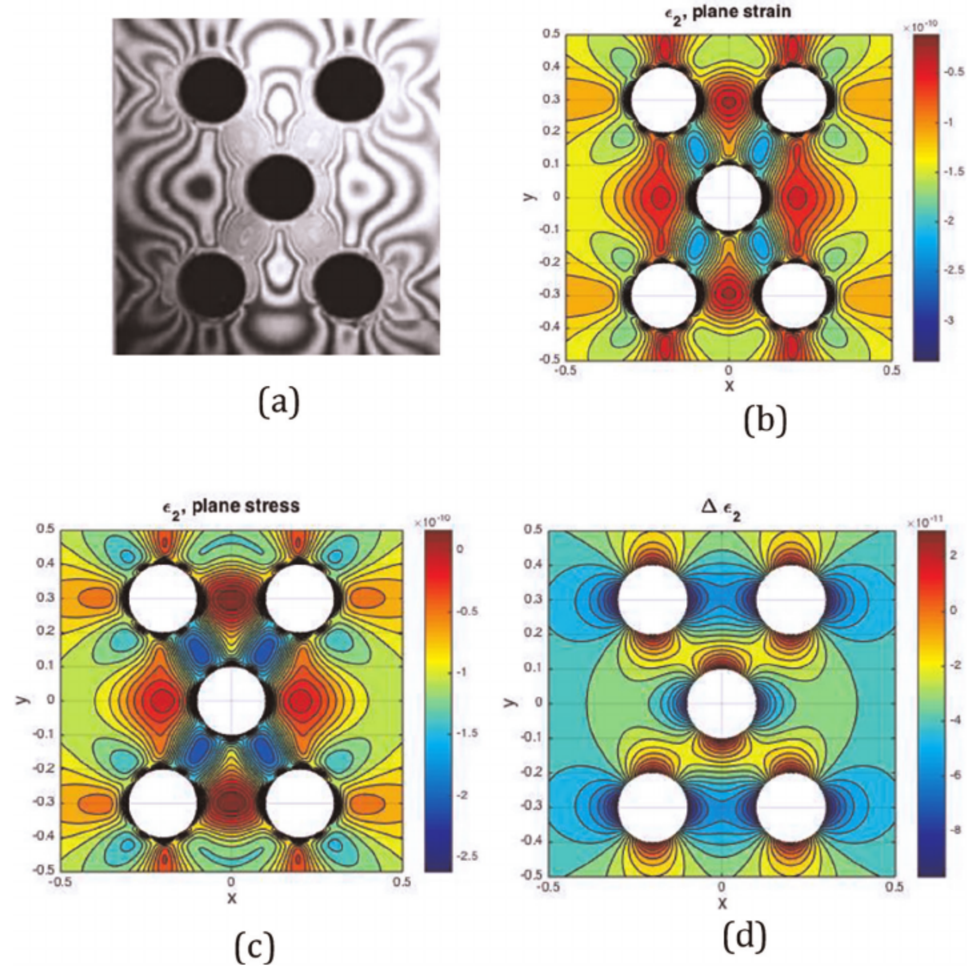

Figure 5.
(a) Photo-elastic fringes near five equal holes due to far-field tension in the vertical direction of image view [10]. (b) LSM plane strain solution for ε_2*. (c) LSM plane stress solution for* ε_2*. (d) the residual between the plane stress and plane strain solutions for* ε_2 *.*

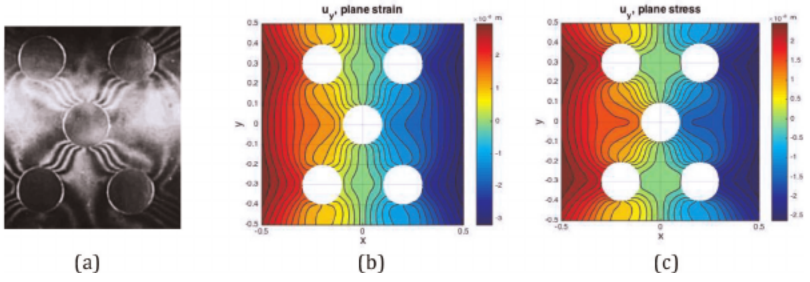

Figure 6.
(a) $u(x, y)$ *displacement magnitude contours [10]. (b) LSM plane strain solution for* u_y *(c) LSM plane stress solution for*u_y*.*

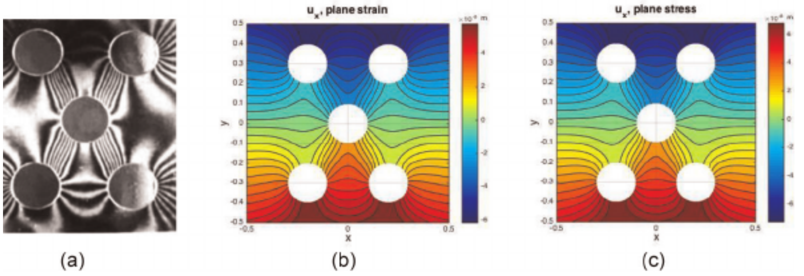

Figure 7.
(a) $v(x,y)$ displacement magnitude contours [10]. (b) LSM plane strain solution for u_x. (c) LSM plane stress solution for u_x.

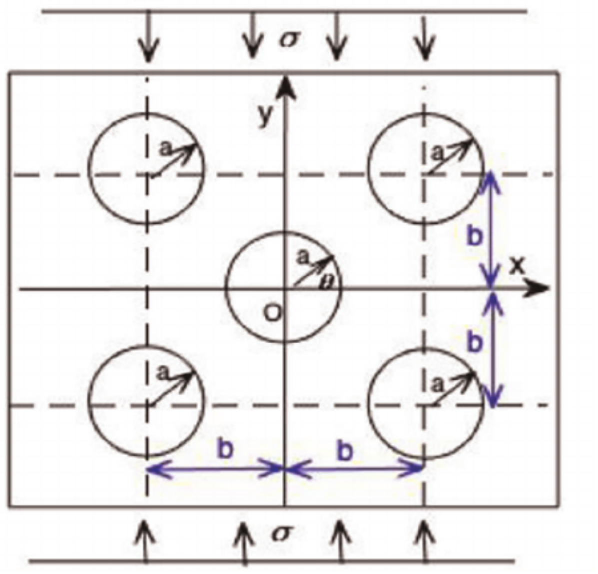

Figure 8.
An infinite plate containing five equal circular holes under axial compressive stress ($b = 3\sqrt{2a}/2$ and $\sigma = 1$). No internal pressure load.

Figure 8, one can next compute the three polar strain tensor components using the following coordinate transformation for the strain tensor elements (e.g., Kelly Notes Solid Mechanics Part 2, Eq. 4.2.17):

$$\varepsilon_r = \varepsilon_{xx}\cos^2\theta + \varepsilon_{yy}\sin^2\theta + \varepsilon_{xy}\sin 2\theta \tag{39}$$

$$\varepsilon_\theta = \varepsilon_{xx}\sin^2\theta + \varepsilon_{yy}\cos^2\theta - \varepsilon_{xy}\sin 2\theta \tag{40}$$

$$\varepsilon_{r\theta} = \left(\varepsilon_{yy} - \varepsilon_{xx}\right)\sin\theta\cos\theta + \varepsilon_{xy}\cos 2\theta \tag{41}$$

Please note that for the un-pressurized hole subjected to (only) far-field stress, the radial strain, ε_r at the hole, the boundary will vanish (only at the hole boundary and not beyond).

Path 2: Revert to the original displacement equations in polar coordinates (Sections 2.1 to 2.5) and compute the displacement gradients in polar coordinates:

$$\varepsilon_r = \frac{\partial u_r}{\partial r} \tag{42}$$

$$\varepsilon_\theta = \frac{1}{r}\frac{\partial u_\theta}{\partial \theta} + \frac{u_r}{r} \tag{43}$$

$$\varepsilon_{r\theta} = \frac{1}{2}\left(\frac{1}{r}\frac{\partial u_r}{\partial \theta} + \frac{\partial u_\theta}{\partial r} - \frac{u_\theta}{r}\right) \tag{44}$$

After having obtained the polar displacement gradients, one may compute the stresses for a plane stress (thin plate) problem from the following constitutive equations:

$$\sigma_r = \frac{E}{1-\nu^2}\left(\varepsilon_r + \varepsilon_\theta \nu\right) \tag{45}$$

$$\sigma_\theta = \frac{E}{1-\nu^2}\left(\varepsilon_\theta + \varepsilon_r \nu\right) \tag{46}$$

$$\sigma_{r\theta} = \frac{E}{2(1+\nu)}\varepsilon_{r\theta} \tag{47}$$

For plane strain (thick plate) problem, the corresponding constitutive equations are ([32], Eq. (5-38)):

$$\sigma_r = \frac{2G}{1-2\nu}\left[(1-\nu) + \varepsilon_\theta \nu\right] = \frac{E}{(1+\nu)(1-2\nu)}\left[(1-\nu) + \varepsilon_\theta \nu\right] \tag{48}$$

$$\sigma_\theta = \frac{2G}{1-2\nu}\left[\varepsilon_\theta(1-\nu) + \varepsilon_r \nu\right] = \frac{E}{(1+\nu)(1-2\nu)}\left[\varepsilon_\theta(1-\nu) + \varepsilon_r \nu\right] \tag{49}$$

$$\sigma_{r\theta} = G\varepsilon_{r\theta} = \frac{E}{2(1+\nu)}\varepsilon_{r\theta} \tag{50}$$

For completeness, polar strain tensor components can be computed from the stress tensor components as follows ([32], Eq. (5-37)):

$$\varepsilon_r = \frac{1}{2G}\left[\sigma_r(1-\nu) - \sigma_\theta \nu\right] \tag{51}$$

$$\varepsilon_\theta = \frac{1}{2G}\left[\sigma_\theta(1-\nu) - \sigma_r \nu\right] \tag{52}$$

$$\varepsilon_{r\theta} = \frac{\sigma_{r\theta}}{G} \tag{53}$$

The polar strain tensor components can be converted to the Cartesian components at any one time using the polar coordinate transformations [e.g. [12], Eq. (48)]:

$$\varepsilon_{xx} = \varepsilon_r \cos^2\theta + \varepsilon_\theta \sin^2\theta \tag{54}$$

$$\varepsilon_{yy} = \varepsilon_r \sin^2\theta + \varepsilon_\theta \cos^2\theta \tag{55}$$

$$\varepsilon_{xy} = \frac{\varepsilon_r - \varepsilon_\theta}{2} \sin 2\theta \tag{56}$$

4.2.4 Case 2–2: results

The results of our benchmark test for Case 2–2, as per the methodology outlined above, are given here. First, a baseline solution for the tangential stress around a single hole (Case 1–1) is given in **Figure 9**. An important finding is that the plane stress solution for tangential stress concentrations around the hole is less sensitive to the Poisson's ratio compared with the plane strain solution as shown in **Figure 9a, b**, and **Table 3** (for positive values of ν). This subtle difference has not been emphasized before. Overall, the delta between the plane strain and plane stress solutions becomes larger for larger Poisson's ratios, resulting in the stress concentration factor being 3 for the plane stress boundary condition, increasing to nearly 4 for the plane strain boundary condition.

The impacts of the Poison ratio and different boundary conditions were analyzed in more detail, based on the displacement fields quantified in Appendix C, which led to the following conclusions:

- Displacements in the x-direction are insensitive to the value of ν in case of plane stress.
- Displacements in the x-direction are slightly sensitive to the value of ν in case of plane strain.
- Displacements in the y-direction are sensitive to the value of ν in both plane strain and plane stress.

When the Poisson's ratio is 0, the stress concentrations, according to our LSM models, are the same for plane stress and plane strain boundary conditions (**Figure 9a**). This matching in the concentrations at $\nu = 0$ between the plane stress and plane strain solutions can also be seen in Eq. (46), for plane stress, and Eq. (49), for plane strain. For the higher Poisson's ratio $\nu = 0.3$, the plane strain

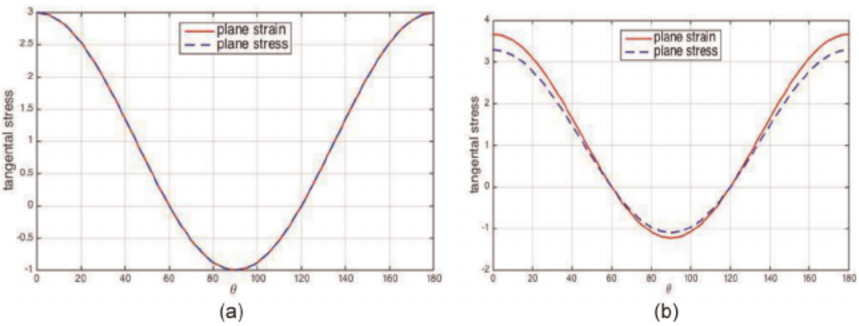

Figure 9.
Tangential stress concentration variations around the rim of a single hole (case 1–1). (a) Poisson's ratio $\nu = 0.0$*, and (b)* $\nu = 0.3$*.*

Poisson's ratio ν [−]	Plane strain		Plane stress	
	$\max_{0\le\theta\le\pi}(\sigma_\theta)$	$\min_{0\le\theta\le\pi}(\sigma_\theta)$	$\max_{0\le\theta\le\pi}(\sigma_\theta)$	$\min_{0\le\theta\le\pi}(\sigma_\theta)$
−0.5	3.3749	−1.1249	3.9999	−1.3333
−0.4	3.2666	−1.0888	3.5714	−1.1904
−0.3	3.1687	−1.0562	3.2967	−1.0989
−0.2	3.0857	−1.0285	3.1250	−1.0416
−0.1	3.0249	−1.0083	3.0303	−1.0101
0.0	3.0000	−1.0000	3.0000	−1.0000
0.1	3.0374	−1.0124	3.0303	−1.0101
0.2	3.1999	−1.0666	3.1250	−1.0416
0.3	3.6749	−1.2249	3.2967	−1.0989
0.4	5.4000	−1.8000	3.5714	−1.1904
0.5	INF	-INF	3.9999	−1.3333

Table 3.
Maximum and minimum tangential stress (σ_θ) around the rim of the central hole in a single hole problem (case 1–1) corresponding to different values of Poisson's ratio ν. The max of σ_θ occurs at $\theta = 0$ and π. The minimum of σ_θ is at $\theta = \frac{\pi}{2}$.

solution starts to show a higher stress concentration than the plane stress solution (**Figure 9b**).

Next, we show the 5-hole (Case 2–2) stress concentrations around the central hole (**Figure 10a, b**). For the small Poisson's ratio of $\nu = 0$, stress concentrations of LSM solutions under plane strain and plane stress boundary conditions are identical (**Figure 10a**). However, for $\nu = 0.3$, the plane strain solution shows higher stress concentrations at locations $\theta = 0, \pi$ (**Figure 10b**) with a maximum value of 3.7728 corresponding to the maximum value for the plane stress solution 3.3481 (see **Table 4**). Overall, the minimum stress concentrations at $\theta = \pi/2$ approach -2 (due to stress interference effects between the central hole and its surrounding 4 holes). The maximum stress concentration at $\theta = 0, \pi$ is decreased from 3 (for a single hole with $\nu = 0$, **Figure 9a**) to 2.9695 (for 5-holes with $\nu = 0$, **Figure 10a**).

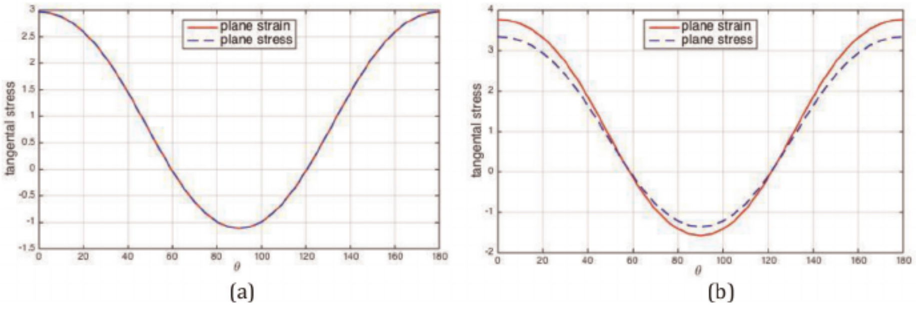

(a) (b)

Figure 10.
Tangential stress concentration variations around the rim of the central hole in a 5-hole problem (case 2–2). (a) Poisson's ratio $\nu = 0.0$, and (b) $\nu = 0.3$.

Poisson's ratio ν [−]	**Plane strain**		**Plane stress**	
	$\max\limits_{0\le\theta\le\pi}(\sigma_\theta)$	$\min\limits_{0\le\theta\le\pi}(\sigma_\theta)$	$\max\limits_{0\le\theta\le\pi}(\sigma_\theta)$	$\min\limits_{0\le\theta\le\pi}(\sigma_\theta)$
−0.5	3.2441	−1.0121	3.7877	−1.2170
−0.4	3.1534	−1.0876	3.4125	−1.1344
−0.3	3.0738	−1.0782	3.1783	−1.0913
−0.2	3.0102	−1.0765	3.0396	−1.0762
−0.1	2.9706	−1.0859	2.9735	−1.0842
0.0	2.9695	−1.1135	2.9695	−1.1135
0.1	3.0356	−1.1725	3.0255	−1.6531
0.2	3.2361	−1.2948	3.1469	−1.2435
0.3	3.7728	−1.5748	3.3481	−1.3559
0.4	5.6541	−2.4860	3.6577	−1.5167
0.5	INF	-INF	3.1310	−1.7523

Table 4.
Maximum and minimum tangential stress (σ_θ) around the rim of the central hole in a 5-hole problem (case 2–2) corresponding to different values of Poisson's ratio ν. The max of σ_θ occurs at $\theta = 0$ and π. The minimum of σ_θ is at $\theta = \frac{\pi}{2}$.

Figure 11a and **b** include the prior solutions for the same 5-hole problem configuration using a numerical solution method in ref. [11] and Laurent series method in ref. [31]. Unfortunately, the Poisson's ratio is not specified by either [11] or [31]; neither was the boundary condition made explicit. However, **Figure 11a** shows that the plane strain solution is closer to [11, 31] results than the plane stress for $\nu = 0.3$, and for $\nu = 0.4$, the plane stress solution is closer than the plane strain. As for the photoelastic comparison of Case 2–1, the prototype used in Case 2–2 has finite lateral width, due to which the LSM for a similar domain but based on an infinite plate solution will be progressively mismatching.

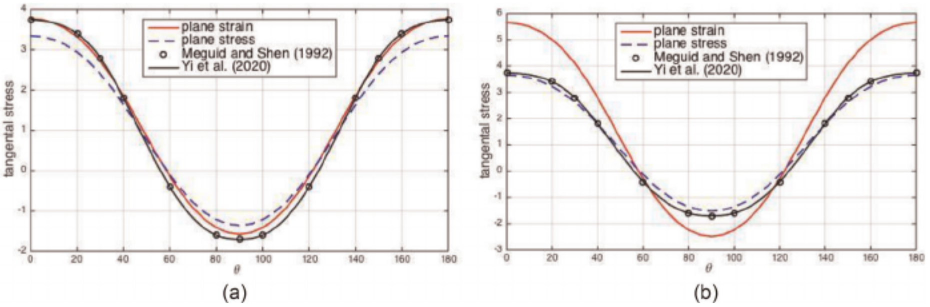

Figure 11.
Comparison of the stress concentrations around the rim of the central hole in a 5-hole problem (case 2–2) using (1) LSM solutions (red line for plane strain and blue line for plane stress boundary conditions) and (2) the prior solutions for the same 5-hole problem configuration using a numerical solution method [11] (solid black line) and Laurent series method [31] (black circles). (a) Poisson's ratio $\nu = 0.3$, and (b) $\nu = 0.4$.

5. Discussion

Usually, convenient simplifications are adopted when we develop mathematical descriptions of a physical process, such as the elastic displacements due to boundary forces and internal discontinuities such as circular cylindrical perforations. Examples are the description of two extreme types of boundary conditions—plane stress (thin-plate approach) and plane strain (thick-plate approach).

In spite of these model simplifications, the results of the computations based on the thin- and thick-plate approaches are routinely used in many practical applications. However, the disparities between the model results and actual displacements in the natural prototype can rarely be evaluated in detail, but some theoretical extrapolations are still possible (see ref. [10] for some experimental methods).

The present study documents a careful evaluation of the delta's arising in resulting stress concentrations due to a prototype that would behave like a thick medium (plane strain boundary conditions) but is treated with a plane stress boundary condition solution (thin-plate medium). This treatment is basically due to applying Kirsch [1] solutions to quantify the stress concentration on the rim of the hole in a thick plate (where, σ_{zz} is locally zero likewise everywhere in the thin-plate case). Such loose application of boundary constraints routinely occurs in wellbore stability problems, as detailed in this paper.

This paper specifically discussed the relevance of our findings for borehole stability studies. Traditionally, wellbore stability computations are based on analytical solutions [1] for stresses near a hole in an elastic plate. The Kirsch [1] solution is valid for a plane stress boundary condition; this is a so-called thin-plate solution $\left(\frac{a}{h} \rightarrow \infty\right)$, for which everywhere $\sigma_{zz} = 0$. The opposite end of the spectrum is a plane strain boundary condition (*i.e.*, $\varepsilon_{zz} = 0$) or a thick plate $\left(\frac{a}{h} \rightarrow 0\right)$ approach, where σ_{zz} is locally zero but in places may be either larger or smaller than zero, as has been quantified in Appendix C of our study. In our present study, we quantified, σ_{zz}, spatially everywhere normal to both a thick plate and thin plate with thickness $2h$, perforated by either single or multiple hole(s) of typical hole radius a (see Appendix C). Solutions were also given for cases with internal pressure loading.

According to the new results presented in our study, after evaluating the stress concentrations and transverse σ_{zz} for the perfect plane strain case $\left(\frac{a}{h} \rightarrow 0\right)$ not only at the rim of the holes but everywhere in a finite domain around the hole(s), we can confirm that even for the most extreme case of plane strain (as opposed to plane stress, $\frac{a}{h} \rightarrow \infty$) where σ_z vanishes in all locations, the difference between the respective solutions remains minimal.

6. Conclusion

Our study articulates that, in fact, any real elastic medium with a finite thickness, for cases involving circular cylindrical holes (single or multiple), will behave in a way intermediate between the plane stress and plane strain end members. We have resorted to [14] scalar $\frac{a}{h}$ as a very useful metric to estimate where the real prototype with finite thickness occurs between the end-member solutions. For $\frac{a}{h} \ll 1$ and $\frac{a}{h} \rightarrow 0$, we have tiny holes in a very thick plate. Many prototypes of stress concentrations near boreholes in the geological subsurface will be adequately described by the plane strain boundary condition. For $\frac{a}{h} \gg 1$ and $\frac{a}{h} \rightarrow \infty$, we have large holes in a very thin plate, for which prototypes exist in riveted wing panels for airplanes. Of course, there exists an unlimited range of prototypes that fall somewhere in between the extremes, and $\frac{a}{h}$ provides a metric to estimate how far the solution remains separated from the two end members.

Several specific cases have been analyzed in our study and we have quantified the delta of the displacements, strain, and stresses, as well as the Poisson's ratio for the two end-members (see Appendices to this study). Based on these specific cases, the following conclusions can be drawn (with emphasis on the delta's arising when applying either plane stress or plane strain approximate solutions):

- For multi-hole problems, we considered the 5-hole photo-elastic prototype shown in **Figure 4**. For this elastic prototype, the ratio between the holes' radii and the plate thickness is $\frac{a}{h} = 2$, which is theoretically closer to plane stress (thin plate) than to a plane strain (thick plate) boundary condition. The analytical LSM plane stress and plane strain solutions in **Figures 5–7**(b, c) along with the small deltas quantified in **Figure 5d** validate this theoretical deduction.

- We also analyzed the impact of the Poisson's ratio on the tangential stress concentrations around the central hole in a 5-hole problem surrounded by four symmetrically distributed circular holes (see **Figure 8**). We conclude that the plane strain solution is more sensitive to the Poisson's ratio than the plane stress solution. This different sensitivity increases the delta between plane strain and plane stress solutions for the tangential stress concentrations around the central hole when ν increases (**Figures 9** and **10**).

- The difference between the plane strain and plane stress solutions indicates that the prior solutions for the same 5-hole problem using a numerical solution method in ref. [11] and Laurent series method in ref. [31] were most likely for the plane strain boundary condition with $\nu = 0.3$, or possibly for plane stress with $\nu = 0.4$ (see **Figure 11**).

- For holes subjected to an internal pressure only, there is no delta between the plane stress and plane strain solutions of the principal stress distributions σ_1 and σ_2; the displacement fields will remain identical for both cases (see **Figure 2**).

- For a combination of far-field stress and the internal hole pressure, the displacements due to the internal pressure on the hole add lateral uniform volumetric displacements, effectively shifting the locations where the deltas occur (see **Figure 3**).

In a more general sense, the following was observed:

- Stress concentrations near tiny holes in a very thick plate approach the solution of plane stress boundary condition.

- Stress concentrations near large holes in a very thin plate approach the solution of plane strain boundary condition.

- For most practical cases, the response will be intermediate between the plane stress and plane strain end members, depending on the relative dimensions of the plate thickness and hole diameter.

- For holes subjected to an internal pressure only, there is no difference between the plane stress (thin-plate solution) and plane strain solutions (thick-plate solutions)

- For cases with far-field stress, the plane strain solution is more sensitive to the Poisson's ratio than the plane stress solution.

Acknowledgements

This research did not receive any specific grant from funding agencies in the public, commercial, or not-for-profit sectors. However, the authors acknowledge the generous support provided by the Department of Mathematics and the College of Petroleum Engineering & Geosciences (CPG) at King Fahd University of Petroleum & Minerals (KFUPM).

A. Validate the computational integrity of the plane strain displacement solutions of Section 2.2 using the plane stress solutions of Section 2.3

The plane strain solution, Eqs. (5) and (6), can be obtained directly from the plane stress solution, Eqs. (9) and (10), by replacing E with $E/(1-v^2)$, and v with $v/(1-v)$ as follows:

Starting from the stress solution given by Eq. (9)

$$u_r = \sigma_{xx-\infty}\left(\frac{1+v}{2Er}\right)\left\{\frac{1-v}{1+v}r^2 + a^2 + \left(\frac{4a^2}{1+v} + r^2 - \frac{a^4}{r^2}\right)\cos 2\theta\right\} \tag{A1}$$

and applying the above replacements we get

$$\begin{aligned} u_r &= \sigma_{xx-\infty}\left(\frac{1+\left(\frac{v}{1-v}\right)}{2\left(\frac{E}{1-v^2}\right)r}\right)\left\{\frac{1-\left(\frac{v}{1-v}\right)}{1+\left(\frac{v}{1-v}\right)}r^2 + a^2 + \left(\frac{4a^2}{1+\left(\frac{v}{1-v}\right)} + r^2 - \frac{a^4}{r^2}\right)\cos 2\theta\right\} \\ &= \sigma_{xx-\infty}\left(\frac{1+v}{2Er}\right)\left\{(1-2v)r^2 + a^2 + \left(4a^2(1-v) + r^2 - \frac{a^4}{r^2}\right)\cos 2\theta\right\} \\ &= \sigma_{xx-\infty}\left(\frac{1+v}{2Er}\right)\left\{r^2(1-2v+\cos 2\theta) + a^2\left[1 + \left(4(1-v) - \frac{a^2}{r^2}\right)\cos 2\theta\right]\right\} \end{aligned} \tag{A2}$$

Eq. (A2) represents the plan strain solution as given by Eq. (5). Similarly, one can obtain Eq. (6) from (10) using the same modification.

B. Converting the polar coordinate of the displacement field to the cartesian coordinate

B.1 Plane strain solution

Recall the plane strain solution for the hole with uniaxial far-field stress given by Eqs. (5) and (6)

$$u_r = \sigma_{xx-\infty}\left(\frac{1+v}{2Er}\right)\left\{r^2(1-2v+\cos 2\theta) + a^2\left[1+\left(4(1-v)-\frac{a^2}{r^2}\right)\cos 2\theta\right]\right\} \tag{B1}$$

$$u_\theta = -\sigma_{xx-\infty}\left(\frac{1+v}{2Er}\right)\left[r^2 + a^2\left(2(1-2v)+\frac{a^2}{r^2}\right)\right]\sin 2\theta \tag{B2}$$

Applying equations Eqs. (5) and (6) into

$$u_x = u_r\cos\theta - u_\theta\sin\theta, \quad u_y = u_r\sin\theta + u_\theta\cos\theta$$

we get,

$$\begin{aligned} u_x = {} & \left[\sigma_{xx-\infty}\left(\frac{1+v}{2Er}\right)\left\{r^2(1-2v+\cos 2\theta)\right\}\right] + a^2\left[1+\left(4(1-v)-\frac{a^2}{r^2}\right)\cos 2\theta\right]\cos\theta \\ & - \left[-\sigma_{xx-\infty}\left(\frac{1+v}{2Er}\right)\left[r^2 + a^2\left(2(1-2v)+\frac{a^2}{r^2}\right)\right]\sin 2\theta\right]\sin\theta \end{aligned} \tag{B3}$$

$$\begin{aligned} u_y = {} & \left[\sigma_{xx-\infty}\left(\frac{1+v}{2Er}\right)\left\{r^2(1-2v+\cos 2\theta)\right\}\right] \\ & + a^2\left[1+\left(4(1-v)-\frac{a^2}{r^2}\right)\cos 2\theta\right]\sin\theta \\ & + \left[-\sigma_{xx-\infty}\left(\frac{1+v}{2Er}\right)\left[r^2 + a^2\left(2(1-2v)+\frac{a^2}{r^2}\right)\right]\sin 2\theta\right]\cos\theta \end{aligned} \tag{B4}$$

Simplify Eqs. (B3) and (B4) and make use of the straightforward coordinate transformation formula:

$$x = r\cos\theta, \quad y = r\sin\theta, \quad r^2 = x^2 + y^2$$

to get the following

i. Before replacing $r^2 = x^2 + y^2$

$$\begin{aligned} u_x = {} & \sigma_{xx-\infty}\left(\frac{1+v}{2Er}\right)\Bigg\{\left[r^2\left(1-2v+\frac{x^2-y^2}{r^2}\right) + a^2\left[1+\left(4(1-v)-\frac{a^2}{r^2}\right)\frac{x^2-y^2}{r^2}\right]\right]\frac{x}{r} \\ & + \left[\left[r^2 + a^2\left(2(1-2v)+\frac{a^2}{r^2}\right)\right]\frac{2xy}{r^2}\right]\frac{y}{r}\Bigg\} \\ = {} & \sigma_{xx-\infty}\left(\frac{1+v}{2E}\right)\Bigg\{\Bigg[r^2(1-2v) + x^2 - y^2 + a^2 + 4a^2(1-v)\left(\frac{x^2-y^2}{r^2}\right) \\ & - a^4\left(\frac{x^2-y^2}{r^4}\right)\Bigg]\frac{x}{r^2} + \left[2xy + (1-2v)\left(\frac{4a^2xy}{r^2}\right) + \frac{2a^4xy}{r^4}\right]\frac{y}{r^2}\Bigg\} \end{aligned} \tag{B5}$$

$$
\begin{aligned}
u_y = {} & \sigma_{xx-\infty}\left(\frac{1+v}{2Er}\right)\Bigg\{\Bigg[r^2\left(1-2v+\frac{x^2-y^2}{r^2}\right)+a^2\left[1+\left(4(1-v)-\frac{a^2}{r^2}\right)\frac{x^2-y^2}{r^2}\right]\Bigg]\frac{y}{r} \\
& -\Bigg[\Bigg[r^2+a^2\left(2(1-2v)+\frac{a^2}{r^2}\right)\Bigg]\frac{2xy}{r^2}\Bigg]\frac{x}{r}\Bigg\} \\
= {} & \sigma_{xx-\infty}\left(\frac{1+v}{2E}\right)\Bigg\{\Bigg[r^2(1-2v)+x^2-y^2+a^2+4a^2(1-v)\left(\frac{x^2-y^2}{r^2}\right) \\
& -a^4\left(\frac{x^2-y^2}{r^4}\right)\Bigg]\frac{y}{r^2}-\left[2xy+(1-2v)\left(\frac{4a^2xy}{r^2}\right)+\frac{2a^4xy}{r^4}\right]\frac{x}{r^2}\Bigg\} \qquad \text{(B6)}
\end{aligned}
$$

ii. After replacing $r^2 = x^2 + y^2$

$$
\begin{aligned}
u_x = {} & \sigma_{xx-\infty}\left(\frac{1+v}{2E}\right)\Bigg\{\Bigg[(x^2+y^2)(1-2v)+x^2-y^2+a^2+4a^2(1-v)\left(\frac{x^2-y^2}{x^2+y^2}\right) \\
& -a^4\left(\frac{x^2-y^2}{(x^2+y^2)^2}\right)\Bigg]\left(\frac{x}{x^2+y^2}\right)+\left[2xy+(1-2v)\left(\frac{4a^2xy}{x^2+y^2}\right)+\frac{2a^4xy}{(x^2+y^2)^2}\right]\left(\frac{y}{x^2+y^2}\right)\Bigg\}
\end{aligned}
\qquad \text{(B7)}
$$

$$
\begin{aligned}
u_y = {} & \sigma_{xx-\infty}\left(\frac{1+v}{2E}\right)\Bigg\{\Bigg[(x^2+y^2)(1-2v)+x^2-y^2+a^2+4a^2(1-v)\left(\frac{x^2-y^2}{x^2+y^2}\right) \\
& -a^4\left(\frac{x^2-y^2}{(x^2+y^2)^2}\right)\Bigg]\left(\frac{y}{x^2+y^2}\right)-\left[2xy+(1-2v)\left(\frac{4a^2xy}{x^2+y^2}\right)+\frac{2a^4xy}{(x^2+y^2)^2}\right]\left(\frac{x}{x^2+y^2}\right)\Bigg\}
\end{aligned}
\qquad \text{(B8)}
$$

B.2 Delta between plane strain and plane stress solutions

Applying equations Eqs. (11) and (12) into

$$
u_x = u_r\cos\theta - u_\theta\sin\theta, \quad u_y = u_r\sin\theta + u_\theta\cos\theta
$$

we get

$$
\begin{aligned}
u_x = {} & \left(-\sigma_{xx-\infty}\left(\frac{v^2}{Er}\right)(r^2+2a^2\cos 2\theta)\right)\cos\theta-\left(\sigma_{xx-\infty}\left(\frac{v^2}{Er}\right)(2a^2\sin 2\theta)\right)\sin\theta \\
= {} & -\sigma_{xx-\infty}\left(\frac{v^2}{Er}\right)[(r^2+2a^2\cos 2\theta)\cos\theta+(2a^2\sin 2\theta)\sin\theta] \\
= {} & -\sigma_{xx-\infty}\left(\frac{v^2}{E(x^2+y^2)}\right)\left[\left(x^2+y^2+2a^2\frac{x^2-y^2}{x^2+y^2}\right)x+\left(4a^2\frac{xy}{x^2+y^2}\right)y\right] \qquad \text{(B9)}
\end{aligned}
$$

and

$$
\begin{aligned}
u_y &= \left(-\sigma_{xx-\infty}\left(\frac{v^2}{Er}\right)(r^2+2a^2\cos 2\theta)\right)\sin\theta + \left(\sigma_{xx-\infty}\left(\frac{v^2}{Er}\right)(2a^2\sin\ 2\theta)\right)\cos\theta \\
&= -\sigma_{xx-\infty}\left(\frac{v^2}{Er}\right)[(r^2+2a^2\cos 2\theta)\sin\theta-(2a^2\sin\ 2\theta)\cos\theta] \\
&= -\sigma_{xx-\infty}\left(\frac{v^2}{E(x^2+y^2)}\right)\left[\left(x^2+y^2+2a^2\frac{x^2-y^2}{x^2+y^2}\right)y-\left(4a^2\frac{xy}{x^2+y^2}\right)x\right] \qquad \text{(B10)}
\end{aligned}
$$

We, also, can obtain Eqs. (B9) and (B10) by subtracting the Cartesian equations of the plane strain and the plane stress as follows:

$$
\begin{aligned}
u_x = {} & \sigma_{xx-\infty}\left(\frac{1+v}{2E}\right)\Bigg\{\Bigg[(x^2+y^2)(1-2v)+x^2-y^2+a^2+4a^2(1-v)\left(\frac{x^2-y^2}{x^2+y^2}\right) \\
& -a^4\left(\frac{x^2-y^2}{(x^2+y^2)^2}\right)\Bigg]\left(\frac{x}{x^2+y^2}\right)+\left[2xy+(1-2v)\left(\frac{4a^2xy}{x^2+y^2}\right)+\frac{2a^4xy}{(x^2+y^2)^2}\right]\left(\frac{y}{x^2+y^2}\right)\Bigg\} \\
& -\sigma_{xx-\infty}\left(\frac{1+v}{2E}\right)\Bigg\{\left[\frac{1-v}{1+v}(x^2+y^2)+a^2+\left(\frac{4a^2}{1+v}+x^2+y^2-\frac{a^4}{x^2+y^2}\right)\left(\frac{x^2-y^2}{x^2+y^2}\right)\right] \\
& \times\left(\frac{x}{x^2+y^2}\right)+\left[\left(\frac{1-v}{1+v}2a^2+x^2+y^2+\frac{a^4}{x^2+y^2}\right)\left(\frac{2xy}{x^2+y^2}\right)\right]\left(\frac{y}{x^2+y^2}\right)\Bigg\}
\end{aligned}
$$

$$
\begin{aligned}
= {} & \sigma_{xx-\infty}\left(\frac{1+v}{2E}\right)\Bigg\{\Bigg[(x^2+y^2)(1-2v)+x^2-y^2+a^2+4a^2(1-v)\left(\frac{x^2-y^2}{x^2+y^2}\right) \\
& -a^4\left(\frac{x^2-y^2}{(x^2+y^2)^2}\right)\Bigg]\left(\frac{x}{x^2+y^2}\right)+\left[2xy+(1-2v)\left(\frac{4a^2xy}{x^2+y^2}\right)+\frac{2a^4xy}{(x^2+y^2)^2}\right]\left(\frac{y}{x^2+y^2}\right) \\
& -\left[\frac{1-v}{1+v}(x^2+y^2)+a^2+\left(\frac{4a^2}{1+v}+x^2+y^2-\frac{a^4}{x^2+y^2}\right)\left(\frac{x^2-y^2}{x^2+y^2}\right)\right]\left(\frac{x}{x^2+y^2}\right) \\
& -\left[\left(\frac{1-v}{1+v}2a^2+x^2+y^2+\frac{a^4}{x^2+y^2}\right)\left(\frac{2xy}{x^2+y^2}\right)\right]\left(\frac{y}{x^2+y^2}\right)\Bigg\}
\end{aligned}
$$

$$
\begin{aligned}
= {} & \sigma_{xx-\infty}\left(\frac{1+v}{2E}\right)\Bigg\{\Bigg[(x^2+y^2)\left(1-2v-\frac{1-v}{1+v}\right)+x^2-y^2-(x^2+y^2)\left(\frac{x^2-y^2}{x^2+y^2}\right) \\
& +a^2-a^2+4a^2(1-v)\left(\frac{x^2-y^2}{x^2+y^2}\right)-a^4\left(\frac{x^2-y^2}{(x^2+y^2)^2}\right)+\left(\frac{a^4}{x^2+y^2}\right)\left(\frac{x^2-y^2}{x^2+y^2}\right) \\
& -\left(\frac{4a^2}{1+v}\right)\left(\frac{x^2-y^2}{x^2+y^2}\right)\Bigg]\left(\frac{x}{x^2+y^2}\right)+\Bigg[2xy-(x^2+y^2)\left(\frac{2xy}{x^2+y^2}\right)+(1-2v)\left(\frac{4a^2xy}{x^2+y^2}\right) \\
& -\frac{1-v}{1+v}2a^2\left(\frac{2xy}{x^2+y^2}\right)+\frac{2a^4xy}{(x^2+y^2)^2}-\left(\frac{a^4}{x^2+y^2}\right)\left(\frac{2xy}{x^2+y^2}\right)\Bigg]\left(\frac{y}{x^2+y^2}\right)\Bigg\}
\end{aligned}
$$

$$= \sigma_{xx\,-\infty}\left(\frac{1+v}{2E}\right)\left\{\left[\left(x^2+y^2\right)\left(1-2v-\frac{1-v}{1+v}\right)+4a^2\left(1-v-\frac{1}{1+v}\right)\left(\frac{x^2-y^2}{x^2+y^2}\right)\right]\right.$$

$$\left.\left(\frac{x}{x^2+y^2}\right)+\left[(1-2v)\left(\frac{4a^2xy}{x^2+y^2}\right)-\frac{1-v}{1+v}2a^2\left(\frac{2xy}{x^2+y^2}\right)\right]\left(\frac{y}{x^2+y^2}\right)\right\}$$

$$= \sigma_{xx\,-\infty}\left(\frac{1+v}{2E}\right)\left\{\left[\left(x^2+y^2\right)\left(1-2v-\frac{1-v}{1+v}\right)\right.\right.$$

$$\left.+4a^2\left(1-v-\frac{1}{1+v}\right)\left(\frac{x^2-y^2}{x^2+y^2}\right)\right]\left(\frac{x}{x^2+y^2}\right)$$

$$\left.+\left[\left(1-2v-\frac{1-v}{1+v}\right)\left(\frac{4a^2xy}{x^2+y^2}\right)\right]\left(\frac{y}{x^2+y^2}\right)\right\}$$

$$= \sigma_{xx\,-\infty}\left(\frac{1+v}{2E}\right)\left\{\left[\left(x^2+y^2\right)\left(\frac{1+v-2v-2v^2-1+v}{1+v}\right)\right.\right.$$

$$\left.+\,4a^2\left(\frac{1+v-v-v^2-1}{1+v}\right)\left(\frac{x^2-y^2}{x^2+y^2}\right)\right]\left(\frac{x}{x^2+y^2}\right)$$

$$\left.+\left[\left(\frac{1+v-2v-2v^2-1+v}{1+v}\right)\left(\frac{4a^2xy}{x^2+y^2}\right)\right]\left(\frac{y}{x^2+y^2}\right)\right\}$$

$$= \sigma_{xx\,-\infty}\left(\frac{1+v}{2E}\right)\left\{\left[\left(x^2+y^2\right)\left(\frac{-2v^2}{1+v}\right)+4a^2\left(\frac{-v^2}{1+v}\right)\left(\frac{x^2-y^2}{x^2+y^2}\right)\right]\left(\frac{x}{x^2+y^2}\right)\right.$$

$$\left.+\left[\left(\frac{-2v^2}{1+v}\right)\left(\frac{4a^2xy}{x^2+y^2}\right)\right]\left(\frac{y}{x^2+y^2}\right)\right\}$$

$$= \sigma_{xx\,-\infty}\left(\frac{-2v^2}{2E}\right)\left\{\left[\left(x^2+y^2\right)+2a^2\left(\frac{x^2-y^2}{x^2+y^2}\right)\right]\left(\frac{x}{x^2+y^2}\right)+\left[\left(\frac{4a^2xy}{x^2+y^2}\right)\right]\left(\frac{y}{x^2+y^2}\right)\right\}$$

$$= -\sigma_{xx-\infty}\left(\frac{v^2}{E\left(x^2+y^2\right)}\right)\left\{\left[\left(x^2+y^2\right)+2a^2\left(\frac{x^2-y^2}{x^2+y^2}\right)\right]x+\left[\left(\frac{4a^2xy}{x^2+y^2}\right)\right]y\right\}$$

$$= \text{(B9)}$$

Following the same steps, we can obtain Eq. (B10).

C. Single hole analysis

Comprehensive results are given here for the vector displacement fields, strain tensor components, principal strains, stress tensor components, and principal stresses. The first column images are for plane strain; the second column images are for plane stress; and the third column quantifies the delta between plane strain and plane stress solutions. We will consider the three cases presented in Section 4.1 for the elastic plate model with a central single hole.

Case 1–1: a far-field stress only,
Case 1–2: an internal pressure only,
Case 1–3: the superposed Cases 1–1 and 1–2.

C.1 Single-hole subject to far-field stress (Case 1–1)

1. Displacement fields

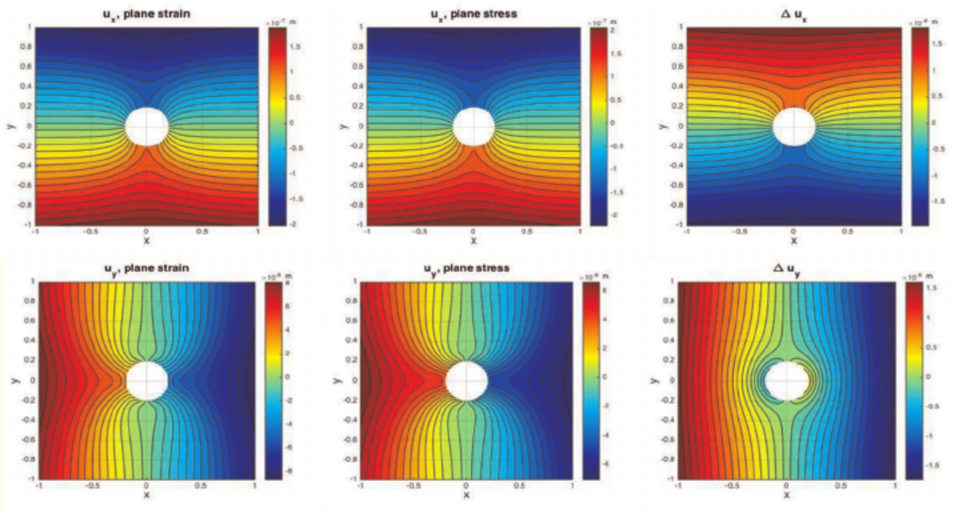

Figure C1.
Complete results of the elastic displacement solutions around single hole in an elastic plate subjected to far-field stress. First column is for the plan strain solution given by Eqs. (15) and (16). Second column is the plane stress solution given by Eqs. (17) and (18). Third column quantifies the delta (difference) between plane strain and plane stress solutions using Eqs. (25) and (26).

2. Strain tensor components.

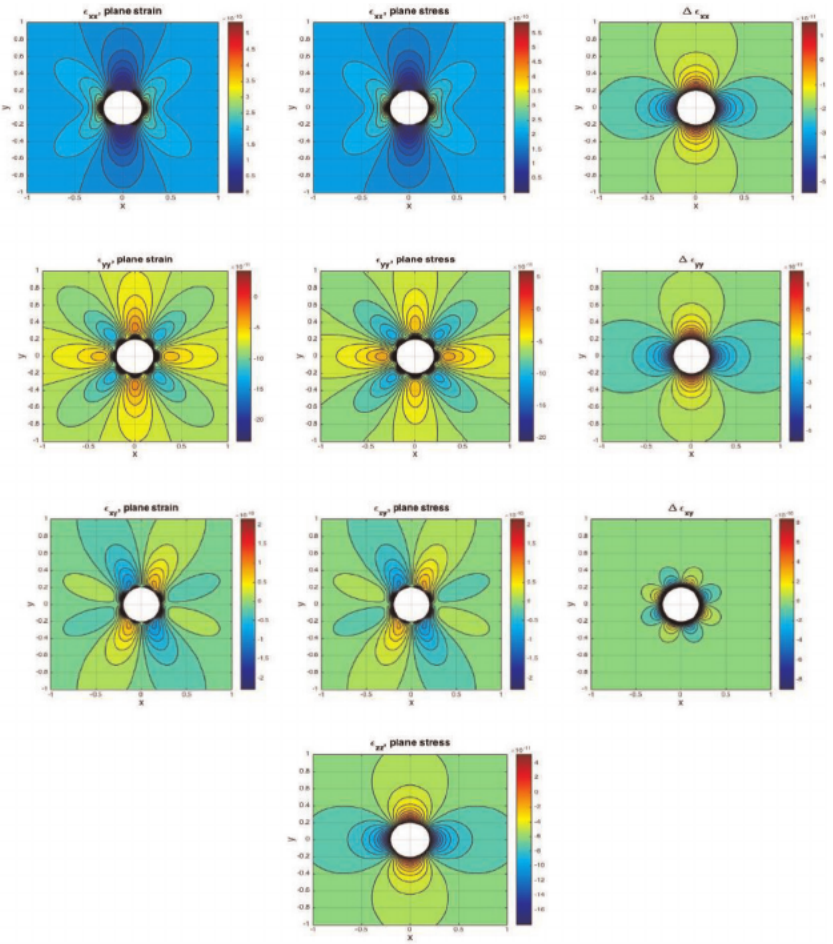

Figure C2.
Strain tensor components around the single hole in an elastic plate subjected to far-field stress. First column is for the plan strain solution. Second column is the plane stress solution. Third column quantifies the delta (difference) between plane strain and plane stress solutions. These solutions are obtained by analytical differentiation of the displacement components in ***Figure C1*** *in both x and y directions. See Eqs. (29)–(31) Note that* $\varepsilon_{zz} = 0$ *for the plane strain solution and therefore there is no delta in z−direction.*

3. Principal strains.

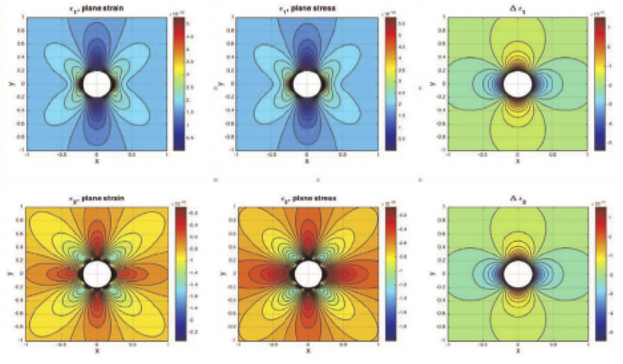

Figure C3.
Principles strains around the single hole in an elastic plate subjected to far-field stress. These solutions are obtained by applying Eq. (36) for the principal strain magnitude solution using the strain tensors in ***Figure C2****.*

4. Stress tensor components.

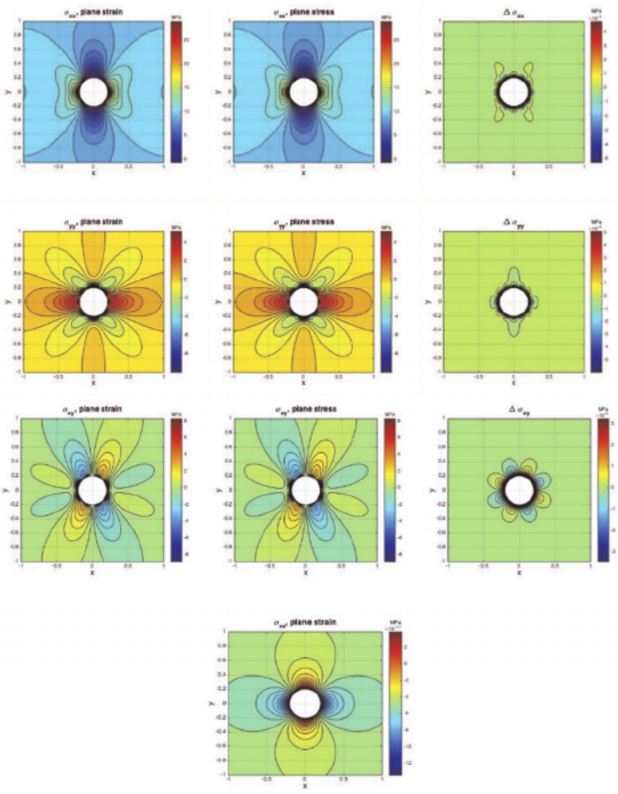

Figure C4.
Stress tensor components around the single hole in an elastic plate subjected to far-field stress. First column is for the plan strain solution. Second column is the plane stress solution. Third column quantifies the delta (difference) between plane strain and plane stress solutions. These solutions are obtained from the relations between the strain tensor components and the stress tensor components shown in Eqs. (32)–(34). Note that $\sigma_{zz} = 0$ for plane stress solution and therefore there is no delta in the $z-$direction.

5. Principal stresses.

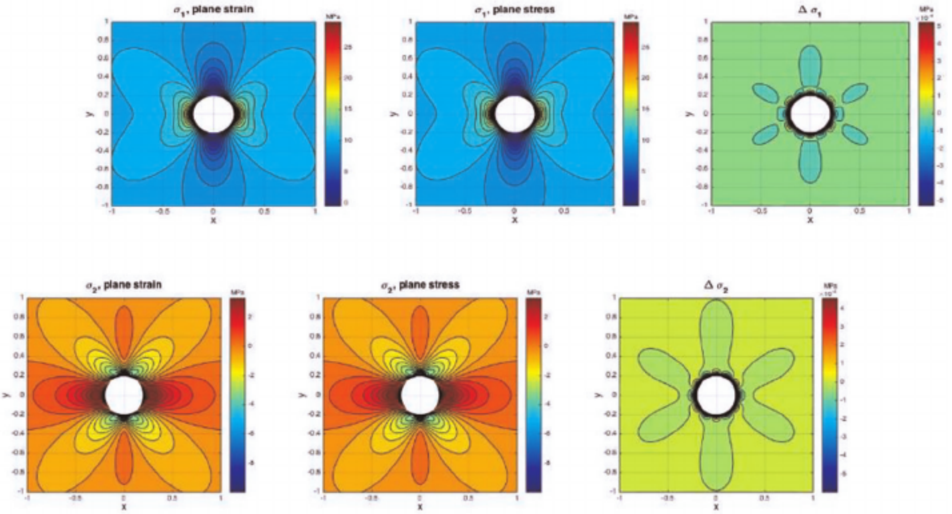

Figure C5.
*Principal stresses around the single hole in an elastic plate subjected to far-field stress. These solutions are obtained by applying Eqs. (37) and (38) using the tensor stress components in **Figures C4**.*

6. Displacement field with respect to different values of Poisson's ratio.

In **Figures C5** and **C6**, we show the impact of the Poisson's ratio on the plane strain and plane stress displacement considering the model Case 1–1 of the elastic plate with a single hole. The model inputs are fixed as given in **Table 1** except for the Poisson's ratio that takes three different values $\nu = 0, 0.2$, and 0.4. We can see from **Figure C6** the following results (as presented before in Case 2–2 results):

i. Displacements in the x-direction are insensitive to the value of ν in case of plane stress.

ii. Displacements in the x-direction are little bit sensitive to the value of ν in case of plane strain.

iii. Displacements in the y-direction are sensitive to the value of ν in both plane strain and plane stress.

Therefore, this impact will extend to the resulting plane strain and plane stress solutions for the strain and stress tensor components computed based on the displacement results. This impact can be also generalized to the model of the elastic plate with 5-holes presented in Case 2–2. **Tables 3** and **4** illustrate, numerically, the impact of Poisson's ratio on the maximum and minimum values of the tangential stress (σ_θ) around the rim of the central hole in model Case 1–1 and model Case 2–2, respectively.

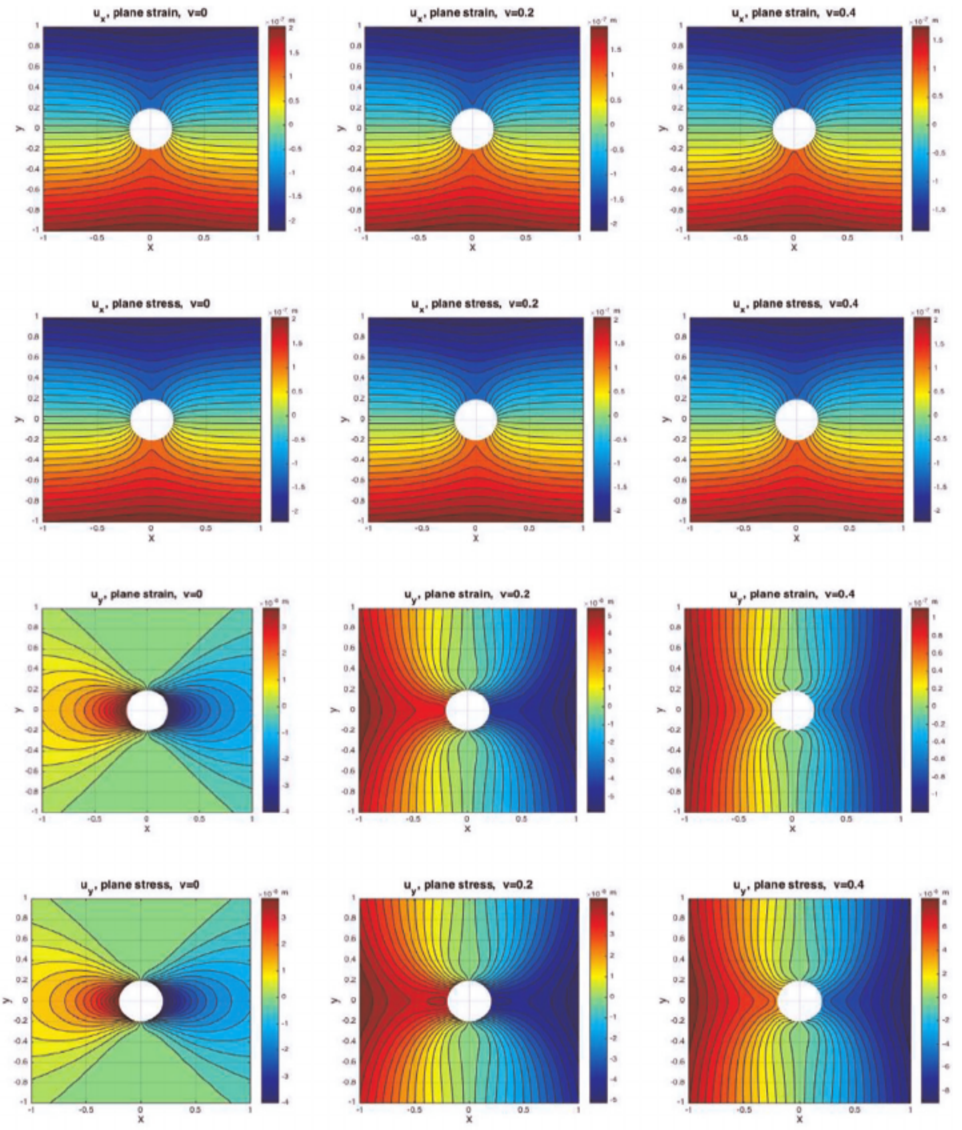

Figure C6.
The plane strain and plane stress displacement solutions against different values of Poisson's ratio: $\nu = 0$ first column, $\nu = 0.2$ second column, and $\nu = 0.4$ third column. The first two rows are for the displacement in $x-$direction and the last two rows are for the displacement in $y-$direction.

C.2 Single-hole subject to the internal hole pressure (Case 1–2)

1. Displacement fields.

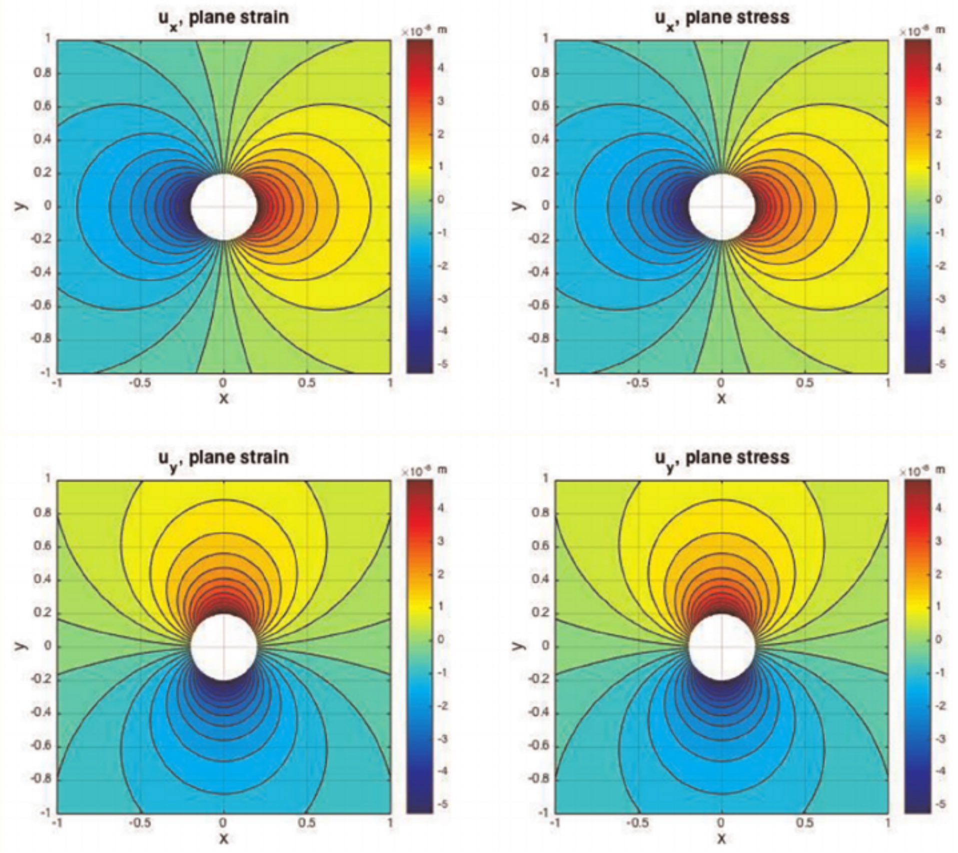

u_x, plane strain

u_x, plane stress

u_y, plane strain

u_y, plane stress

Figure C7.
*Complete results of the elastic displacement solutions around the single hole in an elastic plate subjected to internal pressure. First column is for the plan strain solution. Second column is the plane stress solution. In the case when the elastic plate is subjected to internal pressure only, the plane strain and plane stress are identical and given by Eqs. (27) and (28). Therefore, there is no delta in this case. As in Case1–1 input parameters are listed in **Table 1**.*

2. Strain tensor components.

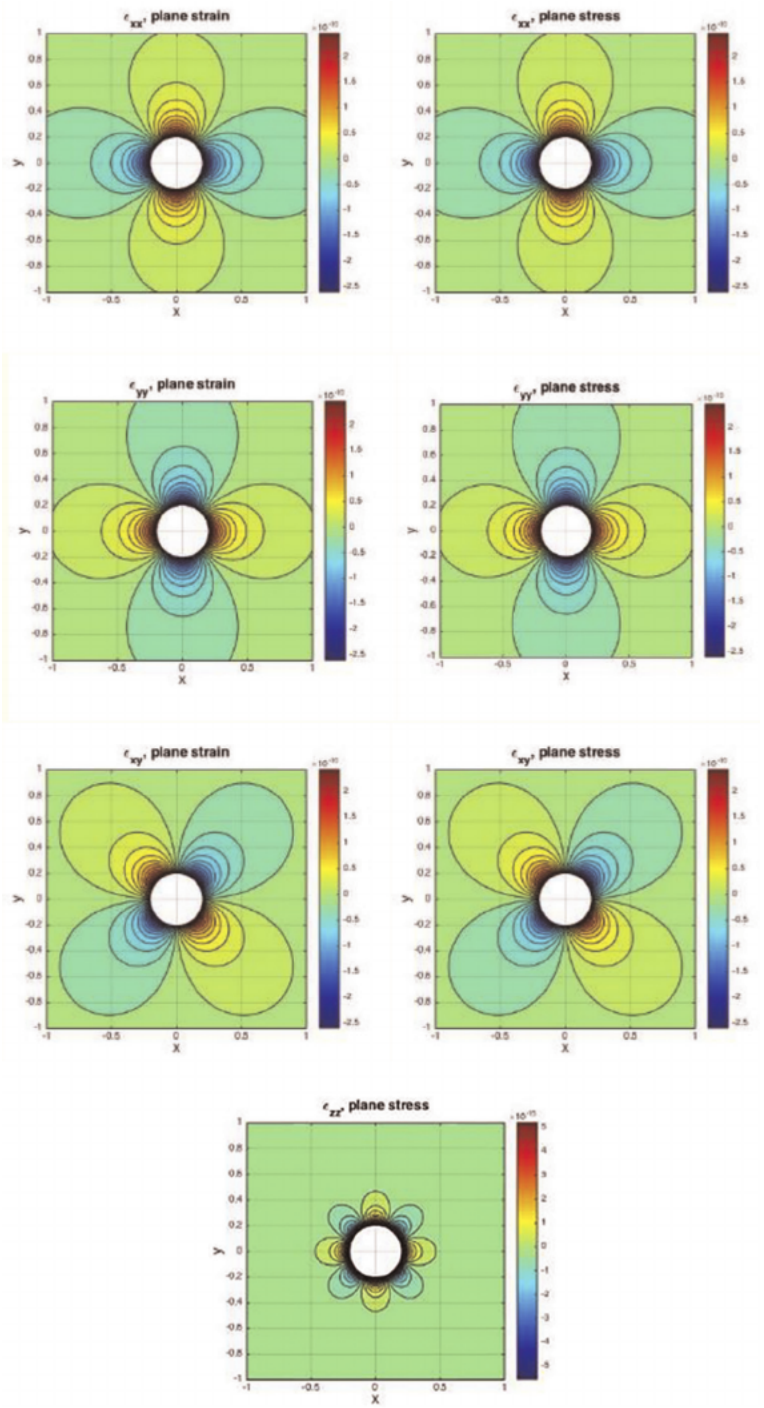

Figure C8.
*Strain tensor components around the single hole in an elastic plate subjected to internal pressure. First column is for the plan strain solution. Second column is the plane stress solution. These solutions are obtained by analytical differentiation of the displacement components in **Figure C7** in both x and y directions.*

3. Principal strains.

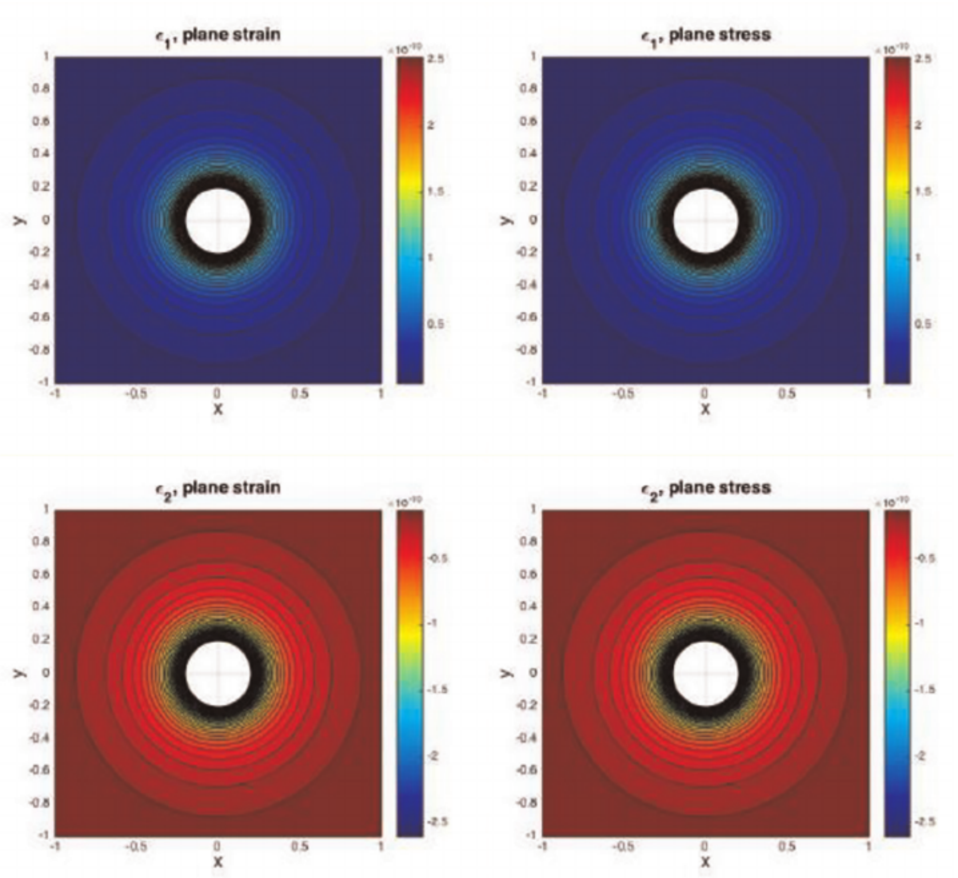

Figure C9.
*Principles strains around the single hole in an elastic plate subjected to internal pressure. These solutions are obtained by applying Eqs. (36) for the principal strain magnitude solution using the strain tensors in **Figure C8**.*

4. Stress tensor components.

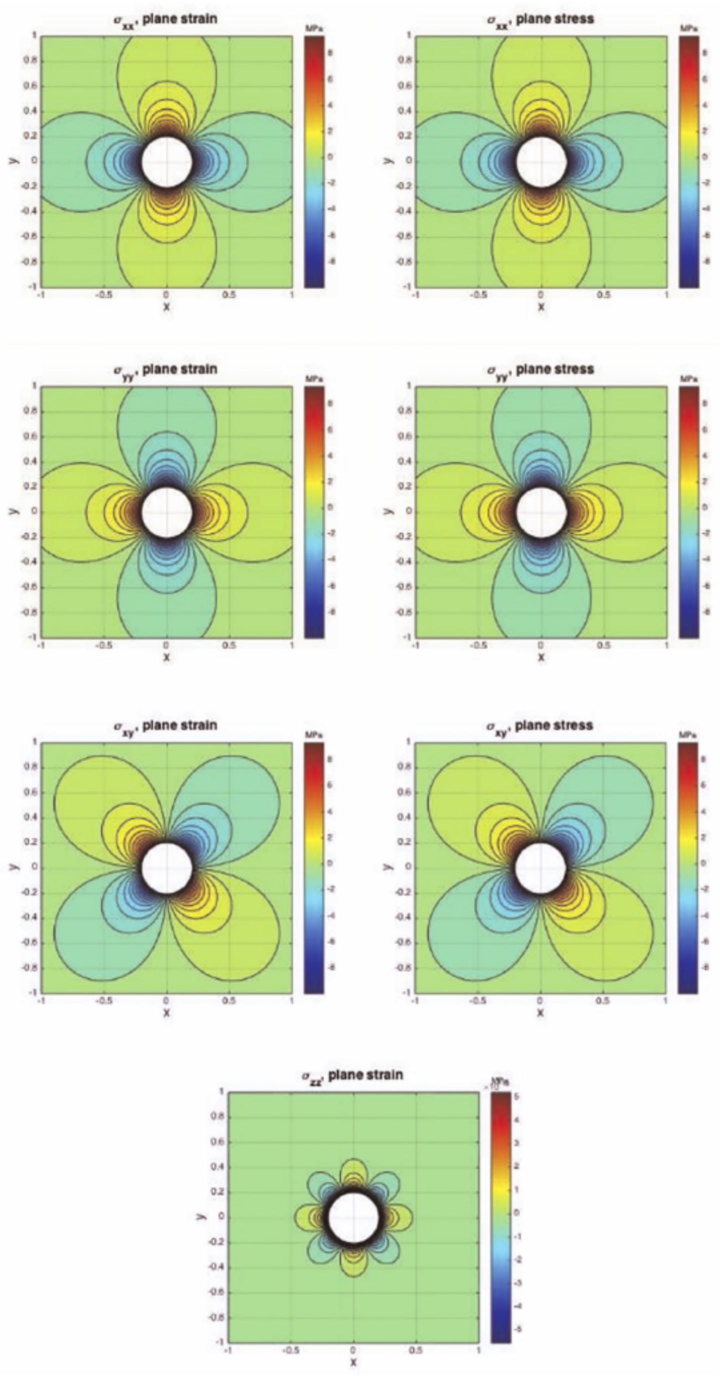

Figure C10.
Stress tensor components around the single hole in an elastic plate subjected to internal pressure. First column is for the plan strain solution. Second column is the plane stress solution. These solutions are obtained from the relations between the strain tensor components and the stress tensor components shown in Eqs. (32)–(34).

5. Principal stresses.

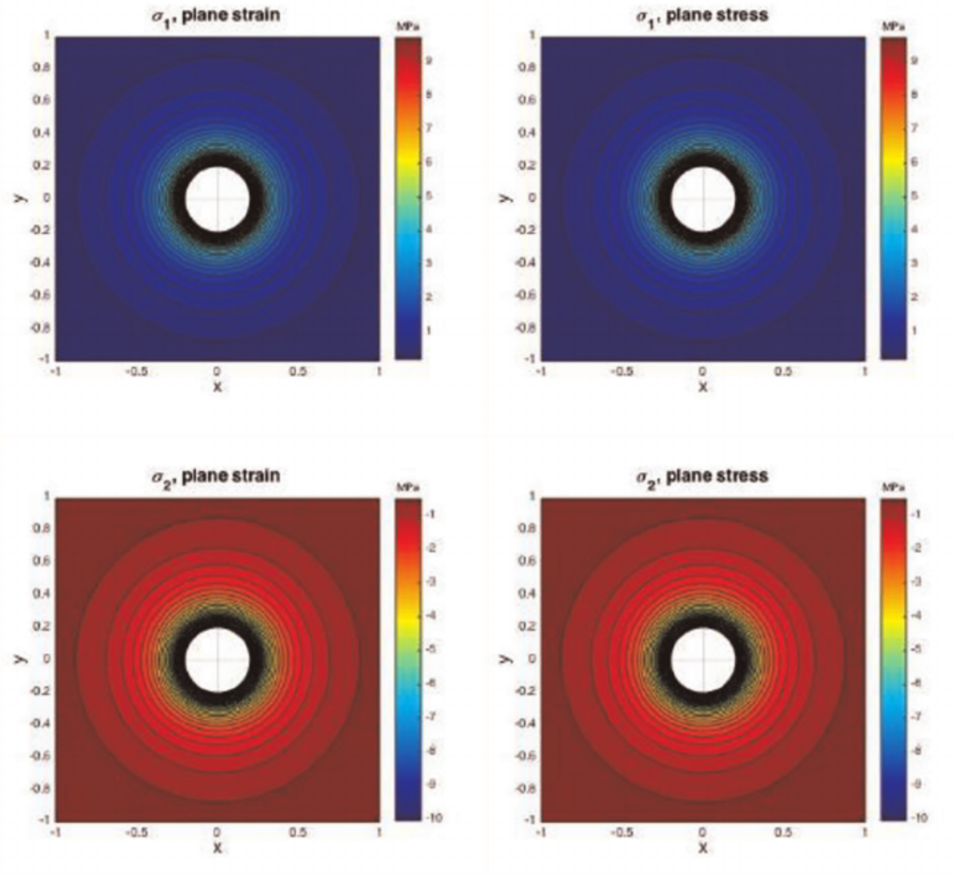

Figure C11.
*Principal stresses around the single hole in an elastic plate subjected to internal pressure. These solutions are obtained by applying Eqs. (37) and (38) using the tensor stress components in **Figure C10**.*

C.3 The superposed Cases 1–1 and 1–2 (Case 1–3)

In this section, we consider Case 1–3 of the superposed of Cases 1–1 and 1–2. The plane strain displacement solutions in both directions are the sum of Eqs. (15), (16) and (27), (28). Similarly, the plane stress displacement solutions in both directions are the sum of Eqs. (17) and (18) and (27), (28). The strain tensor components, principal strains, stress tensor components, and principal stresses will be computed accordingly. As in the results of the previous two cases, the first column images are for plane strain; the second column images are for plane stress; and the third column quantifies the delta between plane strain and plane stress solutions.

1. Displacement fields.

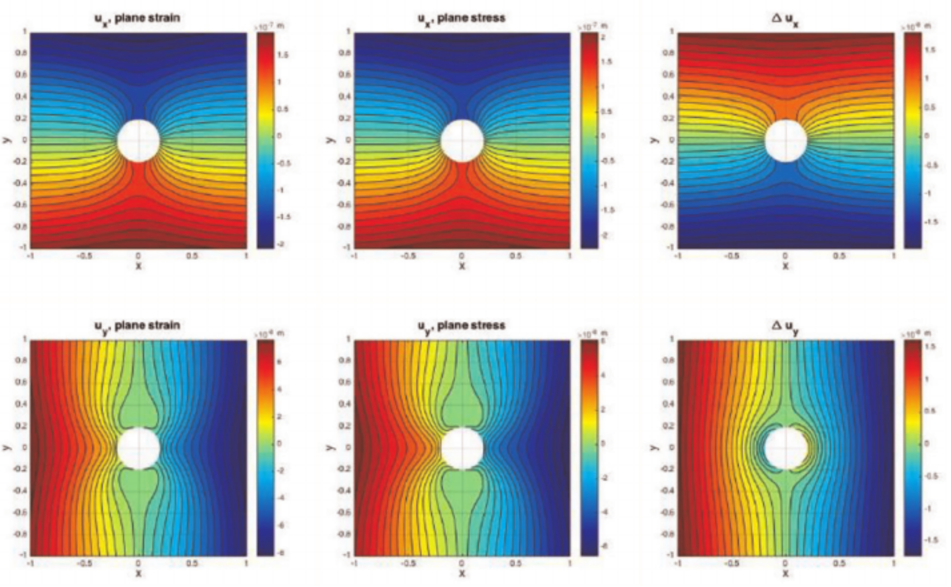

Figure C12.
*The elastic displacement solutions around the single hole in an elastic plate subjected to both far-field stress and internal pressure. First column is for the plan strain solution, which is the sum of the results in the first column of **Figures C1** and **C7**. Second column is the plane stress solution, which is the sum of the results in the second column of **Figures C1** and **C7**. Third column quantifies the delta between plane stress and plane strain solutions. Since there is no displacement difference corresponding to the internal pressure effect, the deltas presented in the third column of this figure are identical to those in the third column of **Figures C1**.*

2. Strain tensor components.

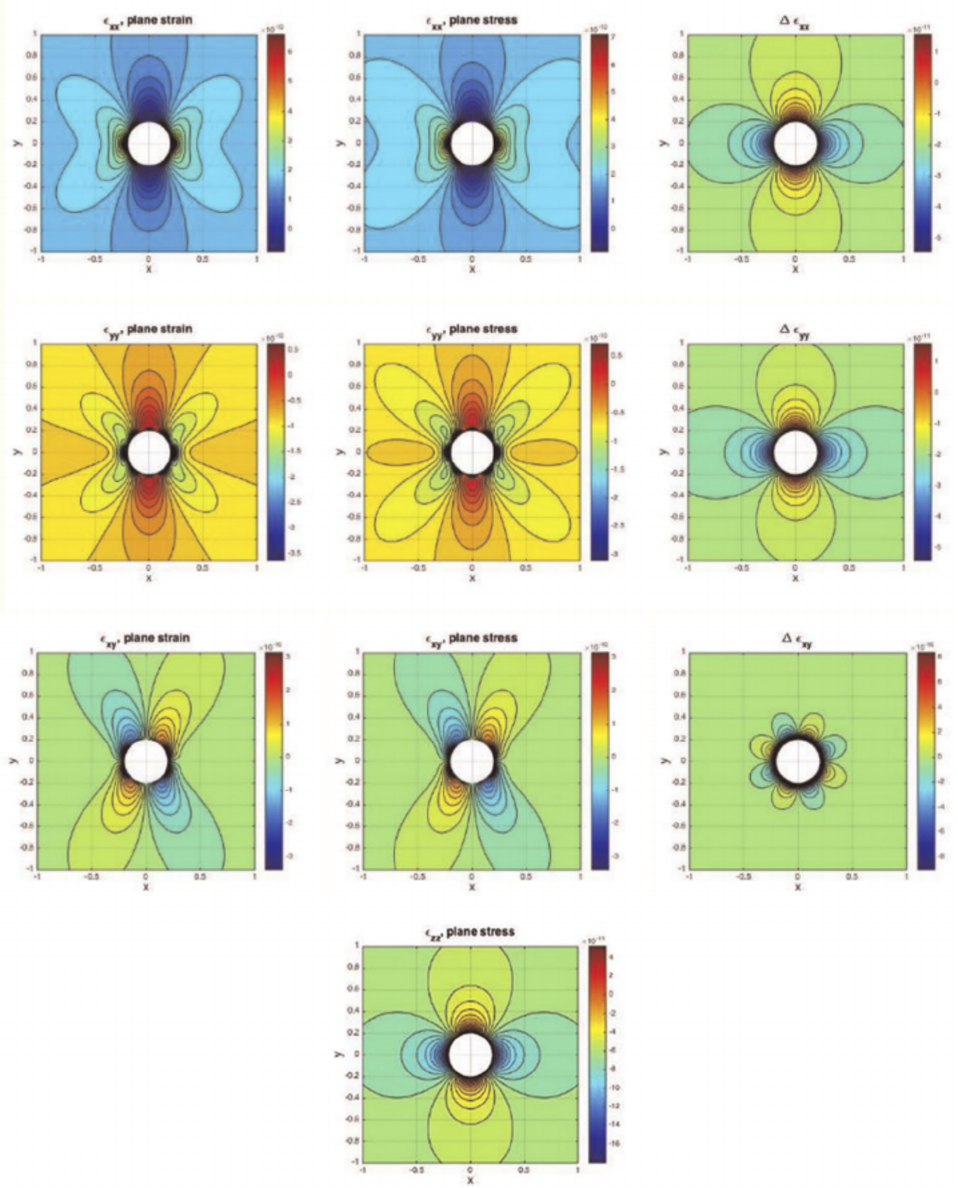

Figure C13.
Strain tensor components around the single hole in an elastic plate subjected to both far-field stress and internal pressure. These solutions are obtained by analytical differentiation of the displacement components in ***Figure C12*** *in both x and y directions.* $\varepsilon_{zz} = 0$ *for the plane strain solution and therefore there is no delta in z−direction.*

3. Principal strains.

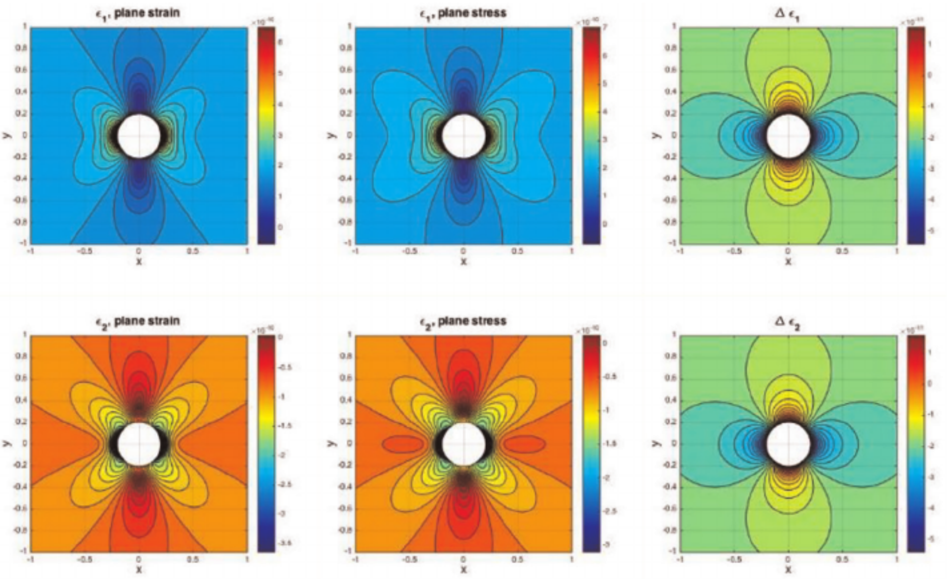

Figure C14.
Principles strains around the single hole in an elastic plate subjected to both far-field stress and internal pressure. These solutions are obtained by applying Eq. (36) for the principal strain magnitude solution using the strain tensors in ***Figure C13****.*

4. Stress tensor components.

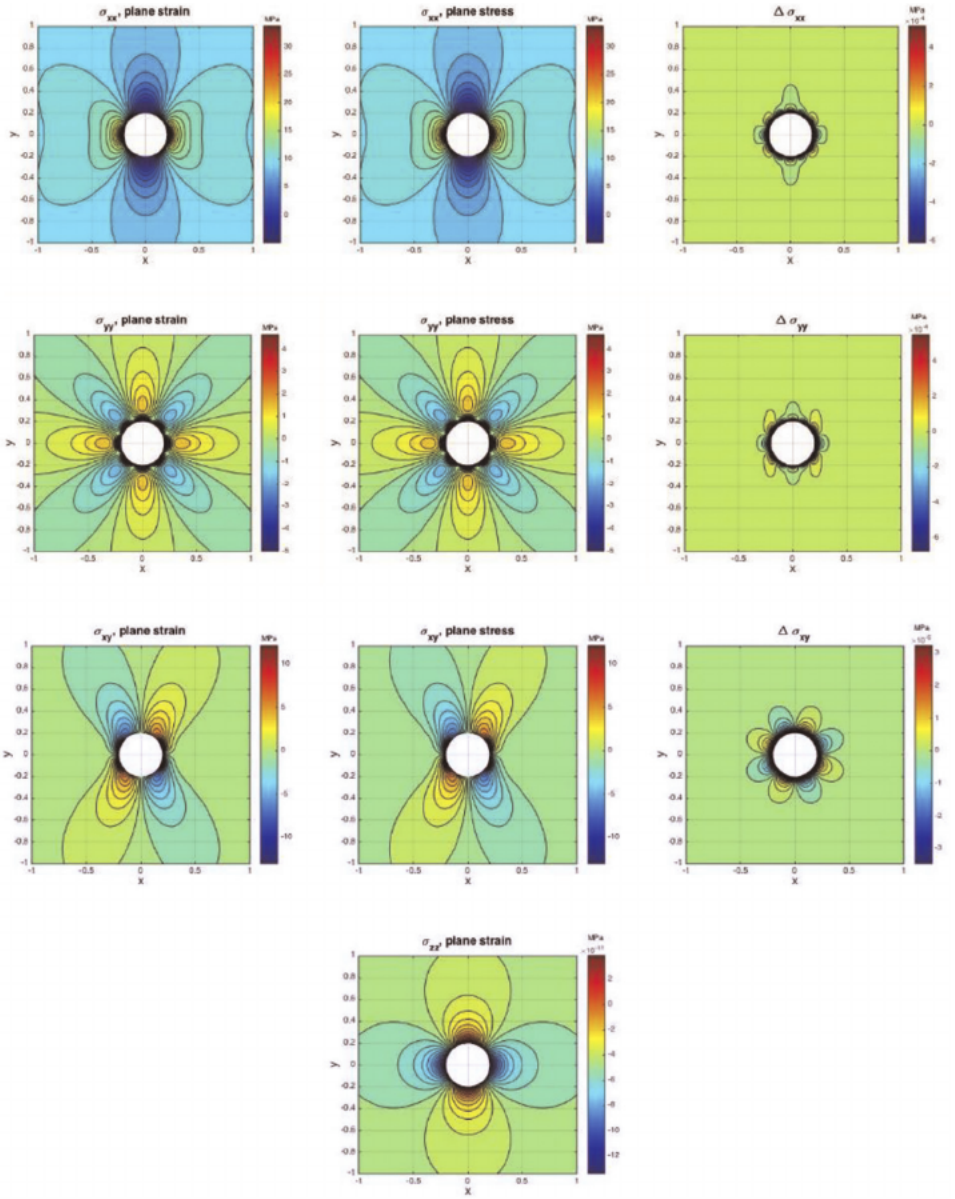

Figure C15.
Stress tensor components around the single hole in an elastic plate subjected to both far-field stress and internal pressure. These solutions are obtained from the relations between the strain tensor components and the stress tensor components shown in Eqs. (32)–(34). Note that $\sigma_{zz} = 0$ *for plane stress solution and therefore there is no delta in the* $z-$*direction.*

5. Principal stress.

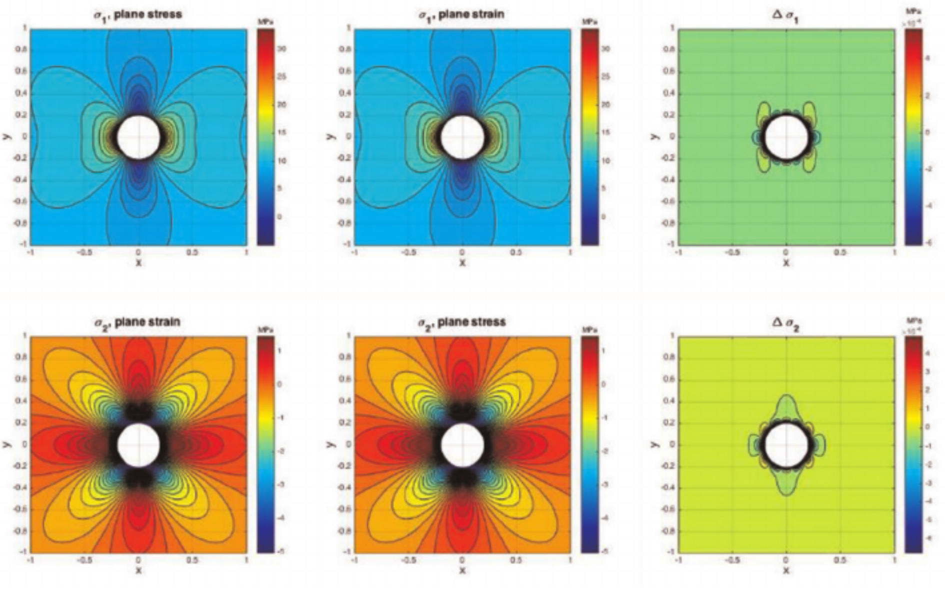

Figure C16.
*Principal stresses around the single hole in an elastic plate subjected to both far-field stress and internal pressure. These solutions are obtained by applying Eqs. (37) and (38) using the tensor stress components in **Figure C15**.*

D. Multi-hole analysis: 5-hole problem (Case 2–1)

Comprehensive results are given here for the vector displacement fields, strain tensor components, principal strains, stress tensor components, and principal stresses for the elastic plate model represented in Case 2–1 with 5-holes subjected to far-field stress. The model input parameters are as given in **Table 2**. The first column images are for plane strain; the second column images are for plane stress; and the third column quantifies the delta between plane strain and plane stress solutions.

1. Displacement fields.

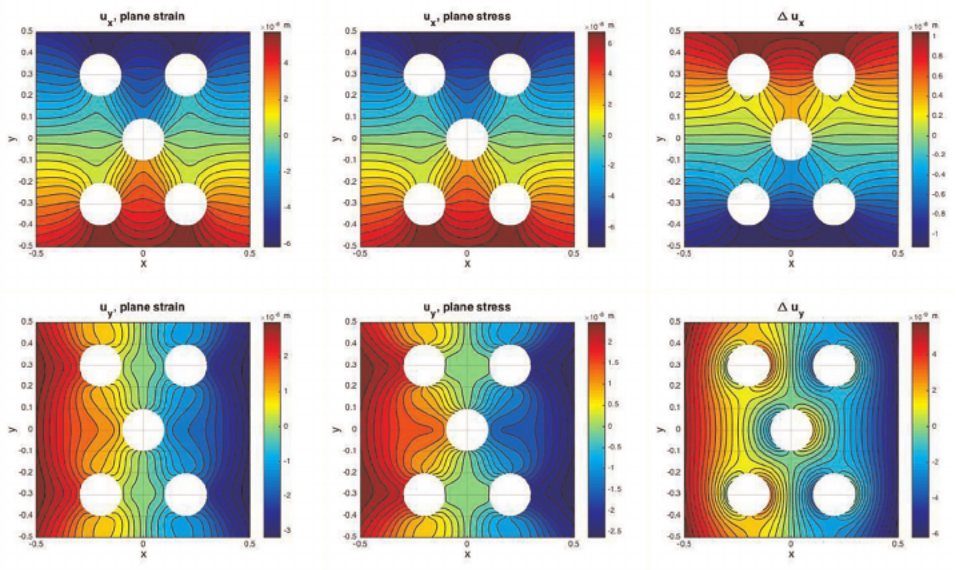

Figure D1.
*Complete results of the elastic displacement solutions around 5-holes with equal radii (r = 0.1) in an elastic plate subjected to far-field stress. First column is for the plan strain solution given by Eqs. (15) and (16) for each single hole and then use Eqs. (23) and (24) to compute the total displacement vectors ($u_{x,\text{total}}$ and $u_{y,\text{total}}$) due to all holes combined. Second column is the plane stress solution given by Eqs. (17) and (18) and, similarly, using Eqs. (23) and (24) to compute the total displacement vectors due to all holes combined. Third column quantifies the delta (difference) between plane strain and plane stress solutions using Eqs. (25) and (26). Input parameters for this model are listed in **Table 2**.*

2. Strain tensor components.

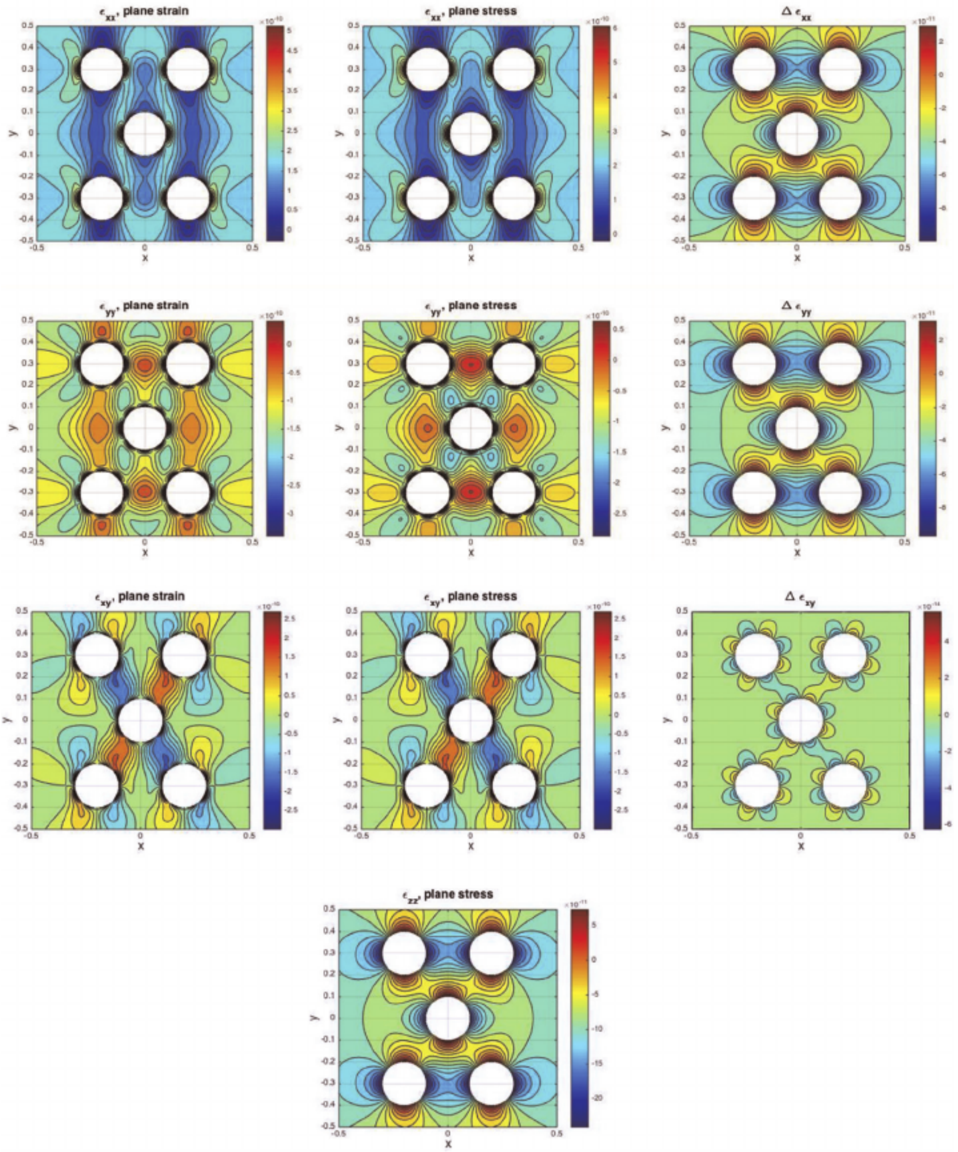

Figure D2.
Strain tensor components around 5-holes with equal radii (r = 0.1) in an elastic plate subjected to far-field stress. First column is for the plan strain solution. Second column is the plane stress solution. Third column quantifies the delta (difference) between plane strain and plane stress solutions. These solutions are obtained by analytical differentiation of the displacement components in ***Figure D1*** *in both x and y directions. Since $\varepsilon_{zz} = 0$ for the plane strain solution there is no delta in z−direction.*

3. Principal strains.

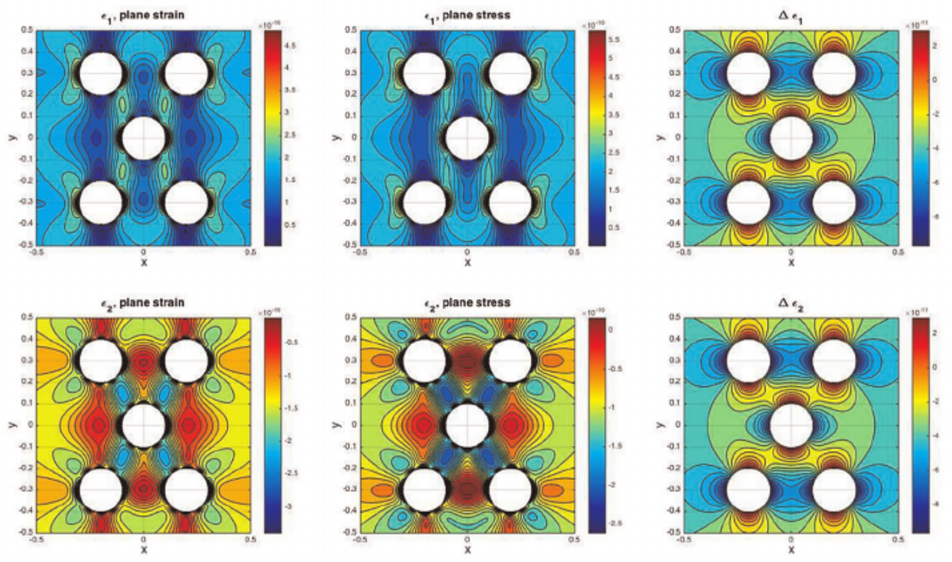

Figure D3.
*Principles strains around 5-holes with equal radii (r = 0.1) in an elastic plate subjected to far-field stress. These solutions are obtained by applying Eq. (36) for the principal strain magnitude solution using the strain tensors in **Figure D2**.*

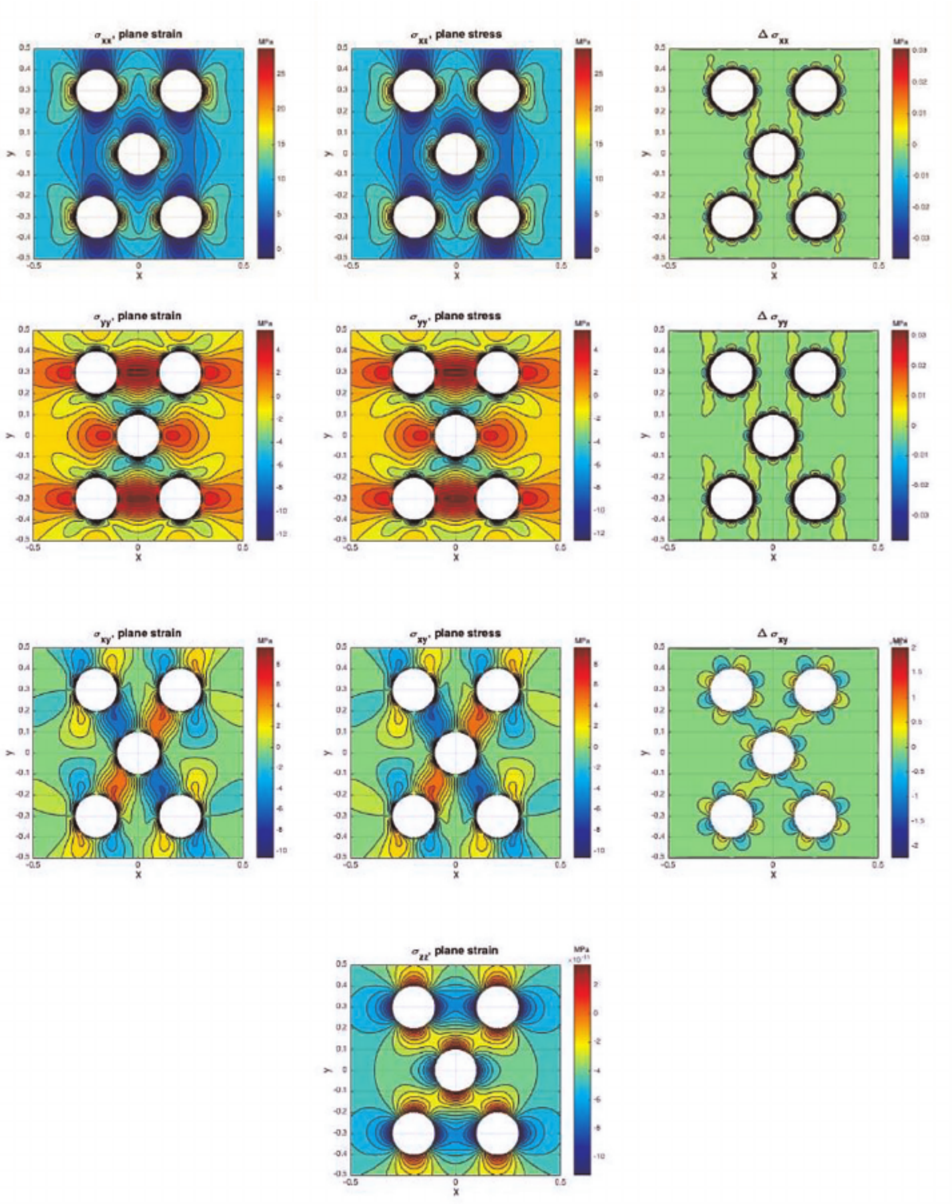

Figure D4.
Stress tensor components around 5-holes with equal radii (r = 0.1) in an elastic plate subjected to far-field stress. These solutions are obtained from the relations between the strain tensor components and the stress tensor components shown in Eqs. (32)–(34). Since $\sigma_{zz} = 0$ for plane stress solution there is no delta in the $z-$direction.

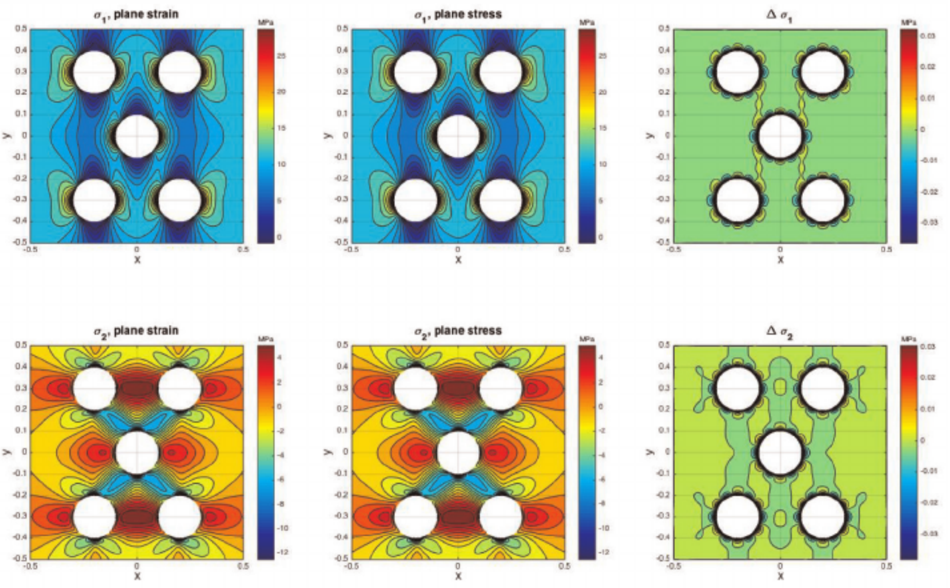

Figure D5.

Principal stresses around 5-holes with equal radii (r = 0.1) in an elastic plate subjected to far-field stress. These solutions are obtained by applying Eqs. (37) and (38) using the tensor stress components in ***Figure D4****.*

4. Stress tensor components.
5. Principal stresses.

See (**Figure D5**).

References

[1] Kirsch C. Die theorie der elastizitat und die bedurfnisse der festigkeitslehre. Zeitschrift des Vereines Deutscher Ingenieure. 1898;**42**:797-807

[2] Thomas N, Weijermars R. Comprehensive atlas of stress trajectory patterns and stress magnitudes around cylindrical holes in rock bodies for geoscientific and geotechnical applications. Earth-Science Reviews. 2018;**179**:303-371

[3] Weijermars R, Pham T, Ettehad M. Linear superposition method (LSM) for solving stress tensor fields and displacement vector fields: Application to multiple pressure-loaded circular holes in an elastic plate with far-field stress. Applied Mathematics and Computation. 2020a;**381**:125234. DOI: 10.1016/j.amc.2020.125234

[4] Weijermars R, Wang J, Nelson R. Stress concentrations and failure modes in horizontal wells accounting for elastic anisotropy of shale formations. Earth-Science Reviews. 2020b;**200**:102957. DOI: 10.1016/j.earscirev.2019.102957

[5] Aadnoy BS, Looyeh R. Petroleum Rock Mechanics: Drilling Operations and Well Design. Boston: Gulf Professional Publishing; 2012. DOI: 10.1016/C2009-0-64677-8

[6] Fjaer E, Holt RM, Horsrud P, Raaen AM. Petroleum Related Rock Mechanics. 2nd ed. Elsevier; 2008

[7] Jaeger JC, Cook NG, Zimmermann RW. Fundamentals of Rock Mechanics. 4th ed. John Wiley & Sons; 12 March 2009. pp. 475

[8] Weijermars R. Stress cages and fracture cages in stress trajectory models of wellbores: Implications for pressure management during drilling and hydraulic fracturing. Journal of Natural Gas Science and Engineering. 2016;**36**:986-1003

[9] Wang J, Weijermars R. Expansion of horizontal wellbore stability model for elastically anisotropic shale formations with anisotropic failure criteria: Permian Basin case study. In: 53rd US Rock Mechanics/Geomechanics Symposium. OnePetro; 2019

[10] Koslowska B. Experimental investigations of elastic-plastic strain states on various stages of material plastifying. Journal of Theoretical and Applied Mechanics. 2016;**54**(2):489-501. DOI: 10.15632/jtam-pl.54.2.489

[11] Yi W, Rao Q, Ma W, Sun D, Shen Q. A new analytical-numerical method for calculating interacting stresses of a multi-hole problem under both remote and arbitrary surface stresses. Applied Mathematics and Mechanics. 2020; **41**(10):1539-1560

[12] Green AE, Taylor GI. Stress systems in aeolotropic plates, III. Proceedings of the Royal Society of London. Series a. Mathematical and Physical Sciences. 1945;**184**(997):181-195

[13] Clark RA. Three-dimensional corrections for a plane stress problem. International journal of solids and structures. 1985;**21**(1):3-10

[14] Green AE. Three-dimesnional stress systems in isotropic plates. I. Philosophical transactions of the Royal Society of London. Series A, Mathematical and Physical Sciences. 1948;**240**(825):561-597

[15] Yang Z, Hou J, Wang GY, Xiong ZH. The stress and strain concentrations associated with two interacting holes in a finite thickness elastic plate subjected to

tensile stress. In: Key Engineering Materials. 2011;**462**:48-53 Trans Tech Publications Ltd

[16] Filon LN. On an approximate solution for the bending of a beam of rectangular cross-section under any system of Lond, with special reference to points of concentrated or discontinuous loading. Philosophical transactions of the Royal Society of London. Series A, Containing Papers of a Mathematical or Physical Character. 1903;**201**(331–345):63-155

[17] Jaeger JG, Cook NGW. Fundamentals of Rock Mechanics. 3rd ed. London: Chapman & Hall; 1979

[18] Goodman RE. Introduction to Rock Mechanics. Vol. 2. New York: Wiley; 1989 Jan 17

[19] Jussila P. Analytical solutions of the mechanical behaviour of rock with applications to a repository for spent nuclear fuel. 1979. https://www.osti.gov/etdeweb/biblio/599095

[20] Brady BHG, Brown ET. Rock Mechanics for Underground Mining. 3rd ed. Dordrecht: Kluwer Academic Publishers; 2005

[21] Valkó P, Economides MJ. Hydraulic Fracture Mechanics. Chichester: Wiley; 1995

[22] Saada AS. Elasticity Theory and Applications. 2nd ed. Malabar, Florida: Krieger Publishing Company; 1993

[23] Lamé G. Leçons sur la théorie mathématique de l'élasticité des corps solides. Paris: Bachelier; 1852

[24] Green AE. General bi-harmonic analysis for a plate containing circular holes. Proceedings of the Royal Society of London. Series a. Mathematical and Physical Sciences. 1940;**176**(964):121-139

[25] Ling CB. On the stresses in a plate containing two circular holes. Journal of Applied Physics. 1948;**19**(1):77-82

[26] Haddon RA. Stresses in an infinite plate with two unequal circular holes. The Quarterly Journal of Mechanics and Applied Mathematics. 1967;**20**(3): 277-291

[27] Kooi CB, Verruijt A. Interaction of circular holes in an infinite elastic medium. Tunnelling and Underground Space Technology. 2001;**16**(1):59-62

[28] Wang J, Crouch SL, Mogilevskaya SG. A complex boundary integral method for multiple circular holes in an infinite plane. Engineering Analysis with Boundary Elements. 2003; **27**(8):789-802

[29] Weijermars R, Wang J, Pham T. Borehole failure mechanisms in naturally fractured formations. Rock Mechanics and Rock Engineering. May 2022:**55**(5): 3001-3022

[30] Weijermars R, Ettehad M. Displacement field potentials for deformation in elastic media: Theory and application to pressure-loaded boreholes. Applied Mathematics and Computation. 2019;**340**:276-295

[31] Meguid SA, Shen CL. On the elastic fields of interacting defense and main hole systems. International Journal of Mechanical Sciences. 1992;**34**(1):17-29

[32] Nádai A, Hodge PG Jr. Theory of Flow and Fracture of Solids. Vol. II. New York, NY: McGraw-Hill Book Company Incorporated; 1963

Chapter 6

Modeling and Analysis Techniques for Solving Mechanical Pipe Sticking Problems in Drilling Equipment

Hani Mizhir Magid

Abstract

Mechanical pipe sticking is the important reasons which has a direct impact on the drilling process efficiency. The problems of pipe sticking during drilling, and the other problems associated with this case is a crucial task that must be early identified to find the causing factors before any further action. The main objectives of this study are to predict and specify the main causes of these problems through modeling and simulation processes. Consequently, the (ANSYS Workbench/2019 R3) Commercial version has been adopted for this analysis purposes. This analysis have been carried out based on the actual interaction and contact between the active working parts to simulate the actual process. In this simulation process, the non-deformable parts like drill pipe, and wellbore sleeve are considered (Masters), while deformable parts are (slaves). Simulation results approved that the pipe stick happened due to high values of generation stresses. The plot of maximum induced stresses shows that the generated stresses in the interaction zone between the outer surface of the drilling pipe and mud are (15) % more than in the other zones. Also, the probability of sticking during drilling can be predicted according to the relation between the drill depth with time and drag forces. It's concluded that for freeing the stuck pipe it's very necessary to predict the problems from the beginning. This type of analysis can assure the percentage accuracy for stuck pipe prediction is more than (70) %.

Keywords: modeling and analysis, pipe sticking, drill string, wellbore, FEM

1. Introduction

During drilling, the pipe is said to be stuck when the drill string cannot rotate or move. Pipe stuck is happened due to many reasons like inadequate hole cleaning, fractured and faulted formation, and junk inside the hole. There are two mechanisms of pipe sticking; mechanical sticking and differential sticking. Both mechanisms are affected by fluid design and mud cake [1]. Mechanical pipe sticking occurs due to many drilling obstructions like inclination of the well or key seat difficulty, wherefore high attention, and continuous measurement are required to prevent any changes in bore deflection [1, 2]. There are many reasons for pipes being stuck such as the inefficiency of lifting the excavated rock fragments, swelling of the shale layers, or the drilling column being lowered in narrow areas. Mechanical sticking happens when the pipe is in motion and sticks due to insufficient cutting slip velocity, poor mud properties, and Poor hole-cleaning. The friction between the tube and wall,) as the well wall generates a groove (which causes inflexibility. Well demolition or rock pieces accumulation inside the mud due to bad clay properties of viscosity also leads to bad sticking and high difficulty of pulling or lowering the pipe during connection [3, 4]. Due to rock interaction, the nature of induced drill strings will be non-smooth. The desirable response of the system is to operate in equilibrium, with a constant rotation, but permanent vibrations or permanent sticking can occur due to large perturbation in the system. Borehole instability is a problem associated with shear failure at the wellbore walls. When the mud pressure is not enough for backing the wellbore, in this case, the peripheral stresses around the wellbore will exceed the rock strength and mechanical sticking will occur. In vertical and deviated wells, the significant wellbore instability problem is a stuck pipe which causes the non-productive time for the majority field's development [5].

The problems and challenges that result in the possibility of blockage of the drilling pipes are included a decrease in productivity, loss of time, and additional operations that lead to the cost increase [6]. All operations will temporarily stop during the nonproductive time while drilling. In addition to financial losses and lost time, there will be a possibility leading to weakening the economics of a project [7]. The mitigation of stick-slip problems via analysis is a very important step in controlling the effective parameters. The parameter combinations that are affected by the rough nature of rock interaction should be determined previously to suppress and control the stick-slip during the drilling process [8]. The main optimization drilling factors are concerned with the rate of penetration, intelligent drilling, wellbore design, and increasing drill tool life. At this point, drilling technologies start using some special analysis trajectories for implementing directional wells in hard rock, and deep well. However, these trajectories may involve some types of complex drilling and will lead to a high-cost increase [9]. Moreover, drilling performance can be limited and effect by many parameters like shocks and drill string vibrations. The mechanical sticking due to the interactions between the borehole wall, drill string, and mud cake during the drill string stopping needs to be predicted to avoid the risks. Drilling problems like loss of circulation, torque, drag, and cuttings transport can be predicted and solved by using the general scheme by utilization of effective drilling data [10]. The crucial task to preventing a stuck pipe is the early identification of the problem. Spotting oil around the pipe section is the more usual way to reduce the pressure and free the stuck pipe [11].

A theoretical evaluation method is a measurement tool used to investigate and control a drilling string. Stuck pipe occurrence is an undesirable event and leads to string failure. Consequently, the analysis and calculation of the drilling conditions are very essential. Pipe sticking that happened in some deviated wells is considered a significant drilling problem. Simulation and analysis are accurate tools for predicting and avoiding severe collapse or failure and decreasing uncertainties of nonproductive time [12]. Predicting method like Artificial Neural Network (ANN) is the most powerful tools to avoid stuck pipe risks and can be employed for modifying the drilling variables. It's applicable whenever the relationships between parameters are complicated, and the prediction accuracy may exceed 90% [13]. The Genetic algorithm optimization-based artificial intelligence (AI) is used as an efficient predictive analytics technique for drilling pipe stuck. The key contribution was to mitigate the pipe stuck through automate pipe stuck classification by using ML algorithms. During a drilling operation, the most expensive problem that can occur is the pipe stick. Complications of this problem can account for approximately half of the total drilling cost. A genetic algorithm (GA) can optimize the drilling parameters and be used to mitigate the risk of drilling pipe stuck [14]. There are some important procedures and considerations that should follow for the best results in pipe releasing. It involves that the pipe should be free in a short time after sticking. The procedure of freeing the pipe is shown in **Figure 1** [15]. Sufficient hole cleaning is one of the essential factors of a drilling operation's success. Inadequate hole cleaning and wellbore instability are the main factors that caused the mechanical sticking. Non-sufficient hole cleaning is one of the crucial causes of non-successful drilling operations, especially in deviated wells when the inclination angle is between 30 and 60 degrees.

In this chapter, the main causes of mechanical stuck pipe problems have been explained. The finite element software (ANSYS/2019 R3), has been adopted for this analysis to find some possible solutions for mitigating these effects on the drilling process. The findings of this study present the outcome analysis of mechanical stuck pipe which is summarized by dynamic analysis.

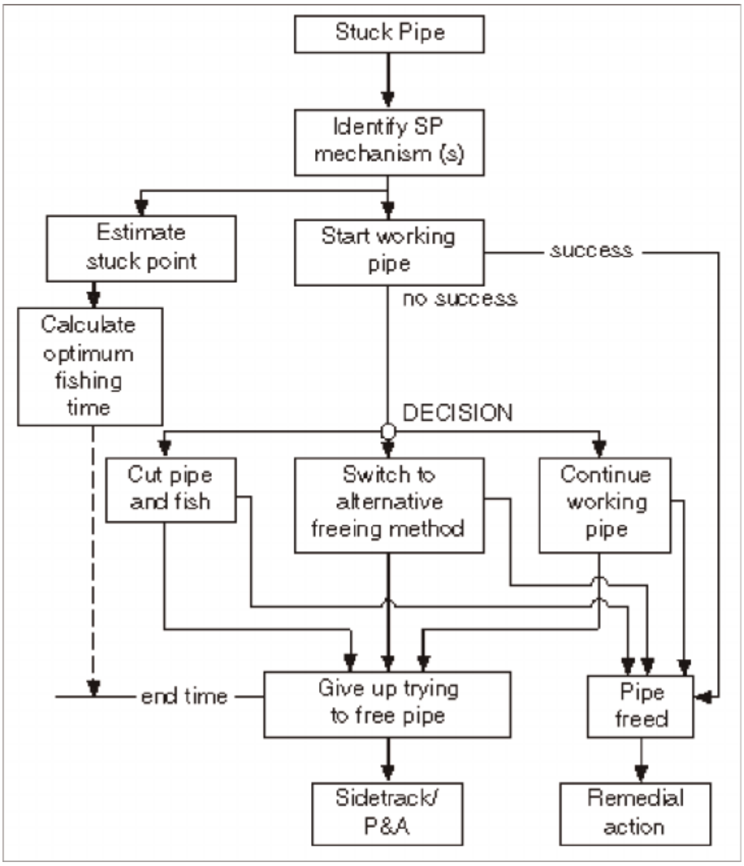

Figure 1.
The procedure of freeing the pipe [15].

2. Materials and method

2.1 Main objectives

The main objectives of this study are to specify the main causes for mechanical stuck pipes and to provide suitable suggestions and solutions that can mitigate and eliminate this important problem through modeling and simulation processes.

2.2 Modeling and analysis process

As far as mechanical pipe sticking is concerned, determining the relationship between all effecting factors on the drill string is necessary. At this point, studying the

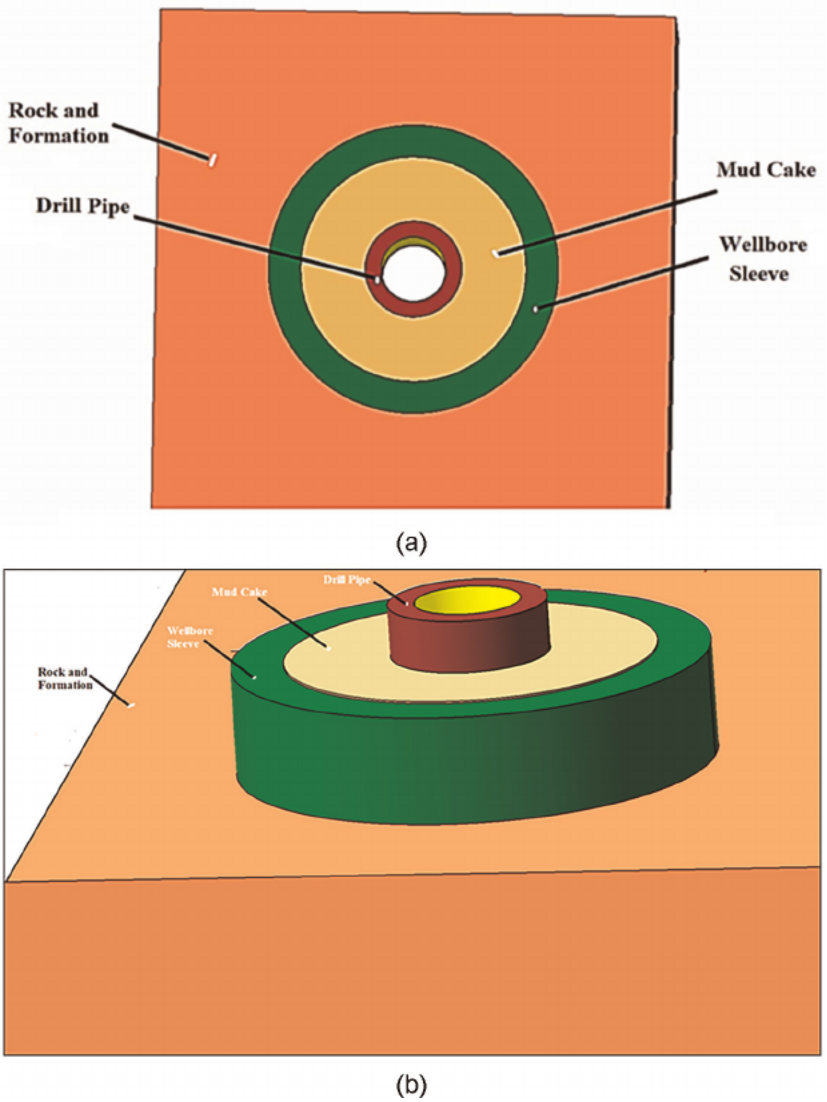

Figure 2.
(a) The model components in (2-D); and (b) The model components in (3-D).

mechanical behavior and interaction between the drilling system parts during the actual condition will lead to a better understanding and solution as well as support the decision-making. Consequently, modeling and analyzing this complex process which consists of many interaction parts with different boundary conditions like pressure, forces, stress, and others is a significant challenge in predicting and preventing or mitigating the sticking problem during drilling. Based on the foregoing information, the physical model is created to simulate the actual case with similar operating conditions. The main parts consist of the drill pipe, mud cake, wellbore housing, and the surrounding formation. **Figure 2A** and **B** illustrates these model components in (2D) and (3D).

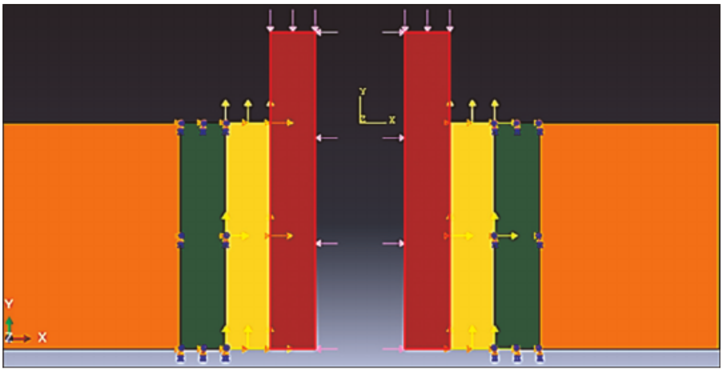

Figure 3.
Contact behavior between the interaction parts.

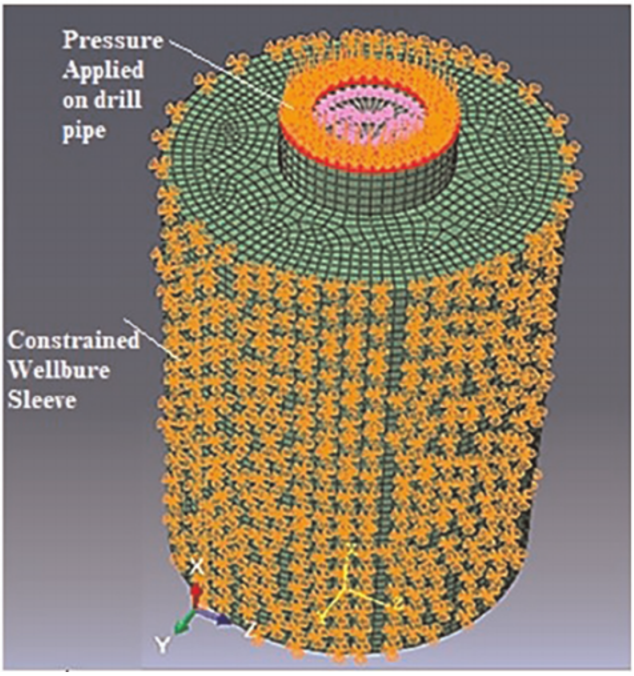

Figure 4.
The boundary condition includes constraining the wellbore from any movements and applying downward pressure on the drill pipe.

The interaction and constrain between these parts were defined according to their function. The drill pipe is modeled as a rigid body (non-deformable part), while the mud in contact with the outer surface of the pipe is modeled as a deformable region. Also, the wellbore sleeve is considered as a rigid body and reacts as a non-deformable part.

Figure 3 is an illustration of the contact behavior between these parts and the direction of the applied loads.

The boundary condition is built according to the main function of this process. The wellbore sleeve is restricted and constrained in all directions to prevent any possible movements. While the boundary condition (move down) will apply on the upper surface of the drill pipe in order to allow the pipe to move downward direction. **Figure 4** shows the constraints on the wellbore, and applied pressure on the drill pipe to move down.

3. Main calculations

For a quick approximation, here below introduced some mathematical formulas for calculating the required force to free the stuck string and the depth of the stuck pipe [15].

$$Depth\ of\ stuck\ pipe(feet) = Pipe\ stretch(inch) \times Free\ point\ constant(FPC)/Pull\ force(k - lbs) \tag{1}$$

$$FPC = As \times 2500 \tag{2}$$

As is the pipe wall cross-sectional area (sq. inch).

$$As = (0.5)^2 \left(OD^2 - ID^2\right) \times \pi = \left(OD^2 - ID^2\right) \times 0.7854 \tag{3}$$

Where;

ID is the inner diameter of the drill pipe in inches.

OD is the outer diameter of the drill pipe in inches.

Alternatively, the stuck depth can also be calculated using this approach;

$$Stuck\ depth = 735.294 \times E \times Drill\ Pipe\ Weigh/Differential\ Pull \tag{4}$$

735.294 is a constant.

$$Differential\ pull = higher\ pull\ on\ (lb)\text{–}lower\ pull\ of\ (lb) \tag{5}$$

$$\mathrm{E} = Higher\ pull\ pipe\ stretch\ (in)\text{–}lower\ pull\ pipe\ stretch\ (in) \tag{6}$$

$$Axial\ force\ required\ to\ free\ pipe = \mu \times Pull\ force/1000 \tag{7}$$

4. Finite element analysis

The Commercial software (ANSYS/2019 R3) has been adopted for the analysis and simulation of this process.

ANSYS is a finite-element modeling package normally used for numerically solving mechanical problems such as structural analysis. There are two methods used in (ANSYS) namely; graphical user interface (GUI) and the command line interface (CLI). Factors, such as the interaction type between the contact parts, material properties, and element type according to the mesh method are the main input variables. The Mapped Face Meshing method has been used to facilitate and extracted the element size. The method-based analysis is the failure criteria that have been incorporated to predict the problems of stuck pipes. It depends on estimating the mechanical properties of formations and the state of stresses. It also depends on the effect of the intermediate principal stress component in the failure analysis. The type of contact between the interacting parts is categorized and defined according to their functions. Bonded and non-separation contact is the suitable contact type for defining the nature of contact between these parts during drilling, and the adaptive meshing technique is also used to enhance the results and findings of this analysis. **Figure 5** illustrates the contact and mesh types.

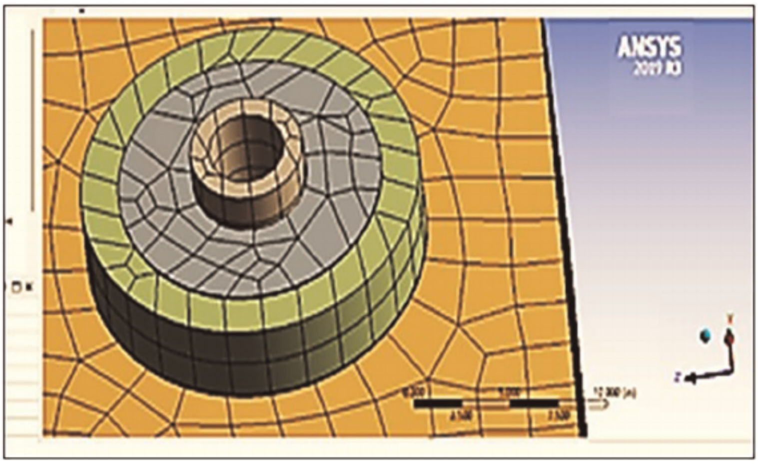

Figure 5.
The contact and mesh type.

Figure 6 illustrates the nature of interaction and the applied load during the total deformation option. This type of deformation is defining the elements of the part that are subjected to deformation to be classified as (Slaves), while the non-deformable elements are classified as (Masters).

The drill pipe displacement is assumed to be a small value at the beginning of the drilling process due to the high resistance and high frictional forces between the contact surfaces. However, displacement of the drill pipe will increase rapidly and in proportion with the applied pressure due to an increase in contact surface area between the parts.

In this analysis model, many failure criteria have been incorporated to predict the problems of stuck pipes and estimate the mechanical stability of drilling string.

During the drilling process, the total deformation interaction will impose on the contact between the formation rock and drill pipe. Consequently, a large deformation (elastic-plastic type), and a high amount of material flow will result due to severe contact and high frictional forces between these surfaces.

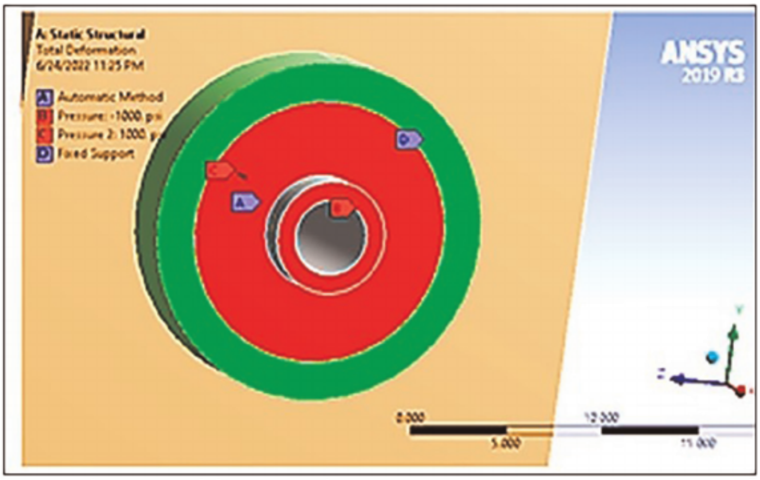

Figure 6.
The fixed support constraints and applied load.

5. Results and discussion

The calculation of embedment drill string depth in the mud cake is a difficult process and mostly depends on the interaction between the mud cake and downhole tools. It also depends on the mechanical properties of the mud cakes.

It's more realistic and reliable to predict and estimate the minimum and maximum stresses. The contour plot in **Figure 7** indicates the values and direction of the minimum and the maximum vertical stress.

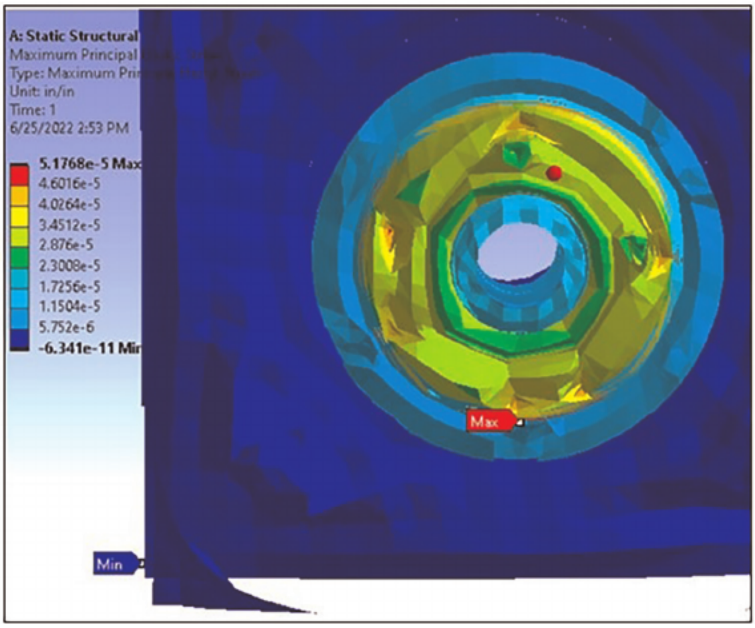

Figure 7.
Contour plot of maximum induced stresses.

In this contour, it's clear that the maximum stresses will be concentrated at the contact surfaces between the drill pipe and the wellbore house. This is due to the high contact pressure and high friction force between the pipe and mud.

The various failure criteria are resulting during overbalance pressure conditions, which caused mechanical pipe sticking. The contour plot of total deformation shown in **Figure 8** illustrates the severe deformation that happens during the downward movement of the drill pipe. In this case, the deformable part (mud cake) will deforms, while the non-deformable part (drill pipe and well bore sleeve) doesn't.

The equivalent strain in this process is illustrated in the contour plot as shown in **Figure 9**. The relative displacement of both drill pipe and mud cake is represented in their movement downward for drill pipe and upward for mud cake

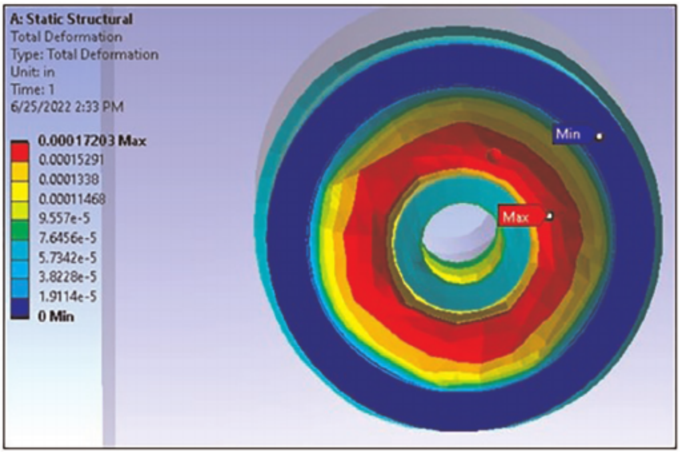

Figure 8.
Contour plot of total deformation.

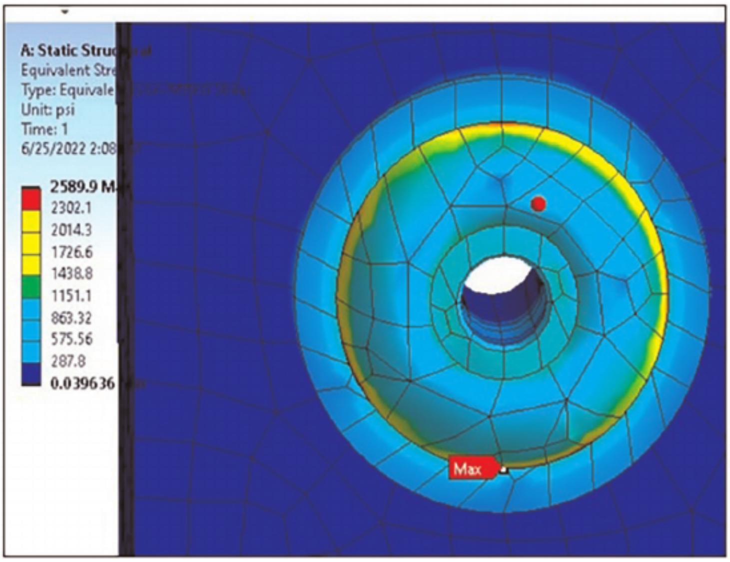

Figure 9.
Contour plot of equivalent strain.

The overall deformation occurrence according to the relative interaction between the parts shows that high deformation values will take place around the drill pipe and will cause high mechanical sticking with time as shown in **Figure 10**.

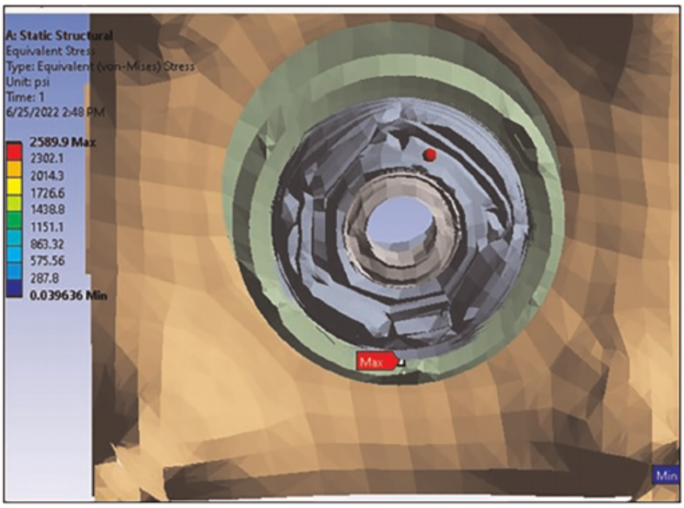

Figure 10.
Total system deformation.

Regarding the high contact forces between the parts, the probability of pipe stick will become serious, and the probability of freeing the pipe against soaking with time will be very difficult. **Figure 11** shows the difficulty of freeing the drill pipe with soaking time. Consequently, calculating the required time before backing off and circulating out is very essential.

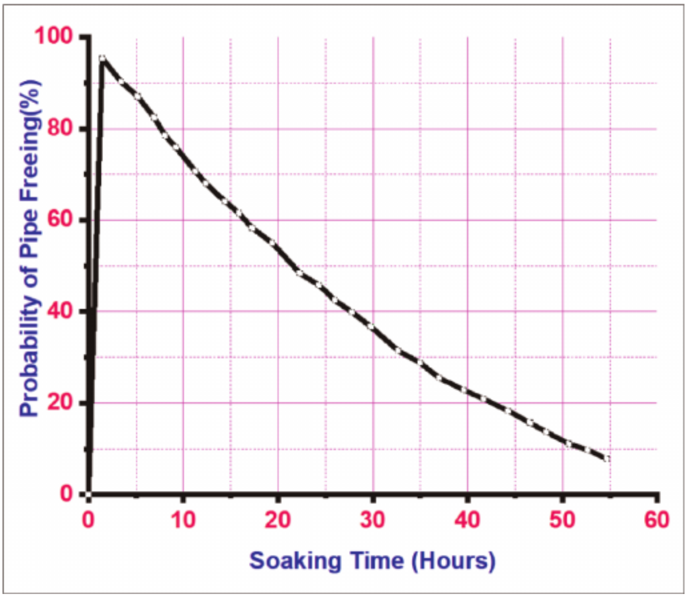

Figure 11.
The probability of freeing the pipe against soaking time.

Based on the foregoing, and due to high sticking forces between the contact surfaces along the drill pipe, so the drag force will be inversely proportional to pipe drill depth. **Figures 12** and **13** are an illustration of the relationship between pipe depth and both drag force and the percentage probability of getting stuck.

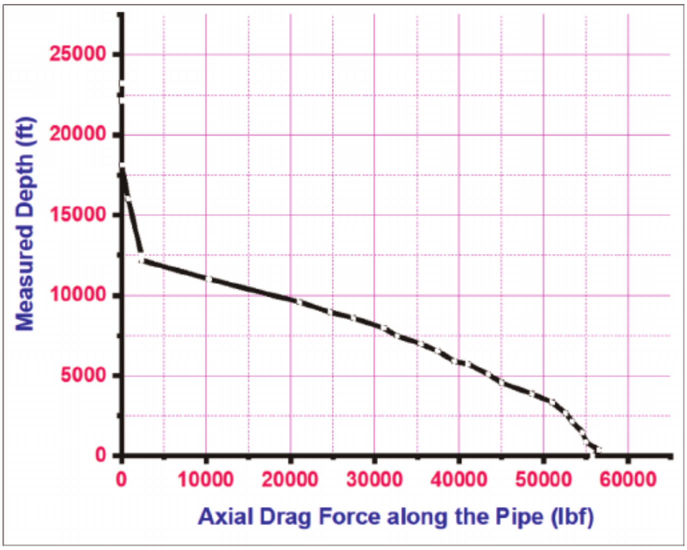

Figure 12.
The relation between pipe depth and drag force.

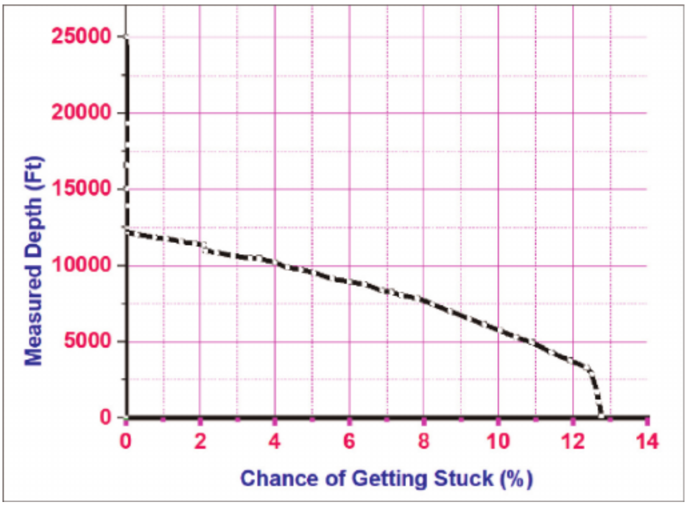

Figure 13.
The relation between pipe depth and the percentage probability of getting stuck.

6. Suggested solutions for mechanical pipe sticking

According to the foregoing, and based on a wide range of literature scanning, here below are some suggested solutions to free a stuck drill string in mechanical pipe sticking:

- Control the mud flow rate through suitable circulation.
- Control the direction of applied torque according to the stuck position
- Decrease the contact area between the pipe and formation.
- Early detection of pipe stuck.
- Adding crude oil to drilling mud in order to control the water seepage and facilities slippage.
- It's advised to make short trip drilling withdrawals and downloads continuously.
- Reducing the thickness of the drilling cake by reducing the seepage from the drilling fluid by treating it with the appropriate additives
- Reducing the drilling speed in some areas, especially in large cavities, to offer enough time to lift the rock fragments.
- In the case of non-return drilling, a high viscosity slurry should be pumped in before attaching a new pipe to help suspend the crumbs.

7. Conclusions

This paper provided an explanation of drilling wells using some ideas to resist the mechanical pipe stuck. The following conclusions were made according to this study:

1. To prevent stuck pipes, it's very essential in adhering to the criterion of drilling calculation and assures the efficiency of drilling system cleaning. This will reduce the possibility of sticking and collapse.
2. There's a high indication that failure and wellbore collapse is always associated with a stuck pipe that has been drilled with low mud weight.
3. Consequently, the parameters that have a significant impact on the failure mechanisms are mechanical properties, high-stress contrast, and well trajectory design.

It's found from some other expert literature that diesel oil pills and stuck breakers can successfully be used to release the mechanical pipe sticking if implemented accurate procedure.

Since the severity of mechanical stuck is associated with cutting head (drill collar and bit), so minimize the interaction and contact area between mud cake, drill-string, and the wellbore is important to offer sufficient exposure time with a low flow rate to ensure an effective process.

Acknowledgements

The author would like to express high appreciation to members of the IntechOpen for their valuable advice and support.

Funding information

This research received no external funding.

References

[1] Pacis FJC. An End-To-End Machine Learning Project for Detection of Stuck Pipe Symptoms During Tripping Operations. Stavanger: Stavanger University; 2021). Master thesis

[2] Naraghi ME, Ezzatyar P, Jamshidi S. Prediction of drilling pipe sticking by active learning method (ALM). Journal of Petroleum and Gas Engineering. 2013; **4**(7):173-183. DOI: 10.5897/JPGE2013.0166

[3] Salminen K, Cheatham C, Smith M, Valiulin K. Stuck Pipe Prediction Using Automated Real-Time Modeling and Data Analysis. 2016). IADC/SPE-178888-MS. DOI: 10.2118/178888-MS

[4] Magana-Mora A, Affleck M, Ibrahim M, Makowski G, Kapoor H, Otalvora WC, et al. Well Control Space Out: A Deep-Learning Approach for the Optimization of Drilling Safety Operations. IEEE Xplore; 2021. DOI: 10.1109/ACCESS.2021.3082661. https://ieeexplore.ieee.org/document/9438629

[5] Al-Hameedi AT, Alkinani HH, Dunn-Norman S. Insights into Mechanical and Differential Pipe Sticking with Case Histories from Sindbad Field. (2020). Iraq, AADE-19-NTCE-020. Available from: https://www.aade.org/application/files/5315/7132/0375/AADE-19-NTCE-020_-_Al-Hameedi.pdf

[6] Amina NS, Alhaleem AA. Analysis of stuck pipe incidents in Khabaz field. Iraqi Journal of Chemical and Petroleum Engineering. 2018;**19**(4):47-53. DOI: 10.31699/IJCPE.2018.4.6

[7] Oriji BA, Aire IS. A model approach to analytically identify stuck pipe and its mechanism in Wellbore. JERS, European Journal of Engineering Research and Science, 3. 2020;**5**. DOI: 10.24018/ejers.2020.5.3.1845

[8] Lin W, Chavez JP, Liu Y, Yang Y, Kuang Y. Stick-slip suppression and speed tuning for a drill-string system via proportional-derivative control. Applied Mathematical Modelling. 2020; **82**(2020):487-502. http://creativecommons.org/licenses/by/4.0/

[9] Dong G, Chen P. A Review of the Evaluation, Control, and Application Technologies for Drill String Vibrations and Shocks. Vol. 2016. Article ID 7418635. Hindawi Publishing Corporation Shock and Vibration; 2016. p. 34. DOI: 10.1155/2016/7418635

[10] Lourenço AMF. A Decision Support Model for Differential Sticking Avoidance. Curtin University; 2012. Doctor of Philosophy thesis. https://core.ac.uk/download/pdf/195631363.pdf

[11] Rafiqul Islam M, Enamul Hossain M. Advances in Managed Pressure Drilling Technologies. Book Chapter. Science Direct; 2021. DOI: 10.1016/B978-0-12-820193-0.00005-8. https://www.sciencedirect.com/science/article/pii/B9780128201930000058?via%3Dihub

[12] Ethar H, Alkamil K. A proactive drilling system t e drilling system to prevent stuck pipe and different stuck pipe and differential sticking. Missouri University Of Science And Technology; 2018. pp. 2883. Doctoral Dissertations. 2883. https://scholarsmine.mst.edu/doctoral_dissertations/2883/

[13] Shadizadeh SR, Karimi F, Zoveidavianpoor M. Drilling stuck pipe prediction in iranian oil fields: An artificial neural network approach. Iranian Journal of Chemical Engineering.

2010;7. http://www.ijche.com/article_10326.html

[14] Elmousalami HH, Elaskary M. Drilling stuck pipe classification and mitigation in the Gulf of Suez oil fields using artificial intelligence. Journal of Petroleum Exploration and Production Technology. 2020, 2020;**10**:2055-2068. DOI: 10.1007/s13202-020-00857-w

[15] Lapeyrouse NJ. Formulas and Calculations for Drilling, Production and Workover. 2011. Available from: https://books.google.iq/books?id=XXyAaiIBTxcC&printsec=frontcover&source=gbs_atb#v=onepage&q&f=false

Chapter 7

Estimation of Equivalent Thermal Conductivity Value Using Correlation Relationships with Other Oil Reservoir Properties

Chiș Timur, Jugastreanu Cristina and Renata Rădulescu

Abstract

In the exploitation of oil and gas reservoirs, thermal conductivity is the property of greatest importance in the application of secondary and tertiary oil fluid recovery techniques. This is why this property has been analyzed by estimating its value using several calculation models. But each model for calculating the value of this property is burdened by the fact that in the reservoir, the rocks are not like the chosen models (being made up of geological conglomerates with various inclusions). This paper presents a technique for estimating thermal conductivity (by energy transfer between overlying strata) and determining its value by a new calculation model. The paper also determined the thermal conductivity values for several rocks constituting some Romanian reservoirs, the aim of this material being to analyze the thermal behavior of rocks in condensed gas-rich areas.

Keywords: thermal conductivity, numerical modeling, heat transfer, collector rocks, oil, gas, condensate

1. Introduction

The conductivity of rocks, the constituents of oil and gas reservoirs, has not been a parameter investigated for a long time, because it was difficult to predict how fluids flowed and their temperature loss (heat transfer) in reservoir rocks [1].

After 1970, thermal conductivity was also used as a parameter in the development of hydraulic simulation models, due to the increased cost of discovery and preparation for extraction of oil and associated gas from new hydrocarbon reservoirs [2].

Models for calculating and estimating thermal conductivity were developed when tertiary oil recovery was discussed, using thermal techniques (injection of steam into the reservoir, underground combustion, flushing the collecting rocks with hot water, injection of CO_2 and flue gas, etc.) [3].

All these models developed had the ultimate goal of increasing the recovery factor of crude oil at the lowest possible price [4].

Any systematic geothermal research requires knowledge of how to transfer heat in the research environment [5, 6].

Heat transfer in oil and gas fields takes place through three main processes, namely: conduction, convection, and radiation.

Heat transfer by conduction occurs only in solid media by molecular interaction [7].

It is the main mechanism of heat transfer in the Earth's crust and the most important in geothermal probe research.

Convective heat transfer is associated with the free movement of fluids between two environments at different temperatures.

It is becoming important in geothermal areas, in particular in areas with volcanic activity and in areas with active groundwater circulation [8].

The mechanism of heat transfer by convection must be taken into account in geothermal research conducted in boreholes, because it plays a significant role in changing the natural thermal regime of the geological formations crossed.

Radiative heat transfer occurs only on the Earth's surface due to the exchange of heat between the Earth and the Sun, the rocks affected by this transfer being those from the surface or the first layers in depth (maximum 10 m).

For temperatures encountered at usual probe depths, including deep probes, the radiative transfer is negligible.

The ability of deposits of useful mineral substances to transmit and absorb thermal energy depends on the thermal conductivity of the constituent rocks.

The experimental law of thermal conduction in rocks and civil structures or Fourier's law very well defines the transfer of heat through conduction and is represented by the relation:

$$Q = -\lambda \bullet A \bullet grad\ T \tag{1}$$

But the nature of the body through which the heat transfer takes place is characterized by a parameter λ, defined in the literature as the coefficient of thermal conductivity (the amount of heat required to increase by 1 K the temperature of a surface equal to a unit of measurement, in a time unit), A is the heat transfer area (surface area), and T is the temperature difference between the heat transfer zone at the inlet and outlet:

$$\lambda = \frac{Q}{A\left|-\frac{\partial T}{\partial n}\right|} \tag{2}$$

Thermal conductivity defines the ability to accumulate and transfer a quantity of heat by the collecting rocks and the constituent fluids of the deposits of useful mineral substances.

The thermal processes that develop within the oil and gas deposits, following the application of a heat treatment or the extraction process, can be due to:

a. Conductive heat transfer due to free electrons in the outer layer of interacting rocks,

b. Radiative transfer (less existing in these deposits and due to the adsorption of energy by the black body),

c. Convective transfer due to the release of heat from moving fluids in the field.

In non-ionized gases, gases at $t \leq 1800°C$, the conductive transport of heat takes place mainly under the effect of molecular oscillations (photonic gas), which have a small amplitude, and as a result they are bodies that are poorly conductive heat.

In the case of Newtonian liquids and non-metallic solids, heat transfer through conductivity takes place both through the oscillations of molecules, because the distance between them is relatively small, and through radiation [9].

The coefficient of thermal conductivity varies with the nature of the body, with its state of aggregation, with temperature and pressure, with body moisture, with porosity, with the nature and concentration of impurities contained in the body, etc. (**Table 1**).

In the case of solutions (emulsions), the thermal conductivity is equal to the values:

- Distilled water $\lambda = 0.611$.
- Crude oil – water $\lambda = 0.133$ (Saturation with water and crude oil (35% water and 65% crude oil)).

Fluid-saturated porous medium	Porosity Φ, (%)	Density ρ, (kg/m^3)	Caloric capacity c, (kJ/kg K)	Equivalent thermal conductivity λ, (W/mK)
Saturated tiles	19,6	2080	0,766	0,877
-with air		2275	1055	2,75
-with water		-		1,36
-with crude oil		-		2,47
-with oil and gas				
Saturated clay shale (marl)	7,1	2320	0,804	1,04
- with air		2390	0,892	1,69
-with water				
Saturated limestone	18,6	2195	0,846	1,70
-with air		2390	1114	3,55
-with water				2,15
-with crude oil				2,92
-with oil and gas				
Fine saturated sand	38	1635	0,766	0,672
- with air		2020	1419	2,75
-with water				
Saturated coarse sand	34	1745	0,766	0,557
-with air		2080	1319	3,07
-with water				1,64
-with crude oil				
Saturated disaggregated tiles	40	1440	0,837	0,493
-with air		1840	1566	1,82
-with water				1,00
-with crude oil				
Saturated disintegrated silt	36	1540	0,846	0,585
-with air		1890	1476	1,79
-with water				0,96
-with crude oil				

Table 1.
Properties of porous media saturated with various fluids, at 32.2°C (90°F) [10].

The coefficient of thermal conductivity can be written as a scalar value in the case of isotropic media.

In the case of anisotropic media (inhomogeneous crystals or stratified rocks), the coefficient of thermal conductivity will be defined vectorially (in the directions of orientation):

$$\lambda_{jk} = \begin{Vmatrix} \lambda_{11} & \lambda_{12} & \lambda_{13} \\ \lambda_{21} & \lambda_{22} & \lambda_{23} \\ \lambda_{31} & \lambda_{32} & \lambda_{33} \end{Vmatrix} \tag{3}$$

Onsanger's postulate shows that the thermal conductivity matrix is symmetrical and therefore [11–13]:

Since the experiments did not confirm the existence of the rotary conduction $\lambda_{jk} = 0, \ \text{for} \, j \neq k$), the matrix (3) is reduced to the equation:

$$\lambda_{jk} = \lambda_{kj}, j \neq k \tag{4}$$

$$Q = -\lambda \bullet A \bullet grad\ T \tag{5}$$

2. Estimation of the equivalent thermal conductivity of petroleum fluid deposits

Thermal conductivity is that property defined as the heat flux (amount of heat) Q, which flows in a time τ, through a body with a given cross section and length, whose opposite faces are at temperatures t_1 and t_2:

$$\lambda = \frac{\Delta Q}{\Delta \tau} \bullet \frac{L}{A \Delta T} \tag{6}$$

The estimation of the thermal conductivity of the oil fluid deposits was made on the basis of theoretical models to describe this property and following the use of practical methods of determination in the laboratory.

The estimation of thermal conductivity can best be done based on virtual models of behavior of oil and gas fields.

The first model used to determine thermal conductivity was the series-developed geological layer model, with heat flow Q being directed perpendicular to the layers.

In this case, the thermal conductivity calculation relation can be written as:

$$\frac{1}{\lambda_z} = \frac{\Phi}{\lambda_f} + \frac{1 - \Phi}{\lambda_s} \tag{7}$$

Where:

- λ_f is the coefficient defining the thermal conductivity of the reservoir fluid, W/(m K),

- λ_s is the coefficient of thermal conductivity of the constituent rocks of the deposit, in which the oil fluids are located, W/(m K),

- Φ is the porosity of the rocks.

This model considers imperfections to be nonexistent and therefore a model developed for geological layers parallel to the direction of flow of the thermal flux was chosen.

The thermal conductivity equation of the petroleum fluid reservoir can be written as follows:

$$\lambda_z = \Phi\lambda_f + (1 - \Phi)\lambda_s \tag{8}$$

Where:

- λ_f is the coefficient defining the thermal conductivity of the reservoir fluid, W/(m K),

- λ_s is the coefficient of thermal conductivity of the constituent rocks of the deposit, in which the oil fluids are located, W/(m K),

- Φ is the porosity of the rocks.

This model takes into account the porosity of the rocks, but there are errors in the conductivity estimate due to the possibility of material inclusions in the reservoir's protective rocks.

A cumulative variant of the two models is expressed by the weighted geometric model, which considers that the oil fluid constituting the collecting rocks has the largest weight in the calculation of thermal conductivity:

$$\lambda_z = \lambda_f^{\Phi}\lambda_s^{1-\Phi} \tag{9}$$

where:

- λ_f is the coefficient defining the thermal conductivity of the reservoir fluid, W/(m K),

- λ_s is the coefficient of thermal conductivity of the constituent rocks of the deposit, in which the oil fluids are located, W/(m K),

- Φ is the porosity of the rocks.

Paper 14 presents a model for determining thermal conductivity, based on the Maxwell equation, which assumes the reduction of petroleum fluids to interacting spheres (Euken):

$$\lambda_z = \lambda_f \frac{2\Phi\lambda_f + (3 - 2\Phi)\lambda_s}{(3 - \Phi)\lambda_f + \Phi\lambda_s} \tag{10}$$

Where:

- λ_f is the coefficient defining the thermal conductivity of the reservoir fluid, W/(m K),
- λ_s is the coefficient of thermal conductivity of the constituent rocks of the deposit, in which the oil fluids are located, W/(m K),
- Φ is the porosity of the rocks.

For rocks with porosity $\Phi < 0.5$ and the thermal conductivity ratio of rocks and fluids, λs/λf, in the range 1 ÷ 300, the thermal conductivity was expressed by Beck's relation:

$$\lambda_z = \lambda_s \left[\frac{\left(2\frac{\lambda_s}{\lambda_f} + 1\right) - 2\Phi\left(\frac{\lambda_s}{\lambda_f} - 1\right)}{\left(2\frac{\lambda_s}{\lambda_f} + 1\right) + \Phi\left(\frac{\lambda_s}{\lambda_f} - 1\right)} \right] \tag{11}$$

Where:

- λ_f is the coefficient defining the thermal conductivity of the reservoir fluid, W/(m K),
- λ_s is the coefficient of thermal conductivity of the constituent rocks of the deposit, in which the oil fluids are located, W/(m K),
- Φ is the porosity of the rocks.

The model developed by Vries is based on the idea that the constituent rocks of the oil reservoir consist of ellipsoidal particles dispersed in the oil fluid being analyzed.

$$\lambda_z = \frac{\Phi\lambda_f + (1 - \Phi)G\lambda_s}{\Phi + (1 - \Phi)\rightleftarrows G} \tag{12}$$

Where:

$$G = \frac{1}{3}\sum_{j=1}^{3}\left[1 + \left(\frac{\lambda_s}{\lambda_f} - 1\right)\xi_j\right]^{-1} \text{ş}i \sum_{j=1}^{3}\xi_j = 1 \tag{13}$$

and:

- λ_f is the coefficient defining the thermal conductivity of the reservoir fluid, W/(m K),
- λ_s is the coefficient of thermal conductivity of the constituent rocks of the deposit, in which the oil fluids are located, W/(m K),
- Φ is the porosity of the rocks.

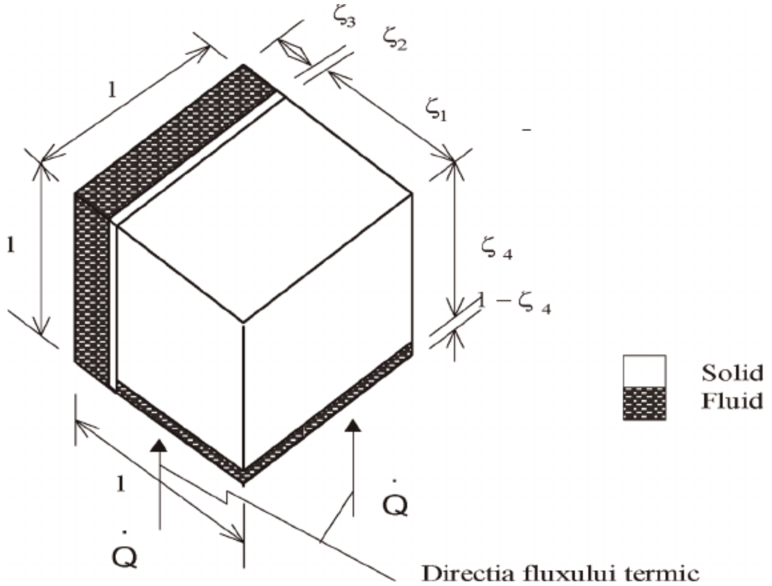

Figure 1.
Schematic of the model for calculating the thermal conductivity of petroleum fluid deposits taking into account the possibility of considering a resistor-type structure (Wyllie and Southwick) [14].

In relation 13, ξ_j is a parameter that defines the shape of the particles.

If $\xi_1 = \xi_2 = \xi_3$. then Eq. 13 reduces to Eq. 10. Also de Vries considered that $\xi_1 = \xi_2 = 1/8$, $\xi_3 = 3/4$, the oil deposit consists of ellipsoids of resolution with the long axis equal to six times the short axis.

The model developed by Woodside and Messmer (**Figure 1**) is a model resulting from the determination of conductivity by heating rocks and oil fluids with electromagnetic bridges and determining this property from the idea that the oil reservoir is made up of a series of particles and electolite over which geological structures are arranged in parallel.

$$\lambda_z = \frac{\zeta_1 \lambda_s \lambda_f}{\lambda_s (1-\zeta_4) + \zeta_4 \lambda_f} + \zeta_2 \lambda_s + \zeta_3 \lambda_f \tag{14}$$

Where:

- λ_f is the coefficient defining the thermal conductivity of the reservoir fluid, W/(m K),
- λ_s is the coefficient of thermal conductivity of the constituent rocks of the deposit, in which the oil fluids are located, W/(m K),
- Φ is the porosity of the rocks.

In Eq. 14, the coefficients ζ_1, ζ_2, ζ_3, ζ_4 have values given by certain forms of rock and electrolyte arrangement.

These values of the parameters ζ_1, ζ_2, ζ_3, ζ_4 are required for the calculation of the equivalent electrical conductivity.

The use of the relation (14) for the calculation of the thermal conductivity of an unconsolidated oil fluid field leads to values very close to those obtained experimentally, when the following coefficients are used:

$$\zeta_2 = 0, \zeta_3 = \Phi - 0,03, \zeta_1 = 1 - \zeta_3, \zeta_4 = \frac{(1-\Phi)}{\zeta_1} \tag{15}$$

And this model has errors in calculating the real value of thermal conductivity, based on the idea of forming the oil field from electrolytic systems (optimal heat transfer).

Analyzing 165 thermal conductivity values, where the optimal calculation porosity was between 0.215 and 0.476, *Krupiczka* was found that in 76% of the values calculated with relation 16, the difference between the values obtained experimentally and those calculated has errors of ±30%,

The calculation formula for calculating the thermal conductivity proposed by this model is:

$$\lambda_z = \lambda_f \left(\frac{\lambda_s}{\lambda_f}\right)^{A' + \grave{B}\, log\frac{\lambda_s}{\lambda_f}} \tag{16}$$

Where:

$$A^{,} = 0,280 - 0,757 log\Phi \text{ şi} B^{,} = -0,057 \tag{17}$$

and:

- λ_f is the coefficient defining the thermal conductivity of the reservoir fluid, W/(m K),
- λ_s is the coefficient of thermal conductivity of the constituent rocks of the deposit, in which the oil fluids are located, W/(m K),
- Φ is the porosity of the rocks.

3. Evaluation of thermal conductivity simulation models

Following the experiments on the cores extracted from potential areas supplying oil fluids, we managed to determine the conductivity of the rocks, their porosity and density.

The data obtained were used to simulate the thermal conductivity of deposits saturated with gas, water (density is 1000 kg/m^3), pure crude oil (density is 790 kg/m^3), and crude oil mixed with 35% water ((density is 863 kg/m ^{3}).

At the same time, we created our own model for simulating thermal conductivity, based on the statistical interpretation of the data obtained from the calculations performed with five analyzed models (**Tables 2–5**).

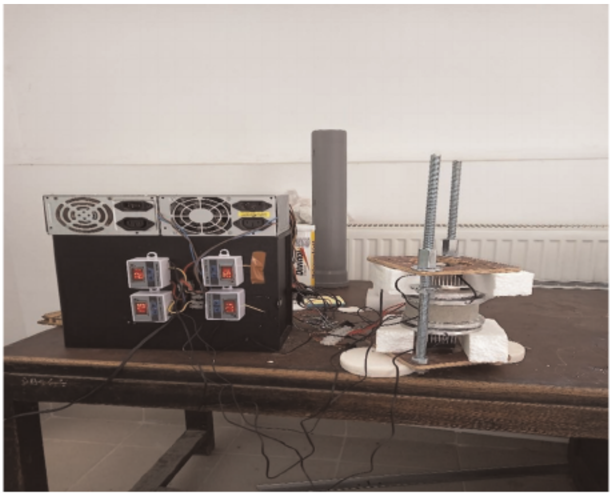

Figure 2.
Thermal conductivity tester.

The model developed in this paper starts from the idea that the analyzed rock is not pure (i.e., the density of the analyzed rock was introduced in the calculation).

The model was tested on the cores analyzed in the apparatus of **Figure 2** and shown in the tables below for all existing fluids in the field.

We also introduced porosity in the calculation as a basic factor in the calculation of total conductivity.

$$\lambda_z = \frac{1}{\left(\rho_r\right)} \bullet \left(\lambda_f^{(1-\theta)} \bullet \lambda_f^{\theta}\right) \tag{18}$$

Where:

- λ_f is the coefficient defining the thermal conductivity of the reservoir fluid, W/(m K),
- λ_s is the coefficient of thermal conductivity of the constituent rocks of the deposit, in which the oil fluids are located, W/(m K),
- Φ is the porosity of the rocks,
- ρ_r is density of the rocks, kg/m^3,
- λ_z is conductivity of fluids of the reservoir, W/m K,

Figures 3–**6** give the differences between the calculated values of thermal conductivity with the six models, with porosity and thermal conductivity (kr) determined using the apparatus in **Figure 2**.

Figures 7 and **8** show the calculated thermal conductivity values with the six models according to literature data.

Rock type	**k_r W/mK**	**porosity, (10%)**	**Series model k_z**	**Parallel model k_z**	**Weighted geometric model, k_z**	**Beck model k_z**	**Model Krupiczka k_z**	**Chiș, Jugăstreanu k_z**
Cracked limestone chalk	0,831,936	0,5	4,45	0,48	0,294	0,42	1,35	1,07
Chalk	1,145,466	2,2	15,88	1,09	0,405	−0,50	1,21	1,37
Compact clay	0,267,246	1,9	11,25	0,01	0,094	0,04	0,34	0,35
Marl	0,285,348	1,2	8,53	0,10	0,101	0,11	0,38	0,37
Chalk	0,476,826	1,3	9,37	0,03	0,168	0,06	0,61	0,61
Conglomerate	0,454,902	1,2	8,79	0,07	0,161	0,08	0,60	0,63
Compact clay	0,723,492	1,5	10,85	0,17	0,256	0,06	0,89	0,95
Compact clay	0,814,926	1,9	13,51	0,49	0,288	0,22	0,93	1,05
Floor tiles	0,878,766	1,99	14,18	0,61	0,311	0,28	0,99	1,12
Cracked limestone/ dolomite	0,701,568	1,02	7,82	0,12	0,248	0,12	0,95	1,08
Compact limestone	0,826,812	3	20,66	1,26	0,292	0,51	0,84	1,04
Compact limestone/ dolomite	0,869,232	1,5	10,96	0,24	0,307	0,10	1,05	1,09
Marne with inclusions	0,38,199	1,4	9,72	0,03	0,135	0,06	0,49	0,54
Limestone tiles	0,635,334	1,1	8,30	0,08	0,225	0,09	0,84	0,83
Chalk	0,664,734	1,5	10,79	0,14	0,235	0,04	0,82	0,85

Table 2.
The values of thermal conductivity calculated with simulation models, the fluid in the rock is crude oil.

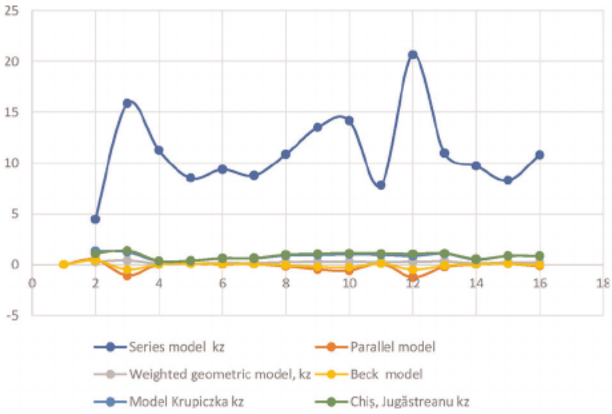

Figure 3.
The variation of the conductivity parameters of the analyzed deposits of the fluid contained in the rocks is crude oil.

Rock type	k_r W/mK	porosity, (10%)	Series model k_z	Parallel model k_z	Weighted geometric model, k_z	Beck model k_z	Model Krupiczka k_z	Chiș, Jugăstreanu k_z
Rock type	0,83	0,5	0,23	0,23	0,301	0,43	1,32	1,09
Cracked limestone chalk	1,15	2,2	0,06	0,06	0,414	0,50	1,19	1,40
Chalk	0,27	1,9	0,09	0,09	0,097	0,05	0,33	0,36
Compact clay	0,29	1,2	0,12	0,12	0,103	0,11	0,37	0,38
Marl	0,48	1,3	0,11	0,11	0,172	0,06	0,60	0,62
Chalk	0,45	1,2	0,12	0,12	0,164	0,09	0,58	0,64
Conglomerate	0,72	1,5	0,09	0,09	0,262	0,06	0,87	0,98
Compact clay	0,81	1,9	0,08	0,08	0,295	0,22	0,91	1,08
Compact clay	0,88	1,99	0,07	0,07	0,318	0,28	0,97	1,15
Floor tiles	0,70	1,02	0,13	0,13	0,254	0,12	0,92	1,10
Cracked limestone/ dolomite	0,83	3	0,05	0,05	0,299	0,51	0,82	1,07
Compact limestone	0,87	1,5	0,09	0,09	0,314	0,10	1,03	1,11
Compact limestone/ dolomite	0,38	1,4	0,11	0,11	0,138	0,06	0,48	0,55
Marne with inclusions	0,64	1,1	0,12	0,12	0,230	0,10	0,82	0,84
Limestone tiles	0,66	1,5	0,10	0,10	0,240	0,04	0,80	0,87

Table 3.
The values of thermal conductivity calculated with simulation models, the fluid in the rock is water and crude oil.

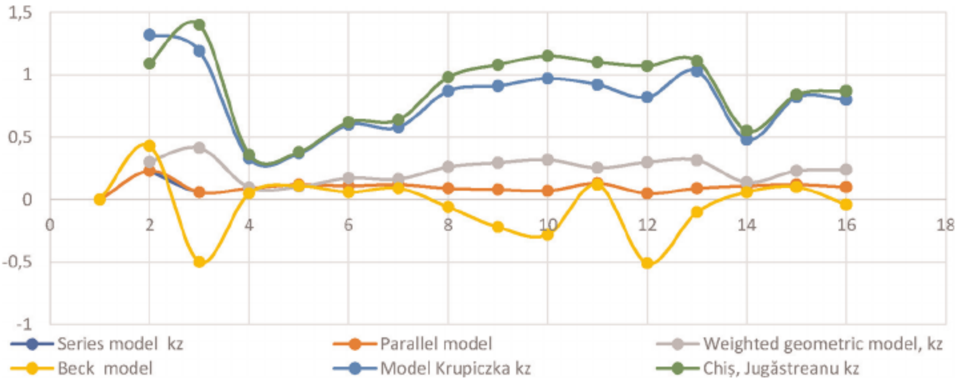

Figure 4.
The variation of the conductivity parameters of the analyzed deposits of the fluid contained in the rocks is water and crude oil.

Rock type	k_r W/mK	porosity, (10%)	Series model k_z	Parallel model k_z	Weighted geometric model, k_z	Beck model k_z	Model Krupiczka k_z	Chiş, Jugăstreanu k_z
Rock type	0,83	0,5	0,70	0,72	1382	0,72	0,25	5,01
Rock type	1,15	2,2	0,39	0,03	1902	0,15	0,31	6,45
Cracked limestone chalk	0,27	1,9	3,88	0,92	0,444	1,33	0,08	1,65
Chalk	0,29	1,2	0,79	0,68	0,474	0,71	0,08	1,76
Compact clay	0,48	1,3	0,67	0,65	0,792	0,66	0,14	2,87
Marl	0,45	1,2	0,66	0,64	0,756	0,65	0,13	2,95
Chalk	0,72	1,5	0,57	0,55	1202	0,56	0,21	4,48
Conglomerate	0,81	1,9	0,50	0,43	1353	0,45	0,23	4,96
Compact clay	0,88	1,99	0,47	0,35	1460	0,39	0,24	5,27
Compact clay	0,70	1,02	0,61	0,61	1165	0,61	0,20	5,07
Floor tiles	0,83	3	0,40	0,18	1373	0,28	0,23	4,90
Cracked limestone/ dolomite	0,87	1,5	0,53	0,48	1444	0,50	0,25	5,10
Compact limestone	0,38	1,4	0,80	0,70	0,634	0,73	0,11	2,54
Compact limestone/ dolomite	0,64	1,1	0,61	0,61	1055	0,61	0,18	3,88
Marne with inclusions	0,66	1,5	0,59	0,58	1104	0,59	0,19	4,00

Table 4.
The values of thermal conductivity calculated with simulation models, the fluid in the rock is water.

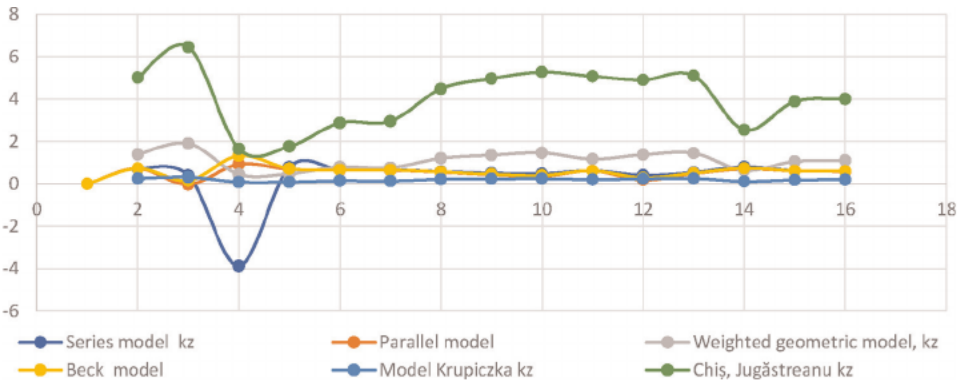

Figure 5.
The variation of the conductivity parameters of the analyzed deposits of the fluid contained in the rocks is water.

Rock type	k_r W/ mK	porosity, (10%)	Series model k_z	Parallel model k_z	Weighted geometric model, k_z	Beck model k_z	Model Krupiczka k_z	Chiş, Jugăstreanu k_z
Rock type	0,83	0,5	0,07	0,43	0,077	0,36	5,91	0,28
Rock type	1,15	2,2	0,02	1,30	0,106	0,62	3,99	0,36
Cracked limestone chalk	0,27	1,9	0,02	0,18	0,025	0,08	1,15	0,09
Chalk	0,29	1,2	0,03	0,02	0,026	0,00	1,40	0,10
Compact clay	0,48	1,3	0,03	0,10	0,044	0,05	2,24	0,16
Marl	0,45	1,2	0,03	0,05	0,042	0,02	2,20	0,16
Chalk	0,72	1,5	0,02	0,31	0,067	0,17	3,14	0,25
Conglomerate	0,81	1,9	0,02	0,67	0,075	0,34	3,15	0,28
Compact clay	0,88	1,99	0,02	0,80	0,081	0,40	3,30	0,29
Compact clay	0,70	1,02	0,03	0,02	0,065	0,02	3,60	0,28
Floor tiles	0,83	3	0,01	1,55	0,076	0,62	2,59	0,27
Cracked limestone/ dolomite	0,87	1,5	0,02	0,38	0,080	0,21	3,73	0,28
Compact limestone	0,38	1,4	0,02	0,11	0,035	0,05	1,76	0,14
Compact limestone/ dolomite	0,64	1,1	0,03	0,03	0,059	0,01	3,16	0,22
Marne with inclusions	0,66	1,5	0,02	0,28	0,061	0,15	2,90	0,22

Table 5.
The values of thermal conductivity calculated with simulation models, the fluid in the rocks is natural gases.

The relative error (**Tables 7–9**) of the computationally determined data with the six models compared with the literature data shows that the Chiș model is closest to the values determined in other laboratories.

The error is due to the fact that the analyzed samples are impure.

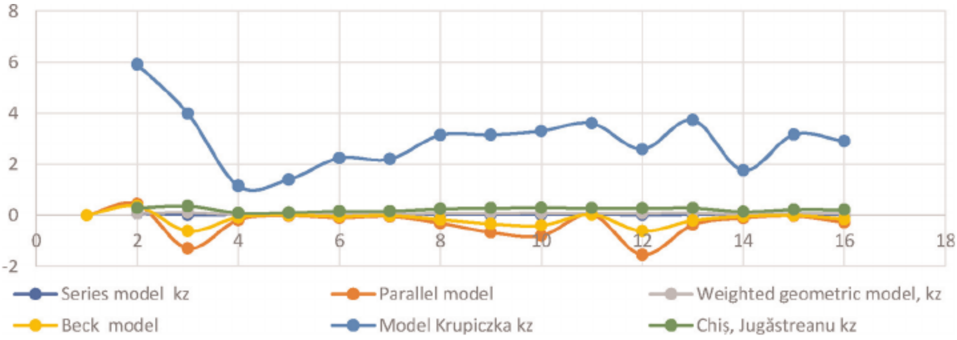

Figure 6.
*Variation of the conductivity parameters of the analyzed deposits of the fluid contained in the rocks is natural gases (**Table 6**).*

Fluid-saturated porous medium	Thermal conductivity W/mK, k_l	Series model k_z	Parallel model k_z	Weighted geometric model, k_z	Beck model k_z	Model Krupiczka k_z	Chiș, Jugăstreanu k_z
with air	0,877	0,02	0,80	0,081	0,40	3,30	0,29
with water	2,75	0,47	0,35	1460	0,39	0,24	5,27
with oil	1,36	14,18	0,61	0,311	0,28	0,99	1,12
with oi land gas	2,47	0,07	0,07	0,318	0,28	0,97	1,15

Table 6.
*Thermal conductivity values calculated with simulation models and taken from the literature (**Table 1** and references [10]) for saturated tiles.*

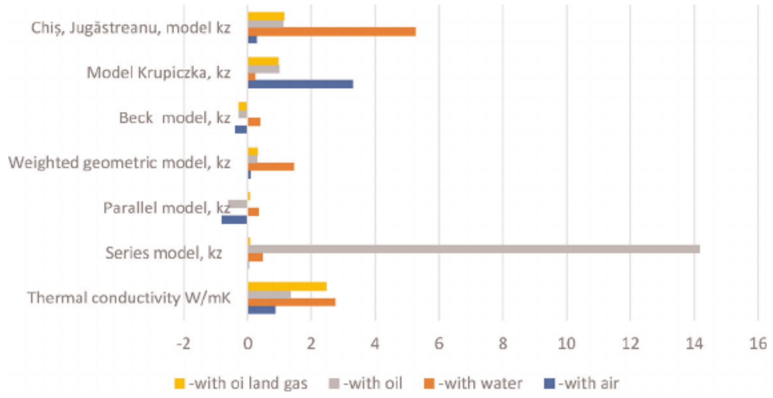

Figure 7.
Thermal conductivity values calculated with simulation models and taken from the literature for saturated tiles.

Fluid-saturated porous medium	Thermal conductivity W/mK, kl	Series model kz	Parallel model kz	Weighted geometric model, kz	Beck model kz	Model Krupiczka kz	Chiş, Jugăstreanu kz
-with air	0,88	0,98	1,91	0,91	1,46	2,76	0,67
-with water	2,75	0,83	0,87	0,47	0,86	0,91	0,92
-with oil	1,36	9,43	1,45	0,77	1,21	0,27	0,18
-with oil land gas	2,47	0,97	0,97	0,87	1,11	0,61	0,53

Table 7.
Relative error of the chosen model calculation based on literature values for saturated tiles.

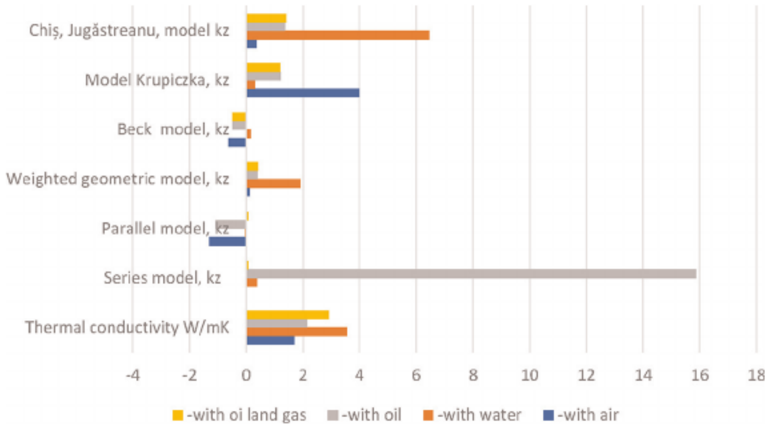

Figure 8.
Thermal conductivity values calculated with simulation models and taken from the literature for chalk.

Fluid-saturated porous medium	Thermal conductivity W/mK, k_l	Series model k_z	Parallel model k_z	Weighted geometric model, k_z	Beck model k_z	Model Krupiczka k_z	Chiş, Jugăstreanu, model k_z
-with air	1,7	0,02	1,30	0,106	0,62	3,99	0,36
-with water	3,55	0,39	0,03	1902	0,15	0,31	6,45
-with oil	2,15	15,88	1,09	0,405	0,50	1,21	1,37
-with oi land gas	2,92	0,06	0,06	0,414	0,50	1,19	1,40

Table 8.
*Thermal conductivity values calculated with simulation models and taken from the literature (**Table 1** and references [15]) for chalk.*

Fluid-saturated porous medium	Thermal conductivity W/mK, kl	Series model kz	Parallel model kz	Weighted geometric model, kz	Beck model kz	Model Krupiczka kz	Chiş, Jugăstreanu kz
-with air	0,88	0,99	1,76	0,94	1,36	1,35	0,79
-with water	2,75	0,89	1,01	0,46	0,96	0,91	0,82
-with oil	1,36	6,39	1,51	0,81	1,23	0,44	0,36
-with oil land gas	2,47	0,98	0,98	0,86	1,17	0,59	0,52

Table 9.
Relative error of the chosen model calculation based on literature values for chalk.

4. Conclusion

Analyzing the values obtained through models with data from the literature, we can say the following:

- The values closest to the data from the specialized literature are offered by the Chis model, Jugastreanu,
- The parallel model and the Beck model provide negative conductivity results,
- The Chiş model, Jugastreanu has errors in the calculation of the thermal conductivity of the deposits affected by water, because the reservoir water was not introduced in the calculation but water without salinity,
- Air testing, compared with the calculation of the conductivity of rocks with natural gas, brings higher values of the conductivity of the deposits.

In conclusion, we can say that the theoretical models for calculating the thermal conductivity coefficient are useful in defining how to establish the optimal tertiary oil recovery technique, but for the correct estimation of the amount of petroleum products in the field, it is necessary to determine this property (thermodynamic coefficient) by laboratory analysis.

References

[1] Abdulagatova ZZ, Abdulagatov IM, Emirov SN. Effect of pressure, temperature, and oilsaturation on the thermal conductivity of sandstone up to 250 MPa and 520 K. Journal of Petroleum Science and Engineering. 2010;**73**:141-155

[2] Alishaev MG, Abdulagatov IM, Abdulagatova ZZ. Effective thermal conductivity of fluid saturated rocks: Experiment and modeling. Engineering Geology. 2012;**135–136**:24-39

[3] Burger J, Sourieau P, Combarnous M. Title Thermal Methods of Oil Recovery. Houston, TX: Gulf Pub; 1986

[4] Cai KP, Fan SH, Zhang BJ, et al. Reservoir on sedimentation diagenetic feature and reservoir relationship of Shaximiao formation in South District of West Sichuan. Natural Gas Exploration & Development. 2004;**27**(3):11-17 (in Chinese with English Abstract)

[5] Woodside W, Messmer J. Thermal conductivity of porous media: I. unconsolidated sands. Journal of Applied Physics. 1961;**32**:1688-1699

[6] Woodside W, Messmer J. Thermal conductivity of porous media: II. Consolidated sands. Journal of Applied Physics. 1961;**32**:1699-1706

[7] Ray L, Bhattacharya A, Roy S. Thermal conductivity of higher Himalayan Crystallines from Garhwal Himalaya. India Tectonophysics. 2007; **434**:71-79

[8] Ren JS. On the post-Variscan global tectonic stages. Acta Geologica Sinica. 1987;**61**(1):21-31 (in Chinese with English Abstract)

[9] Tabatabai SM, Jugastreanu C, Chis T. Mathematical modeling of the geothermal gradient of oil and gas deposits. International Journal of Engineering Research and Applications. 2022;**12**(2):21-27 (Series-I) indexată în Google Scholar

[10] Jugastreanu C, Tabatabai SM, Chis T. Thermal properties of oil and gas reservoires rocks modeling. International Journal of Research – GRANTHAALAYAH. 2022;**10**(2): 125-144

[11] Tabatabai SM, Jugastreanu C, Chis T. New equation of geophysical prospecting of oil and gas field. IOSR Journal of Applied Geology and Geophysics (IOSR-JAGG). 2022;**10**(1): 25-32

[12] Jugastreanu C, Tabatabai SM, Chis T. History of research on the thermal regime of oil and gas fields. International Journal of Innovations in Engineering and Technology. February 2022;**21**(3): 37-43. ISSN: 2319-1058. DOI: 10.21172/ijiet.213.05

[13] Jugastreanu CR, Petrache ST, Chis T. The impact of offshore seismic studies on the marine environment. American Journal of Engineering Research (AJER). 2021;**10**(8):109-113

[14] Jugastreanu CR, Petrache ST, Chis T. Numerical modeling of oil pollution. International Journal of Engineering Science Invention (IJESI). 2021;**10**(7): 56-60

[15] Petrache S, Jugastreanu CR, Chis T. Numerical modeling of sulfur removal from waste gas from oil refining process. International Journal of Engineering Research and Applications. 2021;**11**(7): 12-16